THE ROLE OF PASSIVE JOINT STIFFNESS AND ACTIVE KNEE CONTROL IN ROBOTIC LEG SWINGING: APPLICATIONS TO DYNAMIC WALKING

A Thesis
Presented to
The Academic Faculty

by

Shane A. Migliore

In Partial Fulfillment
of the Requirements for the Degree
Doctor of Philosophy in Electrical and Computer Engineering in the
School of Electrical and Computer Engineering

Georgia Institute of Technology
April 2008

THE ROLE OF PASSIVE JOINT STIFFNESS AND ACTIVE KNEE CONTROL IN ROBOTIC LEG SWINGING: APPLICATIONS TO DYNAMIC WALKING

Approved by:

Dr. Stephen P. DeWeerth, Advisor
School of Electrical and Computer
Engineering
Georgia Institute of Technology

Dr. Lena Ting
School of Electrical and Computer
Engineering
Georgia Institute of Technology

Dr. Robert Butera
School of Electrical and Computer
Engineering
Georgia Institute of Technology

Dr. Ayanna Howard
School of Electrical and Computer
Engineering
Georgia Institute of Technology

Dr. Charlie Kemp
School of Electrical and Computer
Engineering
Georgia Institute of Technology

Date Approved: December 03, 2007

ACKNOWLEDGEMENTS

An interdisciplinary project of this magnitude invariably requires the assistance and support of many people. The foundations of this doctoral work began in 2001 and lasted nearly six and a half years. Throughout this time, I had the pleasure of working with many very talented graduate students in fields ranging from neuroscience to mechanical engineering who provided me with invaluable advice and expertise. I would especially like to thank: Mike Reid for always having well-documented answers to my many questions and for providing excellent technical writing reviews; Kartik Sundar for his expertise in the real-time control of robotic hardware and for all of his eleventh-hour assistance as I struggled to complete my dissertation on time; Jim Ross for his creativity and ability to always lighten the mood; Jevin Scrivens for his mechanical design expertise; Carrie Williams for her help with the development and analysis of Matsuoka oscillator-based controllers; and Richard Blum for his circuit design expertise. Others who have also provided technical, motivational, and social support have included Kate Williams and her "Tiffany cuff links"[1], Kyla Ross, Michael Sorensen, Scott Buscemi, Alex Bragg, Joanna Todd, Amanda Zimmerman, Chris Lessing, Frank Lin, Shawn O'Connor, Murat Sekerli, Randy Weinstein, William Gerken, Luke Purvis, Brock Wester, Torrence Welch, and Lucas McKay.

I would like to thank the faculty and staff of the Laboratory for Neuroengineering for providing a quality research environment that continues to expand and strengthen, especially Edgar Brown, Dr. Stefan Clemens, Amber Burris, Bryan Williams, and Jon Hall.

I would like to thank the members of my committee for their direction as I navigated through the tumultuous dissertation process: Dr. Lena Ting, Dr. Charlie Kemp, Dr. Robert Butera, and Dr. Ayanna Howard.

I would like to thank my advisor, Dr. Stephen DeWeerth, for his guidance and support

---

[1]See the movie *Full Metal Jacket.*

TABLE OF CONTENTS

LIST OF TABLES

LIST OF FIGURES

SUMMARY

The field of autonomous walking robots has been dominated by the trajectory-control approach, which rigidly dictates joint angle trajectories at the expense of both energy efficiency and stability, and the passive dynamics approach, which uses no actuators, relying instead on natural mechanical dynamics as the sole source of control. Although the passive dynamics approach is energy efficient, it lacks the ability to modify gait or adapt to disturbances. Recently, *minimally actuated walkers*, or *dynamic walkers*, have been developed that use hip or ankle actuators—knees are always passive—to regulate mechanical energy variations through the timely application of joint torque pulses. Despite the improvement minimal actuation has provided, energy efficiency remains below target values and perturbation rejection capability (*i.e.,* stability) remains poor. In this dissertation, we develop and analyze a simplified robotic system to assess biologically inspired methods of improving energy efficiency and stability in dynamic walkers. Our system consists of a planar, dynamically swinging leg with hip and knee actuation. Neurally inspired, nonlinear oscillators provide closed-loop control without overriding the leg's natural dynamics. We first model the passive stiffness of muscles by applying stiffness components to the joints of a hip-actuated swinging leg. We then assess the effect active knee control has on unperturbed and perturbed leg swinging. Our results indicate that passive joint stiffness improves energy efficiency by reducing the actuator work required to counter gravitational torque and by promoting kinetic energy transfer between the shank and thigh. We also found that active knee control 1) is detrimental to unperturbed leg swinging because it negatively affects energy efficiency while producing minimal performance improvement and 2) is beneficial during perturbed swinging because the perturbation rejection improvement outweighs the reduction in energy efficiency. By analyzing the effects of applying passive joint stiffness and active knee control to dynamic walkers, this work helps to bridge the gap between the performance capability of trajectory-control robots and the energy-efficiency of passive dynamic robots.

CHAPTER I

INTRODUCTION

In contrast to their prevalent and commonly antagonistic role in science fiction, robots have traditionally been confined to bleak roles on the manufacturing floor, performing low-level, routine tasks that remove both the need for human labor and the chance of human error. Because these industrial machines offer little, if any, of the adaptability of humans, their tasks must be well-defined and their environments must be highly controlled. These requirements necessarily prevent physical human interaction; "working envelopes" are typically established for each robot that humans must avoid to prevent serious injury [118].

Although industrial automation robots will continue to exist for the foreseeable future, their dominance of the field of robotics is being threatened by the development of autonomous robots that can operate in unpredictable environments and can physically interact with humans. For example, *partner robots* are being designed with the intention of providing the elderly and disabled with home healthcare assistance and companionship [52, 67]. Robots are also being developed for tasks such as exploration or search and rescue in regions that are remote or hazardous to humans. To provide practical benefit, these autonomous robots must be capable of adapting to constantly changing environments in an energy-efficient manner.

The development of robotic technology that closely emulates the mechanics and control of biological systems may increase the energy efficiency, stability, and capabilities of robots. To explore this possibility, the method by which robots actuate their joints and control their movements must be modeled as close as possible to biology. For land-based locomotion, this typically means implementing robotic legs since many diverse species use them to maneuver through uneven terrain, to avoid obstacles, and to manage various types of discontinuities (*e.g.,* span gaps, climb stairs). Legs have been used by robots to perform

a diverse set of movements, including jumping, squatting, kicking, pushing, and manipulating their environment, although their implementation and control techniques often lack similarity to biology.

Bipedal robots are typically designed using either the trajectory-control approach, which rigidly dictates joint angles, or the passive dynamics approach, which uses no actuators and requires a small downhill slope for input energy. Although trajectory control is the more prevalent approach and is used by many of the most advanced robots, it suffers from poor energy efficiency, task specificity, and high sensitivity to sensor/actuator accuracy. The passive dynamics approach mimics natural joint mechanics well because joint trajectories arise naturally from the robots' passive dynamics. However, this approach lacks the higher-level control needed for tasks such as initiating locomotion, changing gait, or adapting to disturbances.

In this research, we combine principles of the trajectory-tracking and passive dynamic approaches to create an energy efficient, stable, "naturally actuated" robotic leg. Our long-term goal is to design and build a human-sized bipedal robot capable of a wide range of tasks, such as walking, running, jumping, and maintaining balance. As a first step, this research focuses on the design, fundamental actuation, and basic control principles for a single, planar robotic leg with hip and knee actuation. We use neurally inspired, nonlinear oscillators at each joint to provide closed-loop control without overriding the leg's natural dynamics. In this manner, the leg can produce energy efficient resonant motion, while the controller provides real-time adaptation to environmental perturbations.

1.1 Background and Significance

This section provides background and a literature review of legged robot locomotion, the neural control rhythmic movement, and the analysis of rhythmic movement using principles from nonlinear dynamics. These topics provide the motivation for our approach, and they serve as the basis for making recommendations regarding future robot development.

1.1.1 Approaches to Legged Locomotion

The bipedal robotics community is largely divided into two groups—those who favor precise actuation of joint trajectories and those who prefer to exploit the passive dynamic movements of mechanisms as a source of control. Animals, however, use elements of both approaches, depending on the task at hand.

1.1.1.1 Trajectory-Control Approach

Trajectory control is the more prevalent approach to robotic joint control and is used by many of the most advanced robots, including ASIMO [45], WABIAN [135, 86], JOHN-NIE [65], QRIO [28], HRP-2 [55], RABBIT [102], KHR-2 [57], Lucy [120], and BIP [3]. The reference trajectories for the joints can either be 1) anthropomorphic trajectories that mimic an animal's joint kinematics or 2) predetermined joint angle/torque trajectories optimized for a given task. Online control in these robots is achieved using complex algorithms, such as the zero moment point (ZMP) criterion [121], to calculate desired angle or force trajectories offline [12]. These trajectories are then used by online motor controllers (*e.g.,* PID), which compare desired and current limb positions and determine the most appropriate motor command signals. This approach requires controllers to use precise models of the robot's dynamics, and it requires the robots either to have accurate *a priori* knowledge of its environment or to have sensors that can quickly and sufficiently detect relevant details of the environment [35]. The accuracy of the algorithms and corresponding motor controllers is limited by the robot's joint actuation accuracy. Thus, two common optimizations used in these robots are: 1) high-gain feedback loops that are used to maximize the apparent output inertia of the motors and override the natural dynamics of the appendage and 2) algorithms that actuate joints in a manner that cancels out joint interaction torques.

Four primary drawbacks exist for the trajectory-control approach. The first is the lack of true autonomy that results from the need for predetermined functionality. Even advanced versions of this approach, which use online adaptation, select appropriate responses from a finite number of known routines. Thus, there is an inherent difficulty to adapt to scenarios that have not been considered by the designers. Despite the lack of full autonomy,

this approach has been shown effective in the control of posture and walking in controlled environments [45, 28] because, in both of these tasks, all constraints are known and static stability can be maintained. Static stability is defined as the maintenance of a robot's center of gravity projection within its base of support [125].

The second drawback to the trajectory-control approach is the reliance on static, rather than dynamic, stability. In dynamically stable locomotion, the periodic gait is stable, but the limb movements cannot be stopped at an arbitrary point in time without a fall occurring. For example, during each step in normal human walking, the body effectively "falls" forward after mid-stance until the swing foot is placed in front of the body to catch its weight. If the swing-leg foot is not placed correctly, the person can fall [4]. Statically stable robots, however, can at all times be stopped without a loss of balance because they restrict the effects of passive leg movements and constantly bend their knees so that balance is maintained and singularities are prevented [84]. As a result, these robots walk with leg kinetics and kinematics that do not match those of the animals they are attempting to emulate.

The third drawback to the trajectory-control approach is the high energy consumption that occurs. Because legs swing most efficiently at their natural frequency, this method, which constantly applies torques to the legs that force them to follow specific trajectories, can waste energy. Furthermore, because these robots rely on static stability, they specifically avoid singularities by maintaining a bent-knee posture [61]. Singularities at the knee are exploited by humans to provide an energy-efficient means of supporting the body's weight [81]. By maintaining an unnatural, bent-knee posture, these robots must continuously expend energy to maintain weight support. The bent-knee posture also requires that during step-to-step transitions, energy must simultaneously expended to produce positive work with one leg and negative work with the other [61]. The energy efficiency that results from this approach can be quantified by calculating the *specific cost of transport*, which is a dimensionless quantity equal to the energy needed to move a unit weight a unit distance [117]. Using this measure, human walking is found to be an order of magnitude more efficient in humans than in ASIMO, which uses ZMP-based control [16].

The forth drawback to the trajectory-control approach is the need for highly accurate actuators and sensors. Inaccurate actuators can produce errant movements that may destabilize the robot, while inaccurate sensors may incorrectly report joint movements or disturbances [60]. Furthermore, because, in general, motor controllers require real-time feedback for proper operation, any delays in the feedback loop can be destabilizing. Despite these four drawbacks, many robots continue to perform statically stable walking because it provides total control of the robot at all times and therefore has a lower risk of falling than other approaches in controlled environments.

1.1.1.2   Passive Dynamics Approach

Another approach to robot locomotion control—inspired by a walking toy—exploits the passive mechanics of a robot as the sole source of control [97, 74]. Because these robots have no actuators, they require a small downhill slope to compensate for the energy losses that occur at heel-strike, at knee-lock, and as a result of joint friction [62]. With careful design, dynamically stable locomotion can be physically and computationally produced in either two [87, 74, 75, 76, 60] or three [17, 133, 131] dimensions. These robots use a limit cycle-based control scheme that often has a small stability region. As a result, perturbations, inappropriate initial conditions, or variations in the slope angle can cause excessively high or low energy levels and cause destabilizing limit cycle deviations. To increase the stability region, *minimally actuated walkers* (also called *dynamic walkers*) have been developed that use their actuators strictly to compensate for variations in mechanical energy [89, 133, 16, 131]. The actuators used in this type of robot do not *control* joint trajectories, but rather they regulate the robot's mechanical energy level through the application of joint torques [60, 16]. Because dynamic walkers remain largely passive throughout much of their gait cycle, their energy efficiency can match that of human walking [16]. However, Tad McGeer, who developed the original passive dynamic walker, and others in the dynamic walking community expect that agile walkers can be developed that operate at twice the efficiency of humans [77].

Despite the improvement provided by minimal actuation, low stability remains the primary disadvantage of dynamic approach to robotic walking. One source of instability is the lack of continuous, closed-loop control by the joint actuators. Current dynamic walkers use state-machine controllers that inject energy impulsively at discrete points in the gait cycle (*e.g.,* at toe-off [60, 16]). This type of controller cannot provide immediate recovery torques for perturbations that occur between the gait cycle points (*e.g.,* during leg swing) As a result, the robot may fall before the controller can attempt recovery.

Another related source of instability is that all dynamic walkers have been designed with passive knees that cannot respond actively to perturbations [133, 16, 131]. Passive knees have been implemented because they best emulate the traditional view of walking as a primarily ballistic behavior [81]. To improve efficiency, these robots exploit the singularity at knee extension by latching it during stance and release it at the beginning of swing. In human studies, however, the knee has been shown to provide a larger active response to swing-leg perturbations than either the hip or ankle [29]. Whether the stability of dynamic robots could be improved by adding minimal actuation to the knee remains an open question.

1.1.1.3 Biological Approach

As mentioned, robots are typically designed to use either the trajectory-control or the passive dynamics approach. Animals, however, regularly use elements of both, depending on the task it faces. For example, during undisturbed walking, it is energetically most efficient to allow the swing leg to rotate forward at its natural angular velocity with minimal muscle use [78, 81]. This most closely resembles the minimally actuated walkers mentioned in Section 1.1.1.2. Leg swing is influenced by muscles [93], however, and there are times when the natural leg dynamics must be overridden either to preserve stability in the presence of perturbations [91] or to more precisely control joint movements in complex environments or during complex tasks. In these scenarios, the more complex and precise control techniques common in the trajectory-control approach become necessary because the passive dynamic approach would produce instability.

1.1.2 Neural Control of Rhythmic Locomotion

Legged locomotion is part of an interesting subset of animal movements that are rhythmic in nature such as walking, chewing, swimming, and breathing. The mechanisms that control these and nearly every other animal movement are poorly understood primarily because their complexity and, in the case of the underlying neural circuits, their inaccessibility. An advantage of rhythmic movements is that their repetitiveness allows comparisons to be made across cycles, and therefore the effects of altering parameters (*e.g.,* joint stiffness, feedback signal strength) may be analyzed.

1.1.2.1 Central Pattern Generators

To produce rhythmic movements, animals use networks of neurons in the central nervous system called central pattern generators (CPGs) that produce coordinated patterns of oscillatory neural activity to control muscle contraction [10]. CPGs use sensorimotor feedback signals to maintain stability and to adapt to system perturbations and changing conditions.

A variety of approaches have been used to study CPGs and the muscles they control, including biological experimentation, computational modeling, and physical modeling. Biological experiments have provided empirical evidence that the spinal cord is capable of producing rhythmic motor output in the absence of sensory feedback [88] and that this output is significantly different than the output when sensory feedback is included [40, 136]. Computational models give researchers the unparalleled ability to control and observe parameters and state variables and have therefore been used to predict neural circuits within the spinal cord that could lead to biologically observed behavior [11, 123, 122, 34, 27]. Physical models, including electric circuits and mechanical devices, are more difficult to create and study than computational models, but they have the advantage that they are governed by some of the same laws of nature as biological systems. Moreover, physical models are subject to some of the same limitations as biology, such as component mismatch and noisy actuators/sensors. These imperfections can actually contribute to a model's robustness because they force the model's controller to perform stably despite the non-idealities.

CPGs have been used previously to control robotic systems. These systems have ranged

from simple two-cell CPGs that controlled a single-degree-of-freedom (DoF) mechanical system [109, 126] to more complex arrangements of cells that control multi-joint limbs during locomotion [115, 113, 114, 34, 28]. A number of types of oscillators have been used in the literature to control rhythmic robotic movement, including the van der Pol oscillator [111], the Matsuoka neural oscillator [72, 73], and the Hodgkin–Huxley model neural oscillator [47]. While each oscillator essentially models the same neural circuit, the approaches vary in complexity. The Matsuoka and van der Pol oscillators are empirical or "black box" models that mimic the output behavior of a biological CPG. These types of models use simple mathematical functions to describe the input-output relationship of a CPG, with no regard as to why this relationship exists. The output waveform of each oscillator models the firing rate envelope of a biological CPG and is therefore smooth and continuous. Conversely, the Hodgkin–Huxley oscillator is a mechanistic model. By emulating the underlying mechanisms of biological neurons (*e.g.,* ion channels, electric potential, diffusion forces, chemical synapses), this model more accurately describes the functionality of living neurons and therefore of a biological CPG. A trade-off exists between the use of empirical and mechanistic neural models: empirical models often have less complex dynamics that are faster to simulate and are more suitable for analytical analysis, while mechanistic models can more accurately explain neural responses to stimuli and can offer more accurate predictions of responses to previously untested stimuli.

1.1.2.2   Resonance Tuning

One of the primary characteristics of CPGs is that they have endogenous oscillation frequencies, which in general do not correspond to the resonant frequency of the mechanical (*e.g.,* musculoskeletal or robotic) systems that they control. When used in an open-loop configuration, the natural (resonant) dynamics of the mechanical system do not influence the CPG controller, which prevents the controller from adapting to the system most energy efficient mode of operation. The resonant frequency of a mechanical system is a function of 1) the configuration and physical properties of its segments and 2) the stiffness and damping of its joints. In the human leg, the mass of each segment is fixed, but the resonant frequency

of the leg can be controlled either by changing the state of the actuating muscles, which alters the joints' stiffness and damping, or by changing the leg's configuration, which alters its moment of inertia [2].

When sensory feedback is added, the CPG frequency can be modified so that it entrains to the mechanical resonant frequency of the system it controls. This behavior, called *resonance tuning*, is seen in biological systems [43, 1, 101] and is common in rhythmically controlled movement. The type of sensory feedback used plays an important role in whether resonance tuning occurs. Joint position (*i.e.,* angle) is often used as a negative feedback source for robotic control and has been shown to produce stable resonance tuning provided the mechanical resonant frequency is greater than the controlling CPG's oscillation frequency [43, 128]. A recent study has demonstrated that positive feedback can also be used to produce resonance tuning when the mechanical resonant frequency is less than the oscillation frequency of the controlling CPG [126].

1.1.2.3   *Energetic Advantages to Moving at Resonance*

To demonstrate the advantage of moving limbs at their resonant frequency, consider that a swinging leg can be modeled as a pendulum with a natural oscillation (resonance) frequency [81]. Optimum energy efficiency occurs when the pendulum is swung at exactly its resonance frequency. When the swing frequency is either above or below this value, additional energy must be used by the actuator to accelerate and decelerate the pendulum during each half cycle. The following analysis (previously presented in [25]) demonstrates this effect by calculating the work rate needed to swing a pendulum over a range of frequencies.

The equation of motion for a simple pendulum is:

$$J\ddot{\theta} + B\dot{\theta} + K\theta + mgL_{\mathrm{cm}}\sin\theta = \Gamma \tag{1}$$

where J is the moment of inertia (MoI) of the pendulum, B is the joint's damping coefficient, K is the joint's stiffness coefficient, m is the mass of the pendulum, L_{cm} is the distance from the joint to the center of mass, θ is the joint angle relative to the vertical, and Γ is the actuator-applied joint torque. Removing damping and making the small angle

9

approximation (*i.e.,* $\sin\theta \approx \theta$), this equation can be rearranged as:

$$\ddot{\theta} + \omega_{\mathrm{n}}^2\theta = T \tag{2}$$

where

$$\omega_{\mathrm{n}} = \sqrt{\frac{mgL_{\mathrm{cm}} + K}{J}} \tag{3}$$

is the natural frequency of the pendulum, and $T = \Gamma/J$ is the applied joint torque normalized by the pendulum inertia. We now make the assumption that the pendulum moves approximately sinusoidally, such that:

$$\theta(t) = A\cos\omega t \tag{4}$$

where A is the oscillation amplitude and ω is the oscillation frequency. Substituting Equation 4 into Equation 2, we get the torque required by the actuator to maintain the pendulum oscillation at steady state:

$$T(t) = A(\omega_{\mathrm{n}}^2 - \omega^2)\cos\omega t \tag{5}$$

During each oscillation, both positive and negative mechanical work is required. Work is calculated as the integral of the product of torque applied and angular displacement. Therefore, the rate of work (*i.e.,* power) applied in this case can be calculated as the average positive work performed during half of the oscillation cycle:

$$\dot{W} = \frac{\omega}{\pi}\int_{-\frac{\pi}{2\omega}}^{\frac{\pi}{2\omega}} T\,\dot{\theta}\,dt \tag{6}$$

where W is the work performed by the actuator on the pendulum. Substituting in Equations 4 and 5, Equation 6 can be solved to give the mean work rate:

$$\dot{W} = \frac{A^2}{\pi}\omega\left|\omega^2 - \omega_{\mathrm{n}}^2\right| \tag{7}$$

Figure 1 shows a plot of this theoretical equation for three different oscillation amplitudes, in which the oscillation frequency has been normalized by the pendulum's natural frequency. It can be seen that above ω_{n}, the work rate increases dramatically (with the third power of ω). This is because at high frequencies, the actuator is quickly reversing the rotation direction of the pendulum requiring much work to repeatedly start and stop movement. As
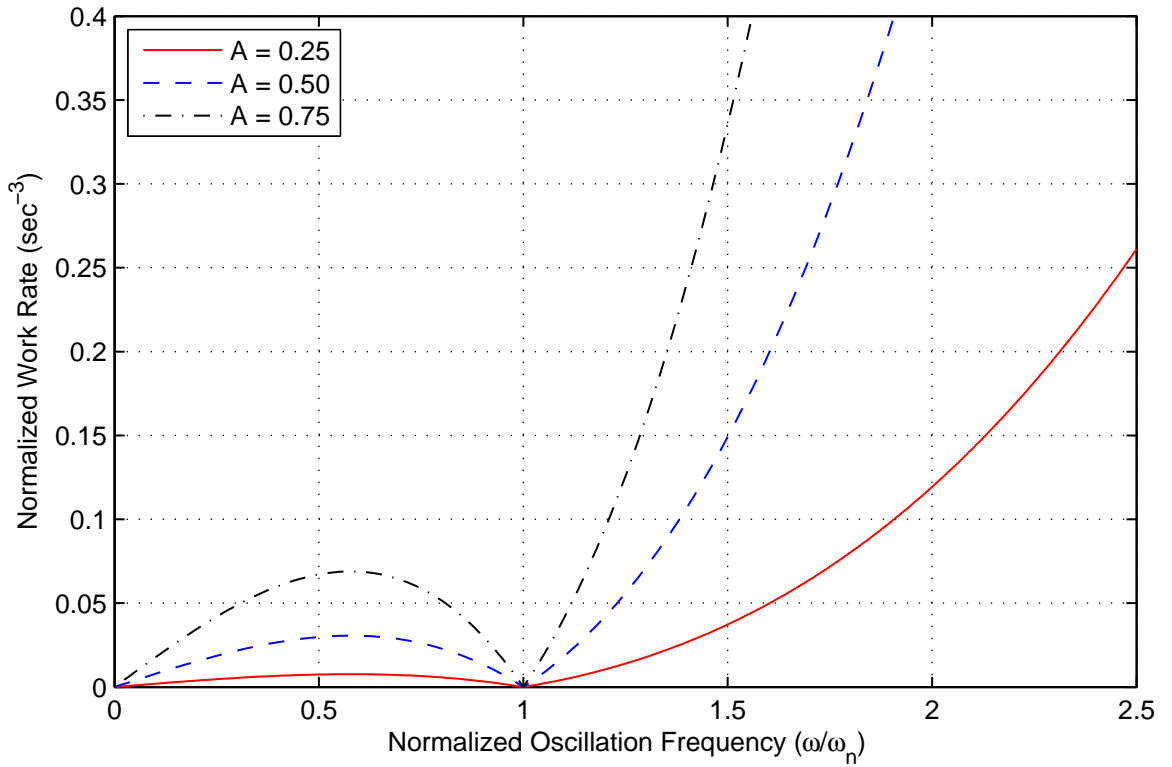
Figure 1: Theoretical work rate required to oscillate a pendulum above and below its resonant frequency. A represents the amplitude of the oscillation, ω represents the oscillation frequency, and ω_n represents the pendulum's natural frequency.

11

ω is reduced below ω_{n}, the work rate initially rises. This happens because torques applied to the pendulum produce angular accelerations proportional to the pendulum's inertia. However, the low oscillation frequency requires the actuator to override and slow down this natural movement, expending more work. As oscillation frequency continues to decrease, the work rate decreases towards zero because the oscillation slows towards steady state and the actuation system performs no work when the pendulum is motionless.

This analysis demonstrates that a significant energetic advantage exists for mechanical systems to be driven at their resonant frequency. It is important, therefore, that robot controllers be capable of using feedback from the mechanical system to dynamically adjust their output frequencies and reduce their work rate. This type of behavior has been observed in simple one-DoF mechanical systems under the closed-loop control of Hodgkin–Huxley [109] and Matsuoka [126] CPGs and in a three-DoF pendulum system under the closed-loop control of van der Pol and Matsuoka CPGs [32].

1.1.2.4   The Hill Muscle Model

In developing biologically inspired control systems, it is important that the actuation systems used closely model the dynamics of muscle. In animals, skeletal (*i.e.,* volitionally controlled) muscle produces both active and passive forces in response to motor neuron command signals and to the muscle's physical state. At the molecular level, active muscle force is produced by the continuous interaction of actin-based thin filaments and myosin-based thick filaments, via the formation of cross bridges. The overlapping arrangement of these contractile components causes the active muscle force to become both length and velocity dependent (*e.g.,* intrinsic muscle stiffness and damping) [53]. Passive forces are produced tendons and intramuscular connective tissue when muscle is stretched beyond its resting length [13].

The Hill muscle model [44] provides a convenient means of modeling the complex actuation dynamics of animals. This model is composed of a contractile element, a series elastic component, and a parallel elastic component. The contractile element models the active force produced by the muscle through thin and think filament interaction. The series elastic

component models the stretch of tendons and some intramuscular components such as the attached cross bridges. The parallel elastic component models the intramuscular connective tissue and generally provides the majority of the passive force production [9].

1.1.3 Joint Stiffness Control

By antagonistically arranging muscles about joints, animals are able to efficiently control both joint angle and joint compliance by varying the levels of differential and common-mode muscle activation, respectively [49, 37, 71]. The ability to dynamically control joint compliance is crucial for animals to adapt to changes in task requirements or in environmental conditions. For example, in human (ballistic) walking, increasing the compliance of a leg's joints during swing allows for the exchange of kinetic and potential energy [13] and reduces the destabilizing effect of a swing-leg perturbation.

In robotics, joint compliance can be produced either passively or actively. Simple passive compliance can be achieved by inserting an elastic component between the actuator and the end-effector [116, 26]. In this case, feedback is unnecessary to maintain a set compliance, but the compliance value is fixed and is therefore not controllable. Passive compliance can also be obtained in a more biological manner by using antagonistic actuators [31, 30, 79, 80, 119, 135, 134, 63, 58, 51, 131] with series-elastic actuation [127, 79, 80, 135, 59, 94, 100]. The term series-elastic actuation refers to the intentional inclusion of an elastic element between the output of a geared-down motor and the load. Its purpose is to reduce the nonlinear effect of load jitter or shock as well as to significantly reduce the output inertia of the motor. With less output inertia, the load is not held as rigidly and the natural dynamics of the actuated device become relevant. Although the antagonistic, series-elastic actuator approach provides the closest model of human joint mechanics and deserves further development, it can be difficult to implement physically [80].

Active compliance is typically implemented by either controlling a variable-stiffness elastic elements, such as leaf springs [82, 83], fiberglass plates [51], conical springs [58], rolamite springs [30], compliant parallel manipulators [112], or by using sensors and feedback algorithms to adjust joint positions or joint torques as necessary to maintain the desired

end-effector compliance with the environment [103, 66, 22, 33]. The advantage of active compliance control is that joint stiffness can be varied quickly without replacing or modifying mechanical components. This research uses *virtual model control* [94, 95, 96], a form of active compliance that has been used to computationally simulate the effect of discrete mechanical components (*e.g.,* springs, dampers) on joint dynamics and to manifest the components' effects by generating joint torques via an actuating motor. The primary limitation of active compliance methods is the need for stable and properly constrained feedback control [15, 56].

1.1.4   Nonlinear Dynamical Analysis

One of the most challenging aspects of developing walking robots is the ability to analyze their complex nonlinear dynamics. The intent of this section is to provide a brief review of some basic concepts from the field of nonlinear dynamics as they apply to robotic system analysis.

The typical form of a series of nonlinear equations is:

$$\dot{\mathbf{x}} = \mathbf{f}(\mathbf{x}) \tag{8}$$

where $\mathbf{x} = (x_1, x_2, ...x_n)$ and $\mathbf{f}(\mathbf{x}) = \big(f_1(\mathbf{x}), f_2(\mathbf{x}), ...f_n(\mathbf{x})\big)$. A *fixed point* is a steady state solution of this system of equations in which the value of all state variables remain fixed (*i.e.,* $\dot{\mathbf{x}} = 0$). A *limit cycle* is a steady state solution in which the values of the state variables form a closed-loop trajectory and nearby state trajectories either spiral toward or away from it. Limit cycles can only occur in nonlinear systems, and are typically displayed using phase portraits [111]. These plots are useful in determining the qualitative behavior of systems that typically cannot be solved analytically. (Example phase portraits for the swinging leg are given later in Section 2.4.1.3.) Fixed points and limit cycles can either be stable or unstable depending on whether they attract or repel nearby solutions.[1]

Calculating the stability of a linear system of equations reduces to finding the eigenvalues of each fixed point and determining whether the magnitude of all eigenvalues are

---

[1]In theory, fixed points and limit cycles can also be marginally stable (or half-stable), but noise prevents this from occurring in real-world applications.
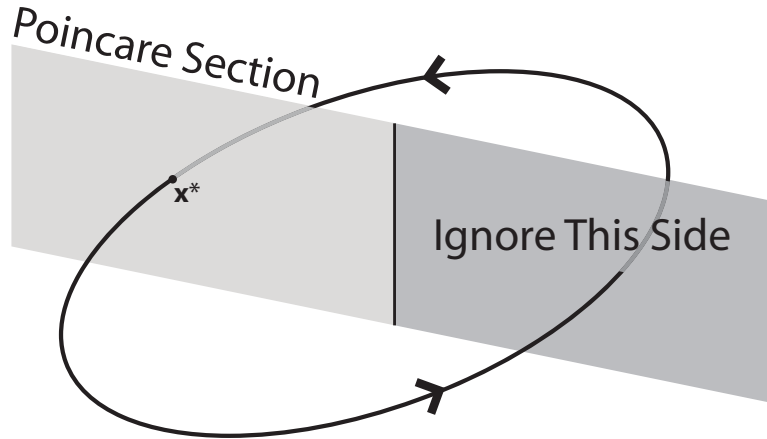
Figure 2: Poincaré section used to determine the effect of a perturbation. Only one side of the plane is effectively used because trajectory crossings are only considered when the trajectory crosses from a certain direction (back to front in this example).

less then zero. Because the analysis of nonlinear systems can be far more complex than that of linear systems, a common analysis technique is to reduce the dimensionality of the nonlinear system [111]. This is done by defining a Poincaré section, or an (n-1)-dimensional (hyper)plane that transverses the state trajectory (*i.e.,* solutions that begin on the plane flow through it, rather than along it) [85]. Figure 2 shows that as time progresses, the state trajectory will normally pass through this half plane once per oscillation. In reality the trajectory must pass through the section at least twice per oscillation because it must return to its original side. We do not care about the return intersection point and, therefore, define the Poincaré section to be one-sided. That is, we only consider the intersection points that pass through the plane in one direction.

From the intersecting points, a Poincaré map can be used to define State x_{i+1} of the system at an intersection point given State x_i. Formally,

$$\mathbf{x}_{i+1} = \mathrm{P}(\mathbf{x}_i) \tag{9}$$

where P is the Poincaré mapping function from one intersection point to the next. If a state $\mathbf{x}^*$ exists such that $\mathbf{x}^* = \mathrm{P}(\mathbf{x}^*)$, then $\mathbf{x}^*$ is a fixed point in the map and corresponds to a closed orbit in state space (*i.e.,* a limit cycle) [85].

It is possible for a closed orbit that starts at $\mathbf{x}^*$ to return to this point again only during every kth iteration through the Poincaré section. We refer to this type of oscillation as a

period-k oscillation. To perform fixed-point analysis on such an oscillation, we must apply the mapping function, P, k times [85]:

$$\mathbf{x}^* = P^k(\mathbf{x}^*) \tag{10}$$

The stability of an orbit can be determined by linearizing the Poincaré map about $\mathbf{x}^*$ and calculating the Monodromy matrix, $\boldsymbol{\Phi}$:

$$\boldsymbol{\Phi} = D_{\mathbf{x}^*}P(\mathbf{x}^*) \tag{11}$$

where $D_{\mathbf{x}^*}$ indicates matrix differentiation with respect to $\mathbf{x}^*$.

The eigenvalues of $\boldsymbol{\Phi}$ are called the Floquet multipliers, λ, and provide an indication of the system's sensitivity to small perturbations. If the magnitude of each multiplier is less than unity, then $\mathbf{x}^*$ is asymptotically stable.[2] Moreover, because the choice of Poincaré section is somewhat arbitrary, the stability of the entire periodic orbit is equivalent the stability of $\mathbf{x}^*$ [85].

Empirical methods for determining the local stability of a closed orbit can be quite involved because calculation of the Monodromy matrix for a system with n state variables requires n data points to be taken. The general process for calculating an estimate for $\boldsymbol{\Phi}$ (as described in [36]) follows (refer to Figure 3).

1. Define an appropriate Poincaré plane and determine the fixed point, $\mathbf{x}^*$, that corresponds to the closed state space orbit.

2. Apply a small perturbation, δ, to the first element of $\mathbf{x}$ and run the system until one complete oscillation has been completed. Record the resulting state as $\mathbf{x}_{\mathrm{p}}$.

3. Set the first column of $\boldsymbol{\Phi}$ equal to:

$$\frac{\mathbf{x}_{\mathrm{p}} - \mathbf{x}^*}{\delta} \tag{12}$$

4. Repeat this process for each element of $\mathbf{x}$.

---

[2]Autonomous systems have one multiplier that is always unity and is not considered when determining stability. For this reason, the unity multiplier is ignored for the remainder of this dissertation.
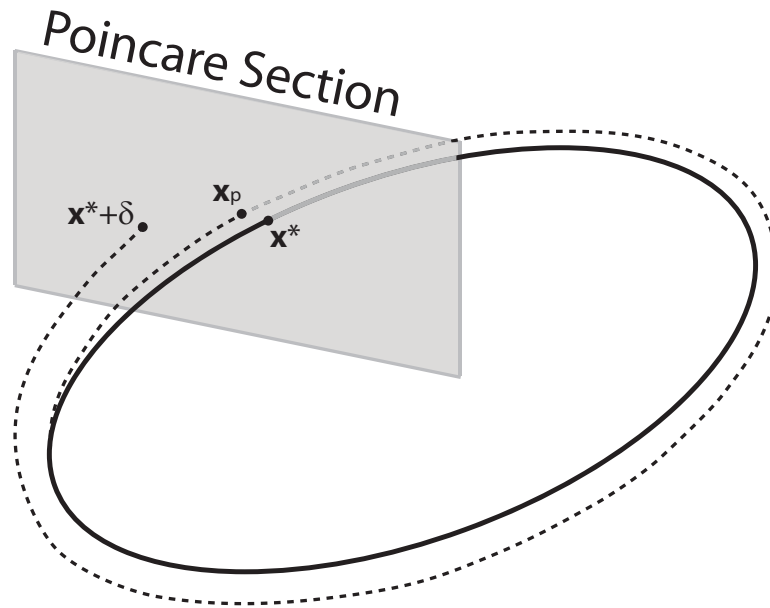
Figure 3: Poincaré section used to determine the effect of a perturbation. The trajectory begins at the point $\mathbf{x}^* + \delta$, where δ is a small perturbation of one of the state variables. After one oscillation, the trajectory intersects the Poincaré section at the point $\mathbf{x}_\mathrm{p}$. The system stability can be determined by repeating this process for each of the state variables and ascertaining the values of δ and $\mathbf{x}_\mathrm{p}$ in each case.

5. Calculate the eigenvalues of Φ and determine if all eigenvalues are less than unity.

The benefit of this method is that it provides all Floquet multipliers. The disadvantage is that it requires n independent tests to be run and can be difficult and time consuming to perform in real systems.

1.2 Summary

A significant effort is currently underway to develop autonomous, legged, interactive robots for use in a variety of challenging fields. Two common requirements in each of these fields are that the robots be adaptive to their environment and that they operate with high energy efficiency. The leading approach to modern robot design—trajectory-control—has produced robots that demonstrate an impressive and continuously improving range of capabilities, but these robots remain unable to operate in unpredictable environments and suffer from poor energy efficiency. The second, less-prevalent approach—passive dynamics—places energy efficiency as its highest priority, to the detriment of stability. In this dissertation, we use

inspiration from biological systems to develop a human-scale, anthropomorphic robotic leg that exploits its natural dynamics to promote energy efficiency while using limited actuation to promote stability. The overall goal of this research is to determine 1) whether passive joint elasticity can improve the energy efficiency of dynamic leg swinging and 2) how active knee control affects the performance of both unperturbed and perturbed leg swing. To this end, the remaining portion of this document is organized as follows. Chapter 2 introduces the swinging-leg model used throughout the dissertation, which includes a two-DoF mechanical leg and a CPG-based, closed-loop controller. We then present the methods used to computationally and physically implement this model, and we conclude with a description of the basic analysis techniques used to measure the model's performance. In Chapter 3, we explore the use of both linear and nonlinear passive joint elasticity in improving the energy efficiency of hip-actuated leg swinging. The nonlinear elasticity is used to emulate the passive joint stiffness properties of the human leg. In both cases, experiments are performed both with and without a human-like asymmetric restriction on knee hyperextension. In Chapter 4, we add active knee control to the swinging leg and perform the following two types of experiments. Steady-state (unperturbed) experiments demonstrate how active knee control influences whole-leg resonance tuning and several other performance criteria, including energy efficiency. Perturbation experiments analyze the ability of active knee control to improve the swing-leg perturbation rejection capabilities of dynamic walkers. Finally, Chapter 5 summarizes the results of this dissertation, discusses contributions made, and suggests future research directions.

CHAPTER II

DEVELOPMENT AND IMPLEMENTATION OF SWINGING-LEG MODEL

In the effort to improve the performance and abilities of walking robots, two of the most important challenges that must be addressed are performance in rough and unpredictable terrain and energy efficiency. We are fortunate that animals in general and humans in particular provide a tremendous example that we as robotics researchers can use to reverse engineer. In order to study the potential benefit of incorporating human motor control elements into walking robots, we must develop a relevant model that can be implemented both computationally and robotically. This chapter begins with an explanation of the model system chosen, and then presents the details of the computational and robotic implementations including all control systems. The final section describes how the resulting data of each implementation was analyzed to produce meaningful information and to make conclusions regarding the system performance.

2.1   Model System

We chose to develop a sagittal plane model of a human leg that has two actuated joints and swings freely without contacting its environment. The three major simplifying assumptions of this model and their associated justifications are as follows.

Movement is restricted to two dimensions Walking robots have been developed to operate in either two [3, 87, 74, 75, 76] or three [45, 28, 55, 135, 17, 132] dimensions. Although the planar robots generally rely on an external support to maintain balance when operating, they can provide much simpler platforms on which to test principles of locomotion because the issue of lateral balance can be safely ignored. These planar robots have demonstrated that lateral movement is not necessary to produce stable, efficient walking robots.

Leg swinging is a sufficient model Although the ultimate goal for this research is improve *walking* robots, the model we have chosen to develop swings freely rather than alternating between swing and stance. Indeed, the ground contact that occurs during stance is important because load-bearing ground contact forces are required for proper stance-phase leg dynamics. These forces provide motion constraints, asymmetrical limb loading, cutaneous stimuli, and work for the leg's extensor muscles [7].

We chose not include ground contact in this research, however, because we felt that inclusion would unnecessarily complicate both our computational and robotic experiments and would obfuscate the overall results. The experimental complexity in the *computational* model arises because ground contact forces are very difficult to simulate [69, 70]; the impact forces associated with ground contact produce highly "stiff" equations of motion that are not easily integrated. The experimental complexity in the *robotic* model arises because additional degrees of freedom (DoFs) are needed to account for the vertical pelvis movement that occurs between mid-stance (high point) and heel-strike/toe-off (low point). Rather than allow this vertical motion, we chose to fix the hip to mechanical ground and limit the DoFs. From a data analysis standpoint, removing the effect of ground contact (*i.e.,* stance phase) removes the discontinuities that occur when the heel first touches the ground to begin stance and when the toes leave the ground to terminate stance. This simplification allows us to use continuous analysis techniques without the need to detect and compensate for discontinuous jumps in state variables.

Although an important phase of walking is not present in our model, the task of leg swinging is an important precursor movement that can be used to analyze the general role of certain physiological components in robot walking. The two primary analysis criteria used in this research are energy efficiency and stability (described in Section 2.4). Direct comparisons cannot be made between leg swinging and normal walking because ground contact forces increase overall energy consumption and can be destabilizing. The approach we have taken in this research is to analyze the effects physiological components have on leg swinging, and then to explore how these effects may also influence robotic walking. For example, leg swinging uses approximately 33% of the net energy used during walking [25]. Because

Segment	Length (cm)	Mass (kg)	CoM (cm)	MoI (kg m^2)
Thigh	40.4	6.24	17.5	0.297
Shank/Foot	47.0	3.81	28.5	0.454
Total Leg	87.4	10.05	39.0	2.404

Table 1: Ideal mechanical properties of each leg segment. The center of mass and moment of inertia are referenced from the proximal extent of the segment.

the swing phase of walking accounts for 40% of the duration of the human stride cycle, a 50% improvement in the energy efficiency of leg swinging could account for a 20% improvement in the energy efficiency of walking. Although this approach relies on assumptions and approximations, it provides a basis for making predictions about the benefit biologically inspired components may have on robot walking.

Only two joints are necessary The swinging-leg model has two joints—a hip and a knee—that are both actuated. We chose to fix the angle of the ankle joint such that the shank and foot were combined into one leg segment. We made this DoF-lowering assumption because the ankle rotates very little during leg swinging and therefore has limited effect on the dynamics of the other limb segments.[1]

2.1.1 Anthropomorphic Details

For ease of comparison to human physiological data from the literature, our model was developed to be full human scale. In particular, we chose our target subject to be an adult female [137]. The leg is restricted to move in the sagittal plane by revolute joints at the hip and knee, and each leg segment is designed such that its length, mass, center of mass (CoM), and moment of inertia (MoI) match those of the female subject. Because the shank and foot were combined into one leg segment, the additional complexity of matching all physical properties each segment individually was unnecessary. The ideal anthropomorphic parameters of the leg are shown in Table 1.

---

[1]Ankle movement cannot be ignored during normal walking because rotations of approximately 20 deg are common [124]. These rotations are crucial because ankle stiffness is a major source of elastic energy storage during stance.

2.1.2 CPG Configuration

Because we are interested in biologically inspired robot control, we have chosen to control the leg with a neural central pattern generator (CPG) comprised of Half Center Oscillators (HCOs). Several architectures exist for coupling HCOs with the actuated joints so that inter-joint synchronization occurs. We have chosen to have each HCO provide independent, closed-loop control of a separate joint such that the only source of synchronization is due to the physical mechanical coupling between joints.

Williamson [129] has offered a good analysis of some of the CPG architectures possible for multi-joint limbs. In Figure 4A, each joint is controlled with an independent HCO. Independence, in this case, means that these HCOs have no synaptic coupling with each other; the only source of inter-joint coordination is provided by the mechanical components (*e.g.,* limb segments) that connect the joints. Figure 4B shows the same system with the addition of inter-HCO connections. Without sensory feedback from the mechanical system, these connections would dictate the relative phases between each HCO. In the full system, however, stability is generally reduced because the synaptic coupling creates a system that is highly parameter sensitive [129]. The sensitivity develops because, in general, it is not possible for both the physical and synaptic coupling to simultaneously dominate the entrainment. Thus, small changes in the relative levels of feedback can significantly alter system performance. Figure 4C shows an architecture in which a single master HCO is used to control the phase of all joints. This configuration is a simplification of the master-slave approach [105] in which the limb-level master HCO unidirectionally controls joint-level slave HCOs. The applicability of this approach is limited because it confines the relative phases of the joints to be fixed at $\pm\pi$. While this approach may work for some simplistic movements, it is not general enough for tasks such as locomotion that have variable inter-joint phase. Figure 4D shows a variation of Figure 4A in which forces have been added to alter the limb's natural dynamics. These forces can be created physically or computationally by either changing the mechanical properties of the limb segments or by applying external forces. This approach is used to change the resonant mechanical properties of the limb, forcing the HCOs to adapt through sensory feedback to a new pattern of oscillation. As an
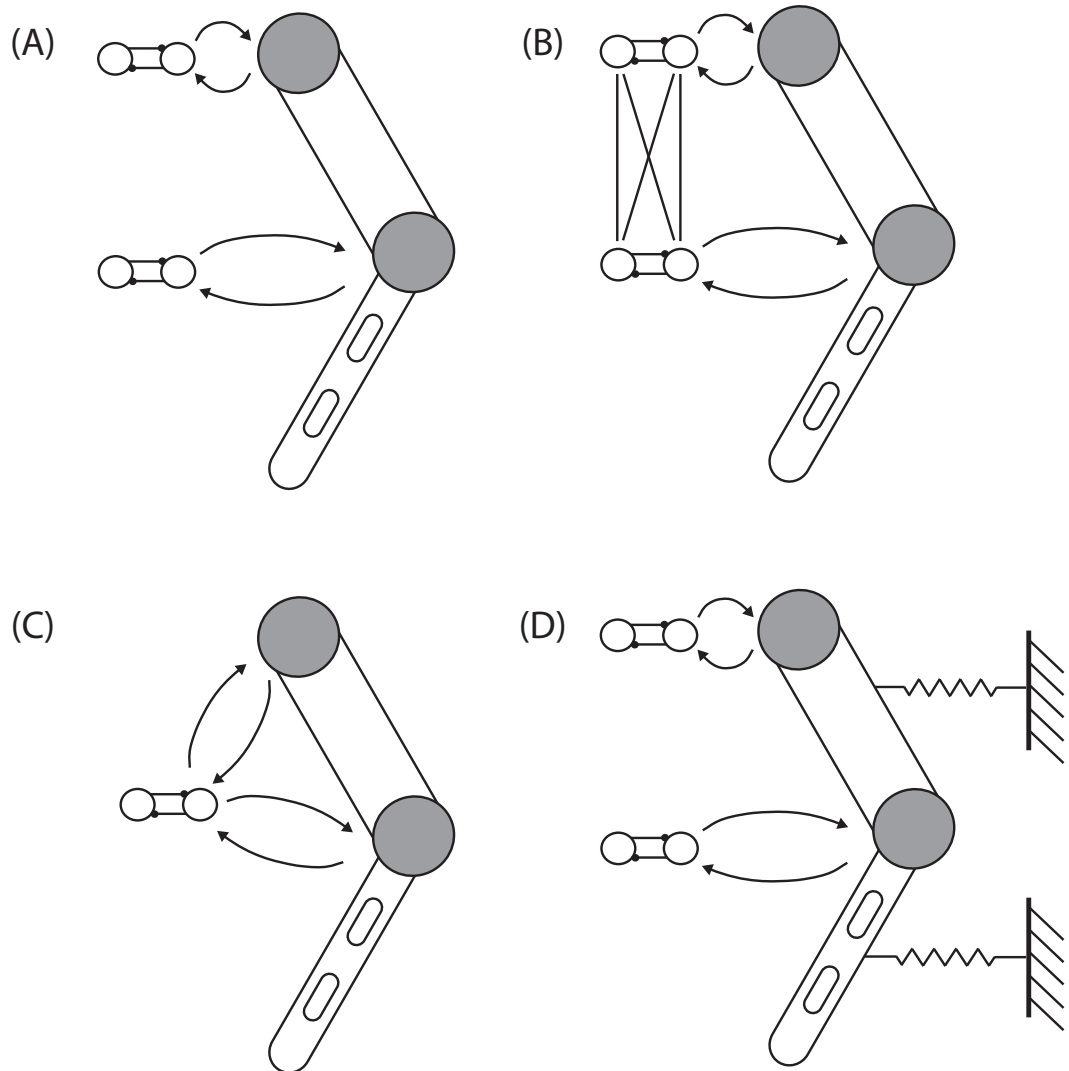
Figure 4: Various neural control architectures possible for a two-joint leg. In each figure, arrows pointing towards the joint represent muscular torque actively applied to the joint; arrows pointing away from the joints represent joint angle feedback. (A) independent HCOs control each joint with mechanical coupling alone providing inter-joint coordination. (B) inter-HCO connections constrain the relative phase of each HCO. (C) one master HCO is used to control the phase of all joints. (D) environmental forces are included that artificially alter the limb's natural dynamics. This figure is adapted from Figures 4-1 and 5-1 of [129].

example, consider a change in the elasticity of a pair of antagonistic joint actuators (*e.g.,* a change in elasticity of the flexor and extensor muscles of a joint). As the elasticity decreases, the corresponding joint's stiffness increases and the natural oscillation frequency of the limb segment distal to the joint increases. Thus, one way to increase joint oscillation speed is to decrease the elasticity of (*i.e.,* stiffen) the leg actuators.

In this research, we have chosen to use the CPG arrangement in Figure 4A. This configuration was chosen based on [129] that demonstrated the stability problems associated with the CPG in Figure 4B and the limited types of motions possible with the CPG in Figure 4C.[2]

2.1.3 Leg Asymmetry

To assure that the swinging dynamics of the leg closely emulate those of the human, we have chosen to limit knee extension past the anatomical (fully straightened) position. Oscillatory controllers of the type used in this research have previously been shown capable of entraining to the dynamics of a multi-joint pendulum [32] and a multi-joint arm [129]. In this research, the mechanical system more closely resembles that of a biological limb because of the asymmetric limit in knee movement. (This limit is crucial to human locomotion because it prevents the leg from buckling during the stance phase of locomotion.) In humans, multiple mechanisms are used to prevent knee hyperextension. The primary mechanism is knee flexion muscles. These muscles are stretched during knee extension, causing them to produce both passive and active (reflexive) forces and resist hyperextension. Another mechanism is the physical construction of the knee, which includes bony constraints and stabilizing ligaments such as the anterior cruciate ligament (ACL). Although the primary role of the ACL is to prevent anterior tibial displacement [124], it is also plays a strong role in preventing knee hyperextension and has been modeled in computational analyses as a hyperextension-limiting mechanism [92]. During passive knee movement, the ACL only produces forces during the last ten degrees of extension, and it can be damaged if the leg is forced to extend more than ten degrees beyond the anatomical position.

---

[2]As a future step in this research, ground contact will be added to the leg, causing the arrangement to change to that in Figure 4D.

In our both our computational and robotics models, knee asymmetry is implemented (*i.e.,* extension past the anatomical position is prevented) using separate mechanisms that model both the knee flexion muscles and the ACL.

2.2 Computational Model and Implementation

In this section, we develop and analyze a computation model of human leg swinging. This computational model is intended to emulate the performance of a human leg with reasonable accuracy and to very accurately model the performance of the robotic leg model that is described in Section 2.3. Computational models are quite useful in the study of any closed-loop system because they provide the designer with complete control over both the system's parameters and environment and can provide a means to quickly analyze large regions of parameter space.

At the most basic level, the role of this computational model is to take a given set of parameters and initial conditions, to run the simulation, and to output a time progression of the system's state variables. We chose to develop the model in object-oriented C++ to provide a balance of computational speed and functionality. The model is comprised of three types of components—the mechanical leg, the neural oscillator, and the control system. These three components were implemented as independent objects that run in parallel with high levels of interaction and inter-dependence.

2.2.1 Mechanical Leg

The first step in modeling a mechanical system is to find the equations of motion (EOMs) that describe its dynamics. These equations can usually be found analytically using approaches such as Kane's Method [54], Lagrange's Method, or the Newton-Euler Method, but the derivations for even modestly complex systems can quickly become intractable [90]. An advantage of Kane's Method, which is based of Newton's Second Law, is that it reduces constrained mechanical systems into an unconstrained system of first-order ordinary differential equations. Deriving the EOMs for a swinging leg is not overly complicated, as the leg can be modeled essentially as a double pendulum. For simplicity and accuracy, however, we chose to find our system's EOM with AUTOLEV (Kane Dynamics, Inc., Stanford, CA), a

Parameter	Description
M_t	mass of thigh
M_s	mass of shank
L_t	length of thigh
L_s	length of shank
$L_\mathrm{cm,t}$	length between hip and thigh center of mass
$L_\mathrm{cm,s}$	length between knee and shank center of mass
J_t	thigh moment of inertia (about thigh center of mass)
J_s	shank moment of inertia (about shank center of mass)

Table 2: Leg mass property parameters.

symbolic mechanical engineering analysis tool based on the use of Kane's Method. Details on our use of AUTOLEV can be found in Appendix A.

While other software packages exist that can find EOMs, AUTOLEV has the ability to analytically find and output the EOMs in a human-readable format. Furthermore, AU-TOLEV can create computationally optimized, stand-alone simulation programs in either C, MATLAB (Mathworks, Cambridge, MA), or Fortran from the EOMs. We used this code-exporting feature extract the EOMs (written in C) for use in the mechanical leg object of our computational model. This code, which was packaged into a C++ object for ease of implementation, receives joint torques to apply at the hip and knee and outputs the corresponding joint angles, joint velocities, and actuator torques. A convenient feature of this approach is that the design of the mechanical system can be easily changed at design time by modifying the AUTOLEV input and updating the EOMs in the C++ object.

In developing the AUTOLEV input file for our swinging leg model, the leg was treated as a non-inverted double pendulum in which the hip was fixed at the origin of the Newtonian reference frame and served as a mechanical ground. The leg was restricted to move only in the sagittal plane, rendering the model two dimensional. A schematic drawing of the leg is presented in Figure 5 showing the length and angle parameters used in our model. A list of all leg mass property parameters used in our model is shown in Table 2.

The four state variables that completely describe the dynamics of the leg are the joint angles of the hip and knee, θ_h and θ_k, and the angular velocities of the hip and knee, ω_h and ω_k. Note that θ_h represents the angle of the thigh relative to the vertical, and θ_k represents
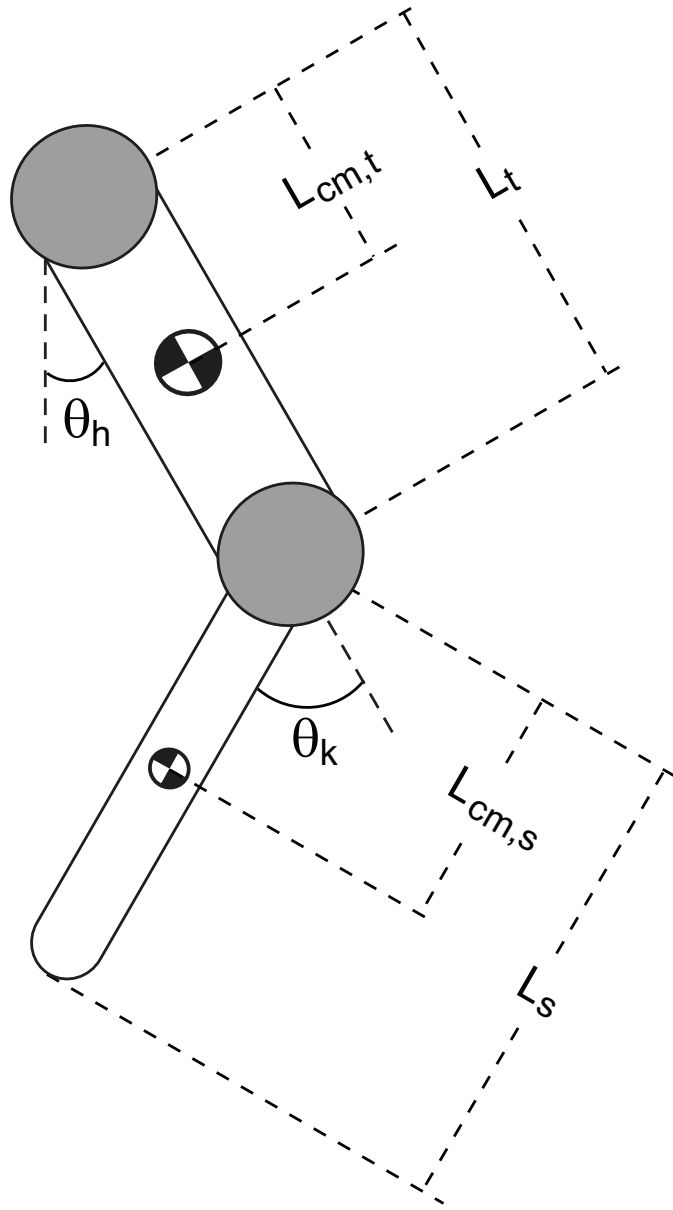
Figure 5: Mass properties of the swinging leg model. L_t represents the length of the thigh. L_s represents the length of the shank. $L_{cm,t}$ represents the distance from the hip to the thigh center of mass. $L_{cm,s}$ represents the distance from the knee to the shank center of mass. θ_h represents the angle of the thigh relative to the vertical. θ_k represents the angle of the shank relative to the thigh. (Not shown are the thigh mass, M_t, the shank mass, M_s, the thigh moment of inertia, J_t, and the shank moment of inertia, J_s.)

the shank angle relative to the thigh. These parameters and state variables were used in the AUTOLEV input file (shown in Appendix A) to compute the dynamic equations of motion for the system.

$$\ddot{\theta}_{\mathrm{h}} = \Bigg[(J_{\mathrm{s}} + M_{\mathrm{s}} L_{\mathrm{cm,s}}^2) \left(\Gamma_{\mathrm{h}} + \Gamma_{\mathrm{k}} - g(M_{\mathrm{s}} L_{\mathrm{t}} + M_{\mathrm{t}} L_{\mathrm{cm,t}}) \sin \theta_{\mathrm{h}} - M_{\mathrm{s}} L_{\mathrm{t}} L_{\mathrm{cm,s}} (\dot{\theta}_{\mathrm{h}} - \dot{\theta}_{\mathrm{k}})^2 \sin \theta_{\mathrm{k}} \right) +$$

$$M_{\mathrm{s}} L_{\mathrm{t}} L_{\mathrm{cm,s}} \cos \theta_{\mathrm{k}} \left(\Gamma_{\mathrm{k}} + g M_{\mathrm{s}} L_{\mathrm{cm,s}} \sin(\theta_{\mathrm{h}} - \theta_{\mathrm{k}}) - M_{\mathrm{s}} L_{\mathrm{t}} L_{\mathrm{cm,s}} \dot{\theta}_{\mathrm{h}}^2 \sin \theta_{\mathrm{k}} \right) \Bigg] /$$

$$\left((J_{\mathrm{s}} + M_{\mathrm{s}} L_{\mathrm{cm,s}}^2)(J_{\mathrm{t}} + M_{\mathrm{s}} L_{\mathrm{t}}^2 + M_{\mathrm{t}} L_{\mathrm{cm,t}}^2) - M_{\mathrm{s}}^2 L_{\mathrm{t}}^2 L_{\mathrm{cm,s}}^2 \cos^2 \theta_{\mathrm{k}} \right) \quad (13)$$

$$\ddot{\theta}_{\mathrm{k}} = \Bigg[- \left(J_{\mathrm{s}} + J_{\mathrm{t}} + M_{\mathrm{s}}(L_{\mathrm{t}}^2 + L_{\mathrm{cm,s}}^2) + M_{\mathrm{t}} L_{\mathrm{cm,t}}^2 + 2 M_{\mathrm{s}} L_{\mathrm{t}} L_{\mathrm{cm,s}} \cos \theta_{\mathrm{k}} \right)$$

$$\left(-\Gamma_{\mathrm{k}} - g M_{\mathrm{s}} L_{\mathrm{cm,s}} \sin(\theta_{\mathrm{h}} - \theta_{\mathrm{k}}) + M_{\mathrm{s}} L_{\mathrm{t}} L_{\mathrm{cm,s}} \dot{\theta}_{\mathrm{h}}^2 \sin \theta_{\mathrm{k}} \right) + (J_{\mathrm{s}} + M_{\mathrm{s}} L_{\mathrm{cm,s}}^2 + M_{\mathrm{s}} L_{\mathrm{t}} L_{\mathrm{cm,s}} \cos \theta_{\mathrm{k}}) *$$

$$\left(\Gamma_{\mathrm{h}} - g(M_{\mathrm{s}} L_{\mathrm{t}} + M_{\mathrm{t}} L_{\mathrm{cm,t}}) \sin \theta_{\mathrm{h}} + g M_{\mathrm{s}} L_{\mathrm{cm,s}} \sin(\theta_{\mathrm{h}} - \theta_{\mathrm{k}}) + M_{\mathrm{s}} L_{\mathrm{t}} L_{\mathrm{cm,s}} (2\dot{\theta}_{\mathrm{h}} - \dot{\theta}_{\mathrm{k}}) \dot{\theta}_{\mathrm{k}} \sin \theta_{\mathrm{k}} \right) \Bigg] /$$

$$\left((J_{\mathrm{s}} + M_{\mathrm{s}} L_{\mathrm{cm,s}}^2)(J_{\mathrm{t}} + M_{\mathrm{s}} L_{\mathrm{t}}^2 + M_{\mathrm{t}} L_{\mathrm{cm,t}}^2) - M_{\mathrm{s}}^2 L_{\mathrm{t}}^2 L_{\mathrm{cm,s}}^2 \cos^2 \theta_{\mathrm{k}} \right) \quad (14)$$

where g is gravity and Γ_{h} and Γ_{k} are the combined torques applied to the hip and knee, respectively, by all passive and active torque-generating components. There are four torque-generating components in our model.

Active Muscle Torque ($\Gamma_{\mathbf{act}}$) serves as the input signal to the mechanical leg object. The basis for this signal is produced by the Neural Oscillator Object (Section 2.2.2) and converted into a useful form by the Control System Object (Section 2.2.3).

Passive Stiffness Torque ($\Gamma_{\mathbf{s}}$) is produced by passive elastic elements included at each joint. The role of these elements is examined in detail in Chapter 3. In this simplest form, the passive stiffness torque is calculated as:

$$\Gamma_{\mathrm{s}} = K(\theta - \theta_{\mathrm{sb}}) \quad (15)$$

where K is the passive stiffness gain, θ is the joint angle, and θ_{pb} is the passive stiffness bias angle.

Passive Damping Torque ($\Gamma_{\mathbf{d}}$) is produced by passive viscous elements included at each joint. The passive damping torque is calculated as:

$$\Gamma_{\mathrm{d}} = B\omega \tag{16}$$

where B is the damping gain and ω is the joint angular velocity.

Dynamic Friction Torque ($\Gamma_{\mathbf{f}}$) is produced by modeling the effects of dynamic friction at each joint. Dynamic friction torque is calculated as:

$$\Gamma_{\mathrm{f}} = \begin{cases} \mu_{\mathrm{dyn}} & \text{if } \omega < 0 \\ -\mu_{\mathrm{dyn}} & \text{if } \omega > 0 \end{cases} \tag{17}$$

where μ_{dyn} is the coefficient of dynamic friction.

At each time step, the effects of all four components for each joint are calculated and summed to produce one net applied torque value per joint (*i.e.,* Γ_{h} and Γ_{k}). The equations of motion are then integrated one time step using both these values and the current system state to compute the change in system state. The system state (comprised of the four state variables) serves as the output of the mechanical leg object.

2.2.2 Neural Oscillator

We have chosen to implement the Matsuoka HCO [72, 73] as the source of control for our swinging-leg model. This decision was made by comparing the Matsuoka model to the Hodgkin–Huxley and van der Pol models, which have also been commonly used to control robotic systems. Compared to the Hodgkin–Huxley model, the Matsuoka model uses significantly less computational resources, has less parameters requiring tuning, and has no need for post-processing of the neural output signals (*i.e.,* filtering of the spikes). Compared to the van der Pol model, the Matsuoka model has been found to have larger stability regions when controlling multi-joint pendulums [32]. The Matsuoka oscillator has also been shown to entrain to the movements of multi-joint limbs quickly and robustly [129, 6]

The Matsuoka oscillator is an empirical model that represents two mutually inhibited neurons that have relaxation dynamics and are capable of sustaining oscillations in the

absence of external stimuli. With only four state variables, which change smoothly over time, the Matsuoka oscillator is a good candidate in these types of applications in which real-time simulation is required.

The Matsuoka oscillator's dynamics are described by the following equations:

$$\tau_1 \dot{x}_1 = c - x_1 - \beta v_1 - \gamma [x_2]^+ - h[e]^+ \tag{18}$$

$$\tau_1 \dot{x}_2 = c - x_2 - \beta v_2 - \gamma [x_1]^+ - h[e]^- \tag{19}$$

$$\tau_2 \dot{v}_1 = [x_1]^+ - v_1 \tag{20}$$

$$\tau_2 \dot{v}_2 = [x_2]^+ - v_2 \tag{21}$$

$$y = [x_1]^+ - [x_2]^+ \tag{22}$$

where $[x_i]^+ = \max(x_i, 0)$, $[e]^+ = \max(e, 0)$, $[e]^- = -\min(e, 0)$, x_i represents each neuron body's membrane potential; v_i represents the amount of each neuron's adaptation (*i.e.,* fatigue); τ_1 and τ_2 are the time constants of the membrane potential and adaptation, respectively; β determines the effect fatigue has on neuron firing rate; γ determines the effect mutual inhibition has on neuron firing rate; c represents the level of tonic input; e represents the level of external inputs (*e.g.,* feedback); h specifies the gain of external inputs (*e.g.,* feedback gain); and y is the output of the oscillator. The four state variables of this HCO are x_1, x_2, v_1, and v_2.

As with the mechanical leg object, the neural oscillator was developed as a C++ object for ease of implementation into the computational model. During a normal simulation, two instances of this object are instantiated because two Matsuoka oscillators (*i.e.,* HCOs) are used in this research—one to control each of the two actuated joints (*i.e.,* hip and knee).

Each HCO object receives, as input, a feedback signal, e, that is related to the angle of the joint it is controlling. Knowing e and the values of the HCO's state variables, Equations 18–22 can be integrated and the HCO output, y, can be computed. This output is then converted by the Control System Object (Section 2.2.3) into a form that provides an active muscle torque signal to the Mechanical Leg Object (Section 2.2.1).
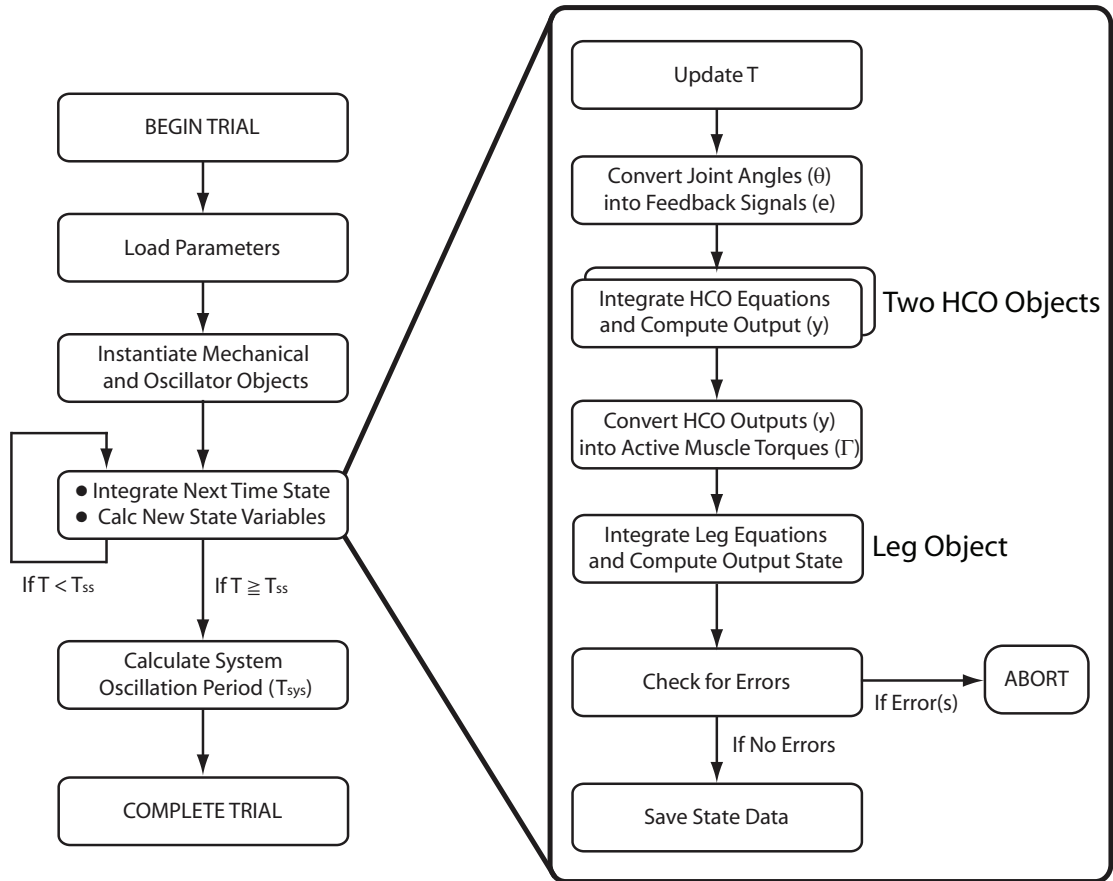
Figure 6: Algorithm used by control system object to perform forward dynamic simulation of closed-loop leg model. After parameters are loaded and required objects instantiated, the algorithm integrates the state equations until steady state is reached ($T = T_{\text{ss}}$). The algorithm then determines whether the trial succeeded by checking for phase locking of all four oscillators—hip, knee, hip HCO, and knee HCO. The blown-up algorithm on the right shows the steps taken to integrate both the leg and HCO state equations.

2.2.3 Control System

The final object that was developed as a part of the computational model was the control system object. This object works to coordinate all interactions between the mechanical and neural objects and dictates what experiments are performed and the conditions under which they are run. A flow chart describing the primary algorithm that this object follows is shows in Figure 6.

After loading system parameters (described further in Section 2.2.4), the algorithm creates an instance of the mechanical leg object and two instances of the HCO object. A forward dynamic simulation then begins by integrating the system's state equations for a

specified time period, $T_{ss} = 150$ sec, to allow the transient response of the system to decay, leaving the steady-state behavior.

The right panel in Figure 6 shows the steps required to coordinate the integration of both the leg's equations of motion and the state equations for both HCOs. For each integration step, the time, T, is incremented by the fixed integration step size (1.0 ms). Next each joint angle, θ, (or initial angle, θ_o, if the simulation is just beginning) must be converted into a feedback signal, e, for its respective HCO using the following equation.

$$e = G_{fb}(\theta - \theta_{ab}) \tag{23}$$

where e represents the external input in Equations 18 and 19, G_{fb} is the feedback gain, θ is the current joint angle, and θ_{ab} is the joint angle at which active torque is zero (bias angle). These feedback signals are then fed into the two HCO objects, and each object performs an independent forth-order, variable step size Runge-Kutta integration of its state equations from the previous time value to the current time.

The output of each HCO object, y, is converted into active muscle torque, which simulates an agonist-antagonist pair of muscles, using the following equation:

$$\Gamma_{act} = G_{ff} \cdot y \tag{24}$$

where Γ_{act} is the active muscle torque and G_{ff} is the feed-forward (*i.e.,* motor neuron) gain. The active muscle torque is then fed to the mechanical leg object, which also uses a forth-order, variable step size Runge-Kutta integration algorithm to compute the updated values of its state variables. At this point, an error check is performed, and the entire algorithm is aborted if any error is detected. Otherwise, the new values of the state variables are saved and this routine is repeated if $T < T_{ss}$. Once $T \geq T_{ss}$, a routine is performed to compute the complete system's oscillation period, T_{sys}, if one exists.

2.2.4 System Parameters

The computational model of the swinging leg involves the coordination of multiple nonlinear systems each with several parameters that must be specified for each trial. The parameters can be divided into three groups—*fixed parameters* that are constant throughout all trials

Type	Object	Param	Nom. Value Hip	Knee	Unit	Brief Description
Fixed Parameters	HCO	β	2.50	2.50	-	modifies neuron firing rate
		γ	2.50	2.50	-	modifies neuron firing rate
		c	1.00	1.00	-	level of tonic input
	Leg	M	6.851	3.952	kg	mass of leg segment
		L	0.404	0.460	m	length of leg segment
		L_{cm}	0.197	0.269	m	length from joint to CoM
		J	0.156	0.128	kg m^2	leg segment MoI
		μ_{dyn}	0.000	0.000	-	coef. of dynamic friction
Initial Conditions	HCO	x_0	0.50	-0.50	-	neuron membrane potential
		v_0	0.50	0.15	-	level of neuron adaptation
	Leg	θ_0	$\pi/4$	0.00	rad	initial joint angle
		ω_0	0.00	1.00	rad/sec	initial joint angular velocity
Test Parameters	HCO	τ_1	-	-	sec	membrane pot. time const.
		τ_2	$2\tau_1$	$2\tau_1$	sec	neural adapt. time const.
	Leg	K	-	-	Nm/rad	passive joint stiffness gain
		θ_{sb}	-	-	rad	passive stiffness bias angle
		B	-	-	Nm sec/rad	passive joint damping gain
	Control	θ_{ab}	-	-	rad	active torque bias angle
		G_{ff}	-	-	-	feed-forward gain
		G_{fb}	-	-	-	feedback gain

Table 3: Summary of all parameters used during simulation of the closed-loop system, including the nominal values.

of an experiment, *initial conditions*, which are the starting values of each state variable, and *test parameters* that are swept from trial to trial. For clarity, the all system parameters are summarized and presented in Table 3.

As shown in this table, the complete closed-loop system has a total of 40 parameters. This large number of parameters was reduced by making some simplifications. First, the values of β, γ, c, x_0, and v_0 were set equal to values known to work well for robotic joint control (shown in Table 3) [129]. Second, τ_2 was set equal to $2\tau_1$, which produces a simple relationship between τ_1 and the HCO's natural oscillation frequency ($\tau_1 = 0.704 \cdot T_{\mathrm{sys}}$ sec/rad). Next, because the leg is modeled after a target human, the mass property parameters (M, L, L_{cm}, and J) for each leg segment were set equal to the anatomical values of our target subject (Table 1). Furthermore, we chose to make the assumption that the coefficient of dynamic friction could be set equal to zero for all experiments in this research without significant affecting the experimental results. (A detailed justification of

this assumption is made in Section 2.3.3.) Finally, we set the initial conditions of the leg based on the total system energy. If too little initial energy is present when the simulation begins, the system may never reach its limit cycle; if too much initial energy is present, the system may quickly go unstable. We adjusted parameters until we found a good set of mechanical initial conditions. The values chosen were $\theta_{h0} = -0.350$ rad, $\theta_{k0} = 0.125$ rad, and $\omega_{h0} = \omega_{k0} = 0.000$ rad/sec. Ignoring the potential energy stored in any passive stiffness components, these initial conditions start the leg with 2.91 J of potential energy and no kinetic energy. Leg energy is discussed in more detail in Section 2.4.2.

Using the simplifications, the number of parameters that needed to be chosen to was reduced to 14. Because we wanted a nominal or canonical parameter set that could be used as a reference point for all experiments, we needed a method for determining a "good" parameter set. We developed a cost function that guarantees 1) that the system is frequency locked (*i.e.*, the two frequencies corresponding to the joint oscillations and the two frequencies corresponding to the HCOs are all closely matched) and 2) that the system is stable (*i.e.*, the magnitude of the system's maximum Floquet multiplier, as described in Section 2.4.3, is less than unity). Once these criteria are met, the cost function is calculated as:

$$\text{cost} = c_1 \cdot \sigma + c_2 \left| (\overline{\theta_h} - \theta_{ab,h}) \right| + c_3 \left| (\overline{\theta_k} - \theta_{ab,k}) \right| \tag{25}$$

where σ is the *specific cost of leg swinging* (as defined in Section 2.4.2), $\overline{\theta_h}$ and $\overline{\theta_k}$ are the mean joint angles for the hip and knee, $\theta_{ab,h}$ and $\theta_{ab,k}$ are the active torque bias angles for the hip and knee (as defined in Section 3.2), and c_i are weighting constants.

Low values of this cost function correspond to parameter sets that produce energy efficient pendulum motion that tracks closely the active torque bias angle. We therefore chose to minimize the cost function and to choose the parameter set with the minimum cost as the canonical parameter set. The large dimensionality of this parameter space prevented the use of simple iterative methods. For example, using 10 points for each of the 14 parameters requires just over 289 billion trials to cover all possible parameter combinations.

In an attempt to reduce the required number of trials significantly, we sought an optimization technique that could quickly find low-cost parameter sets. The first technique attempted was a stochastic gradient decent-type optimization technique [98], which uses the following algorithm.

1. Randomly choose a point, $\mathbf{P}_i$, in the pre-defined n-dimensional parameter space.

2. Evaluate the cost associated with this point of n parameters.

3. If the cost is smaller than the cost of any previously tested point, choose a new set of parameters, $\mathbf{P}_{i+1}$, with values that continue in the same direction as the previous changes in parameter values. If the cost is not smaller, choose $\mathbf{P}_{i+1}$ with values that move in the opposite direction as the previous changes in parameter values. (When choosing new parameter sets, a small amount of stochastic noise is introduced to prevent deterministic solutions that may get caught in local minima.)

4. Repeat this process until the cost of a set of parameters is less than a pre-defined threshold.

The difficulty in using this technique was that the parameter space was highly irregular, or "rough", causing the technique to spend inordinate amounts of time and computational power avoiding local cost minima.

The second technique we used—a standard Monte Carlo optimization—was more successful for this application. In this technique, trials are performed with random sets of parameters. After each trial, the cost is calculated (as with the gradient descent technique), and then a new set of parameters is randomly selected without any regard to the parameters previously chosen. After many trials have been performed, the optimization routine outputs a log of all parameter sets tested with their corresponding costs so that the parameter set with the lowest cost can be chosen. Although Monte Carlo techniques do not, in general, find the parameter set with the lowest possible cost, they are useful in quickly finding sets with relatively low cost. Additionally, because each parameter set is uncorrelated with the others, another benefit is that the effect individual parameters have

Object	Test Parameter	Canonical Value		
		Hip	Knee	Unit
HCO	τ_1	0.23	0.20	sec
Leg	K	0.20	0.20	Nm/rad
	θ_{sb}	0.00	0.30	rad
	B	0.14	1.40	Nm sec/rad
Control	θ_{ab}	0.00	0.25	rad
	G_{ff}	2.50	1.25	Nm
	G_{fb}	2.20	1.80	-

Table 4: Canonical parameter set used for the computational model.

on overall system performance can generally be ascertained. For this system, we performed 2,500 trials and selected the best parameter set to serve as a "canonical parameter set" that could be referred to as a reference point for all experiments. The canonical parameter set is shown in Table 4.

2.3 Robotic Implementation

With the computational implementation in place, we developed a robotic model of human leg swinging that closely emulated the computational model and served as a testing platform for robotic movement control experiments. We chose to physically model the leg because this research is intended to be directly applicable to the improvement of legged robotics and is also the first step toward our development of an anthropomorphic, dynamically walking robot. In addition, the robotic model necessarily includes real-world imperfections such as friction, parameter mismatch, and signal noise. As with the computational model, the mechanical properties of each leg segment were anthropomorphically matched to those of an adult female human [137]. An advantage to developing a full-scale model is that the inertial properties are not dominated by non-conservative forces such as friction. This allows performance comparisons to be made with data from the literature.

2.3.1 Mechanical Design

Figure 7 shows a mechanical drawing of the robotic leg we developed. The top platform models a fixed pelvis (*i.e.,* mechanical ground) from which the leg is suspended; it also provides support for the two motors. As with the computational model, the leg is restricted
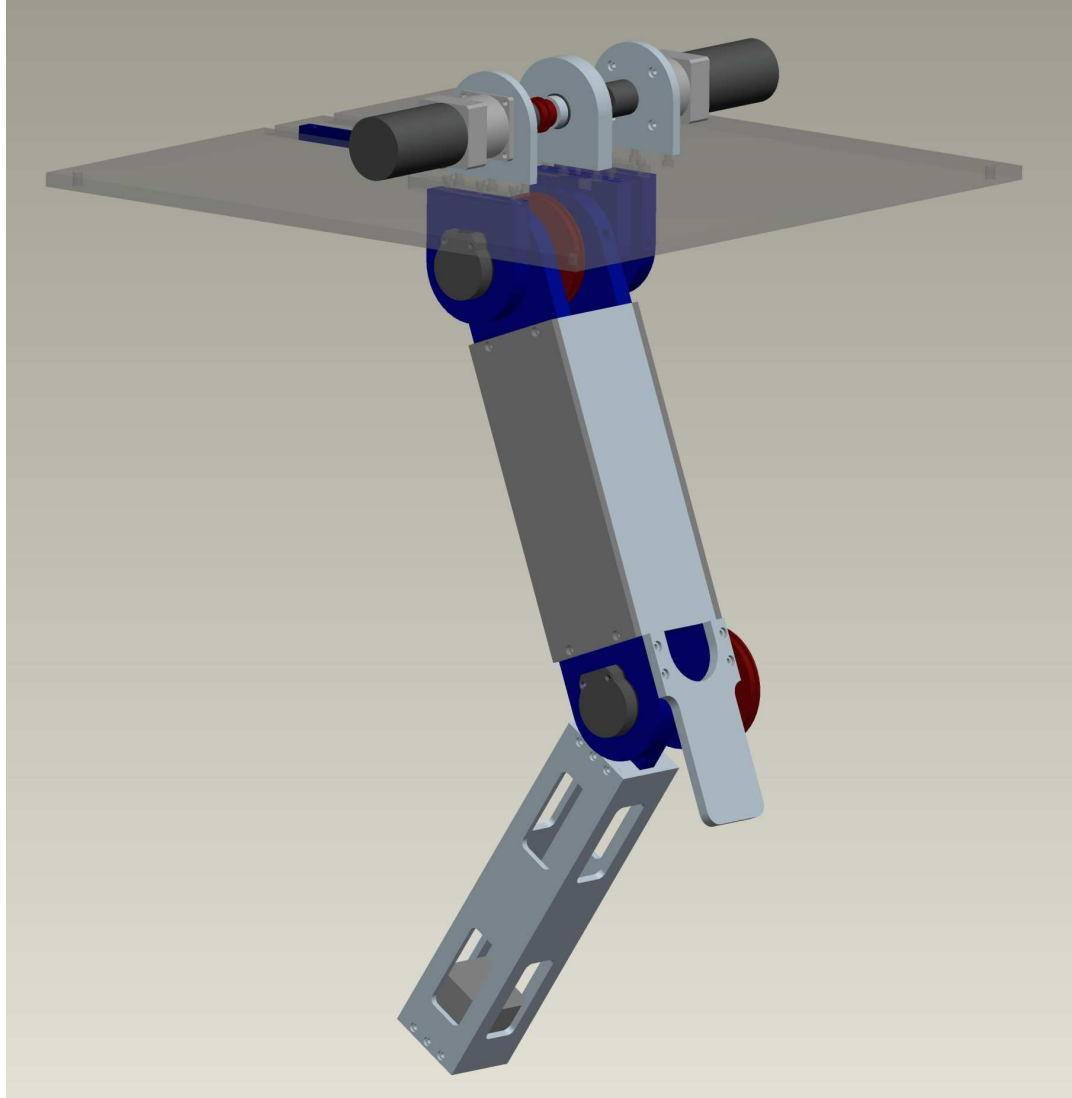
Figure 7: Three-dimensional model of the robotic leg. The top platform suspends the leg and supports both motors. The joints are actuated via transmission cables (not shown) between the motor and joint pulleys (shown in red). Feedback from the leg to the controller is provided by joint angle encoders (shown in black).

Motor Parameter	Nominal Value	Scaling Factor	Apparent Value
Max Continuous Torque (Nm)	0.448	28	12.54
Friction Torque (Nm)	7.06×10^{-3}	28	1.98×10^{-1}
Damping Torque (Nm sec/rad)	8.09×10^{-6}	784	6.34×10^{-3}
Output Inertia (kg m^2)	3.77×10^{-5}	784	2.96×10^{-2}

Table 5: Effect of gear ratio of motor parameters.

to move in the sagittal plane by revolute joints at the hip and knee, and each leg segment is designed such that its length, mass, CoM, and MoI match those of the female subject. Additionally, the shank and foot were combined into one leg segment. The material type and physical design of each component was made to assure the anthropomorphic parameters were matched as closely as possible to the ideal values shown in Table 1. The completed robotic leg is shown in Figure 8.

The choice of motors for this design was critical because the vast majority of DC motors have significant cogging torques and hysteresis torques, which would prevent the leg from moving naturally, and high motor output inertia, which would dominate the inertia of the actual leg. These issues were minimized by selecting a pair of newly developed DC motors (Thin Gap, Inc., Ventura, CA, Model: TGB2011) that eliminate hysteresis and cogging torque and are highly back-drivable (have very low output inertia). The joints are directly driven by the motors using steel transmission cables.

We used a 28:1 gear ratio—7:1 is provided by a gear box (CGI, Inc., Carson City, NV, Model: 023VPX0070) and the additional 4:1 is provided by the cable pulleys. The choice of a gear ratio in this type of situation is a trade off between increasing joint torque and keeping the effects of the parasitic motor properties low. Careful consideration must be given because although the output motor torque is scaled by the gear ratio (*i.e.,* 28), the motor's viscous drag torque (damping) and output inertia are scaled by the *square* of the gear ratio (*i.e.,* 784). The motors' operational and parasitic parameters are summarized in Table 5.

The remote location of the motors assures the ability to match the weight and inertia of each leg segment with the human subject. One complicating factor in the use of transmission cables across a multi-joint limb is that the movement of proximal joints can affect the
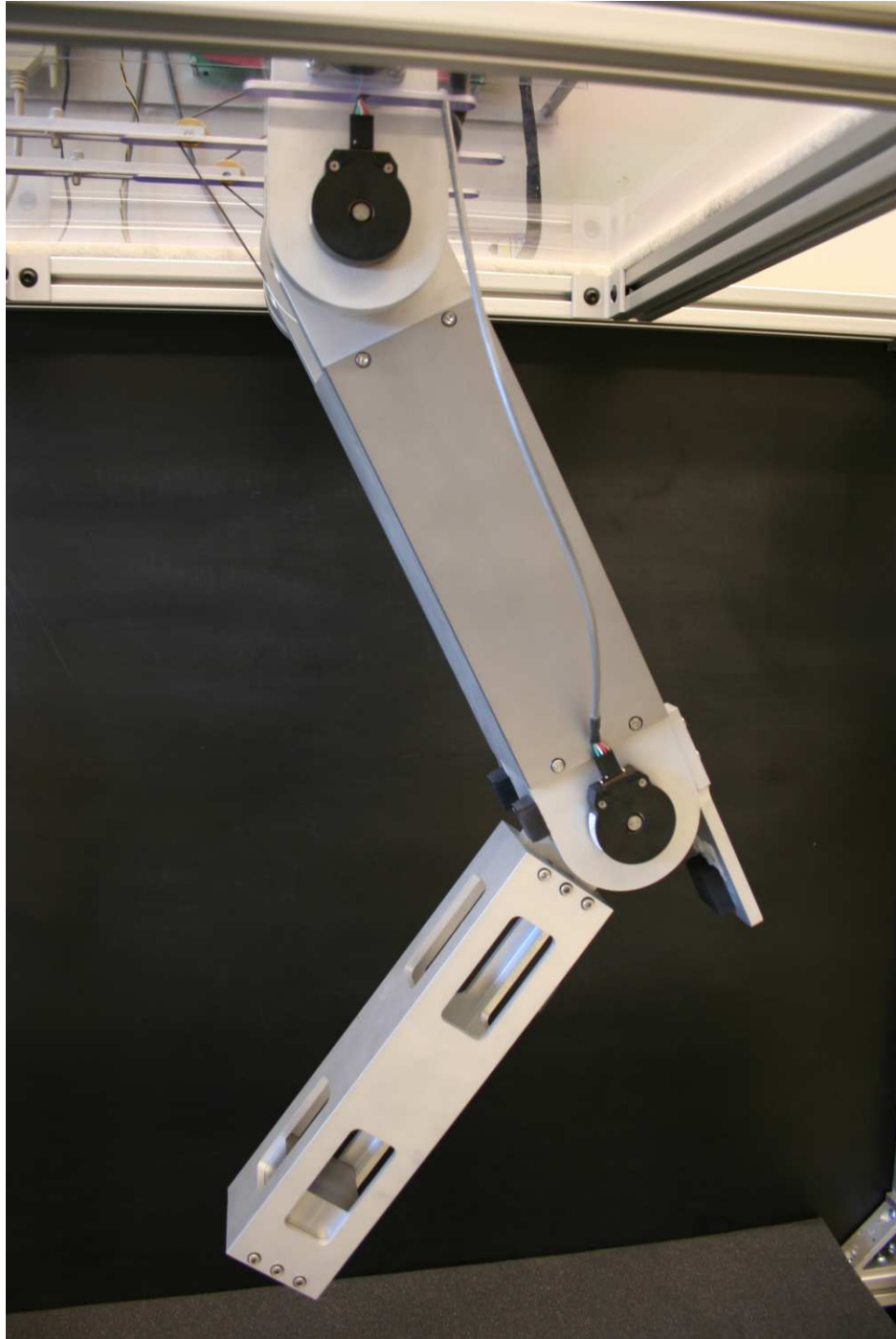
Figure 8: The completed robotic leg with both joint flexed. The joint angle encoders can be seen as the black sensors at each joint. The padded metal component extending from the thigh models the hard-stop component of knee asymmetry.
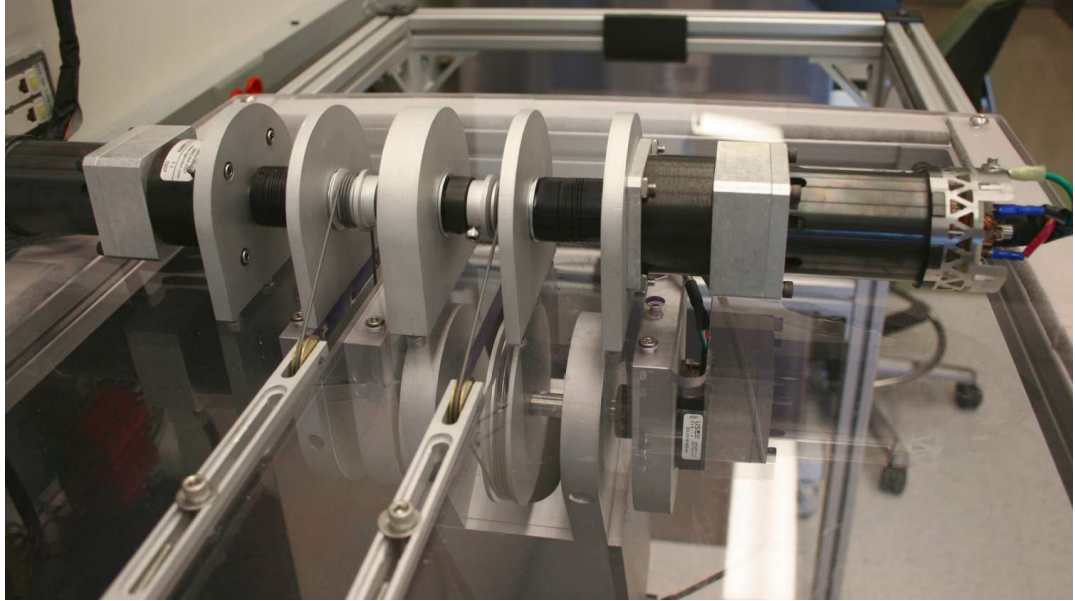
Figure 9: The robotic leg's actuation system. To the far left and right are the DC motors. Working inward, the motors are attached to 7:1 ratio gear boxes, shaft couplers and then a 4:1 cable pulley system. Note that the drive shafts of the two motors are not in any way connected to each other because a gap exists between the two drive shafts within the wider center support. To the near side, are idlers that adjust and maintain tension within the drive cables.

actuation of distal joints because the distance between the distal joint and its actuator can vary. To avoid this problem, we routed the knee's transmission cables as close as possible through the extended axis of the hip. In this manner, the cables always run along the centerline of the leg segments regardless of the hip angle and therefore keep the effective distance between the knee and the knee's actuating motor constant. Figure 9 shows the completed actuation system.

We choose to control the joints using antagonistic, series-elastic actuation. Typically, this is accomplished using two actuators in a pull–pull arrangement with passive components (*e.g.,* springs and dampers) in series with the cables connecting the actuators and the joint. Because we are using one direct-drive (*i.e.,* push–pull) motor per joint, the effects of the passive components must be modeled computationally so that their effects on the joint can be output as a motor torque. This approach is referred to as *virtual model control* [94, 96, 95] and is discussed further is Section 2.3.4.
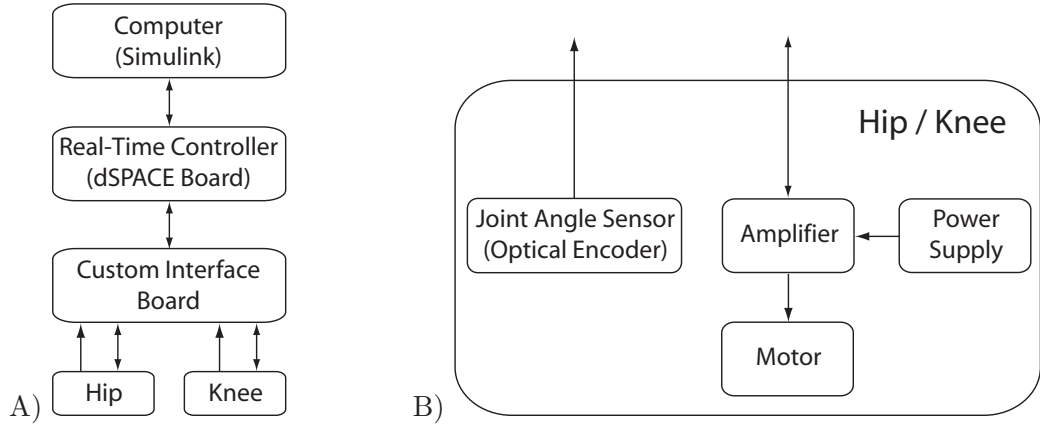
Figure 10: A) Top-level connectivity of the hardware components used in the real-time robotic system. B) Connectivity of the individual components used to actuate and provide feedback from each of the two robotic joints.

2.3.2 Electrical Design

In Section 2.3.4, we present a closed-loop controller that monitors feedback from the joint angle sensors and provides control signals to the actuators. The controller, however, can only handle low-power signals. It is not intended to provide significant power to any external component. Because the sensors and motors require external power to operate properly, it was necessary to develop an electrical system to provide power and signal amplification. An overview of the hardware used for this subsystem is shown in Figure 10. Figure 10A shows a top-level view of the components involved in the robotic model. The top two blocks represent the controller (Section 2.3.4). The custom interface board is a circuit board that routes signals from the controller to the appropriate hardware components and provides power to the angle sensors and visual status indicators (*i.e.,* LED's), and provides emergency shut-off capability for the robotic leg. Figure 10B shows a more detailed view of the individual components that are used to actuate and provide feedback from each of the two robotic joints.

The power supplies (Mean Well, Inc., Fremont, CA, Model: SE-1000-24) supply up to 1.0 kW at 24 VDC to the motor amplifiers (Advanced Motion Control, Inc., Camarillo, CA, Model: 50A8V). By setting these Pulse-Width Modulated (PWM) servo amplifiers to current mode, we were able to control motor currents using analog output signals produced

by the controller. The actual amplifier output to the motors is a 24V PWM signal whose duty cycle (relative to 50%) is proportional to the magnitude of current delivered to the motor. The direction of the current is determined by whether the duty cycle is above or below 50%. Because the amplifiers' output is a high-power AC signal, the amplifier requires the motor inductance to be at least 200 μH to maintain amplifier stability. However, the unique design of the motor that reduces cogging and hysteresis torque also reduces the inductance of the motor to 5.3 μH. This issue was resolved by adding 300 μH inductor boards (Advanced Motion Control, Inc., Camarillo, CA, Model: FC15030) in series between the amplifiers and the motors.

The high-power AC signals that connect the amplifiers to the motors via the inductor boards produce significant electrical noise that has the potential to interfere with the low-power signals used to distribute control and feedback signals throughout the electrical system. To minimize this effect, we used twisted-pair, copper-shielded cables for all high-power connections. Twisting the conductors and using grounded copper shielding acts to reduce the electromagnetic interference (*i.e.,* noise) they produce. To further reduce the effects of electrical noise and to remove any potentially floating grounds, all hardware components (power supplies, amplifiers, inductor boards, motors, and the interface board) were grounded to a common reference point. The complete electrical system is shown in Figure 11.

Besides controlling the motors, the electrical system also serves as the source of two primary sources of proprioceptive feedback to the leg's controllers. Kinematic (joint angle) feedback is provided by optical encoders (US Digital, Inc., Vancouver, WA, Model: E3) at the hip and knee that provide 0.045 deg angular resolution (2000 counts/revolution using a quadrature encoder). Kinetic (joint torque) feedback is provided by current sensors in the motor amplifiers that detect the levels of currents being drawn by the motors. Because motor current is proportional to torque, we can determine the torque being applied to each joint according to the following equation.

$$\Gamma_{\mathrm{j}} = I_{\mathrm{m}} C_{\mathrm{t}} R \tag{26}$$

Figure 11: Electrical system used to provide power and signal amplification to the robotic leg's actuators and sensors. The power supplies are the two large silver boxes at the top; the amplifiers are the two black rectangular components to the center right; the series inductor boards are located at the bottom right; and the custom interface board is located at the bottom left. Directly above the interface board is a grounding strip used to provide a common reference voltage for all components.

where Γ_j is the torque being applied to the joint by the motor, I_m is the current being drawn by the motor (as indicated by the amplifier), C_t is the motor torque constant, and R is the total gear ratio. Kinetic feedback is used solely to validate system performance (*i.e.,* to verify that the desired joint torques are accurately applied to the joints).

The entire robotic leg system including the electrical control hardware is shown in Figure 12.

2.3.3   Characterization

Although efforts will be made during leg construction to match the limb segment properties listed in Table 1, some error is expected that must be quantified. Therefore, before performing any experiments on the robotic leg, we characterized the system to get a thorough understanding of its physical mechanical properties and performance limitations. Physical mechanical property values vary from the design values because of imperfections in the manufactured components, the purchased components, or the assembly. Performance limitations are caused by factors such as actuator/sensor noise and design trade-offs (*e.g.,* motor weight versus power). Section 2.3.3.1 describes how the mass properties of the limb segments were measured both with and without the actuators attached. Section 2.3.3.2 then determines the limitations and performance of the actuation system. Finally, Section 2.3.3.3 explains how the natural frequencies of each joint were calculated.

2.3.3.1   Mass Properties

We began characterizing the leg's performance by measuring the fixed mechanical parameters of each leg segment, specifically those parameters listed in Table 6. The length and mass of each segment was found simply by measuring and weighing each component before assembly. We found the center of mass by determining the length-wise distance from the proximal joint at which the segment balanced on a sharp edge.

The calculation of moment of inertia, J, is more complicated because it requires dynamic testing of the assembled leg (without actuators attached). The procedure we chose is modeled after the "pendulum test", a clinical technique used to measure mass properties in human legs [64, 5]. In this technique, all joints except the one being analyzed are rigidly
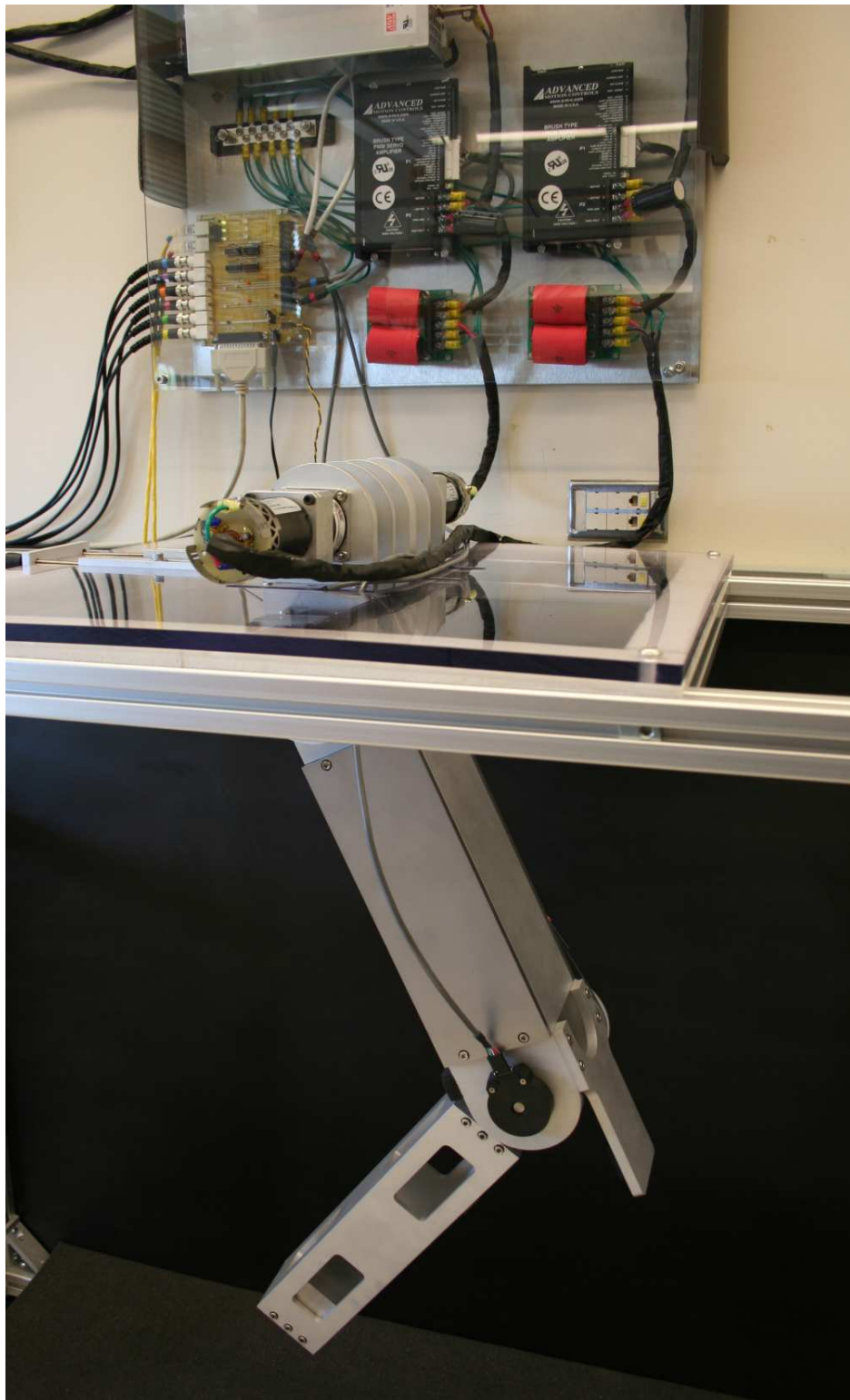
Figure 12: Complete robotic leg including electrical hardware.

held in a straightened configuration. Because only one joint can move, analysis of the hip will yield the MoI of the entire leg, and analysis of the knee will yield the MoI of the shank/foot. The MoI of the thigh can then be found by subtracting the shank/foot value from the whole leg value. It should be noted that during the tests on the knee, the hyperextension-preventing mechanism on the knee was removed, allowing the shank to swing freely.

The "pendulum test" requires that the portion of the leg distal to the joint being analyzed can be modeled as a single DoF pendulum whose dynamics follow the equation:

$$J_\mathrm{j}\ddot{\theta} + B_\mathrm{j}\dot{\theta} + K_\mathrm{j}\theta + mgL_\mathrm{cm}\sin\theta + \Gamma_\mathrm{f} = \Gamma \tag{27}$$

where J_j is the MoI of the pendulum, B_j is the joint's damping coefficient, K_j is the joint's stiffness coefficient, m is the mass of the pendulum, L_cm is the position of the center of mass, Γ_f is the torque due to dynamic friction at the joint, and Γ is the applied joint torque. For simplicity, we made the small angle approximation that $\sin(\theta) \approx \theta$ and the assumption that friction is negligible compared to the inertia of the leg (*i.e.,* $\Gamma_\mathrm{f} \approx 0$). Rearranging this equation gives the system's transfer function in the form of a second-order system:

$$\frac{\theta}{\Gamma} = \frac{\frac{1}{J_\mathrm{j}}}{s^2 + s\left(\frac{B_\mathrm{j}}{J_\mathrm{j}}\right) + \frac{mgL_\mathrm{cm}+K_\mathrm{j}}{J_\mathrm{j}}} \tag{28}$$

The natural oscillation frequency, ω_n, and the damping ratio, ζ, are defined as:

$$\omega_\mathrm{n} = \sqrt{\frac{mgL_\mathrm{cm} + K_\mathrm{j}}{J_\mathrm{j}}} \tag{29}$$

$$\zeta = \frac{B_\mathrm{j}}{2\sqrt{J_\mathrm{j}(mgL_\mathrm{cm} + K_\mathrm{j})}} \tag{30}$$

These parameters can also be calculated empirically by letting the leg oscillate freely and measuring the mean period, T, and the angular velocity, $V(n)$, each time the angle crosses zero. The empirical definitions are:

$$\omega_\mathrm{n} = \frac{2\pi}{T} \tag{31}$$

$$\zeta = \sqrt{\frac{\ln\left(\frac{V(n)}{V(n+1)}\right)^2}{\pi^2 + \ln\left(\frac{V(n)}{V(n+1)}\right)^2}} \tag{32}$$

Segment	Length (cm)	Mass (kg)	CoM (cm)	MoI (kg m^2)	
				Unactuated	Actuated
Thigh	40.4	6.85	19.7	0.423	0.525
Shank/Foot	46.0	3.95	26.9	0.413	0.515
Total Leg	86.4	10.80	37.1	2.330	2.432

Table 6: Empirically determined leg segment mass properties. The mass properties for the total leg were determined for the case when knee angle was 0 deg.

For the "pendulum test", ω_n and ζ are found for the leg segment being tested, and then found again with an external weight of known MoI (relative to the rotating joint) attached to the leg. The leg segment inertia is then calculated according to the equation

$$J = \frac{\epsilon}{r_1 r_2 - 1} \tag{33}$$

where ϵ is inertia added to the leg, r_1 is the ratio of the original natural frequency to the added weight case, and r_2 is the ratio of the original damping ratio to the added weight case. The experimentally obtained values for each leg segment's mass properties are shown in Table 6.

The addition of actuation systems to any mechanism can alter the mechanism's dynamics by changing the apparent values of its mass properties. In our case, connecting the motors can significantly increase the leg segments' apparent MoI. To quantify this effect, we attached the motors to the joints via steel actuation cables and re-calculated the limb segments' MoI. During these experiments, the leg was allowed to oscillate freely with the motor physically connected but turned off (open circuit). The new MoI values are shown in the right-most column of Table 6. Note that the values were increased by 0.102 kg m^2, which represents the actuation system's contribution to the apparent MoI of a limb segment.

The empirically determined mass properties compare favorably with the ideal values of our target female subject (Table 1). The average parameter error is 8.5% in the unactuated case and 11.6% in the actuated case. However, these values are skewed by the large error in the values for the unactuated thigh MoI (42.4% error) and the actuated thigh MoI (76.8% error). The high error in these properties arose because design emphasis was placed on assuring the shank/foot and total leg MoI matched their respective values, as these properties are much more relevant to the leg's dynamics (see Section 2.3.3.3). If the error due to the

thigh MoI is removed from the calculation, the average parameter error is reduced to 5.4% in the unactuated case and 5.6% in the actuated case. To assure that the computational and robotic models are as consistent as possible, the mass properties used for the computational model were altered to match those empirically measured for the robotic model.

2.3.3.2 Actuation System

The characterization up to this point was solely focused on passive properties of the system (*i.e.,* those without any power applied to the leg). The next step was to characterize the performance capabilities and limitations of the actuation system.

Calibration   We began this process by calibrating the actuation system so that the controller can accurately apply joint torques. Once the controller (Section 2.3.4) determines the torque to be applied to each joint, that value must be transformed into an input voltage to the motor amplifier that takes into consideration factors such as the motor torque constant, the amplifier's scaling constant, and the gear ratio. Because these factors are all constant gains, the simplest way to calibrate the output torque signal is to determine the proportionality constant that relates desired motor torque and resulting joint torque. To do this, we swept the desired motor torque signal and measured the actual joint torque produced with a 0.2 N resolution force transducer. The resulting input–output relationships were:

$$\text{HIP:} \quad \Gamma_c = 0.3147 \ \Gamma_j \tag{34}$$

$$\text{KNEE:} \quad \Gamma_c = 0.3092 \ \Gamma_j \tag{35}$$

where Γ_c is the desired motor torque (as determined by the controller) and Γ_j is the actual joint torque produced. We know that the gear ratio is 28:1, and according to manufacturer specifications, the motors' torque constant is 50.0 and the amplifiers' scaling constant is 0.2. Using these values, we calculated the hip calibration coefficient to be $0.3147 \cdot 28.0/50.0/0.2 = 0.881$ and the knee calibration coefficient to be $0.3092 \cdot 28.0/50.0/0.2 = 0.866$. These scaling constants were incorporated into the output stage of the controller as constant gains.

Joint Torque Limitations The range of possible applied torques is limited by the amount of current tolerated in both the motors and the motor amplifiers. The continuous current limit of the motor is 22.4 A and the amplifier can sustain 25.0 A. Each element can withstand peak currents approximately twice as large but only for short durations of less than two seconds. We reduced the allowable continuous output current for the amplifier to 16.7 A to provide a safety margin of more than 30% for the motors and reduce the chances of damage due to overheating. The motors' torque constant is 0.02 Nm/A which makes the maximum possible motor torque 0.334 Nm. With the 28:1 gear ratio, the maximum joint torque that can be continuously applied is 9.35 Nm. Experimentally, we found the maximum to be 8.51 Nm, which represents an error of 9.0%. It should be noted that these motors are not strong enough to lift the entire leg through its range of motion. In fact, when the shank is fully extended, the hip can only continuously maintain an angle of ± 0.22 rad (12.5 deg). We chose not to increase actuation torque with a larger gear ratio to avoid increasing apparent motor output inertia.

Stiffness Joint stiffness is controlled with torques related to the difference between a joint's angle and some bias angle. Neither the physical leg nor the motor have any inherent stiffness (ignoring the apparent stiffness caused by gravity). It was therefore not necessary for the model to provide any compensation for parasitic stiffness. Although there is no theoretical limit to the level of stiffness that can be applied to a joint, the implementation of stiffness is limited in practice by the maximum amount of torque that the motors can produce.

Damping In addition to the joint damping that is actively applied, there are two primary sources of passive damping in the system that need to be accounted for—the mechanical joint and the motor. As before, these two contributions were combined, and we performed a calibration based on the total apparent damping at each joint. To characterize damping, we again used the simplification that the leg could be modeled as a second-order system (*i.e.,* pendulum). Using Equation 32, we showed earlier that the damping ratio, ζ, of the leg can be found using the empirically determined ratio $\frac{V(n)}{V(n+1)}$. Rearranging Equation 30

and setting the joint stiffness to zero, we get

$$B = 2\zeta\sqrt{JmgL_{\mathrm{cm}}} \tag{36}$$

where B is the total apparent damping of the joint, and J is the total apparent MoI of the joint (as determined in Section 2.3.3.1). Using this equation, we swept the desired damping values up from zero and, for each value, measured the resulting damping, B. By performing a linear regression we found the damping calibration for the joints to be:

$$\text{HIP:} \quad B_{\mathrm{m}} = 4.20B - 0.11 \text{ Nm sec/rad} \tag{37}$$

$$\text{KNEE:} \quad B_{\mathrm{m}} = 1.09B - 0.10 \text{ Nm sec/rad} \tag{38}$$

where B_{m} is the measured damping using Equation 36 and B is the damping desired (as determined by the controller). These scaling and offset calibration terms were included into the controller.

Friction   In any real mechanical system, parasitic friction is present. Ideally, we would like to model the static and dynamic friction so that compensatory torques could be added to the system to remove the effect of the friction. However, the nonlinear transitions between the static and dynamic friction components make it difficult to characterize and compensate for friction [41]. One reason for the difficulty is the need to know what forces are being applied to a body. At rest, static friction exactly counters these forces, so without a means to accurately measure applied forces, it is not possible to compensate for them. Once moving, bodies experience dynamic friction, which is velocity independent. Although compensation just requires a constant force to be applied in the direction opposing motion, the discontinuity that occurs at zero velocity can cause oscillatory instability. To avoid these complications, we made the assumption that the effects of friction are negligible because the inertia of each leg segment dominates the joint dynamics.

To justify this assumption, we measured the levels of static and dynamic friction present in the joints with actuators attached but turned off. Static friction was measured by determining the minimum torque needed to begin movement. We found this value to be 0.76 Nm, which is only twice the resolution of our force transducer (0.2 Nm resolution). Dynamic

friction and was determined by allowing the leg to swing freely and analyzing the energy lost from the system during each period. By calculating the component of the energy decay that was independent of velocity magnitude, dynamic friction was calculated to be 0.40 Nm. These values are, on average, an order of magnitude lower that the torque applied the joints during normal experiments and can therefore safely be ignored.

2.3.3.3 Joint Natural Frequencies

The natural frequency, ω_n, of each limb segment is an important value for many of the experiments performed in this research. It is therefore crucial to understand what factors affect the frequency values. From Equation 29, we know that the natural frequency of a pendulum is a function of the stiffness applied to the joint and the pendulum's MoI. Because the shank can be modeled accurately as a single pendulum, the knee's natural frequency is determined by the knee stiffness and the shank's MoI. The hip's natural frequency is more complicated because it is determined by the hip stiffness and the *leg's* MoI. The leg's MoI is a combination of the thigh and shank/foot inertia values (from Table 6) and varies based on the knee angle. The dependence on knee angle occurs because knee flexion lessens the distance between the shank/foot center of mass and the hip, reducing the total leg's MoI. Using the Parallel Axis Theorem, the leg's MoI can be calculated as:

$$J_{l/h} = J_{t/h} + J_{s/h} \tag{39}$$

$$J_{l/h} = J_{t/h} + J_{s/k} + M_s \left(L_t^2 + 2L_t L_{cm,s} \cos \theta_k \right) \tag{40}$$

where $J_{l/h}$ is the MoI of the entire leg relative to the hip, $J_{t/h}$ is the MoI of the thigh relative to the hip, $J_{s/h}$ is the MoI of the shank relative to the hip, and $J_{s/k}$ is the MoI of the shank relative to the knee. Using the parameter values from Table 6, we can show that $J_{l/h}$ is reduced by only 0.51% at 0.17 rad knee flexion, 2.04% at 0.34 rad knee flexion, 4.52% at 0.52 rad knee flexion, and 7.90% at 0.70 rad knee flexion, which represents the maximum extent of the knee's normal range of motion. Because the effect of knee angle on $J_{l/h}$ is minimal and because compensation for this effect would add substantial complexity, we made the simplification that this effect could be ignored and that $J_{l/h}$ could be approximated as the value with the knee angle, θ_k, set equal to 0 rad. With this simplification, the hip's

natural frequency becomes a function of hip stiffness and of the MoI of the leg in the anatomical position. The MoI values shown for the total leg in Table 6 are for the leg in anatomical position.

Because the joints are actuated by motors, the complete equations of motion require the effects of the motors to be included. The equation of motion for a DC motor is:

$$\Gamma_{\mathrm{m}} = B_{\mathrm{m}}\dot{\theta}_{\mathrm{m}} + J_{\mathrm{m}}\ddot{\theta}_{\mathrm{m}} + \Gamma_{\mathrm{f,m}} \tag{41}$$

where Γ_{m} is the torque generated by the motor, B_{m} is the motor damping coefficient, J_{m} is the motor armature's MoI, and $\Gamma_{\mathrm{f,m}}$ is the dynamic friction torque of the motor. The values of each of these parameters are shown in Table 5. As in Section 2.3.3.1, we made the small angle approximation and the assumption that friction can be ignored because its effect is dominated by the inertial dynamics. When Equations 27 and 41 are combined and the effects of gear ratio are considered, the complete equation of motion for an actuated joint becomes:

$$\ddot{\theta}\underbrace{(J_{\mathrm{j}} + R^2 J_{\mathrm{m}})}_{J} + \dot{\theta}\underbrace{(B_{\mathrm{j}} + R^2 B_{\mathrm{m}})}_{B} + \theta(mgL_{\mathrm{cm}} + K_{\mathrm{J}}) = R\,\Gamma_{\mathrm{m}} \tag{42}$$

where θ is the joint angle, R is the gear ratio, and the subscripts $_{\mathrm{m}}$ and $_{\mathrm{j}}$ represent the motor and joint, respectively. The inertia and damping terms have been grouped into J and B for simplicity and because the relative contributions of the mechanical system and the motor to each value are not important. Rather, the total (empirically measured) values are important because they determine the dynamics of the system. This equation can be rearranged to show the standard transfer function of a second order system:

$$\frac{\theta}{\Gamma_{\mathrm{m}}} = \frac{\frac{1}{J}}{s^2 + s\left(\frac{B}{R\,J}\right) + \left(\frac{mgL_{\mathrm{cm}} + K_{\mathrm{j}}}{R\,J}\right)} \tag{43}$$

and the natural frequency and damping ratio can be shown to be:

$$\omega_{\mathrm{n}} = \sqrt{\frac{K_{\mathrm{j}} + mgL_{\mathrm{cm}}}{R\,J}} \tag{44}$$

$$\zeta = \frac{B}{2\sqrt{R\,J(mgL_{\mathrm{cm}} + K_{\mathrm{j}})}} \tag{45}$$

Note that the natural frequency of the actuated joint (Equation 44) is nearly identical to that of the unactuated joint (Equation 29) with the exception of a factor of $\frac{1}{\sqrt{GR}}$.

Using Equation 44 and the mass property values in Table 6, the theoretical values of the joint's natural frequencies become:

$$\omega_{\text{n,h}} = \sqrt{\frac{K_{\text{h}} + 39.3 \text{ Nm}}{68.2 \text{ Nm}}} \tag{46}$$

$$\omega_{\text{n,k}} = \sqrt{\frac{K_{\text{k}} + 10.4 \text{ Nm}}{14.4 \text{ Nm}}} \tag{47}$$

where $\omega_{\text{n,h}}$ is the natural frequency of the hip and $\omega_{\text{n,k}}$ is the natural frequency of the knee.

2.3.4 Robotic Controller

As in the case of the computational model, we chose to use a closed-loop, CPG-based controller for the robotic model because this type of controller can adapt to changes in environment, to perturbations, to actuator/sensor noise, or to other unexpected conditions. Several implementation options exist for closed-loop robot controllers. From a basic perspective, the controller must be able to adeptly control a robot's movements by sending appropriate signals to the actuators based on sensory information. One option is that the controller could be implemented as a custom microprocessor board. The advantage to this approach is that the controller is limited in size and can be placed on the robot to create a potentially mobile solution. The disadvantage with this approach is that the custom design limits flexibility to changes after the design is manufactured. Furthermore, performing real-time data monitoring and analysis is complicated because data must be quickly streamed off board, a process that incurs latency and bandwidth restrictions.

The controller chosen for this research was instead based on a computer-based real-time processor, in which design flexibility and monitoring possibilities were maximized. We selected a dSPACE controller board (dSPACE, Inc., Model: CLP1104, Wixom, MI) as the primary hardware component around which the remaining hardware was chosen. This board uses a custom reprogrammable real-time processor to coordinate any of several digital or analog inputs/outputs. Physically, the dSPACE component consists of a PCI computer board with a PowerPC processor and an external break-out board that supports 8 ADC, 8 DAC, 2 dedicated position encoders reading ports, 2 serial ports and many 14-and 20-bit digital I/O. The control model used by dSPACE can be developed using MATLAB's
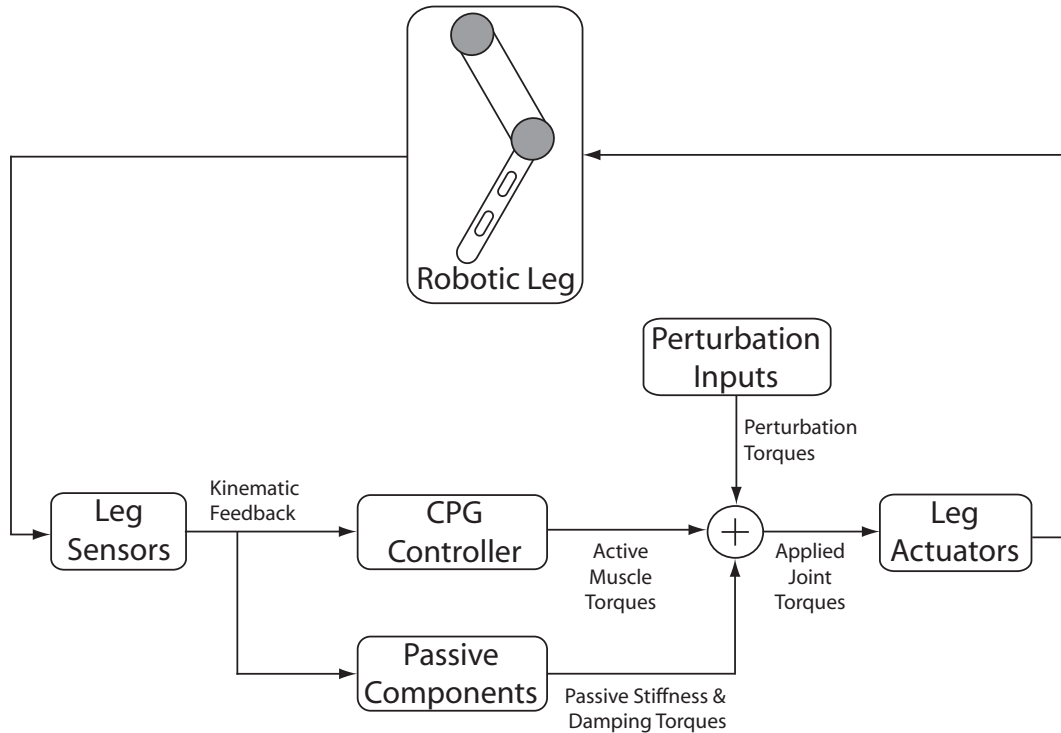
Figure 13: Control schematic for the robotic leg. Kinematic information is recorded from the leg by sensors (left) and is fed to the controller and virtual passive components. Leg actuators (right) are then provided with torque control signals that represent the sum of the active muscle torques produced by the CPG controller, the passive stiffness and damping torques generated by the virtual passive components, and any experiment-specific perturbation torques.

SIMULINK using a dSPACE blockset to coordinate interactions between the model and the dSPACE hardware components. Once developed, the model is compiled using MATLAB's REAL-TIME WORKSHOP and loaded onto the dSPACE processor. The process is quick and the time to compile and load an updated model onto the board is generally less than a minute.

The SIMULINK control model followed the computational control model closely with the exception that the Mechanical Leg Object was replaced with the actual robotic leg. Figure 13 shows an overview of the control schematic implemented in Simulink. The output torque signal is shown to have three sources. The primary signal comes from the CPG Controller, which computes the active muscle torques. Torque is also generated by the virtual passive components (*i.e.,* springs and dampers) and any perturbation torques that are applied as part of an experiment.
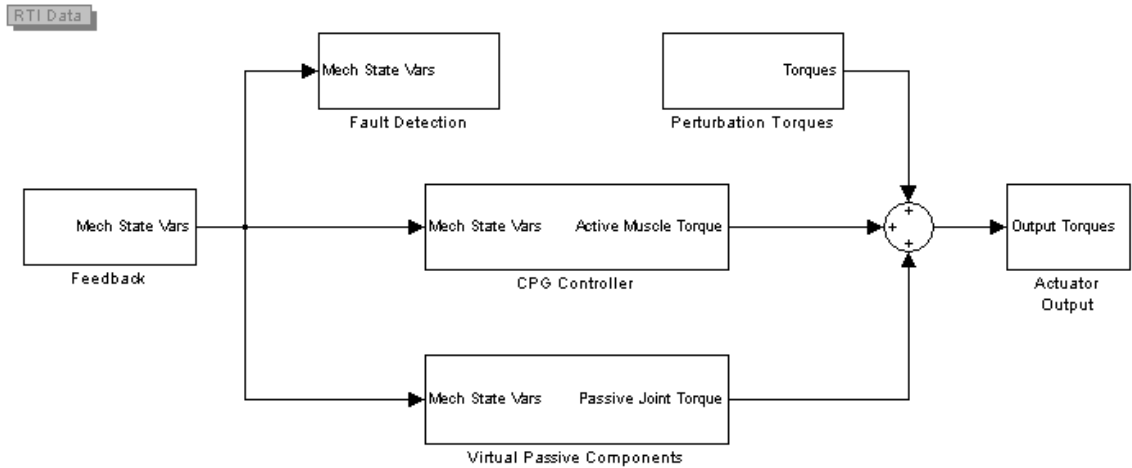
Figure 14: Top-level of SIMULINK model. Sensory feedback information is recorded in the Feedback block and the joint angles and velocities (*Mech State Vars*) are fed to the CPG Controller block, the Virtual Passive Components block, and the Fault Detection block. The torques output by the CPG Controller and Virtual Passive Components blocks are summed with any desired perturbation torques and sent to the Actuator Output block.

Simulink models are developed by graphically laying out blocks in a hierarchical manner much like a drawing of a logical flow chart. As shown in Figure 13, at a basic level the SIMULINK model must read sensor information from the dSPACE board, feed the information to controller, and then output torque signals to the dSPACE board. For clarity, the complete SIMULINK model is presented in block-level detail.

Top Level The top-level of the hierarchical SIMULINK model is shown in Figure 14. At this level, sensory feedback information is recorded and the mechanical state variables are fed to the CPG controller, which calculates the appropriate active muscle torque, and to the virtual passive components, which simulate the torques produced by the passive viscoelastic components. A separate block exists to generate additional perturbation joint torques as needed for individual experiments. All of these torques are summed and output to the motor amplifiers. For increased safety, a fault detection component exists that monitors the system for problems and can shut down the system to prevent damage.

Feedback Block The Feedback block of the SIMULINK model is shown in Figure 15. Kinematic feedback, which serves as the primary source of feedback to the CPG controller,
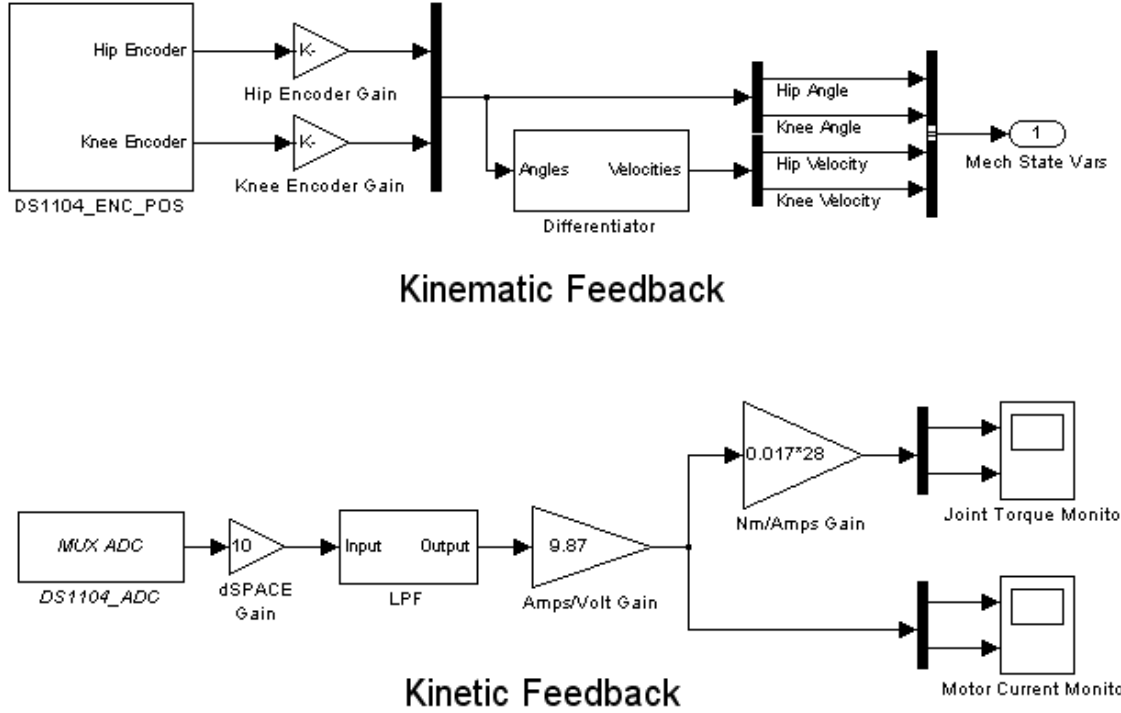
Figure 15: Feedback block of SIMULINK model. The top portion represents the kinematic feedback, which serves as the primary source of feedback to the controller. The block on the far left records the two dSPACE position encoder ports. The signals are then scaled and differentiated and output as the joint angles and velocities in a signal bus named *Mech State Vars*. The bottom portion of the figure represents the kinetic feedback. The dSPACE block on the left records amplifier feedback voltages using the ADC ports. The signals are then low-pass filtered and scaled to produce the applied joint torques and the motor currents. [4]

is based on the angular displacement signals recorded for each joint. The angular encoders we selected output 2000 counts per revolution, requiring $\frac{2\pi}{2000}$ gains to convert their outputs to radians. To calculate angular velocity, the joint angles are passed through a differentiator signal filter (and a 50Hz low-pass filter).

This block also calculated kinetic feedback so that we could monitor the system performance. A feature of the motor amplifiers we selected is that they output a voltage that is proportional to the current being drawn by the motor. We low-pass filtered the signals to remove noise and then multiplied them by the Amps/Volt gain used by amplifier to get the motor currents. We calculated the joint torque by multiplying the motor currents by the product of the motor torque constant (0.017) and the gear ratio (28) (see Equation 26).
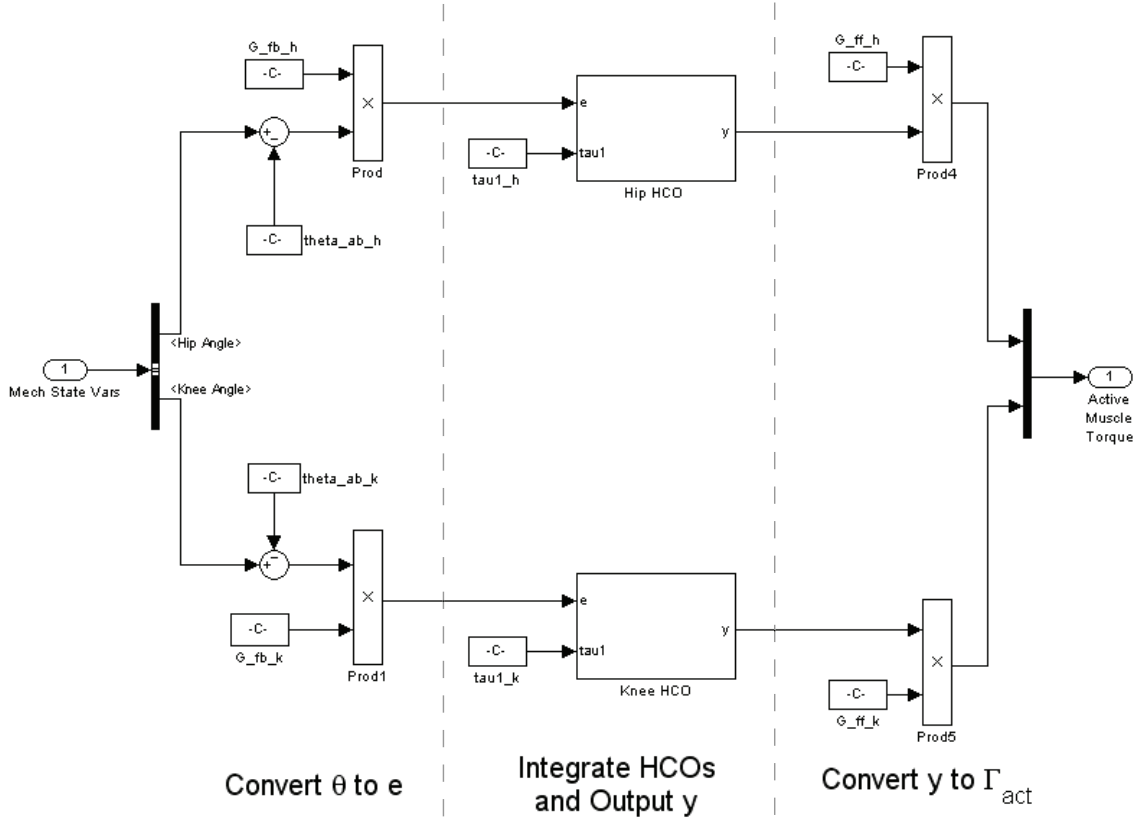
Figure 16: CPG controller block of SIMULINK model. This block has four major sections that correspond to parts of the process followed by the Control System Object of the computational model (Section 2.2.3). The top half of the block processes the hip signals and the bottom half processes the knee signals. On the left, the output of the Feedback block is received as the bus signal *Mech State Vars*. Moving left to right, the joint angle signals are selected and converted into HCO feedback signals (e), used to compute the HCO output (y), and then converted to the active muscle torque (Γ_{act}).

CPG Controller Block The CPG Controller block of the SIMULINK model is shown in Figure 16. In this block, joint angle signals are used to calculate appropriate active muscle torques. Before the joint angles (θ) can be fed to the HCOs, they must be formatted appropriately into HCO feedback signals (e), which simply involves signal scaling and shifting (Equation 23). Next the HCOs process the feedback information and produce their output, y, which is then converted to the active muscle torque, Γ_{act} using Equation 24.

Half-Center Oscillator Block The HCO block of the SIMULINK model is shown in Figure 17. The HCO is computed with four sub-blocks, each calculating one of the four HCO state variables—x_1, x_2, v_1, and v_2—using Equations 18–21. The x_1 and x_2 signals are
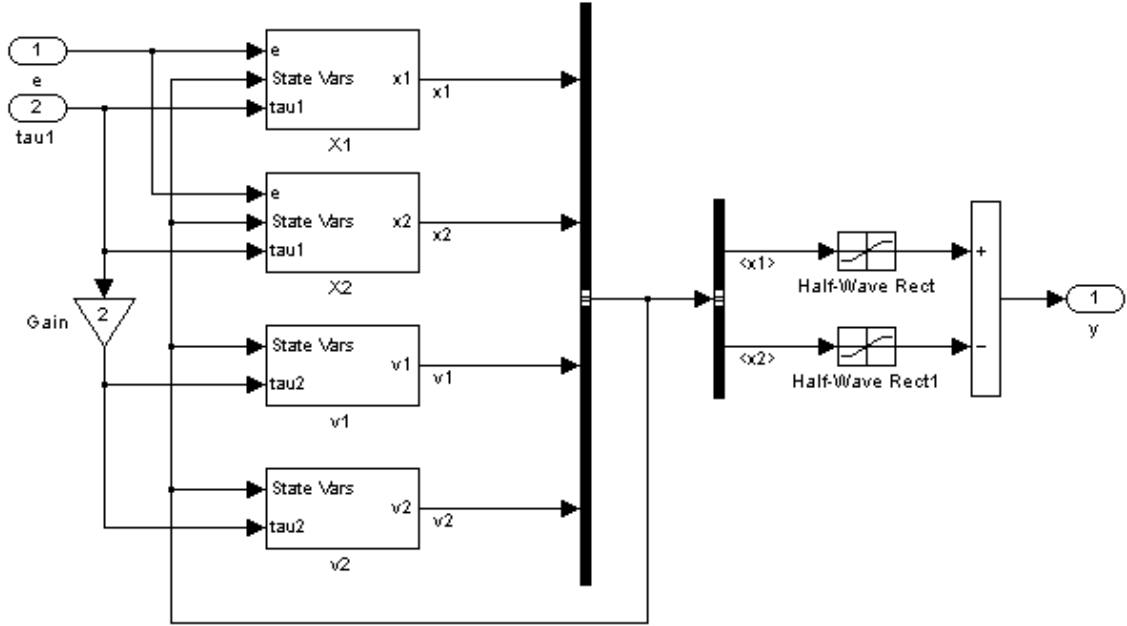
Figure 17: Half-Center Oscillator block of Simulink model. Values for the four HCO state variables (x_1, x_2, v_1, and v_2) are calculated in the blocks on the left and the HCO output (y) is computed on the right.

then half-wave rectified and the difference is taken as the HCO output, y using Equation 22.

Virtual Passive Components Block The Virtual Passive Components block of the SIMULINK model is shown in Figure 18. Passive stiffness torques (Γ_s) are calculated for each joint using Equation 15, and passive damping torques (Γ_d) are calculated using Equation 16. Summing these torques yields the total passive joint torque that is be applied via the actuating motors. This method of virtually adding viscoelastic properties is called *virtual model control*.

Perturbation Torques Block The Perturbation block of the SIMULINK model (not shown) provides a means to apply perturbation torques to either or both joints during an experiment. The perturbations can be impulses, steps, sine waves, random noise, or any pre-programmed signal. These torques are summed with any other model torques and output directly to the motors.
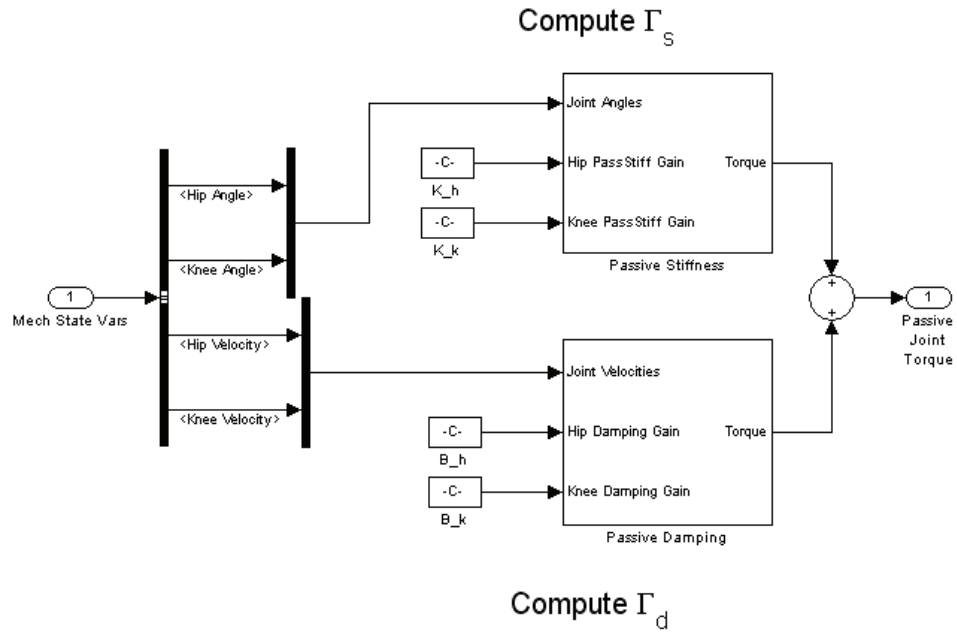
Figure 18: Virtual Passive Components block of SIMULINK model. This block computes torques generated by the passive stiffness (top block) and passive damping (bottom block) components using joint angle and velocity feedback.

Actuator Output Block The Actuator Output block of the SIMULINK model is shown in Figure 19. Once the total desired torque has been computed by the other blocks, the Actuator Output block takes the final value (in Nm) and converts it into an appropriate output voltage. The torque signals are scaled by the inverse of the gear ratio, the motor torque constant, and the amplifier scaling factor before passing through calibration blocks. The calibration factors were empirically determined in Section 2.3.3.2 by measuring the relationships between controller torque signals and actual joint torques. The final output signals are then sent as voltages to amplifiers.

Fault Detection Block The Fault Detection block of the SIMULINK model is shown in Figure 20. The role of this block is to assure safe operation of the leg. The system monitors whether:

- the Emergency Stop button is pressed,

- either of the hip or knee amplifier faults,

- either of the hip or knee power supply faults, or
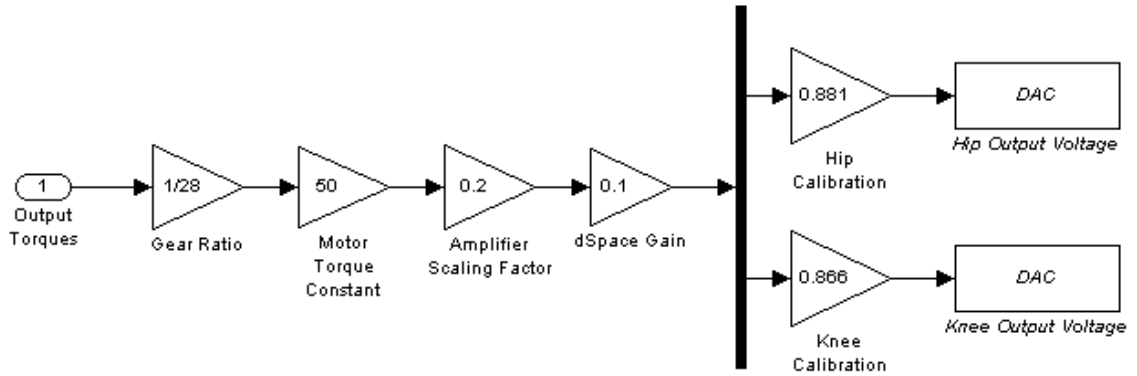
Figure 19: Actuator Output block of SIMULINK model. The torque output signal is converted into appropriate amplifier command voltages by scaling the signal by the inverse of the gear ratio, the motor calibration constant, the amplifiers' scaling factor, and an empirically determined calibration constant to produce the final output voltage signal, which is then sent to amplifiers via the dSPACE DAC blocks (far left). [6]

- either of the hip or knee exceeds its preset angular limits.

If any of these conditions are detected, a system-wide fault occurs, and the power supplies and amplifiers are shut down. As a result, the motors immediately lose power and their output inertia drops to their minimum value. The intention of this process is to maintain safety and to avoid any damage to the leg by preventing it from crashing into its supporting frame.

2.4   Data Analysis Techniques

Once we have completed trials using the computational and robotic models, we need a method to analyze the output data for specific criteria that determine the trial performance. In this section, we detail the methods used to collect and graphically present information regarding the models' performance. We then present the analysis techniques used to determine the models' energy efficiency and stability—the two key criteria on which most experiments in this research are based.

2.4.1   Data Collection and Presentation

The primary outputs of both the computational and robotic models are logs of the time-based trajectories of all state variables. The complete model has twelve state variables—four for each HCO and four for the leg. For analysis purposes, this number can be reduced
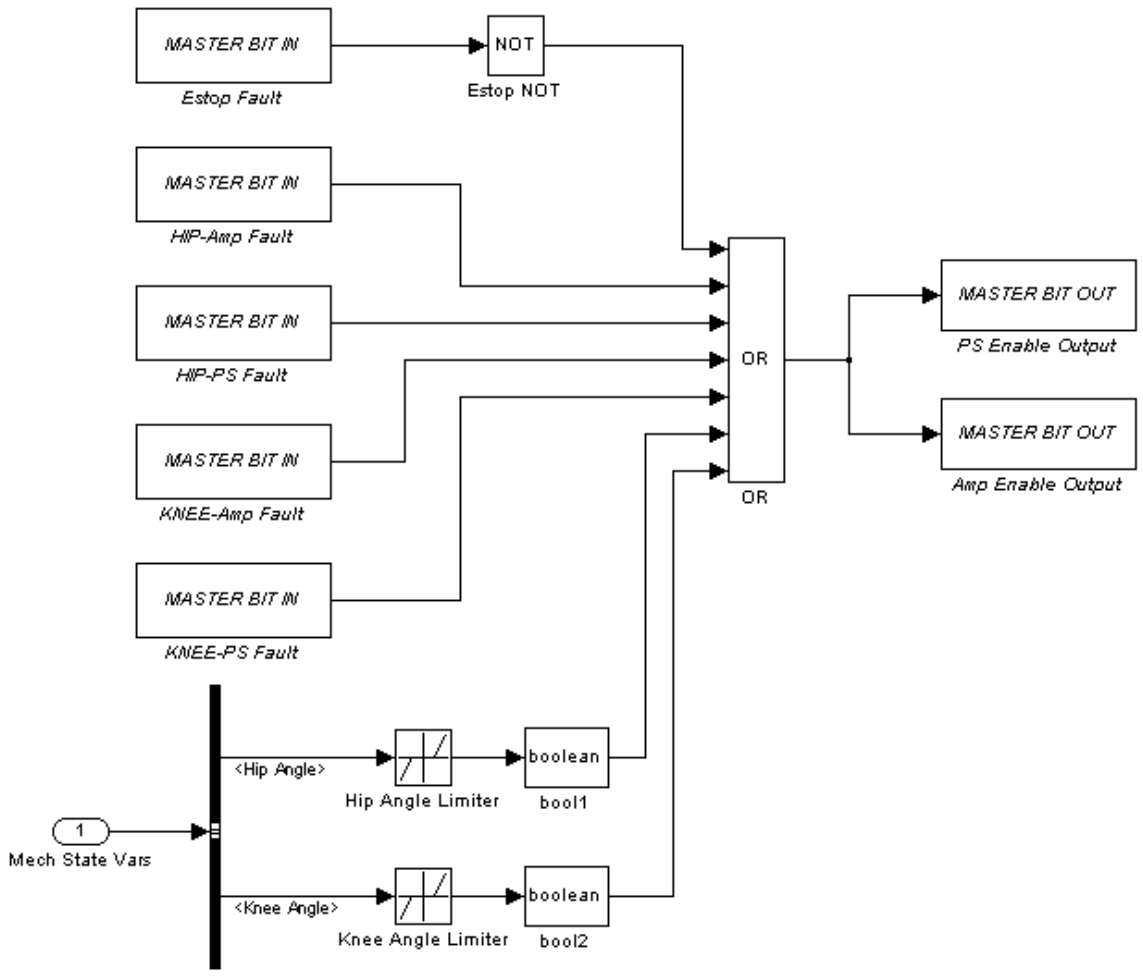
Figure 20: Fault Detection block of Simulink model. This block monitors the status of the Emergency Stop button, the amplifiers, and the power supplies using the digital I/O blocks on the left. The joint angles are also monitored for excursions beyond preset limits. When a fault condition is detected, the output of the OR block becomes binary high, and signals are sent though the dSpace digital I/O to shut down both power supplies and both amplifiers.
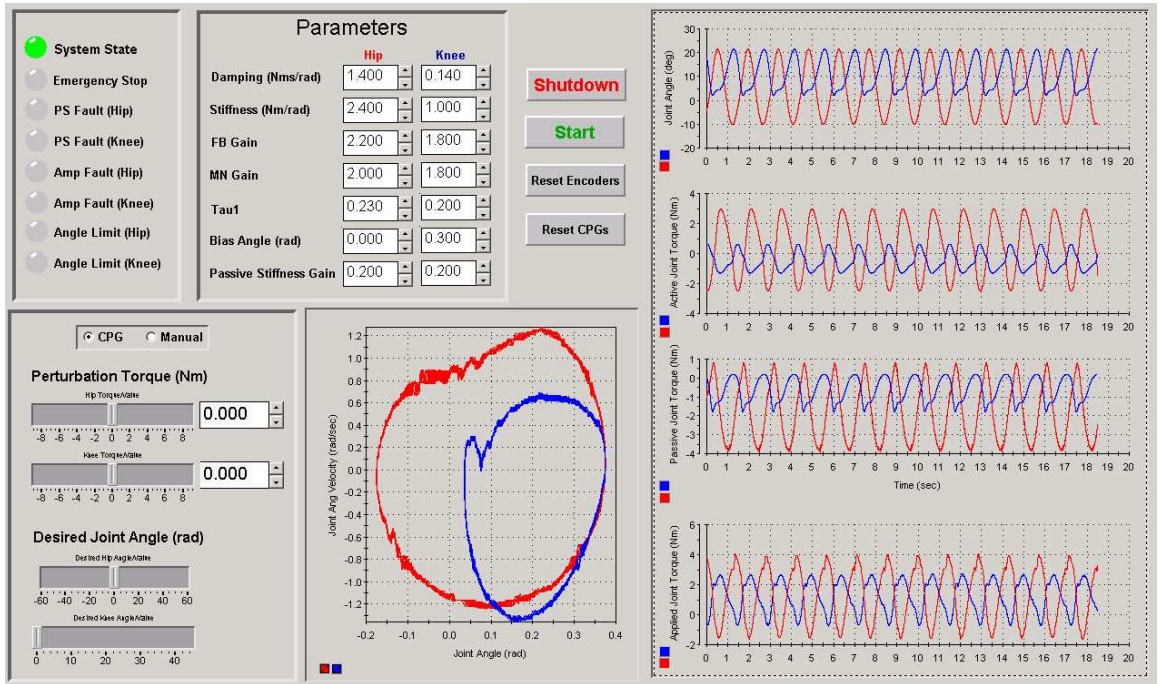
Figure 21: User interface for robotic leg model showing (clockwise from top left) system status indicators; selected test parameters; primary control buttons; plots of joint angle, active joint torque, passive joint torque, and total applied joint torque; phase portraits for the hip and knee joint; and controls to manually override the controller.

to six by replacing the four state variables for each HCO—x_1, x_2, v_1, and v_2—with the HCO output variable, y, from Equation 22. This is an acceptable simplification because the internal state variables do not directly affect the mechanical system; all control is determined by the HCO output variable, y.

After the simplification, we are left with the two joint angles, the two joint velocities, and the two HCO outputs. For simplicity, these six variables will be referred to as the state variables from here on. Each model samples the system state at 1 kHz, and outputs the state variables to data logs. The computational model runs much faster than real time ($\sim$ 25X real time), so detailed progress monitoring is not feasible. Instead, analysis of a trial's success is determined post hoc. The robotic model, however, runs in real time, so a user interface was developed to monitor and control its progress. A screen shot of the user interface is shown in Figure 21.
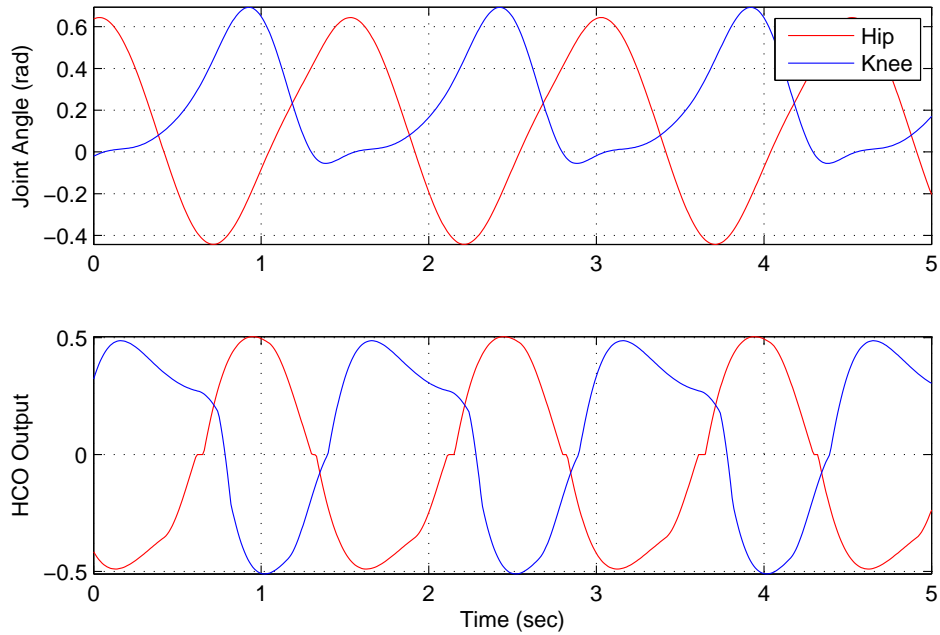
Figure 22: Example of a time domain plot of the leg's joint angles and the outputs of their corresponding HCOs.

2.4.1.1 Time Domain

Time-domain analysis is beneficial because it allows the experimenter to get an idea of the general performance of the system. For example, the analysis can be used to quickly determine whether a system is 1) oscillating, 2) growing, diminishing, or at steady state, and 3) stationary with respect to other signals. In addition, one can calculate a signal's magnitude, frequency, and phase relative to other signals.

A sample plot is shown in Figure 22. The top graph shows a time domain trace of the hip and knee joint angles. We can quickly determine that the signals are oscillating at apparent steady state and that they are stationary with respect to each other. By analyzing the magnitudes and peak times, we can calculate 1) that the hip and knee angle magnitudes are 1.08 rad and 0.74 rad, respectively, 2) that the frequency of both signals is 0.67 rad/sec, and 3) that the knee signal lags the hip signal by 34.4% of the period. Note the offset present in both joints: the hip oscillates between -0.44 and 0.64 rad, and the knee, which is subject to hyperextension restrictions, oscillates between -0.05 and 0.69 rad.

The bottom plot in Figure 22 shows the output of the corresponding HCOs during the

simulation. The top–bottom asymmetry of these signals is caused by the feedback from the mechanical system. Signals that follow the HCO commands closely and have minimal offsets provide small feedback signals to the HCOs, allowing them to behave as though they were in isolation. Larger feedback signals can dramatically alter the shape of the HCO waveform. Two examples of this alteration can be seen in Figure 22. The first example is the flat (horizontal) sections that occur at each zero crossing of the hip HCO signal (shown in red). This phenomenon happens when a controlled joint is oscillating with higher than normal magnitude in at least one direction. This type of oscillation can happen due to movement asymmetry (one direction has higher magnitude) or when an HCO is resonance tuned to a mechanical joint and the joint is operating near the resonant frequency of a second-order system (both directions are higher in magnitude). With a higher magnitude, the HCO does not need to drive the system as hard and the "neuron(s)" within the HCO that drive in those directions can reduce their "firing rates" (*i.e.,* x_1 and x_2 from Equations 18–22 are reduced and less of their signal is above zero). Because the HCO output, y, is a sum of the half-wave rectified x_1 and x_2 signals, regions of zero output arise in y whenever x_1 and x_2 are both less than zero.

The second example of feedback altering an HCO's waveform is the uneven time durations of the above-zero and below-zero phases of the knee HCO signal. Again, due to the offset asymmetry in the knee angle oscillation signal, the HCO receives more feedback during the extension phase of the oscillation than during the flexion phase. Feedback is defined as the difference between the HCO output and the joint angle. When the difference is small (as in knee flexion), the feedback level is low and the HCO output quickly returns to the opposite phase. When the difference is large (as in knee extension), the feedback level is high and the HCO is forced to remain in the current phase for a longer period of time. In this example case, the knee HCO remains above zero (*i.e.,* producing knee extension command torques) for 59.2% of the period.

2.4.1.2   Frequency Domain

Frequency-domain analysis using the Fast Fourier Transform (FFT) provides an alternate technique to analyze system performance. For this research, we primarily plotted the magnitudes of the joint angles and HCO outputs and used the plots to determine the fundamental frequency of each signal. The values of these four frequencies gave us several pieces of information regarding the performance of the complete system. If all four frequencies were the same (to within minimum frequency resolution), we could conclude that the system was frequency locked to a single frequency, ω_{sys}. When ω_{sys} was approximately equal to the natural (*i.e.,* resonant) frequency of the leg, ω_{n}, we could further conclude that the system had achieved frequency lock via resonance tuning (see Section 1.1.2.2). If all four frequencies did not match, we could use the frequency-domain plot to quickly determine which of the four oscillators—hip joint, knee joint, hip HCO, or knee HCO—had different frequencies and use that information to modify parameters. A sample frequency domain plot is shown in Figure 23.

This analysis method is dependent on being able to determine the fundamental frequency of each oscillator. A magnitude plot often consists of a series of several energy peaks that occur at distinct frequencies. The relative energies of these peaks indicate the magnitude of those frequency components in the total signal. For typical oscillations, if a sufficiently long time series is available for the signal, then the fundamental frequency of a signal corresponds to the peak with the largest magnitude. This is not the case in general, however, because it is possible for harmonics of the fundamental frequency to have larger magnitudes than the fundamental frequency. In this case, the fundamental frequency can be chosen erroneously if the peak with the highest magnitude is chosen blindly.

There is no definitive way to determine which peak corresponds to the fundamental frequency when two or more peaks are close in magnitude, especially if the signal is noisy. To reduce the probability of error, we developed a method that finds the highest magnitude peak and then determines if other high-magnitude peaks are subharmonics. If subharmonic peaks are found with this procedure, we declare that the lowest subharmonic frequency is the fundamental frequency of the system. The justification for this method is that there

65
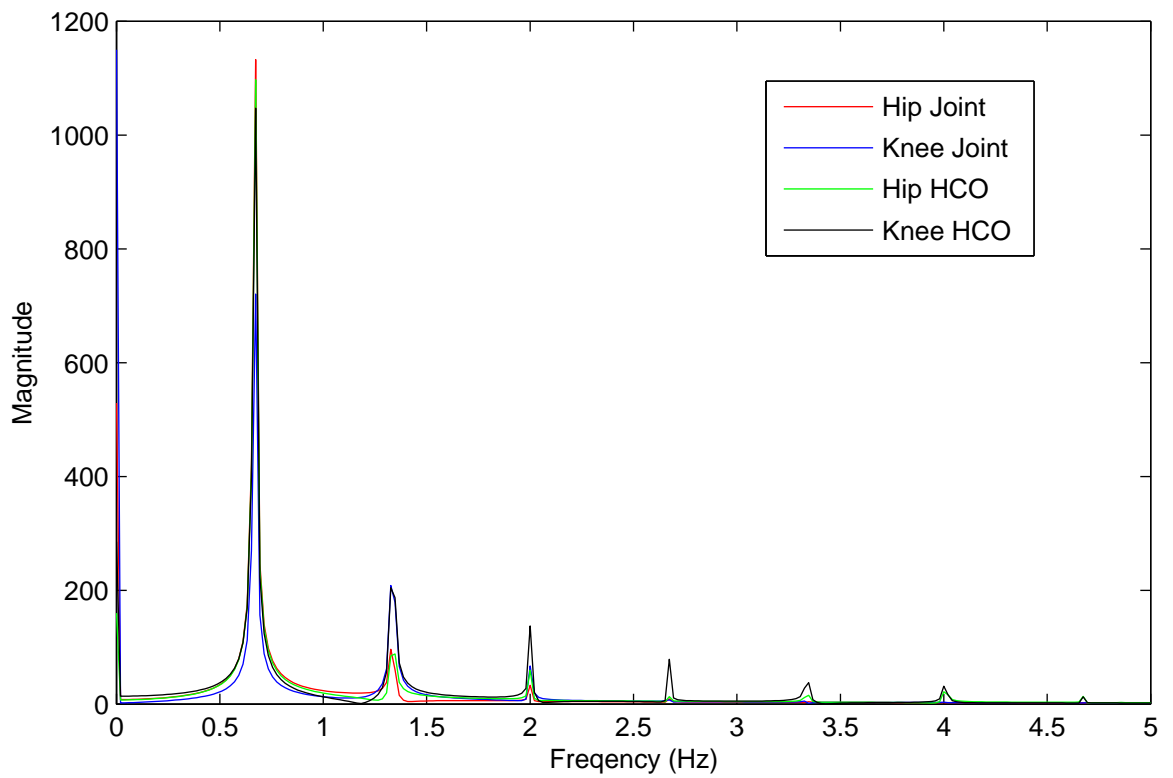
Figure 23: Example of a frequency domain plot of the leg's joint angles and the outputs of their corresponding HCOs.

is a high probability that high-magnitude peaks at subharmonic frequencies are related to the highest-magnitude peak. Our method for identifying subharmonic peaks follows.

1. Find the peak, $P_{\max}$, with the largest overall magnitude and save its magnitude, $M_{\max}$, and frequency, $f_{\max}$.

2. Find all other peaks, $P_{1,2...n}$, with magnitudes at least 50% of $M_{\max}$ and non-zero frequencies less than $f_{\max}$. If no such peaks exist, the fundamental frequency is $f_{\max}$.

3. Starting with P_1 and continuing through P_n, determine if the current peak's frequency, f_i, is a sub-harmonic of $f_{\max}$ by calculating if $f_{\max}$ modulo f_i is within 5% of f_i. If it is, the fundamental frequency is f_i. Otherwise, the process is repeated with the next higher-frequency peak. (The 5% tolerance is used to account for the limited resolution that exists with finite-duration signals.)

4. If no subharmonic matches are found, the fundamental frequency is set equal to $f_{\max}$.

An example of a potential error that this method can detect is shown in Figure 24. In this figure, all four oscillators have their largest magnitude peaks at 0.65 Hz. However, the knee HCO (shown in bold black) also has a large magnitude peak (83% of the maximum peak) located at 0.325 Hz. Using the method detailed above, the smaller peak would be classified as a subharmonic, and the fundamental frequency for the knee HCO would be set to 0.325 Hz. This legitimacy of this classification can be verified by inspection of the time-domain plot for this trial (Figure 25). Note that the knee HCO signal oscillates at half the frequency of the joint angles and the hip HCO.

2.4.1.3 Phase Portraits

Phase portraits provide a third method for visualizing the trial data. They are formed by plotting a state variable versus the derivative of that state variable. We used these plots frequently to display joint angle versus joint velocity so that we could quickly assess the signals' overall stability and periodicity. An example of a phase portrait for the knee joint during steady state is shown in Figure 26. From this figure, we can determine 1) the joint's peak angles and velocities, 2) whether the signal is periodic, and 3) whether the
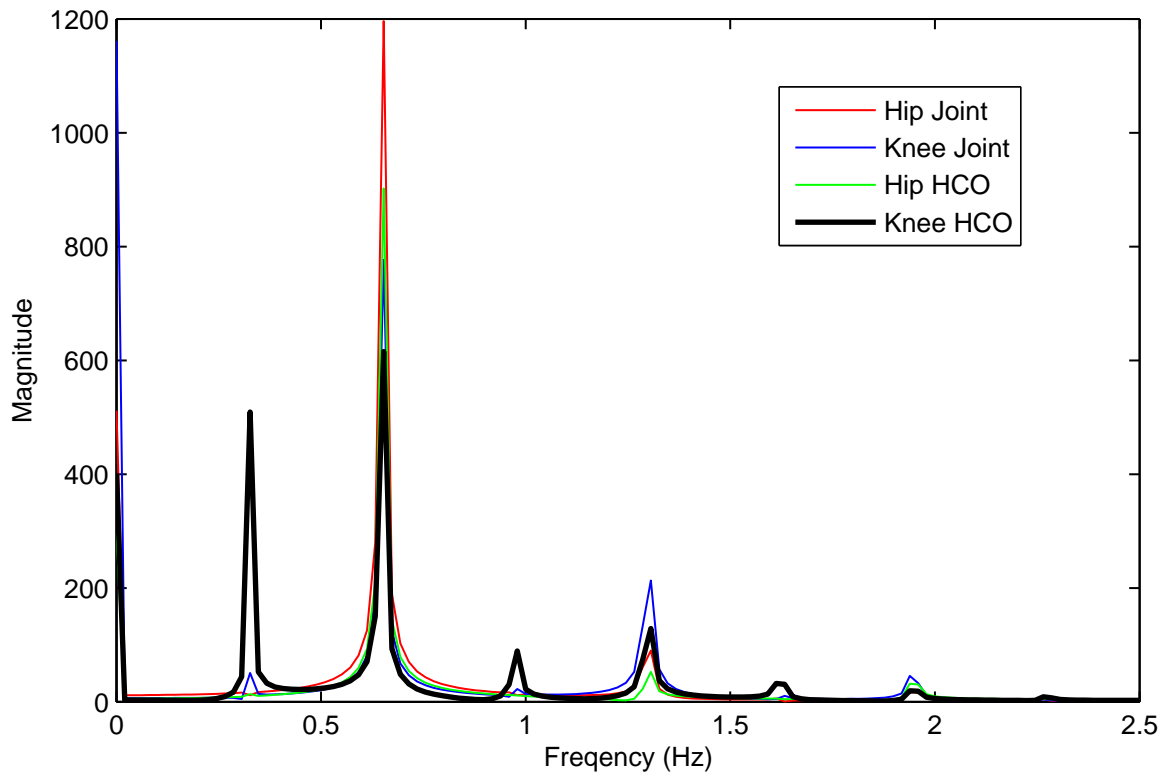
Figure 24: Example of a trial that contains a subharmonic frequency component (shown in bold black). In this example, choosing the maximum magnitude peaks without considering the peaks at subharmonic frequencies would result in an erroneous fundamental frequency for the knee HCO.
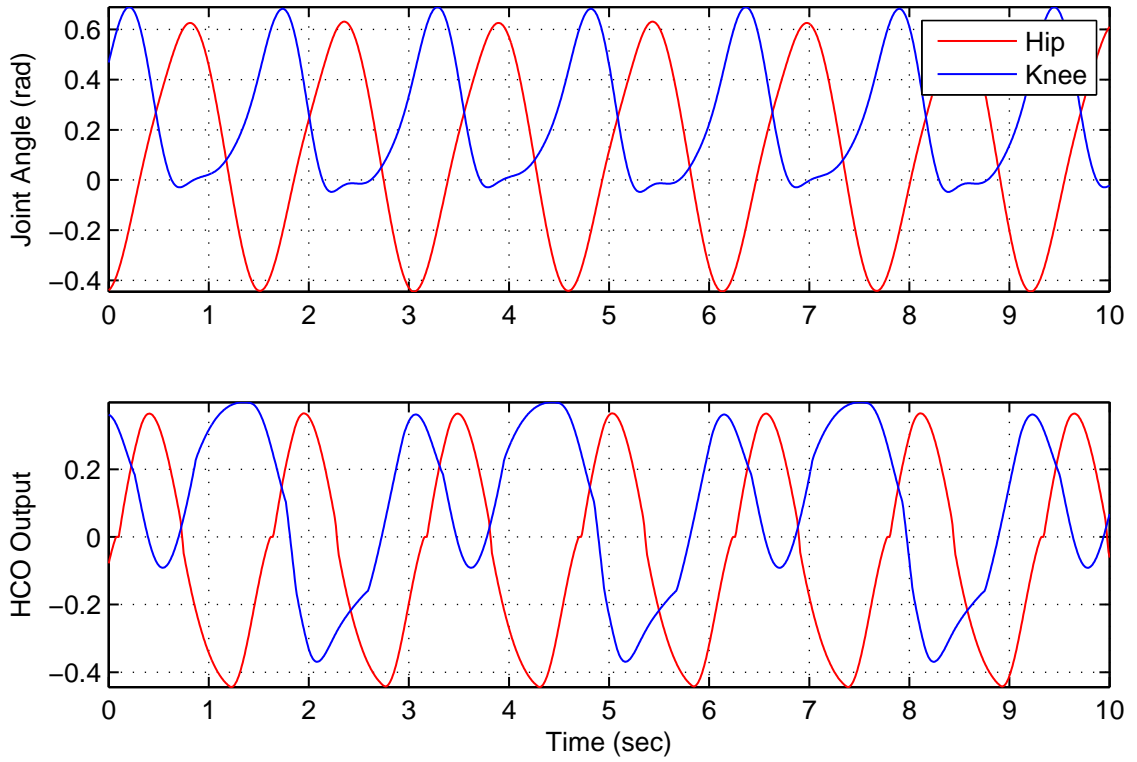
Figure 25: Time domain plot of a trial with a subharmonic frequency component. The knee HCO can be seen to have an underlying fundamental frequency that is half that of the other three oscillators.
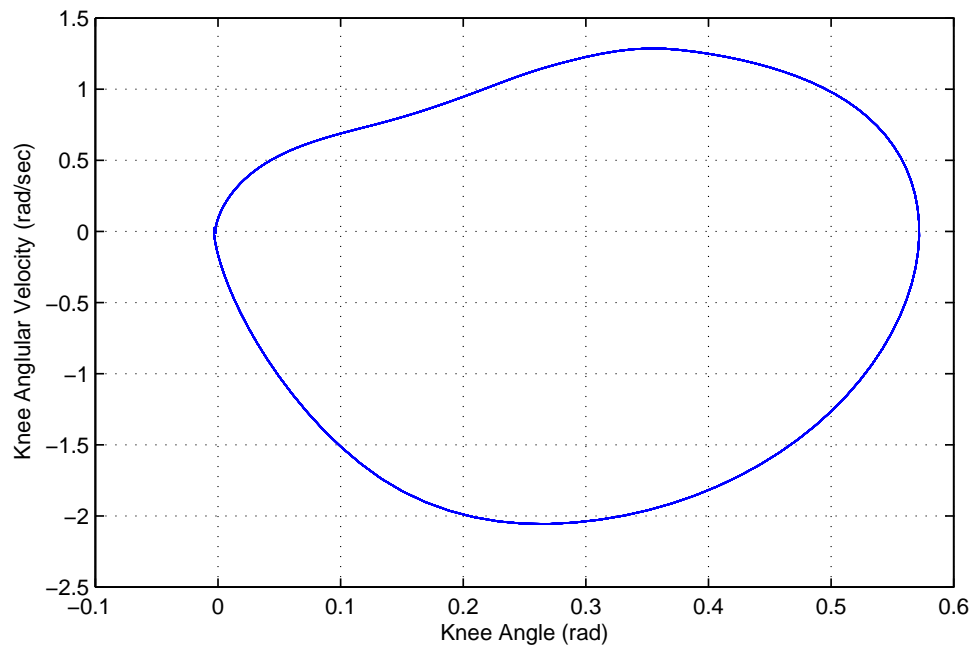
Figure 26: Example phase portrait of the knee joint during steady state.
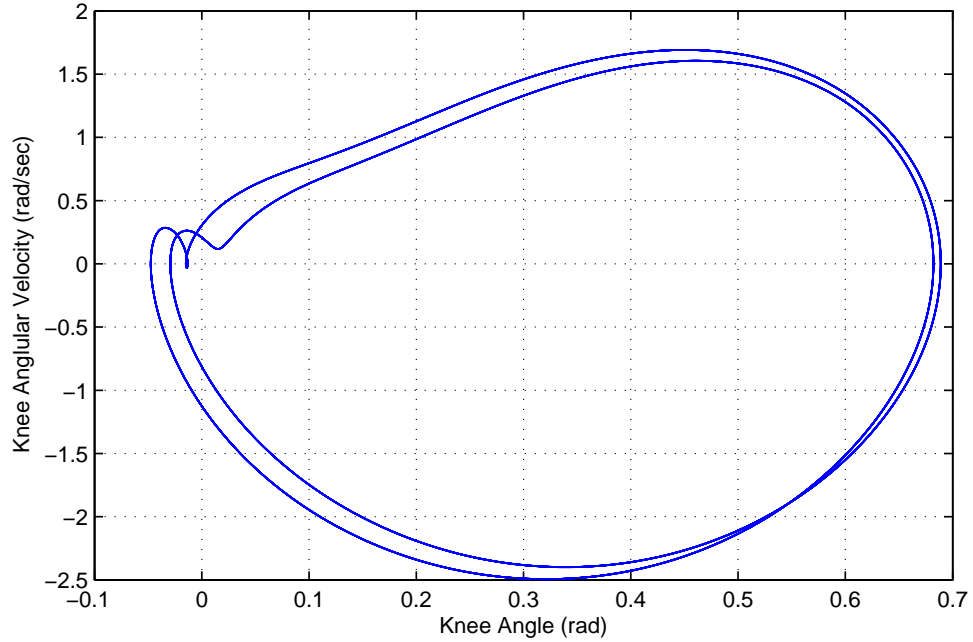
Figure 27: Example phase portrait of a steady state period-2 oscillation of the knee joint.

oscillation is stable (*i.e.,* it is not growing or shrinking as time progresses). Although these observations can be easily made with time-domain plots, the phase portrait also gives the *period number* of the signal. Intuitively, period number is just the number of oscillations a signal must make in a give phase portrait to return to its starting point. In Figure 26, the period number is one because only one oscillation is needed for the signal to return to a given point. An example of a signal with a period number of two is shown in Figure 27.

For this research, we more formally define period number as the maximum number of times the signal can pass through a Poincaré plane during one oscillation. For two-dimensional phase portraits, the Poincaré plane is simply a line drawn from the center of the oscillation radially outward. (A detailed description of Poincaré planes and related analyses is given in Section 2.4.3.) In Figure 26, any radial line drawn from the center of the oscillation, say (0.3 rad, -0.25 rad/sec), will only cross the signal trajectory once. We therefore classify this signal as a period-1 oscillation. The same line in Figure 27 intersects the signal trajectory twice, making this a period-2 oscillation. Higher-order period numbers are common in the output signals of our model. In some cases, these higher-order behaviors can be easily seen in the time-domain plots. However, phase portraits can also readily show

harder cases, such as slight variations in time-domain signal peak amplitudes. For example, the signal shown in Figure 27 corresponds to the trial shown in Figures 25 and 24. In the time-domain view of this trial (Figure 25), the period-2 behavior can be seen as the alternating trough values for the knee angle signal. For each oscillation, the minimum value alternates between -0.032 rad and -0.059 rad.

One additional feature of phase portraits is their ability to present phase-dependent signal phenomena. For example, when designing the robotic leg, the hip joint phase portrait was helpful in detecting a design issue with the leg's support platform. When "bumps" appeared on the phase portrait at a consistent phase point, we discovered that the platform was bowing as the downward force of the leg varied during leg swinging. The issue was rectified by reinforcing the platform with cross braces.

2.4.2 Energy Efficiency Analysis

Energy efficiency, η, is the primary criterion on which most experiments in this research are based. Classically, this term is defined as the ratio of the useful output energy of a system to the input energy. For simplicity, we define the amount of energy input to or output from a closed system as the work, W, done on or done by the system, respectively.

$$\eta = \frac{\text{Energy Output}}{\text{Energy Input}} = \frac{W_{\text{out}}}{W_{\text{in}}} \tag{48}$$

A robot's energy derives from two sources—the starting energy dictated by the initial conditions and the work performed on the robot while walking. The initial energy can include gravitational potential energy, kinetic energy, and elastic potential energy. The energy added during walking is provided by actuators to compensate for the energy lost due to operation.

The output energy of a robot can be calculated by summing the mechanical work performed during locomotion and the heat produced.[7] The total work expenditure, however, is not of great practical use in walking robots because it includes work that does not contribute to the fundamental behavior of walking. In other words, all expended energy that

---

[7]Energy can be expended by electromechanical systems in other ways, but in general, these ways are insignificant when compared to mechanical work and heat production.

does not contribute to robot locomotion is wasted. The most common forms of wasted energy are heat production (*e.g.,* friction, damping, inelastic collisions), non-essential or excessive movements (*e.g.,* "high-stepping"), and negative mechanical work (including co-contraction).

An alternative measure of energy efficiency is the *specific cost of transport*, which is the amount of energy required to carry a unit weight a unit distance over level ground, or:

$$\rho = \frac{E_{\text{c}}}{Mgd} \tag{49}$$

where ρ is the specific cost of transport, E_{c} is the total energy consumed, M is the mass of the robot, and d is the distance traveled [16]. This quantity lends itself well to walking robotics, as it provides a simple way to compare the useful energy efficiency of robots with each other and with animals. As a point of comparison, humans have a specific cost of transport of 0.20. The Cornell Efficient Biped, which is a passive dynamic robot, is the only walking robot to have reached this level of efficiency. The most advanced trajectory-controlled walking robot, Honda's ASIMO, has a specific cost of transport of 3.23 [16].

The specific cost of transport cannot be directly calculated for leg swinging because d, the distance traveled, is always zero. Additionally, it is unfair to directly compare the work used for the two tasks because leg swinging uses significantly less energy than walking because it does not propel the body mass forward [25]. We chose to adapt the definition for the specific cost of transport into a new measure specific to leg swinging, *specific cost of leg swinging*. This quantity is defines as:

$$\sigma = \frac{E_{\text{m}}}{MgL_{\text{s}}} \tag{50}$$

where σ is the specific cost of leg swinging, E_{m} is the active energy injected into the leg by the motor, M is the mass of the swinging leg, and L_{s} is the leg's stride length. For our leg, we defined stride length as the horizontal distance that the leg's center of mass travels during a single stride. This definition is analogous to the step length during normal walking, except that in walking the distance the foot travels would be calculated. For brevity, we refer to the specific cost of leg swinging as *energetic cost* for the remainder of this research.

At a basic level, the net energy consumed (and therefore input by the motor to maintain steady state) during leg swinging can be measured as:

$$E_\mathrm{m} = E_\mathrm{i} - E_\mathrm{f} \tag{51}$$

where E_i is the initial energy in the system and E_f is the final energy of the system. The energy of the system at any point can be calculated as:

$$E = E_\mathrm{k} + U_\mathrm{g} + U_\mathrm{e} \tag{52}$$

where E is the total energy in the system, E_k is the system's kinetic energy, U_g is the system's gravitational potential energy, and U_e is the system's elastic potential energy (*i.e.,* potential energy stored in elastic components).

Kinetic energy is calculated in a rotating and translating system as:

$$E_\mathrm{k} = \underbrace{0.5\left(J_\mathrm{t}\dot{\theta}_\mathrm{h}^{\,2} + J_\mathrm{s}\dot{\theta}_\mathrm{k}^{\,2}\right)}_{\text{rotational}} + \underbrace{0.5\left(M_\mathrm{t}v_\mathrm{t}^2 + M_\mathrm{s}v_\mathrm{s}^2\right)}_{\text{translational}} \tag{53}$$

where v_t and v_s are the translational velocities of the thigh and shank CoM, respectively. The kinetic energy of this system is:

$$E_\mathrm{k} = 0.5\left[J_\mathrm{t}\dot{\theta}_\mathrm{h}^{\,2} + J_\mathrm{s}(\dot{\theta}_\mathrm{h} - \dot{\theta}_\mathrm{k})^2 + M_\mathrm{t}L_\mathrm{cm,t}^2\dot{\theta}_\mathrm{h}^{\,2} + \right.$$
$$\left. M_\mathrm{s}\left(L_\mathrm{t}^2\dot{\theta}_\mathrm{h}^{\,2} + L_\mathrm{cm,s}^2(\dot{\theta}_\mathrm{h} - \dot{\theta}_\mathrm{k})^2 + 2L_\mathrm{cm,s}L_\mathrm{t}\cos(\theta_\mathrm{k})\dot{\theta}_\mathrm{h}(\dot{\theta}_\mathrm{h} - \dot{\theta}_\mathrm{k})\right) \right] \tag{54}$$

Gravitational potential energy is calculated as:

$$U_\mathrm{g} = -g(M_\mathrm{t}y_\mathrm{t} + M_\mathrm{s}y_\mathrm{s}) \tag{55}$$

where y_t and y_s are the height of the thigh and shank centers of mass above their minima, respectively. The gravitational potential energy of this system is:

$$U_\mathrm{g} = -g\left[M_\mathrm{t}L_\mathrm{cm,t}(1 - \cos\theta_\mathrm{h}) + M_\mathrm{s}\left(L_\mathrm{t}(1 - \cos\theta_\mathrm{h}) + L_\mathrm{cm,s}\big(1 - \cos(\theta_\mathrm{h} - \theta_\mathrm{k})\big)\right) \right] \tag{56}$$

The final energy component in Equation 52 is elastic potential energy and is calculated as:

$$U_\mathrm{e} = \int_0^{\theta_h} \Gamma_\mathrm{s,h}(\theta)\,d\theta + \int_0^{\theta_k} \Gamma_\mathrm{s,k}(\theta)\,d\theta \tag{57}$$

73

where $\Gamma_{s,h}(\theta)$ and $\Gamma_{s,k}(\theta)$ are the force functions of the passive elastic components at the hip and knee, respectively. The first term represents the elastic potential energy for the hip component and the second term represents the contribution from the knee component. The final equation for elastic potential energy is not presented here because this evaluation of this equation is dependent upon the choice of elastic components. Chapter 3 gives a detailed presentation of how the choice of elastic component affects system energy.

The robot's motors can produce both positive and negative work. Positive work, W_{p}, is done when torque is applied to a joint in the *same* direction as the joint's movement, increasing system energy; negative work, W_{n}, is done when torque is applied to a joint in the *opposite* direction as the joint's movement, decreasing system energy. To calculate these quantities, we measured the change in joint angle, $\Delta\theta$, and the joint torque applied by the motors, Γ_m, at each time step. If $\Delta\theta$ and Γ_m had the same sign, W_{p} was incremented by $\Delta\theta\Gamma_m$. If they had opposite signs, W_{n} was incremented by $|\Delta\theta\Gamma_m|$.

Our energy cost calculation does not differentiate between positive and negative work. All that is relevant is the total energy used to operate the system. In the case of a motor-actuated system, motor energy is required for performing both positive work, in which energy is transferred to the mechanical system, and negative work, in which energy is dissipated as heat in the motors. Therefore, Equation 51 must be expanded from the *net* energy consumed to the *total* energy consumed.

$$E_{\mathrm{m}} = E_{\mathrm{i}} - E_{\mathrm{f}} + W_{\mathrm{p}} + |W_{\mathrm{n}}| \tag{58}$$

At steady state, the total system energy is identical at a fixed phase on the leg's oscillation cycle. Because energy is constant (*i.e.*, $E_{\mathrm{i}} - E_{\mathrm{f}} = 0.0$ J), the equation for the energetic cost of leg swinging at steady state becomes:

$$\sigma = \frac{W_{\mathrm{p}} + |W_{\mathrm{n}}|}{Mgd} \tag{59}$$

where W_{p} and W_{n} are calculated as the total positive and negative work done by the motors over one complete oscillation.

In our implementation, we have chosen to add virtual passive components rather than physical components for ease of experimentation. This approach requires us to use motor

torques (and therefore external energy) to emulate the effects of the passive components. However, we do not consider this energy when calculating E_m because these passive components would not require external energy if the were attached physically. Therefore, we chose not to penalize the efficiency of our experimental leg controller based on our implementation method. As a result, when calculating work, we only consider the active muscle toque, Γ_act, and ignore the passive stiffness torque, Γ_s, the passive damping torque, Γ_d, and any friction torque, Γ_f.

2.4.3 Stability Analysis

The stability of walking robots is of paramount importance because robots that cannot keep from falling are of little practical use. Because our swinging leg model is a reduced model of human walking, we likewise require our leg to operate stably. The definition of stability for our system, however, differs from that of a walking robot. In the case of a walking robot, stability is defined as the ability to avoid falling; in the case of actuated leg swinging, we define stability as the ability to achieve steady-state oscillations that recover completely from perturbations in finite time. In Section 1.1.4, we reviewed a quantitative method for determining a nonlinear system's stability by calculating its Floquet multipliers. The benefit of this method is that it provides values for all Floquet multipliers. The disadvantage is that it requires n independent tests to be run (where n is the number of state variables) for each set of system parameters tested [36]. This process can be both difficult to perform and time consuming in non-computational systems [68].

For this research, we chose a simpler method than the one above that solely focuses on calculating the largest magnitude Floquet multiplier, λ_max. This method is effective because the system's behavior is dominated by its response along the vector associated with λ_max. If λ_max is greater than unity, then, regardless of the values of the other Floquet multipliers, the system cannot be stable. If λ_max is less than unity, then the decay rate of a perturbation recovery is dominated by the magnitude of λ_max.

In our method, we determine the value of λ_max by analyzing the effect of a single perturbation on the system, rather than the effect of one perturbation for each of the system's

n state variables. In real systems, determining the effect of even a single perturbation can be complicated by the presence of noise [68], resulting in the need for a single trial to be repeated several times and the results ensemble averaged to determine the true response.

We chose to define our Poincaré section as the 11-dimensional hyperplane defined by $\theta_\mathrm{h} = 0.0$ rad. This choice guarantees that if the system has a stable limit cycle that it will intersect the hyperplane during any desirable system oscillation. This assertion can be made because an oscillatory trajectory that avoided the section would imply that the hip is either always flexed or always extended, and this behavior is not seen in normal human walking.

The details of our procedure (as performed on the computational model) are shown as a flow chart in Figure 28. The procedure begins by performing the steps in the top five blocks (described in Section 2.2.3) until $T > T_\mathrm{sys}$. At this point, the oscillation period, T_sys, is calculated by determining whether the fundamental oscillation frequencies of both joints and both oscillators are matched. These four frequencies are required to match because this criterion is necessary for whole-leg resonance tuning. If the frequencies do not match, the trial is aborted and classified as a failure. If they do match, the system has one oscillation frequency, ω_sys, and the trial is classified as a success. The complete system's oscillation period is then calculated as $T_\mathrm{sys} = \frac{2\pi}{\omega_\mathrm{sys}}$.

Once T_sys is calculated and the state space orbit has effectively settled onto a fixed point, $\mathbf{x}^*$, in the Poincaré section, the process enters the Poincaré map analysis region (shown in gray). The first step of this analysis is to forward integrate the system until it nears the Poincaré section for the first time (*i.e.*, $N_\mathrm{sections} = 0$). To determine when the trajectory is "near" a section, we calculate the orthogonal distance from the current point in state space to the Poincaré section, which is just the magnitude of the hip angle since the Poincaré section is defined by $\theta_\mathrm{h} = 0.0$ rad. We can determine that the trajectory has crossed the section when the previous two integration steps produce proximity values of opposite sign. Because we use one-sided sections, we only consider crossings corresponding to trajectories moving from the side with negative hip angle to the side with positive hip angle. When a trajectory is detected as being near a section, it has technically already passed it. For
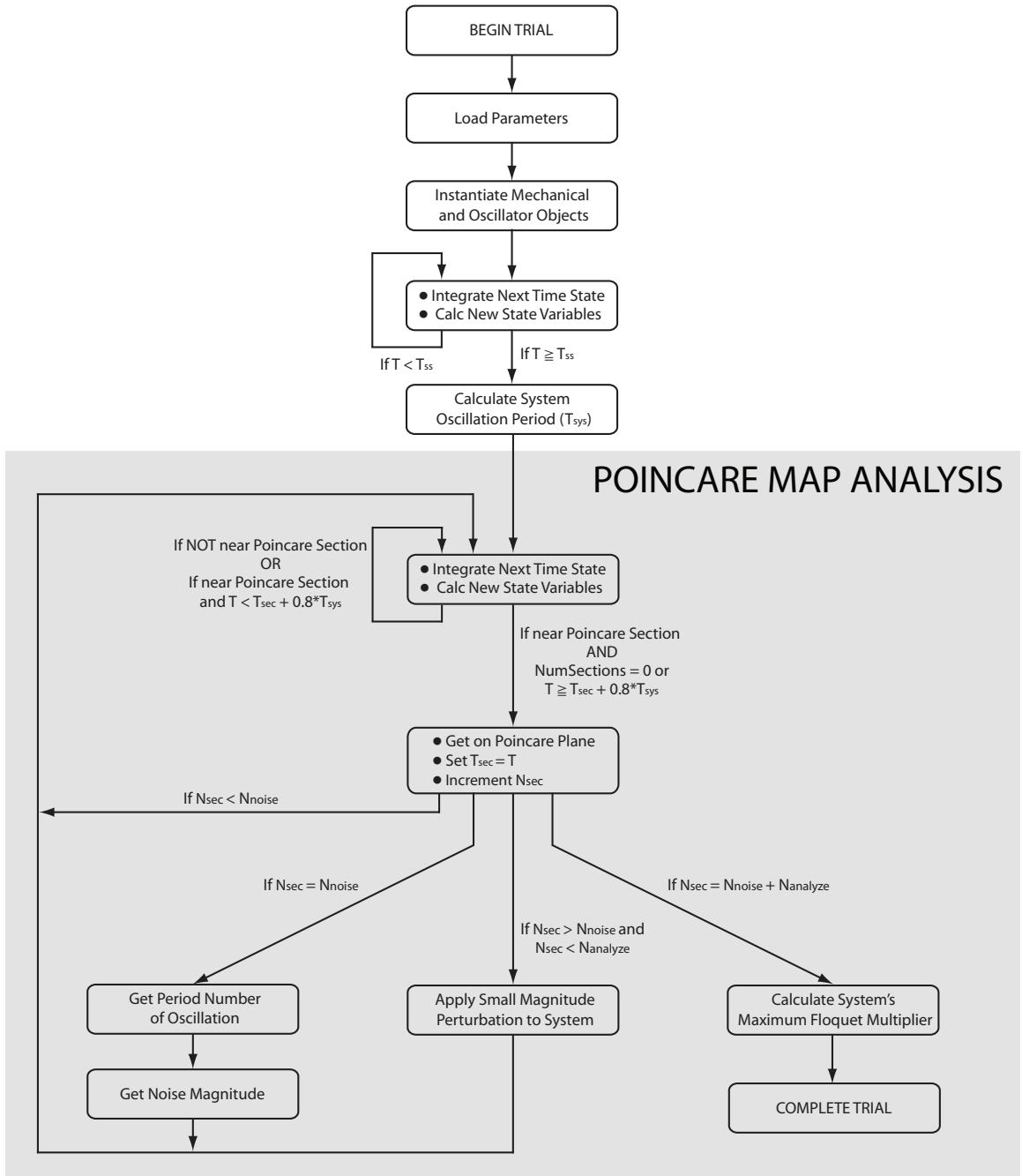
Figure 28: Algorithm flow chart for control system object. After parameters are loaded and required objects instantiated, the algorithm integrates the state equations until steady state is reached $(T = T_{\mathrm{ss}})$. Then the algorithm then performs a Poincaré map analysis to determine whether the steady-state oscillation is period-1 and what the maximum Floquet multiplier is. T_{sec} is the time at which the last Poincaré section was crossed. T_{sys}, is the fundamental period of the system's oscillations. N_{noise} is the number of Poincaré sections to iterate through before calculating oscillation's period number and the level of system noise. N_{analyze} is the number of Poincaré sections to iterate through before calculating the system's maximum Floquet multiplier.

this procedure, we require perturbations to be applied to the trajectory at the point that it crosses the section. Because we integrate the system dynamics in discrete time steps, we must estimate the actual system state at the section crossing based on the state values just before and after the crossing. To do this we perform a linear interpolation of each state variable according to the equation:

$$x = x_{\mathrm{i}} + \left(\frac{\theta_{h_{\mathrm{i}}}}{\theta_{h_{\mathrm{f}}} - \theta_{h_{\mathrm{i}}}} \right) (x_{\mathrm{f}} - x_{\mathrm{i}}) \tag{60}$$

where x_{i} and x_{f} are the values of the state variables before and after crossing the plane, respectively, and $\theta_{h_{\mathrm{i}}}$ and $\theta_{h_{\mathrm{f}}}$ are the hip angles before and after crossing the plane, respectively, which indicate the proximity of the state space points to the Poincaré section. Time is also interpolated during this routine:

$$T = T_{\mathrm{i}} + \left(\frac{\theta_{h_{\mathrm{i}}}}{\theta_{h_{\mathrm{f}}} - \theta_{h_{\mathrm{i}}}} \right) T_{step} \tag{61}$$

where T_{step} is the integration time step.

Once the trajectory is "on" the Poincaré section for the first time, the current time is stored as T_{sec}, the current state is saved for later use as $\mathbf{x}(1)$, the counter variable, N_{sections}, is incremented, and the procedure restarts the integration process, seeking the next Poincaré section. To avoid erroneously choosing section crossings that correspond to higher-period oscillations, the procedure requires that $T \geq T_{\mathrm{sec}} + 0.8\ T_{\mathrm{sys}}$. The process of integrating until the trajectory is near the Poincaré section, getting "on" the section, and saving the resulting time as T_{sec} and state as $\mathbf{x}(i)$ is repeated until $N_{\mathrm{sections}} = N_{\mathrm{noise}}$, where N_{noise} is a constant that indicates the number of states that should be averaged to get a good estimate of the noise is the system. For our system, we chose to set $N_{\mathrm{noise}} = 100$. Once $N_{\mathrm{sections}} = N_{\mathrm{noise}}$, a sub-procedure is started that determines the system's period number and noise magnitude.

The system period number is found by determining what period oscillation best fits the states $\mathbf{x}(1)$ through $\mathbf{x}(N_{\mathrm{noise}})$. The first step is to remove the mean state value from each of the states so that only the variations from the mean are considered. The resulting states are $hat\mathbf{x}(1)$ through $\hat{\mathbf{x}}(N_{\mathrm{noise}})$. Next, the mean distance, MD, of neighboring points on period-1

78
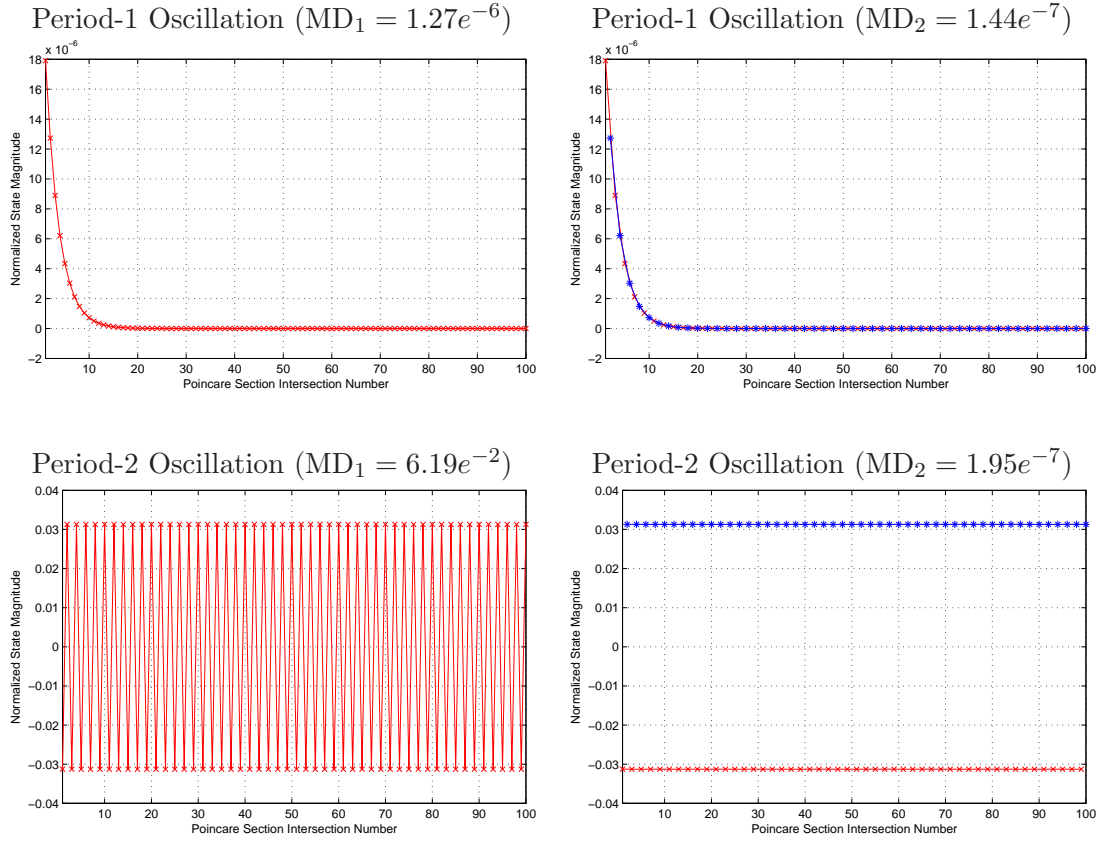
Figure 29: Comparison of period-1 and period-2 fits to period-1 and period-2 oscillations. Each plot shows the normalized magnitude of **x** for the first 100 intersections with the Poincaré section. Top Left: A period-1 oscillation with a period-1 curve fit. Bottom Left: A period-1 oscillation with a period-2 curve fit. Top right: A period-2 oscillation with a period-1 curve fit. Bottom Right: A period-1 oscillation with a period-2 curve fit.

through period-10 curve fits are calculated as:

$$\mathrm{MD_k}(\mathbf{x}) = \frac{1}{\mathrm{N_{noise}} - k} \sum_{i=1}^{\mathrm{N_{noise}}-k} | \, \|\hat{\mathbf{x}}(i+k)\| - \|\hat{\mathbf{x}}(i)\| \, | \tag{62}$$

Example of this fit function for period-1 and period-2 oscillations are shown in Figure 29. The top two plots show the normalized state magnitude progression for a period-1 oscillation. The top left plot shows a period-1 curve fit applied, meaning that a single curve was used to plot all data points. The average distance between neighboring points on this single curve is $\mathrm{MD_1} = 1.27e^{-6}$. In the top right plot, two curves are used to plot the same points. The first curve plots every other point starting at the first point, and the second curve plots every other point starting at the second point. The average distance between neighboring points on both curves is $\mathrm{MD_2} = 1.44e^{-7}$. Note that even though this is a

79

period-1 oscillation, using two curves produces a lower mean distance value. This happens because, even though the system was given time to settle into a steady state orbit, the decay is exponential and some settling will (in theory) always be present. Therefore, any "ringing" in the system will allow higher-order curve fits to appear to be a better match. Furthermore, any integer multiple of given curve fit will always give approximately equal or better results. To assure that a higher order curve fit is actually a better choice than a lower order fit, we required MD for higher order fits to be at least an order of magnitude smaller than that of a lower order fit.

The bottom two plots show the normalized state magnitude progression for a period-2 oscillation. The bottom left plot shows a period-1 curve fit applied, and the bottom right shows a period-2 curve fit applied. Note that these two cases have a significant difference between mean distance vales—$MD_1 = 6.19e^{-2}$ verses $MD_2 = 1.95e^{-7}$. This indicates that the period-2 fit, which uses two curves to fit every other point, has much lower mean distance between neighboring points.

The actual procedure used to find oscillation period number can be summarized as follows.

1. Remove mean state value from $\mathbf{x}$ to get $\hat{\mathbf{x}}$.

2. Calculate the period-1 mean distance, MD_1 and save this value as the lowest (best) value, MD_{low}.

3. Calculate MD_2. If $MD_2 < 0.1* MD_{low}$, then assign $MD_{low} = MD_2$.

4. Repeat the previous step for period-3 through period-10 curve fits.

When this procedure completes, the period number of the best curve fit is output along with the MD value. Note that the procedure also requires the MD value to be lower than a pre-selected overall threshold to make sure that the best curve fit is actually a decent fit. It is possible for none of the curve fits to be good matches, such as in the case of even higher period number (or chaotic) oscillations. We chose only to consider period-1 through period-10 curve fits because we only used 100 data points for $\mathbf{x}$, and we wanted to make

sure each curve within an attempted curve fit had at least 10 points. (In a period-1 fit, the one curve has 100 points. In a period-2 fit, the 2 curves each have 50 points...In a period-10 fit, the 10 curves each have 10 points.)

Once period number has been determined for the oscillation, the next step in algorithm shown in Figure 28 is to calculate the magnitude of the noise in the collection of states stored as $\mathbf{x}$. This is done by removing the mean values of each element, $\overline{\mathbf{x}}$, from $\mathbf{x}$ and calculating the magnitude of the remaining, zero-mean signal values to get $\|\mathbf{x}\|$.

When calculating noise, if the system has a higher-than unity period number, the state vectors stored as $\mathbf{x}$ are down-sampled by the period number to assure that the all states being used to determine noise correspond to the same phase of the oscillation. Also in this case, T_{sys} is reassigned to be equal to the product of T_{sys} and the period number.

With the noise magnitude stored for later use, the algorithm in Figure 28 returns to integration process with one major difference. Each time the trajectory gets "on" a Poincaré section and $\mathbf{x}(i)$ is stored, a small perturbation of $10\|\overline{\mathbf{x}}\|$ is added to the state along the current vector direction, producing the perturbed state, $\mathbf{x}_\mathrm{p}(i)$. The effect of the perturbation can be seen after one oscillation as the state $\mathbf{x}(i+1)$. These state vectors that represent the recovery from the perturbations are stored separately as $\mathbf{x}_\mathrm{r}$. As this process is repeated, the $\mathbf{x}_\mathrm{r}$ state vectors eventually settle onto a single state vector, whose phase indicates the direction of slowest perturbation recovery, and so therefore corresponds to the eigendirection of λ_{max}. Furthermore, λ_{max} can be shown to be:

$$\lambda_{max} = \frac{\|\mathbf{x}_\mathrm{r}\|}{\|\mathbf{x}_\mathrm{p}\|} \tag{63}$$

where $\|\mathbf{x}_\mathrm{r}\|$ and $\|\mathbf{x}_\mathrm{p}\|$ are the magnitudes of the zero-mean averages of the last 25% of the state vectors stored in $\mathbf{x}_\mathrm{r}$ and $\mathbf{x}_\mathrm{p}$, respectively. This process completes when $\mathrm{N}_{\mathrm{sections}} = \mathrm{N}_{\mathrm{noise}} + \mathrm{N}_{\mathrm{analyze}}$. We chose to set $\mathrm{N}_{\mathrm{analyze}} = 100$, as we found that $\mathbf{x}_\mathrm{p}$ was generally settled within 10 iterations, giving us substantial buffer in case a signal took longer to settle.

The effect of adding perturbations to the system can be seen in Figure 30. The first 100 Poincaré section intersections are the same as those shown in the top of Figure 29. At $\mathrm{N}_{\mathrm{sections}} = \mathrm{N}_{\mathrm{noise}} + 1$, we begin applying perturbations to the system each time the
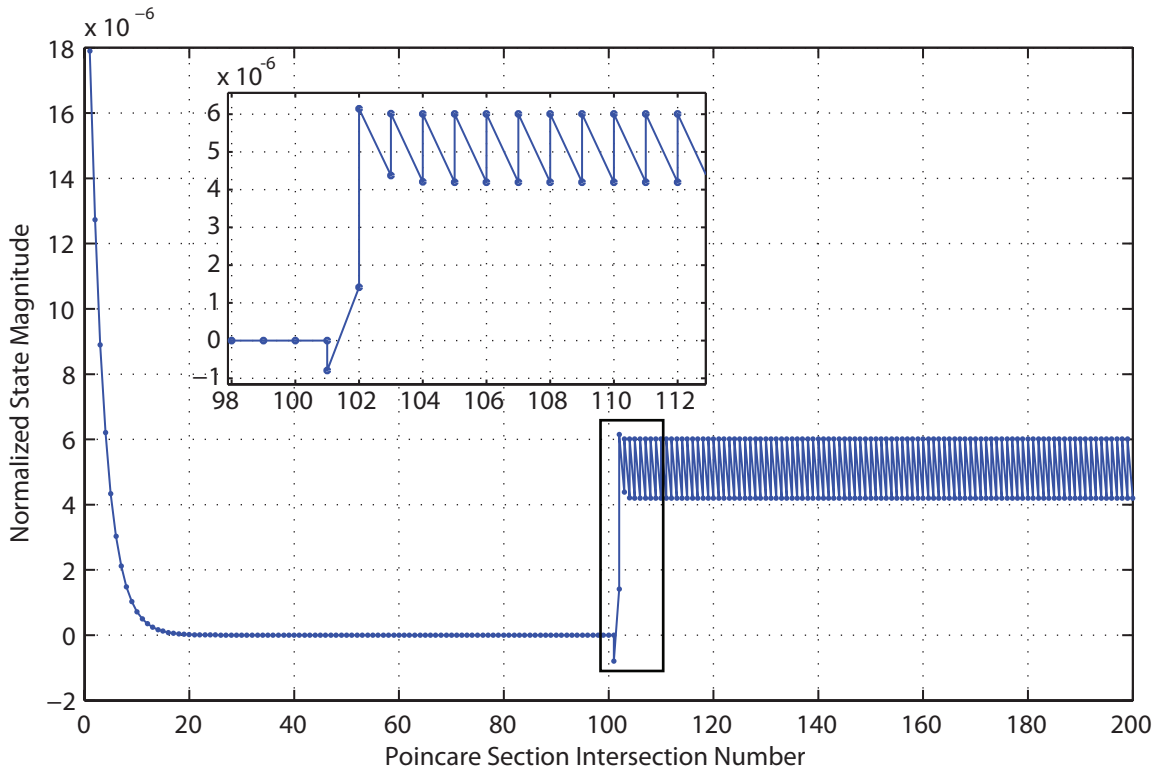
Figure 30: State magnitudes used to determine period number, noise magnitude, and maximum Floquet multiplier. The left half of the plot shows the settling of a period-1 oscillation. When $N_{\text{sections}} > 100$, small perturbations are applied to the system, and the two data points per section represent the magnitudes of x_{p}—the perturbed state—and x_{r}—the recovered state. The inset shows the perturbations applied to the system beginning at $N_{\text{sections}} = 101$. Note that the system quickly converges to a steady state value for both the upper points (x_{p}) and the lower points (x_{r}).
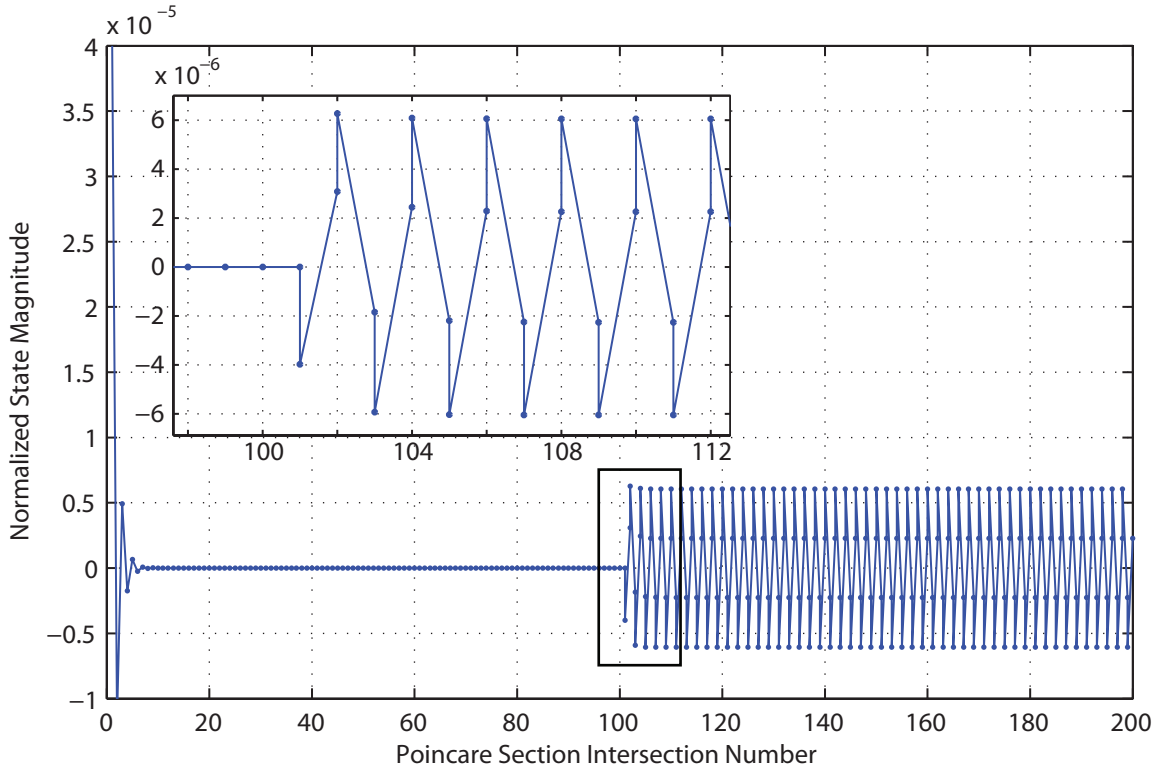
Figure 31: State magnitudes that occur when λ_{max} is negative. The lower magnitude points correspond to $\mathbf{x}_{\mathrm{r}}$, and the larger magnitude points correspond to $\mathbf{x}_{\mathrm{p}}$. Note that, as in the case of positive λ_{max}, the perturbations increase the state magnitude. The primary difference in this case is that the $\mathbf{x}_{\mathrm{r}}$ values alternate signs with each occurrence.

trajectory crosses the section, producing two data points per section. This can be seen in the inset of Figure 30. The first point per section is the magnitude of $\mathbf{x}_{\mathrm{r}}$, the recovered state from the last perturbation. The second point is the magnitude of $\mathbf{x}_{\mathrm{p}}$, which is the newly perturbed state. Note that in this case, within about 5 iterations, the magnitudes of values of both states settle onto steady state values. We determine λ_{max} as the ratio of these steady state values. In this particular case, $\lambda_{max} = 0.699$.

The requirement for stability is that the *magnitude* of λ_{max} be less than unity. No restriction is made on the phase of the corresponding eigenvector, and as a result, two interesting cases can occur that require special handling. The first case is when the eigenvector associated with λ_{max} is negative. In this case, the $\mathbf{x}_{\mathrm{r}}$ states alternate sign with each crossing of the Poincaré section. The resulting magnitude plot such a case is shown in Figure 31. It can be seen in this figure that the steady-state magnitudes of paired $\mathbf{x}_{\mathrm{p}}$
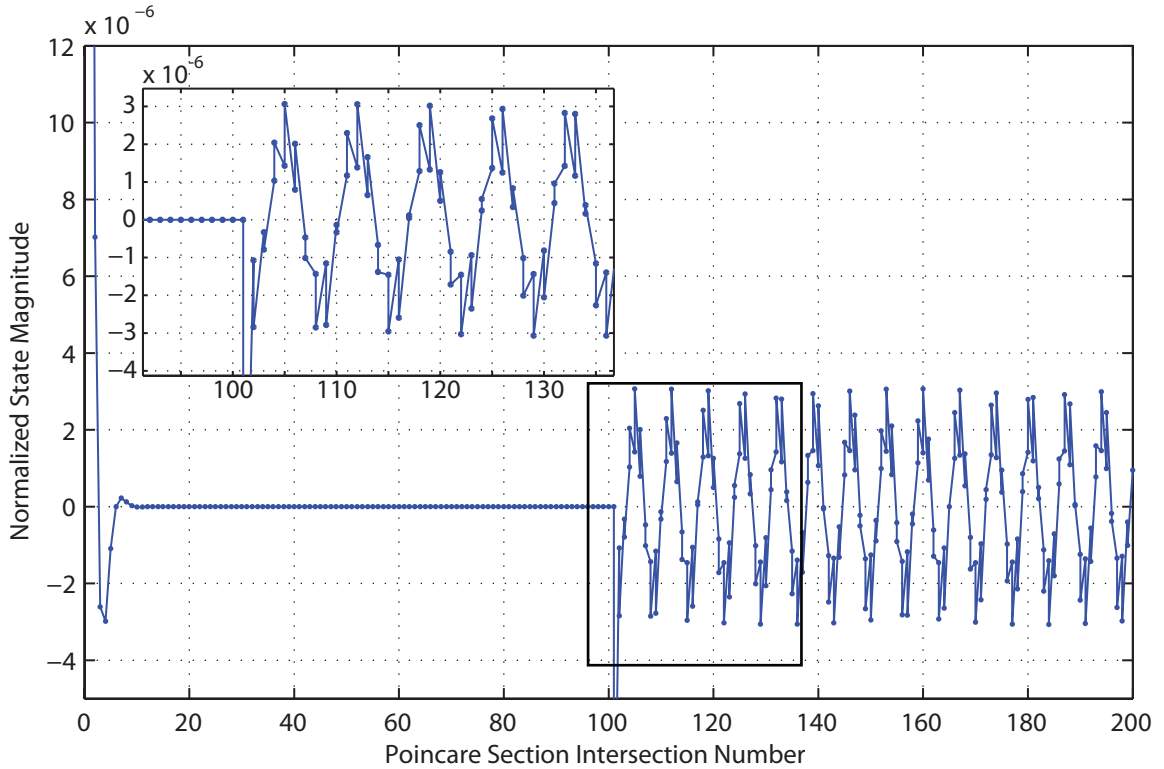
Figure 32: State magnitudes that occur when the eigenvector associated with λ_{max} is a complex conjugate pair. The eigendirection rotates in a 2-dimensional sub-plane of the Poincaré section. As a result, λ_{max} cannot be calculated as a simple ratio because the magnitudes shown in this plot are inconsistent due to the rotation.

and $\mathbf{x}_r$ states have opposite signs. The magnitudes of the perturbed states always have the same sign as the *previous* recovered state because perturbations are always added along the existing eigendirection.[8] In this particular case, $\lambda_{max} = -0.375$.

The second interesting case that requires special handling is when the eigenvector associated with λ_{max} is a complex conjugate pair. In this case, the $\mathbf{x}_r$ vectors rotate in a 2-dimensional sub-plane of the Poincaré section, which itself is an 11-dimensional hyperplane. As a result, simply taking the ratio of the vector magnitudes does not produce a useful result because the magnitudes are not consistent, as shown in Figure 32. This plot shows that the system undergoes a standard settling for $N_{sections} \leq 100$ and then a periodic oscillation in vector magnitudes once the perturbations begin. To determine λ_{max}, we need

---

[8]In reality, the magnitudes of subsequent $\mathbf{x}_r$ states do not change; rather, the associated vectors alternate directions. However, we indicate the presence of alternating vector direction by calculating what the magnitude would need to be if the vector direction was constant.

to plot the projection of the $\mathbf{x}_r$ vectors in the 2-dimensional sub-plane in which it rotates. To do this, we used the following procedure:

1. Choose any two states vectors within $\mathbf{x}_r$. Name them $\mathbf{v}_1$ and $\mathbf{v}_2$.

2. Normalize $\mathbf{v}_1$ to produce the unit vector, $\hat{\mathbf{v}}_1$.

3. To make $\mathbf{v}_2$ orthogonal to $\mathbf{v}_1$, redefine $\mathbf{v}_2$ with the $\hat{\mathbf{v}}_1$ component removed:

$$\mathbf{v}_2 = \mathbf{v}_2 - (\hat{\mathbf{v}}_1 \cdot \mathbf{v}_2)\hat{\mathbf{v}}_1 \tag{64}$$

4. Normalize $\mathbf{v}_2$ to produce the unit vector, $\hat{\mathbf{v}}_2$.

5. Find the 2-dimensional projection, $\mathbf{p}(i)$, of each state vector of $\mathbf{x}_r(i)$ onto $\hat{\mathbf{v}}_1$ and $\hat{\mathbf{v}}_2$:

$$\mathrm{p}_1(i) = \mathbf{x}_r(i) \cdot \hat{\mathbf{v}}_1 \tag{65}$$

$$\mathrm{p}_2(i) = \mathbf{x}_r(i) \cdot \hat{\mathbf{v}}_2 \tag{66}$$

Once the projections are known, the magnitude of each state vector can be calculated as:

$$\|\mathbf{x}_r(i)\| = \sqrt{\left(\mathrm{p}_1(i)\right)^2 + \left(\mathrm{p}_2(i)\right)^2} \tag{67}$$

and the steady-state magnitude, $\|\mathbf{x}_r\|$, can be found by averaging the last 25% of the $\|\mathbf{x}_r(i)\|$ values. We obtain the steady-state magnitude of $\mathbf{x}_p$ by repeating this entire process and substituting $\mathbf{x}_r$ with $\mathbf{x}_p$. Then λ_{max} for this complex case is found using the normal method of taking the ratio of $\|\mathbf{x}_r\|$ to $\|\mathbf{x}_p\|$. In this particular case, $\lambda_{max} = 0.452$.

Figure 33 shows the 2-dimensional plane with the projections of both $\mathbf{x}_r$ (shown as red open circles) and $\mathbf{x}_p$ (shown as blue solid circles). The progression through time is indicated by the grey line connecting the points. Note that the perturbations always push the projection outward radially from the origin, and the recovery returns the projection to the inner oval after a counterclockwise rotation.

2.5   Summary and Conclusion

In this chapter, we have presented the design, development, and analysis techniques for computational and robotic models of human leg swinging. The swinging-leg model is a
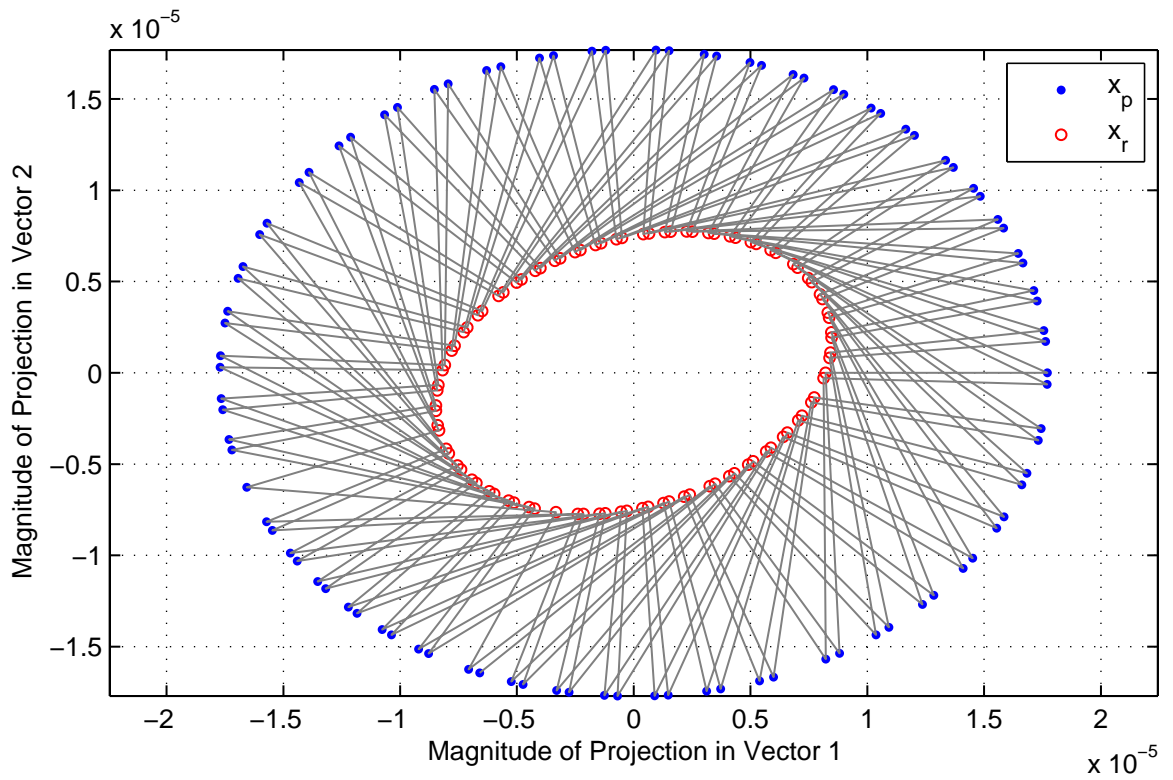
Figure 33: Projection of complex conjugate eigenvectors onto 2-dimensional sub-plane of Poincaré section. The projections of the $\mathbf{x}_r$ state vectors are shown as red open circles and the projections of the $\mathbf{x}_p$ state vectors are shown as blue solid circles. The progression through time is indicated by the grey line connecting the points. λ_{max} is calculated as the ratio of the mean distance of the x_r points from the origin to the mean distance of the x_p points from the origin.

full-scale model of a adult female human leg because the purpose of this research is to determine whether biologically inspired components and can improve the performance of passive dynamic robots. The model was designed anthropomorphically such that the limb segments' mass, length, center of mass, and moment of inertia matched the target human leg as closely as possible.

We chose a biologically inspired control system that uses a neural CPG based on Matsuoka HCOs. One HCO is coupled with each actuated joint—hip and knee—and the HCOs have no direct coupling between them. All inter-joint synchronization that occurs as the leg swings is a result of the mechanical coupling between the joints and feedback from each joint to its respective HCO. The model includes an asymmetric knee angle restriction, which prevents the knee from extending more than a few degrees past the anatomical position.

The model was first implemented computationally using object-oriented C++. Three objects were used to model the complete system—a mechanical leg object, a HCO object, and a coordinator object. The first object models the dynamics of the swinging mechanical leg. The object receives commands from the CPG controller as input and outputs the resulting joints' angles and angular velocities. The dynamic equations of motion for the leg were found using AUTOLEV, a symbolic mechanical engineering analysis tool. There are four sources of torque that can be applied to each joint: 1) active muscle torque, which is produced by the CPG controller, 2) passive stiffness torque, which is produced by passive elastic elements included at each joint, 3) passive damping torque, which is produced by passive viscous elements included at each joint, and 4) dynamic friction torque, which is produced by modeling the effects of dynamic friction at each joint. The second object in the computational implementation models the dynamics of an individual HCO. Two instances of this object are used to create the complete CPG. Each object receives joint angle feedback information from the leg as input and outputs the resulting oscillator state. This third object in the computational implementation provides the top-level control system of the system. This object coordinates all interactions between the mechanical and neural objects and dictates what experiments should be performed and the conditions under which they are executed. Furthermore, this object sets all model parameters.

Parameter values were chosen in various ways. Most of the HCO parameters were selected using published values know to work well for the control of robotic systems. The leg mass properties were chosen by determining the anthropologically appropriate values. The values for the initial conditions were chosen so that the leg was initiated with an acceptable energy level. The remaining parameters were chosen using a Monte Carlo optimization that minimized the energetic cost required to closely track the active torque bias angles.

The swinging leg model was also implemented as a physical robotic leg. Physical implementation was used because this research is intended to be directly applicable to the improvement of legged robotics and because our long-term goal is to develop an anthropomorphic, dynamically walking robot. In addition, the physical implementation necessarily includes real-world imperfections such as parameter mismatch, difficult-to-model friction, and signal noise. In this implementation, the robotic leg swings freely with its hip mechanically grounded to a supporting platform. DC motors directly drive each joint via cables. The gear ratio of the motors was kept low to minimize the parasitic effects of motor friction, damping, and inertia at the joints. Passive viscoelasticity is virtually implemented at the joints by computationally modeling the effects of passive components. These virtual components use real-time feedback information from the leg and apply their resultant torque to the joints using the actuating motors. Once constructed, a series of test were performed to calibrate the system and to characterize the static and dynamic leg properties.

The robotic leg is controlled using a dSPACE real-time I/O controller. This product was chosen because it can be operated in real time, it can interface to several concurrent analog and digital signals, and it can be programmed using MATLAB's SIMULINK. The SIMULINK model was designed hierarchically to closely emulate that of the computational implementation.

The data from both model implementations were analyzed using both the time and frequency domains and using phase portraits. The time domain gave general information regarding the system's performance, such as whether a system is 1) oscillating, 2) growing, decaying, or at steady state, and 3) stationary with respect to other signals. The frequency domain gave information on the fundamental frequency of each signal and whether the

system was frequency locked. Phase portraits were used to determine the period number of the system's oscillations.

The two primary criteria that are used to judge the performance of the swinging leg are energy efficiency and stability. Energy efficiency is evaluated using the *specific cost of leg swinging*, a quantity defined as the energy required to swing a unit mass leg a unit stride length. The stability of the leg is determined using Poincaré sections and Floquet theory. The maximum Floquet multiplier, MFM, is calculated empirically using a sequence of perturbations to the system, and if $|MFM|$ is less than unity the system is stable. We developed algorithms to handle the two special cases that can occur when calculating stability. The special cases are: 1) if MFM is negative or 2) if the state vector associated with MFM is a complex conjugate pair.

This chapter has covered the majority of the engineering needed to perform closed-loop control experiments on a swinging leg model. The computational implementation allows us to do large parameter sweeps quickly; the robotic implementation allows us to validate the results of the parameter sweeps in a physically realistic setting that is applicable to our long-term robotic goals. The neural CPG and control algorithms are similar for both implementations, which permits performance comparisons between them. The next two chapters focus on specific biological components and how their implementation can improve energy efficiency and stability in dynamically walking robots.

CHAPTER III

PASSIVE JOINT STIFFNESS INCREASES ENERGY EFFICIENCY OF LEG SWINGING

Energy conservation is an important consideration in animal locomotion, as it often dictates or at least influences the form of movements that are used to perform a behavior [110]. For example, the transition between gaits as animals change speed often occurs when the energy required to remain in the current gait increases beyond that of an available alternate gait [104]. The two primary energy-conserving mechanisms in human walking are 1) the passive transfer of kinetic and gravitational potential energy [14] and 2) the passive storage and release of energy by elastic tissue components [48]. Using the inverted pendulum model of walking, it has been shown that the maximum theoretical efficiency of the first energy saving mechanism is only 65%, leaving a substantial amount of energy to be either wasted or stored and reused by passive elastic components [104]. The vast majority of walking robots do, in fact, waste this energy by ignoring the potential benefit of using passive elastic components at their joints. In this chapter, we first describe the role of passive stiffness in current robot actuation systems. We then detail how animals use the passive stiffness properties of muscle to improve their locomotion efficiency. Finally, we present a series of experiments that analyze the benefit elastic energy storage can provide passive dynamic robots during leg swinging. We demonstrate that passive stiffness applied at the hip or knee or both can lower the energetic cost of leg swinging 1) by promoting the efficient transfer of mechanical energy and 2) by assisting the actuators in producing anti-gravity joint torques.

3.1 Background

Neither of the two major types of walking robots (discussed in Chapter 1) effectively use passive joint stiffness to reduce energetic cost. Trajectory-control robots have traditionally been focused primarily on task/behavior performance (*e.g.,* walking, running, balancing,

hopping). As a result, the designers have chosen to place a low priority on energy efficiency, opting instead to use inefficient, highly geared actuators to achieve precision movements [45, 135, 86, 65, 28, 55, 57]. In general, relatively high work rates are required in these robots because the frequencies of their movements are not matched to the corresponding limbs' natural frequencies. For robots that perform stereotypical, rhythmic movements such as walking, passive elasticity could be used to alter a joint's natural frequency such that the difference between the desired movement frequency and the natural frequency is reduced. This reduction would lower the actuation work required [25] and improve the robot's efficiency for this task. Passive elasticity could also be used to reduce actuator loads by assisting with anti-gravity movements.

Passive dynamic robots have the potential to use passive joint stiffness to alter their natural dynamics, energy efficiency, and stability, but this approach has not yet been thoroughly explored and has not yet been tested in physical robots. As discussed in Section 1.1.1.2, previous passive dynamic walking robots have operated with an energy efficiency approximately equal to that of human walking [16]. By adding minimal actuation, these robots can increase their stability region by expanding the range of initial and environmental conditions that can be tolerated while still maintaining a tolerable level of mechanical energy. The key to efficiency in these robots, though, is to use actuator work sparingly so that movements can follow the natural leg dynamics and remain largely passive throughout much of the gait cycle. Series-elastic actuation (Section 1.1.3) is one method used to minimize actuator work. By emulating the series (active) elastic component from the Hill muscle model (Section 1.1.2.4), this technique reduces the parasitic effect of actuators, freeing the leg to move naturally.[1] The parallel (passive) elastic component from the Hill muscle model provides joints with elasticity that is independent of actuator output. This component may improve the energy efficiency of robot movements, but this issue remains untested.

The inspiration for incorporating passive elasticity in walking robots comes from animals, which use their muscles as both actuators and sources of compliance (*i.e.,* the inverse

---

[1] A good example of a robot that effectively uses series-elastic actuation is Denise [131], which produces stable walking in three dimensions using McKibben muscles [21, 120] to actuate each hip.

of stiffness) for joints. Actuation is used to produce voluntary movements and to modify natural movements, such as those that occur during passive dynamic leg swinging. Musculotendon compliance allows joint movements to be influenced by natural limb dynamics and by the environment. Musculotendon compliance also provides animals with the ability to temporarily store energy during one phase of a movement so that it can be recovered at a later phase when it is useful for the behavior being performed. For example, in human walking, elastic energy is stored in the Achilles tendon during stance. At toe-off, this passively stored energy is used to supplement active muscle torque such that only a portion of the total push-off force produced by the ankle requires the expenditure of active energy. The amount of mechanical energy stored and released passively during human walking has been estimated to be as much as 50% of the body's total mechanical energy [104].

Animals store and release energy from passive elastic components to reduce the metabolic costs associated with rhythmic movement. Without passive energy storage, quickly reversing a leg's swing direction would require muscles to actively produce negative work to decelerate the leg and then to produce positive work to accelerate it in the opposite direction. Both phases cost energy: negative work wastes energy as heat dissipation, and positive work requires the consumption of metabolic energy. Passive elasticity reduces the energy demand by storing energy during the negative work phase and releasing energy during the positive work phase. Although this mechanism is not 100% efficient and may still require supplemental active muscle work, the total level of metabolic energy required to perform the behavior is reduced.

In addition to providing a means of efficiently storing and releasing energy, passive stiffness is also used by animals to prevent injuries and to stabilize motion [124]. Passive joint stiffness results from the physical properties of the muscles that span it. The lengths, attachment points, and passive tensile forces of all such muscles vector sum to produce a passive stiffness trajectory that is a function of the joint angle and, in the case of multi-articular muscles, of the neighboring joint angles. Because the resting length of muscles generally lie within the middle of the actuated joint's range of motion, passive restoring torques are generally directed away from extreme angles. For example, during leg swinging,

the knee naturally extends towards the anatomical position due to interaction torques. As this happens, knee flexor muscles are passively stretched, and, even if no active muscle force is present, knee flexor torques are produced with increasing magnitude, preventing the knee from reaching its hard hyperextension limit. Avoiding this limit serves two purposes—it prevents potential knee injuries (*e.g.,* ligament tears) and it avoids abrupt and potentially destabilizing changes in the knee's angular velocity.

The goal of this work was to study the efficacy of passive (actuator-independent) elasticity in reducing the actuator work required to produce leg swinging. Specifically, we tested the following hypotheses:

- The addition of passive hip stiffness to a compliant swinging leg can reduce energetic cost by producing anti-gravity torques that lower the amount of actuator work required for leg swinging.

- The addition of passive knee stiffness to a compliant swinging leg can reduce energetic cost by promoting the efficient transfer of kinetic energy between the shank and thigh during swinging movements, increasing the stride length.

3.2   Methods

Experiments were performed on two systems—a single pendulum and the complete leg model (*i.e.,* a double pendulum with knee angle asymmetry). The simple pendulum was tested because it provided a simpler means of exploring the fundamental behavior and performance limitations of this type of neurally controlled, closed-loop system. For each configuration, we examined the energetic cost reduction that occurred with the use of either a simple, constant joint stiffness or a more complex, variable stiffness profile, which emulates the true passive stiffness properties of the human leg.

For each experiment, the following three variables were investigated:

- θ_{ab} (rad) is the actuation bias angle, or the joint angle about which the HCO feedback is biased

- θ_{sb} (rad) is the stiffness bias angle, or the joint angle about which the passive stiffness

function is biased

- K (Nm/rad) is the gain of the passive stiffness function

For clarity, θ_{ab} and θ_{sb} are assumed to be non-negative (*i.e.*, correspond to flexion angles) for all analysis in this research.

3.2.1 Passive Elasticity

Constant joint stiffness was implemented by applying linear elastic elements (*e.g.*, normal linear springs) that applied the following joint torques:

$$\Gamma_{s,h} = K_h(\theta_h - \theta_{sb,h}) \tag{68}$$

$$\Gamma_{s,k} = K_k(\theta_k - \theta_{sb,k}) \tag{69}$$

where $\Gamma_{s,h}$ and $\Gamma_{s,k}$ are the stiffness torques applied at the hip and knee, and K_h and K_k are the gains of the hip and knee stiffness functions.

Variable joint stiffness was implemented as a nonlinear trajectory that, as in humans, varies smoothly as a function of joint angle. Because finding an "ideal" trajectory for our model would have involved a large, complicated parameter search, we chose instead to use an existing model that was developed by curve-fitting empirically measured human data [99]. This "Physiological Model" incorporates uniarticular and biarticular muscles such that the passive stiffness of each joint is a function of both hip and knee angle. Although we planned to incorporate the effects of biarticular muscles, this model's stiffness functions were path dependent and not energy conserving, making analysis of elastic energy storage difficult. We chose to simplify the Physiological Model by removing the stiffness contribution made by biarticular muscles. To remove the contribution, we chose angles for each joint that were at the midpoint of their typical range of motion and used these values for the "biarticular" joint angle each time stiffness was calculated. The modified equations of the Physiological Model that we used to implement variable joint stiffness are:

$$\Gamma_{s,h} = K_h\left(4.047e^{-4.297\theta_h} - 2.430e^{1.748\theta_h} + 8.072\right) \tag{70}$$

$$\Gamma_{s,k} = K_k\left(7.516e^{-2.017\theta_k} - 0.017e^{2.836\theta_k} + 9.207e^{-8.594\theta_k} - 4.820\right) \tag{71}$$
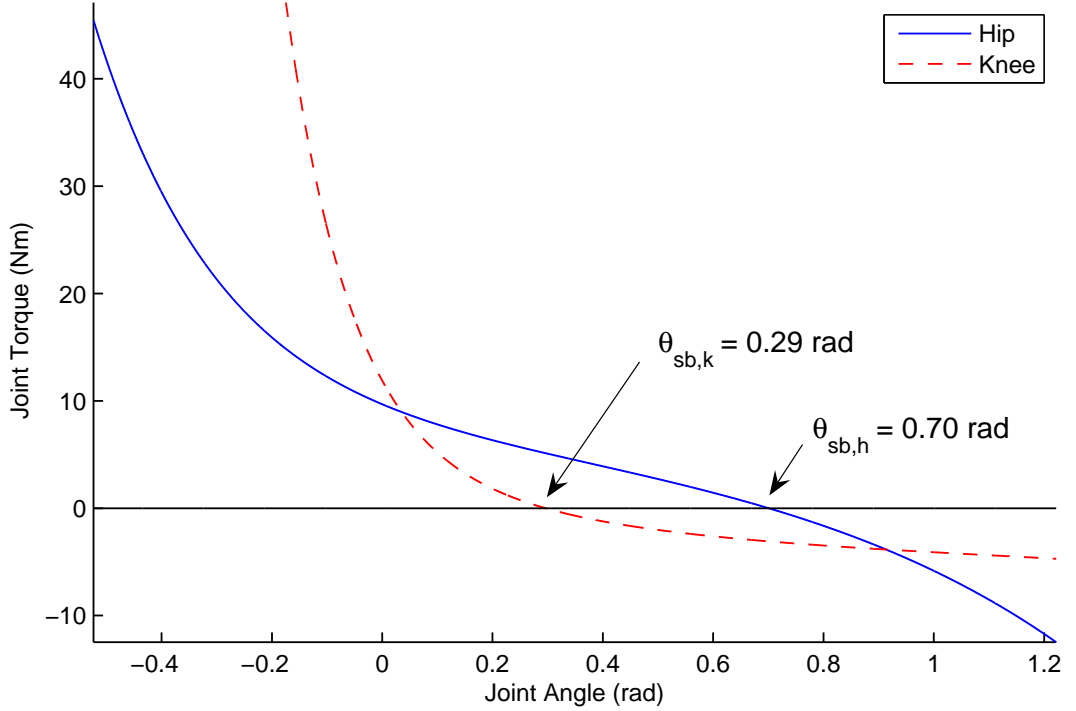
Figure 34: Torque curves used to implement variable joint stiffness with $K_\mathrm{h} = K_\mathrm{k} = 1.0$ Nm. The effective bias angle of each curve, $\theta_{\mathrm{sb,h}}$ and $\theta_{\mathrm{sb,k}}$, were found by determining the joint angle at which stiffness torque is zero.

where the coefficients in the arguments of the exponents are unitless and all remaining coefficients and constants are in units of radians. Figure 34 shows the resulting torque curves produced by these equations with $K_\mathrm{h} = K_\mathrm{k} = 1.0$ Nm.

To avoid complex implementation issues in the robotic model, we used *virtual model control* to actively implement both forms of passive stiffness. We ignored the energy needed to implement passive stiffness when calculating the energetic cost because these passive stiffness components do not require external energy when attached physically. Therefore, we chose not to penalize the energetic cost of our experimental leg controller based on our experimental implementation method.[2]

---

[2]Despite our method of calculating energetic cost for this research, true energetic cost reduction can only occur when passive stiffness is indeed implemented passively. At present, few techniques exist that can passively produce arbitrary joint stiffness profiles [80, 30].

Object	Parameter	Canonical Value
HCO	τ_1	0.75 sec
Pendulum	B	0.14 Nm sec/rad
Control	G_{ff}	9.50
	G_{fb}	10.50

Table 7: Canonical parameters used for the single pendulum experiments.

3.2.2 Single Pendulum Model

We assessed the potential benefit of incorporating passive stiffness properties into robotic joints by first reducing the leg model to a single-DoF pendulum. This was done by using the system described in Chapter 2 and locking the knee such that the pendulum had the mass properties of the entire leg ($M = 10.80$ kg, $L = 0.864$ m, $L_{\text{cm}} = 0.371$ m, $J = 0.846$ kg m^2). Because this model uses only one DoF, the knee HCO was unnecessary and was removed from the CPG controller. We chose values for the four remaining system parameters—τ_1, B, G_{ff}, and G_{fb}—by removing passive stiffness from the model and performing a 2,500-trial Monte Carlo optimization as described in Section 2.2.4. Stiffness was removed for the optimization so that the canonical parameter set would be independent of the stiffness function chosen. The canonical parameters chosen for the single pendulum are shown in Table 7.

3.2.3 Double Pendulum Model

The double pendulum model was implemented as described in Chapter 2 with the exception that the knee was not actuated. We chose not to actively control the knee in these experiments so that comparisons could be made with existing walking robots that use passive knees [131, 16]. This approach also allows us to make predictions regarding the potential benefit of using passive stiffness with these robots. As with the single pendulum model, we removed the knee HCO from the CPG controller because active knee control was not used.

For consistency with the simplified model, the double pendulum used all of the single pendulum parameter values listed in Table 7. With the knee able to bend, the value of an additional parameter—knee damping (B_{k})—had to be determined. We found that setting B_{k} equal to 1.00 Nm/rad provided a balance of low energetic cost, reasonable maximum

Object	Parameter	Canonical Value
HCO	τ_1	0.75 sec
Pendulum	B_h	0.14 Nm sec/rad
	B_k	1.000 Nm sec/rad
Control	G_{ff}	9.50
	G_{fb}	10.50

Table 8: Canonical parameters used for the double pendulum experiments.

Floquet multiplier value (0.71), and underdamped motion that produces significant knee rotation (± 0.32 rad). Lower damping values produced lower energetic costs but moved the system closer to instability. High damping values caused the knee to become overdamped and limited its movement. The canonical parameters used for the double pendulum are shown in Table 8.

Double pendulum experiments were performed both with and without asymmetric restrictions on knee angle. In Section 2.1.3, we describe that the two mechanisms responsible for knee angle asymmetry in humans are: 1) a gradual restriction provided by passive muscle properties and 2) a hard stop provided by the physical construction of the knee (*e.g.*, the anterior cruciate ligament). In the initial experiments, we did not include the hard-stop component, but rather we relied completely on passive stiffness to prevent hyperextension. We then added the hard stop and compared the performance.

To model the knee angle hard stop, we desired a high-stiffness element that begins applying torque when the knee is near full extension and rapidly increases torque output as extension increases. We modeled the hard stop according to the following equation:

$$\Gamma_{HS} = 1.0 \text{Nm/rad} \cdot e^{-15\theta_k} \tag{72}$$

where Γ_{HS} is the torque produced by the knee angle hard stop.

3.2.4 Experimental Technique

We first collected baseline data for the single pendulum by removing passive stiffness from the joint and measuring the effect θ_{ab} had on both the energetic cost and the stability (maximum Floquet multiplier) of the system. We then added constant passive stiffness to the joint and determined if regions in the θ_{ab}, θ_{sb}, K parameter space existed such that the

energetic cost was reduced without significantly reducing stability (increasing the maximum Floquet multiplier).

By definition (in Section 2.4.2), energetic cost is minimized when the pendulum produces large strides with minimal active energy. Therefore, the energetic cost increases 1) when the oscillation amplitude diminishes, which produces smaller a stride length, or 2) when the center of the oscillation becomes offset from θ_{ab}, which increases the feedback (error) signal to the controller, causing the controller to produce higher levels of active energy (actuator work).

To determine whether the single pendulum system could benefit from the use of variable passive stiffness, we replaced the constant stiffness function with the physiologically based model. We used the variable hip stiffness function for the single pendulum because the mass properties of this pendulum were chosen to match those of the entire leg. Parameter searches with the variable stiffness were limited to the K_h, θ_{ab} parameter space because $\theta_{sb,h}$ is fixed by the stiffness model.

A similar experimental procedure was followed with the double pendulum. Baseline data was collected by removing stiffness from the hip and knee and sweeping θ_{ab}. Then, the following experimental conditions were assessed both with and without the hard knee stop included: 1) constant stiffness at the hip only, 2) constant stiffness at the knee only, 3) constant stiffness at both joints, 4) variable stiffness at the hip only, 5) variable stiffness at the knee only, and 6) variable stiffness at both joints.

Several experimental permutations exist for both the single and double pendulums, such as which stiffness function to use and which parameters to sweep. To simplify testing, we assessed the performance of each system using a two-step process. The first step was to fix the value of θ_{ab} to either a zero or non-zero value and then to sweep the values of each stiffness parameter. (For the non-zero value, we chose $\theta_{ab} = 0.15$ rad because this value approximates the center of the hip's range of motion during normal human walking [50].) This step was used to quickly identify good operating regions and behavioral trends. The second step was to fix the stiffness parameters and sweep θ_{ab}. This step provided a more detailed understanding of how energetic cost, stability, and HCO output were affected by

the choice of actuation bias angle.

3.3   Results

The energetic cost of swinging either the single or double pendulum can be reduced by applying stiffness at one or both joints. Energetic cost reductions (relative to the no-stiffness case) of approximately 25% can be achieved using hip stiffness, provided that θ_{ab} is non-zero, and cost reductions of approximately 66% can be achieved using knee stiffness (in the double pendulum).

3.3.1   Single Pendulum Model

Both constant and variable passive stiffness functions are capable of reducing the energetic cost; the amount of reduction is a function of θ_{ab}, and the stiffness function parameter(s). The variable stiffness provides no benefit that warrants its complicated implementation, and neither stiffness function significantly affects the stability of the system. These results are presented in detail in the remainder of this section.

Figure 35A presents the effect that constant passive stiffness has on the system when θ_{ab} is zero. Regardless of the stiffness parameter values, the inclusion of constant passive stiffness results in an increased energetic cost. This cost increase occurs for two distinct reasons: 1) when θ_{sb} is zero, the passive stiffness pulls the pendulum towards the origin ($\theta = 0$ rad), restricting oscillation amplitude, and 2) when θ_{sb} is non-zero, the passive stiffness pulls the pendulum asymmetrically away from θ_{ab}, increasing feedback signal magnitude (and therefore increasing actuator work). In either case, energetic cost increases in a manner directly related to K.

When θ_{ab} is non-zero, the pendulum joint requires additional torque to oscillate symmetrically about θ_{ab} because gravity pulls asymmetrically towards the origin. In the absence of passive stiffness, gravity causes the pendulum to oscillate about an angle between zero and θ_{ab}. In this case, actuator torque is used asymmetrically to "flex" the pendulum's joint toward θ_{ab} and gravity provides all of (or most of) the restoring torque. When gravity provides all of the restoring torque, the CPG controller's output becomes uniphasic such

Single Pendulum with Constant Stiffness
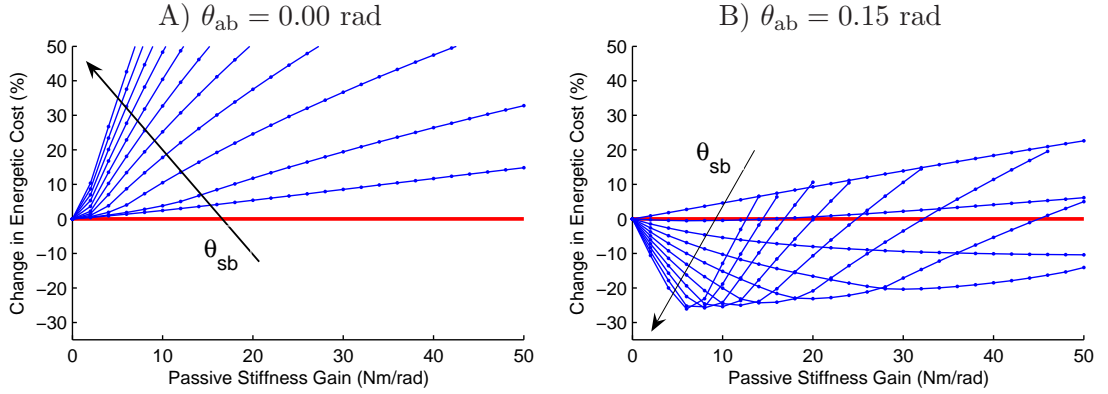
Figure 35: Effect of actuation bias angle on energetic cost reduction in the single pendulum. A) With $\theta_{ab} = 0.00$ rad, any constant stiffness function, regardless of parameters chosen, increases energetic cost. B) With $\theta_{ab} = 0.15$ rad, constant stiffness is capable of reducing energetic cost, given appropriate parameter regions. The individual traces in each plot correspond to fixed values of θ_{sb}. The arrows indicate the effect of increasing θ_{sb} from 0.00 to 1.00 rad in increments of 0.10 rad.

that a non-zero output occurs only during the flexion phase of the oscillation.[3]

Figure 35B presents the effect that constant passive stiffness has on the system with $\theta_{ab} = 0.15$ rad. Adding passive stiffness in this case can either reduce or increase the energetic cost depending on the relationship between θ_{ab} and θ_{sb} and on the value of K. When θ_{sb} is small relative to θ_{ab}, the stiffness assists gravity in pulling the pendulum away from θ_{ab}, causing the energetic cost to increase (*e.g.*, the top trace in Figure 35B). As θ_{sb} increases, the stiffness begins to counter the gravitational effect by storing elastic potential energy as the pendulum joint extends toward the origin and releasing it as the pendulum joint flexes. By countering gravity, this passive elasticity reduces the level of active energy used and therefore lowers the energetic cost (*e.g.*, the bottom traces in Figure 35B).

Figure 35 was most useful in determining ranges of parameters that produced energetic cost reduction. Figure 35A demonstrates that passive stiffness is not beneficial regardless of parameter values when θ_{ab} is aligned with gravity. Figure 35B demonstrates that when $\theta_{ab} = 0.15$ rad, energetic cost is minimized when the passive stiffness function uses high

---

[3]Uniphasic behavior is possible because the output of a Matsuoka oscillator is the difference of two half-wave rectified "neuron" output signals, and strongly asymmetric feedback can drive one of these signals low enough that it never exceeds zero.

values for θ_{sb} and low values for K. The maximum level of energetic cost reduction saturates at about 26% with $\theta_{\text{sb}} = 1.0$ rad and $K = 6.0$ Nm/rad. Increasing θ_{sb} above 1.0 rad can further reduce energetic cost by 1.5%, but doing this significantly reduces the range of K values that produce energetic cost reduction.

Figure 36 shows the effects θ_{sb} and K have on the performance of the single pendulum as θ_{ab} is varied. The values of θ_{sb} and K used for these experiments were chosen using the beneficial parameter ranges from Figure 35B as a guideline. The energetic cost plots (Figure 36A and 36B) and energetic cost reduction plots (Figure 36C and 36D) show that as either K or θ_{sb} increase, the potential reduction in energetic cost increases, along with the value of θ_{ab} at which the reduction is maximized. The stability plots (Figure 36C and 36D) show that increasing K moves the system towards instability, while increasing θ_{sb} maintains the overall stability level. (Stability is discussed in more detail later in this section.)

Figure 36 demonstrates that three distinct operating regions exist in this system. The first region, which has already been discussed, occurs when $\theta_{\text{sb}} << \theta_{\text{ab}}$ and all actuator torque is used to flex the joint away from the origin towards θ_{ab}. This region is characterized by a uniphasic CPG output and can be seen as the flat regions to the left of the troughs in Figure 36E and 36F. Within this region, increasing θ_{sb} reduces the level of energetic cost because the stiffness begins countering the gravitational torque, which reduces actuator work.

The second region occurs as θ_{sb} continues to increase and passive stiffness torques approximately counter the gravitational torque. This operating region is characterized by a biphasic CPG controller output and can be seen as the troughs in Figure 36E and 36F. At some value of θ_{sb}, the two phases of the CPG controller output are symmetric. This operating point occurs at the trough minima in Figure 36A, 36B, 36E, and 36F and represents the value of θ_{sb} that produces the most energetically efficient and stable oscillation dynamics (given values for θ_{ab} and K). When θ_{sb} is slightly above or below this value, the CPG controller maintains biphasic output but the duty cycle of the phases are unequal, the energetic cost is higher, and the stability is reduced.

The third operating region occurs when $\theta_{\text{sb}} >> \theta_{\text{ab}}$ and all actuator torque is used to

Single Pendulum with Constant Stiffness
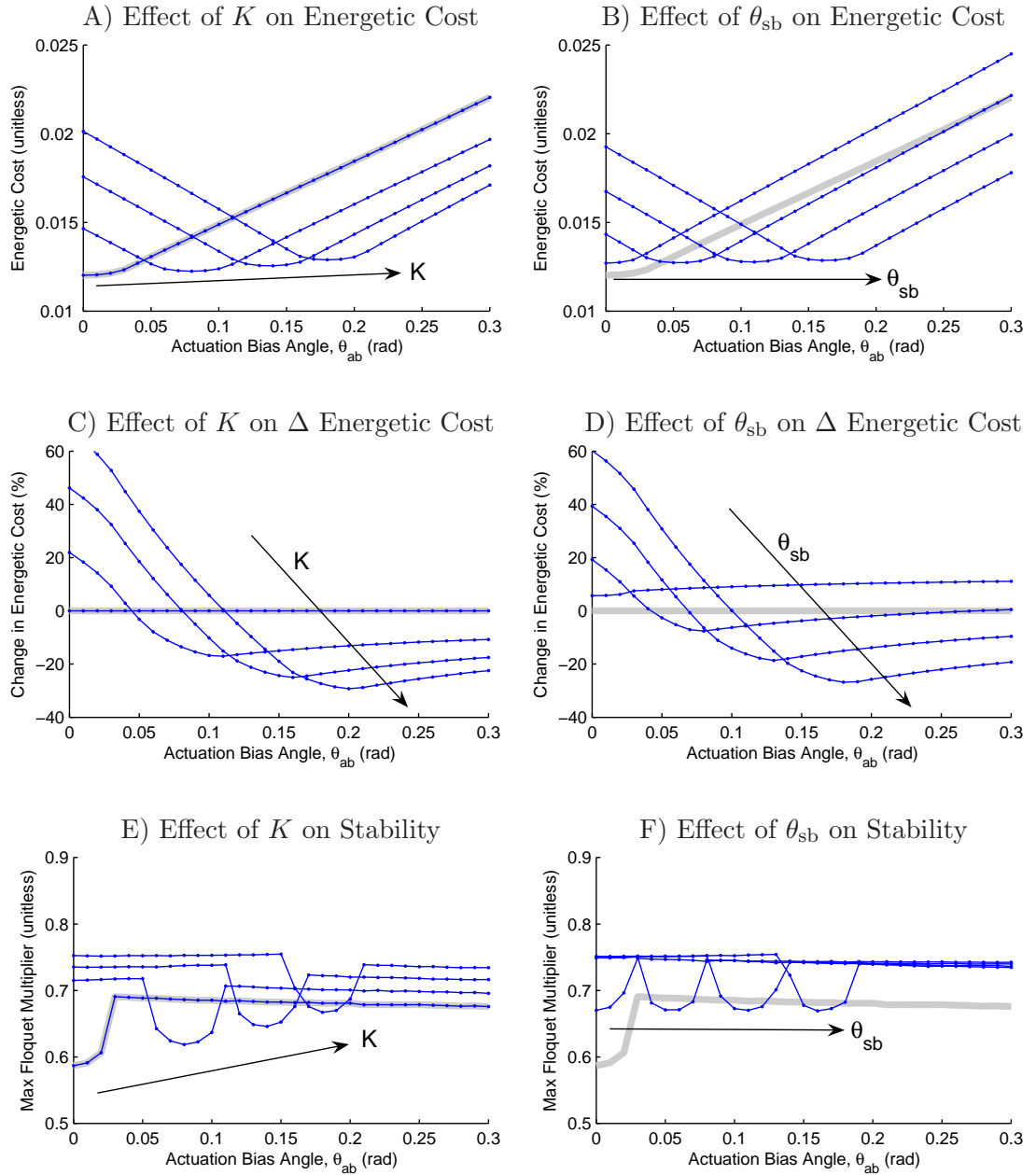
Figure 36: Effect of constant passive stiffness on the energetic cost (plots A and B), energetic cost reduction (plots C and D), and stability (plots E and F) of single pendulum swinging. Plots A, C, and E demonstrate the effect of setting θ_{sb} equal to 0.45 rad and performing tests with K equal to 0.0, 7.0, 14.0, and 21.0 Nm/rad. Plots B, D, and F demonstrate the effect of setting K equal to 21.0 Nm/rad and performing tests with θ_{sb} equal to 0.0, 0.15, 0.30, and 0.45 rad. The arrow in each plot indicates the direction of increasing the test parameter. The thick gray lines indicate the system performance without stiffness applied.

extend the pendulum's joint away from θ_{sb} and towards the origin. This region is also characterized by a uniphasic CPG output. The region can be seen as the flat regions to the right of the troughs in Figure 36E and 36F. Although the first and third regions are both uniphasic, the sign of CPG output is different. In the first region, all actuator torque is positive because positive actuator torques are used to flex the pendulum's joint away from the origin; in the third region, all actuator torque is negative because negative actuator torques are used to extend the pendulum's joint towards the origin. As the value of θ_{sb} continues to increase, the energetic cost increases and cost reduction decreases because higher levels of active work are needed to extend the joint so that the oscillation can remain centered about θ_{ab}.

The preceding analysis details the effect of sweeping θ_{sb}. Similar performance and operating regions occur when K is swept, provided that θ_{sb} is nonzero. We have chosen not to include the description here for brevity.

The parameters θ_{sb} and K have slightly varying effects on stability. Figure 36E and 36F show that increasing either parameter causes the traces to shift toward larger θ_{ab} values. Increasing K also shifts the traces vertically toward larger maximum Floquet multiplier values, indicating that a side effect of varying stiffness gain is that system stability is reduced. However, the largest increase from baseline was only 14% and this increase did not produce behavioral changes significant enough to be noticed by visual inspection. Therefore, although increases in K do move the system towards instability, the effect is not large enough to significantly influence system dynamics.

Based on the performance of the constant stiffness function, we expected that the variable stiffness function would also be capable of reducing energetic cost because the effective bias angle of the variable stiffness function (0.70 rad) exceeds all tested values of θ_{ab}. The experimental results (Figure 37) show that variable stiffness affects the energetic cost (Figure 37A) and stability (Figure 37B) of pendulum dynamics in a manner qualitatively similar to constant stiffness. Furthermore, all operating regions described for the constant stiffness case (including the energy efficient biphasic region) were replicated with the variable stiffness by varying K_{h}.

Single Pendulum with Variable Stiffness

A) Effect of K_h on Δ Energetic Cost   B) Effect of K_h on Stability
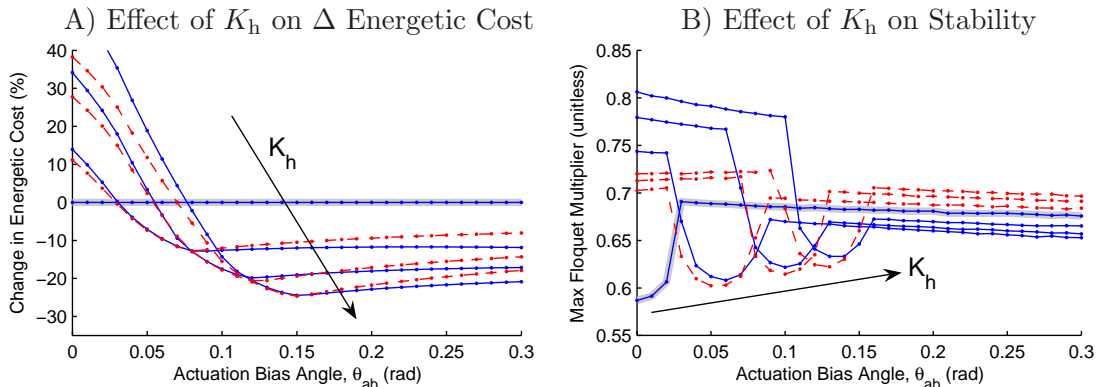
Figure 37: Effect of variable (physiological) passive stiffness on the energetic cost (A) and stability (B) of pendulum swinging. The solid traces represent the variable stiffness function with K_h set equal to 0.0, 0.15, 0.30, and 0.45 Nm. The dashed traces represent the constant stiffness function with $\theta_{sb} = 0.70$ rad and $K_h = 3.00$, 6.00, and 8.00 Nm/rad. Increasing values of K and K_h are indicated by the arrows in each plot. The thick gray lines indicate the system performance without stiffness applied.

The dashed red traces in Figure 37 demonstrate that the variable stiffness effects can be nearly replicated by constant stiffness with θ_{sb} set equal to the inherent bias angle of the variable stiffness (0.70 rad). Additionally, the maximum energetic cost reduction is approximately the same for the variable (25%) and constant (27%) passive stiffness functions.

3.3.2 Double Pendulum

In Section 3.3.1, we showed that energetic cost can be reduced in the single pendulum only when the actuation bias angle, θ_{ab}, is non-zero. In this section, we demonstrate that in the double pendulum this property is true only for hip stiffness. Knee stiffness, especially that which prevents knee hyperextension, can provide energetic cost reduction regardless of actuation bias angle.

We did not include analysis of the effects stiffness has on the maximum Floquet multiplier in this section because, as with the single pendulum, the effects were limited and did not significantly influence the dynamics of the system.

As with the single pendulum model, the first experiment was performed to identify regions in parameter space that produce the largest energetic cost reductions for both zero and non-zero values of θ_{ab}. Figure 38A and 38B show that constant stiffness at the hip

affects the double pendulum in a manner qualitatively similar to that of the single pendulum. This was expected because the only difference between the two cases is whether the knee is allowed to symmetrically bend.

Knee stiffness has a significantly different effect on the dynamics than hip stiffness (Figure 38C and 38D). When θ_{ab} is zero, the most energetically beneficial approach is to apply knee stiffness with a zero bias angle and a high gain. This stiffness restricts the magnitude of knee oscillations without expending energy (as opposed to a damping element) such that the knee remains near the origin. As a result, the double pendulum is able to transfer kinetic and potential energy during swinging with an efficiency closer to that of the single pendulum. Keeping the double pendulum straight reduces energetic cost because kinetic and potential energy are able to efficiently transfer during swinging. Energy is wasted in the case of the free-swinging knee because energy is used to hyperextend and hyperflex the knee, and these movements act to diminish stride length and increase the amount of actuator work required to maintain constant-amplitude oscillations. When the knee stiffness bias angle ($\theta_{sb,k}$) is increased, the knee becomes asymmetrically biased towards flexion, and the energetic cost increases. Knee flexion bias causes a cost increase because interaction torques produce a hip flexion bias, and, as a result, the CPG controller expends additional active energy to keep hip-angle oscillations centered about the origin.

When θ_{ab} is non-zero (Figure 38D), the double pendulum is much more sensitive to changes in the value of K_k than to changes in $\theta_{sb,k}$. For the range of parameters tested, increasing K_k reduced the energetic cost by up to 48%; increasing $\theta_{sb,k}$ only reduced the energetic cost by up to 7%. The difference in the magnitude of these effects is a result of the two parameters working in different ways. As K_k is increased, the magnitude of the knee oscillations are restricted, which improves the transfer of mechanical energy. As $\theta_{sb,k}$ is increased, an effective hip bias angle is created (via interaction torques) that promotes hip flexion and reduces the level of active energy expended. The larger effect of changing K_k indicates that efficient mechanical energy transfer is more important than assistive joint torques in reducing energetic cost in this system.

We used Figure 38B and 38D and similar plots for the variable stiffness (not shown)
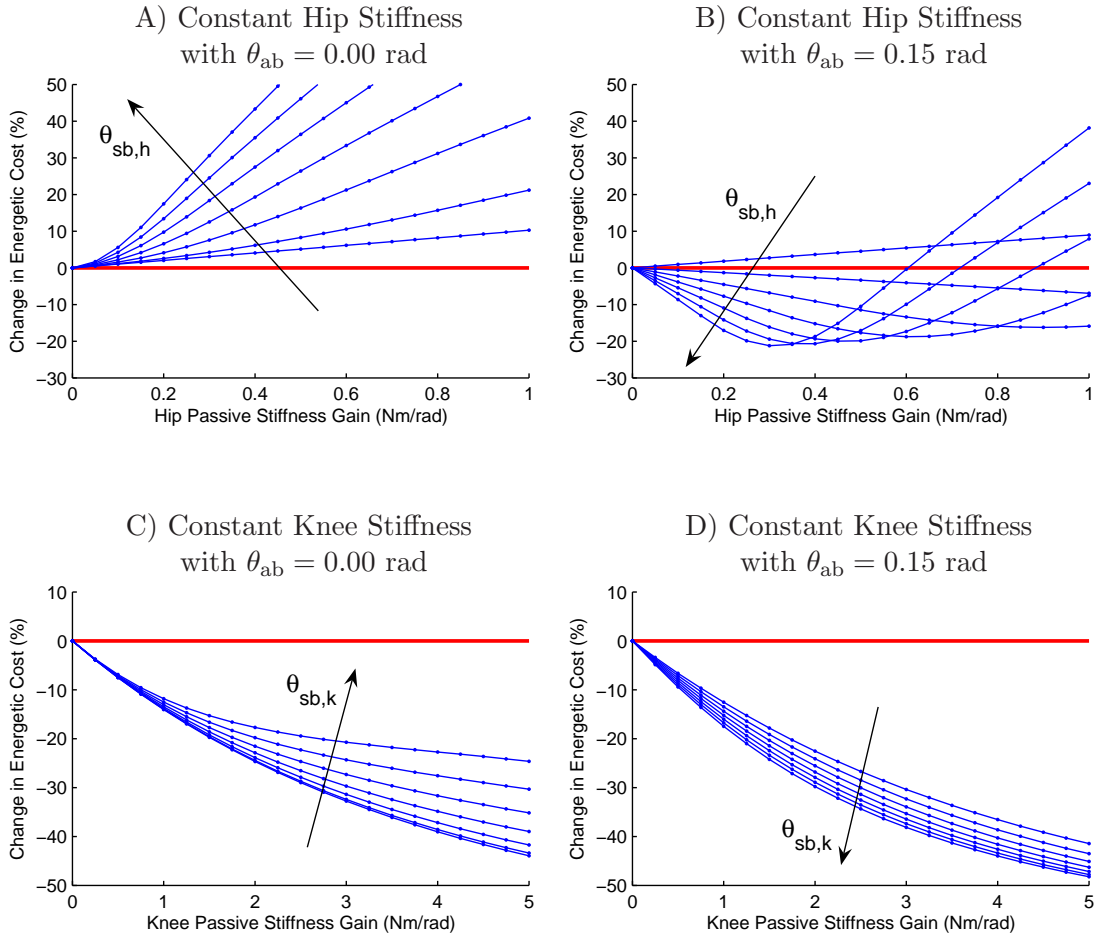
Figure 38: Change in energetic cost of double pendulum swinging with constant passive stiffness applied to the hip and knee. The individual traces in each plot correspond to fixed values of θ_{sb}. In Plots A and B, constant stiffness is applied only at the hip, and the knee swings freely with no restrictions applied. The arrows indicate the effect of increasing $\theta_{\mathrm{sb,h}}$ from 0.00 to 12.00 rad in increments of 2.00 rad. In Plots C and D, constant stiffness is applied only at the knee. The arrows indicate the effect of increasing $\theta_{\mathrm{sb,k}}$ from 0.00 to 0.60 rad in increments of 0.10 rad.

Stiffness Type	Parameter	Canonical Value
Constant	K_{h}	0.30 Nm/rad
	K_{k}	4.00 Nm/rad
	$\theta_{\mathrm{sb,h}}$	12.00 rad
	$\theta_{\mathrm{sb,k}}$	0.60 rad
Variable	K_{h}	0.30 Nm/rad
	K_{k}	1.00 Nm/rad

Table 9: Canonical stiffness parameters used for the double pendulum experiments.

to determine a canonical set of stiffness parameter values (Table 9) that could be used to compare the relative efficacy of each stiffness implementation. With the exception of the variable hip stiffness gain, we chose the value of each parameter as that which produced the lowest energetic cost. The value of the variable hip stiffness gain was chosen separately because all non-zero values of this parameter produce increased energetic cost, and therefore cost is minimized when the gain is zero. To compare the effect of this parameter with all others, we arbitrarily chose the value of the variable stiffness gain to be 1.00 Nm/rad.

Using the canonical stiffness parameters, we conducted a series of experiments that demonstrate how the various stiffness implementations affect the energetic cost of double pendulum swinging. The results (shown in Figure 39) indicate that constant hip stiffness, constant knee stiffness, and variable knee stiffness reduce energetic cost and that the amount of reduction can be increased with the application of the knee angle hard stop. In contrast, the use of variable hip stiffness increases energetic cost.

Constant hip stiffness (Figure 39A) affects energetic cost in a manner similar to that of the single pendulum: at low values of θ_{ab}, energetic cost is increased because the stiffness asymmetrically pulls the joint away from θ_{ab}, increasing actuator work; at higher values of θ_{ab}, energetic cost decreases in a manner directly related to K_{h}. The level of energetic cost reduction at higher values of θ_{ab} is increased when the knee angle hard stop is applied because the restriction improves the transfer of mechanical energy between the shank and thigh. The increased energy transfer allows the hip to reach more flexed angles and centers the hip oscillation closer to θ_{ab}.

The most energetically beneficial operating point for the constant hip stiffness function occurs when the value of $\theta_{\mathrm{sb,h}}$ is large and the value of K_{h} is small. This trend indicates that
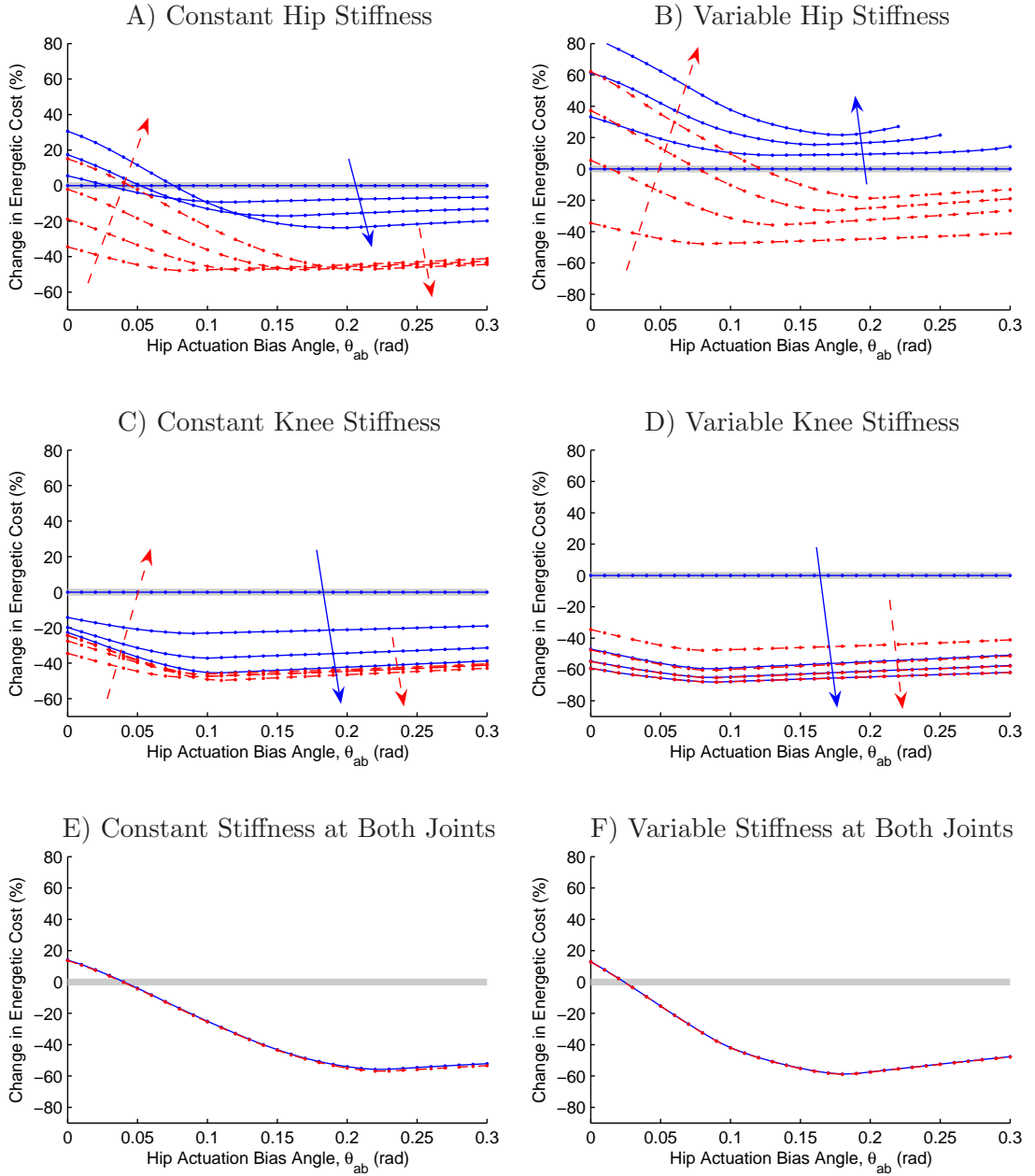
Figure 39: Effects of constant and variable passive stiffness on the energetic cost of double pendulum swinging. Each trace represents a single set of stiffness parameters and the arrows indicate the effect of increasing the stiffness gain from zero to its canonical value (Table 9). Solid blue traces represent the double pendulum experiments performed without the knee angle hard stop, and dashed red traces represent experiments with the hard stop.

constant hip torque could produce larger energy reductions than an elastic torque, which changes magnitude as the hip angle varies. A comparison of the relative benefits of using elastic and constant hip torque is shown later in Figure 40.

Variable hip stiffness (Figure 39B) affects energetic cost in a manner qualitatively similar to that of constant hip stiffness for low values of θ_{ab} (*i.e.*, increasing K_h increases energetic cost). At higher values, however, variable hip stiffness *increases* energetic cost in a manner directly related to K_h. Although the addition of the knee angle hard stop reduced the energetic cost, variable hip stiffness consistently produces cost increases that are directly related to stiffness gain. Therefore, at any value of θ_{ab}, the use of variable stiffness at the hip increases energetic cost.

Constant knee stiffness (Figure 39C) reduces energetic cost for all values of θ_{ab}, and the reduction level is directly related to K_k. The knee angle hard stop can provide energetic cost benefit, but this effect is limited primarily to low-gain stiffness. Furthermore, once the hard stop has been applied, stiffness does not provide additional benefit of any significance. In these tests, energetic cost reduction is achieved by preventing the knee from hyperextending and therefore promotes the efficient transfer of kinetic energy between the shank and thigh during swinging. The gradual energetic cost benefit provided by the hip stiffness results from the need for sufficient gain to oppose hyperextension. The more immediate benefit of the hard stop arises because this mechanism prevents knee hyperextension by design.

Variable knee stiffness (Figure 39D) has a similar effect to constant knee stiffness. The level of energetic cost reduction is higher than the constant stiffness case because the variable stiffness trajectory can create high stiffness near the origin without the side effects of either 1) having a large bias angle that hyperflexes the knee or 2) having a large stiffness gain that rigidly holds the knee and prevents natural swing dynamics. As with the constant knee stiffness, the addition of the hard stop does not provide significant benefit.

Figure 39E and 39F show the effect of applying stiffness at both the hip and knee. In both the constant and variable stiffness cases, the application of the knee angle hard stop had no significant effect. The maximum amount of energetic cost reduction was approximately the same in both cases (57% in the constant stiffness case and 59% in the variable stiffness
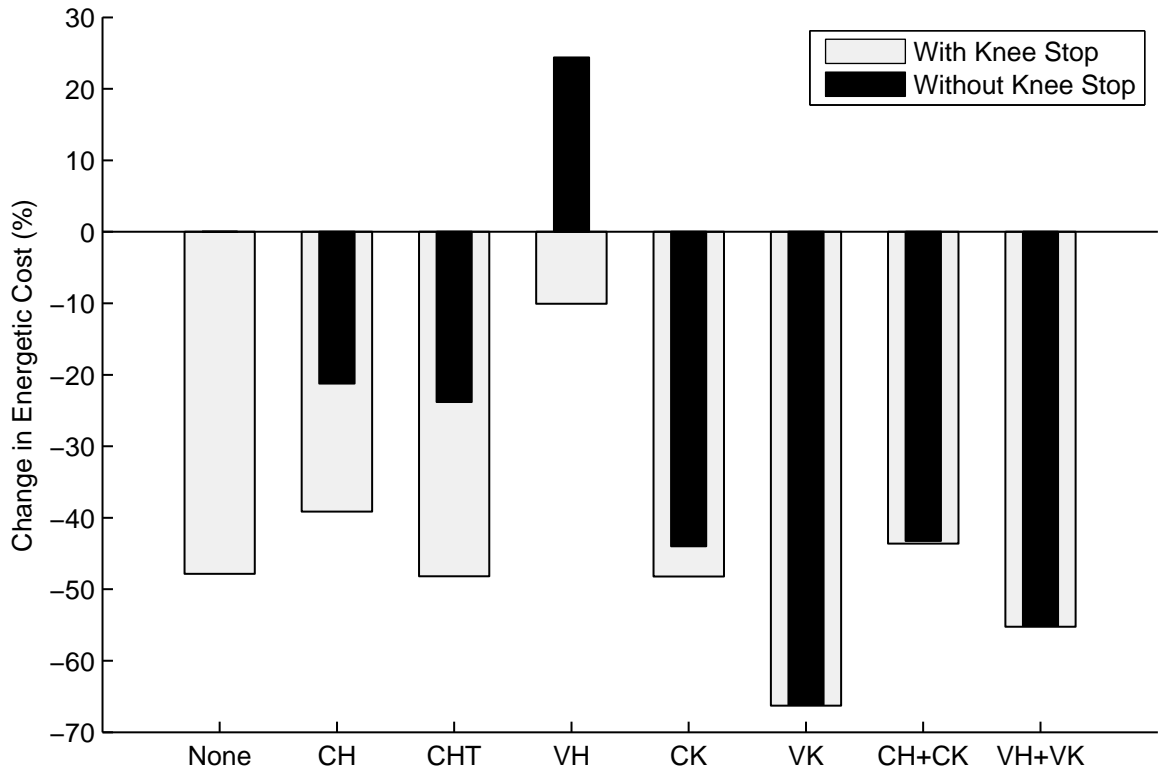
Figure 40: Comparison of the effects various stiffness implementations have on energetic cost. The energetic cost values were chosen from Figure 39 at $\theta_{ab} = 0.15$ rad. The labels at the bottom of the plot indicate which passive stiffness implementation was used and are defined as follows: None–no stiffness at either joint, CH–constant hip stiffness, CHT–constant hip torque, VH–variable hip stiffness, CK–constant knee stiffness, VK–variable knee stiffness, CH+CK–constant stiffness at both joints, and VH+VK–variable stiffness at both joints.

case). The only difference was that the minima occurred at different values of θ_{ab} (0.18 rad in the constant stiffness case and 0.22 rad in the variable stiffness case).

To quantitatively compare the different methods of applying passive stiffness, we selected the value of the energetic cost in each case at $\theta_{ab} = 0.15$ rad, which is the center of the hip's range of motion during normal human walking [50]. The results (shown in Figure 40) demonstrate that nearly all of the stiffness implementations are capable of reducing energetic cost. The one exception—variable hip stiffness—does not reduce energetic cost because this implementation produces passive hip torques that reduce significantly as the hip flexes. We found previously that the hip passive stiffness functions that produce the largest energetic cost reduction have large bias values and small gain values. Because these functions produce

torques that remain approximately constant as the hip rotates, we sought to maximize the energetic cost reduction by replacing the passive stiffness with a constant torque. The results (Figure 40) show that without the knee angle hard stop, variable stiffness, which has a small bias angle of 0.70 rad, increases energetic cost by 24%; constant hip stiffness, which has a large bias angle of 12.00 rad, reduces energetic cost by 21%; and a constant hip torque of 3.80 Nm, which can be considered a stiffness function with infinitely large bias angle, reduces energetic cost by 24%.

The largest energetic cost reduction in these experiments was achieved using variable knee stiffness. Because these results depend on the choice of canonical parameters, the more important observations are that 1) mechanisms that restrict the knee from hyperextending— the knee angle hard stop, constant knee stiffness, and variable knee stiffness—can provide significant reduction in energetic cost and 2) hip elasticity with a low bias angle can increase energetic cost.

3.3.3 Robotic Leg Validation

All analysis in this study was performed using our computational model of leg swinging (Section 2.2) because computational models are fast and provide a simple means of exploring the role of a wide-range of parameter set. Additionally, the computational model offers the unique ability to measure performance quantities non-invasively and without expensive hardware. Experimentation with the physical robotic model (Section 2.3) is crucial, however, to physically validate the experimental results in an environment subject to noise, difficult-to-model friction, and real-world limitations on the system's actuators and sensors. Because robotic experiments take significantly more time to run than computational experiments (the computational model runs at $\sim$ 25X real time), we did not replicate all experimental data. Rather, we chose to validate sample experiments for both the single- and double-pendulum systems. Figure 41 replicates the results of Figure 35, which demonstrates that a non-zero actuation bias angle, θ_{ab}, is required for passive joint stiffness to produce energetic cost reductions in a single pendulum. Figure 42 replicates the results of Figure 36, which demonstrates that the amount of energetic cost reduction in a single

Robot: Single Pendulum with Constant Stiffness
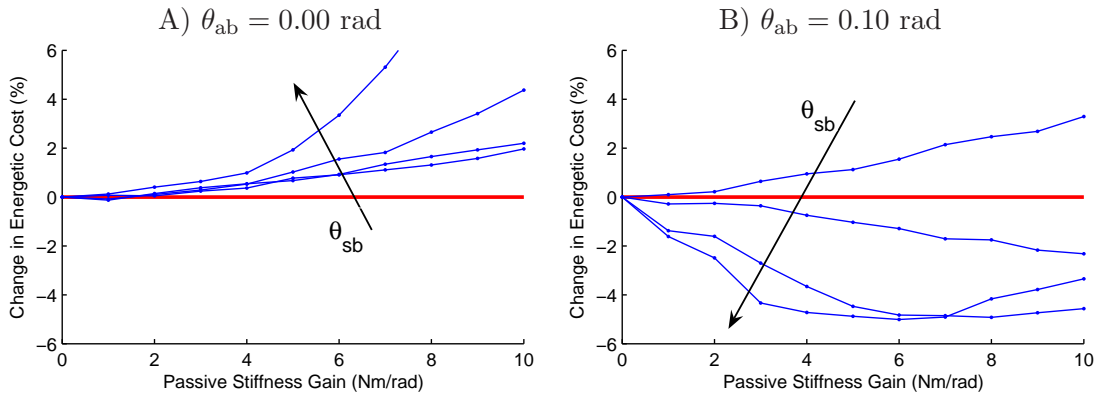
Figure 41: Robotic validation of data presented in Figure 35 demonstrating that passive joint stiffness only produces energetic cost reduction in the single pendulum system when actuation bias angle is non-zero. The individual traces in each plot correspond to fixed values of θ_{sb}. The arrows indicate the effect of increasing θ_{sb} from 0.00 to 0.45 rad in increments of 0.15 rad. The computational model used the following parameter values: $\theta_{ab} = 0.00, 0.15$ rad; $K = 0.0 - 50.0$ Nm/rad; and $\theta_{sb} = 0.0 - 1.0$ rad.

pendulum is a function of the passive stiffness gain, K, and the actuation bias angle. (It is also a function of the passive stiffness bias angle, θ_{sb}, but these results were not replicated.) Finally, Figure 43 replicates the results from Figure 38, which presents the effects of varying the hip and knee passive stiffness bias angles on the energetic cost reduction in the double pendulum.

The qualitative trends in each robotic data figure correspond well their computational counterparts. The primary difference is the data between the two types of experiments was that the changes in energetic cost were reduced in the robotic experiments. This difference resulted from a limit we encountered in the total amount of torque the joint actuators could produce. In a non-experimental robot, the passive torques would be applied by passive elastic components, but our choice to use *virtual model control* required that the actuators produce both the active and passive torques. As a result, we reduced the demand on the actuators by limiting the range of parameters tested. Nonetheless, despite the physical limitations of our robotic leg implementation, the data presented in this section validates that passive joint stiffness does reduce energetic cost in robotic leg swinging.

Robot: Single Pendulum with Constant Stiffness

A) Effect of K on Energetic Cost

B) Effect of K on Δ Energetic Cost
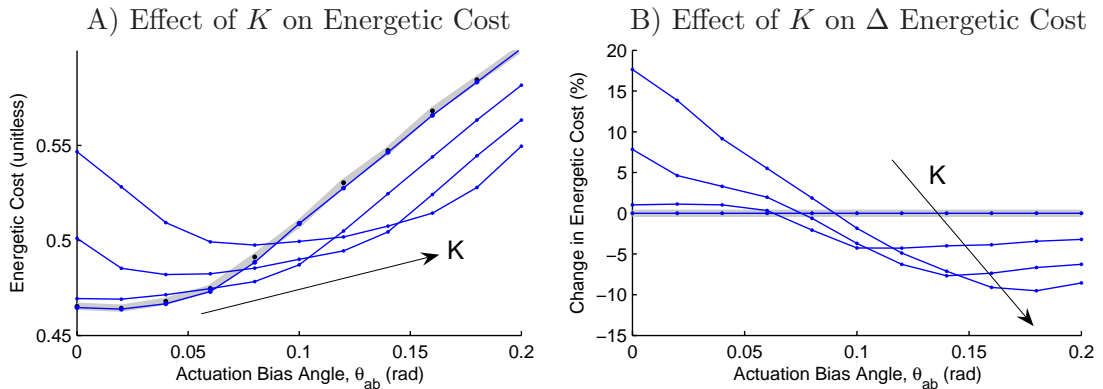
Figure 42: Robotic validation of data presented in Figure 36 demonstrating that the total energetic cost reduction in the single pendulum system is a function of θ_{ab} and θ_{sb}. In each plot, the traces correspond to fixed values of K, and the arrows indicate the effect of increasing K from 0.0 to 12.0 Nm/rad in increments of 4.0 Nm/rad. The computational model used the following parameter values: $\theta_{ab} = 0.00 - 0.30$ rad; $K = 0.0 - 21.0$ Nm/rad; and $\theta_{sb} = 0.45$ rad.

3.4 Discussion

In this chapter, we demonstrated that emulating the physiological use of passive stiffness in passive dynamic robots can reduce the energetic cost of leg swinging without significantly affecting stability. We first simplified the leg model by considering a single-joint pendulum and analyzed the effect passive stiffness had on the energetic cost and the maximum Floquet multiplier of the system. We then implemented the swinging leg model (double pendulum) with a passive knee and performed the same analysis on both joints.

We tested the system with two types of passive elastic elements—constant stiffness springs and a physiologically based variable stiffness trajectory. In the development of walking robots, the use of constant stiffness is preferable because it can be implemented easily by attaching linear elastic elements (*e.g.,* off-the-shelf springs) about the joint such that they apply torque in parallel with the actuators. The disadvantage to using constant elasticity is that the designer is forced to choose one stiffness value that is acceptable for all leg configurations and at all phases of movement. Alternatively, variable stiffness components produce joint torque as a function of joint angle in a physiological manner, but their implementations in robotic systems are significantly more complicated. We avoided
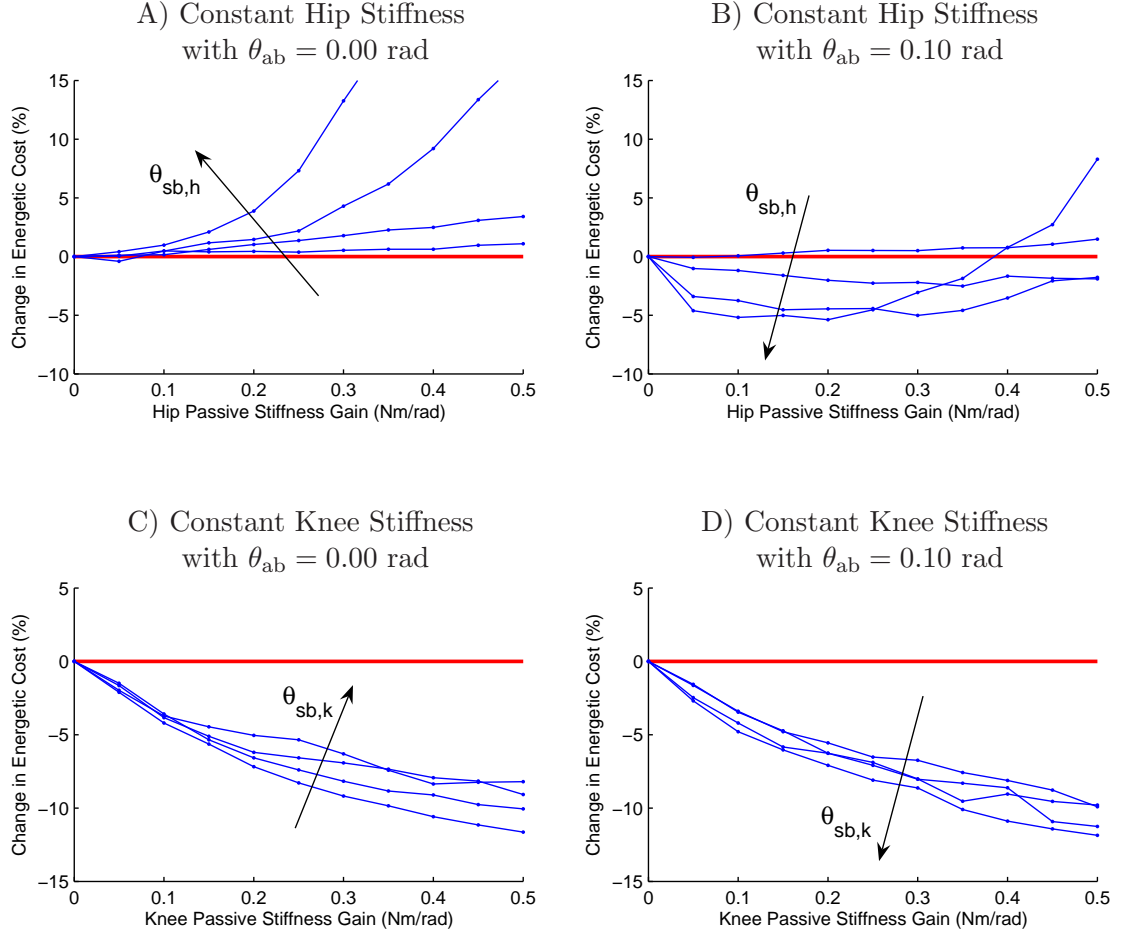
Figure 43: Robotic validation of data presented in Figure 38. Passive hip stiffness only improves the energetic cost of double pendulum swinging when the actuation bias angle is non-zero (A and B). Passive knee stiffness can reduce energetic cost regardless of actuation bias angle; nonzero values of $\theta_{sb,k}$ produce less energetic cost reduction when θ_{ab} is zero and produce more when θ_{ab} is non-zero (C and D). In Plots A and B, the traces correspond to fixed values of $\theta_{sb,h}$, and the arrows indicate the effect of increasing $\theta_{sb,h}$ from 0.0 to 12.0 rad in increments of 4.0 rad. The corresponding parameters used in the computational model were: $\theta_{ab} = 0.00$, 0.15 rad; $K = 0.0 - 1.0$ Nm/rad; and $\theta_{sb} = 0.0 - 12.0$ rad. In Plots C and D, the traces correspond to fixed values of $\theta_{sb,k}$, and the arrows indicate the effect of increasing $\theta_{sb,k}$ from 0.0 to 0.6 rad in increments of 0.2 rad. In this case, the corresponding parameters used in the computational model were: $\theta_{ab} = 0.00$, 0.15 rad; $K = 0.0 - 5.0$ Nm/rad; and $\theta_{sb} = 0.0 - 0.6$ rad.

the implementation obstacle in this research by using *virtual model control* to actively implement all forms of passive stiffness. (We did not consider the energy used to virtually implement the passive stiffness components when calculating energetic cost.)

We hypothesized that passive stiffness at the hip could reduce energetic cost by countering the gravitational torque and, therefore, reducing the actuator load. Using both the single and double pendulum models, we found this to be true only when the hip actuation bias angle does not correspond to the direction of gravity ($\theta_{ab} \neq 0$ rad). Furthermore, using the double pendulum we found that the hip stiffness function that produced the lowest energetic cost had a high stiffness bias angle and a low stiffness gain value. This type of function most closely resembles a constant torque because the joint angle does not significantly affect torque level. In comparing constant stiffness, variable stiffness, and constant torque, we found that the level of energetic cost savings was highly dependent on bias angle. Variable stiffness, which has a relatively low bias angle, increased energetic cost; constant stiffness, which has a high bias angle, decreased energetic cost significantly; and constant torque provided the maximum cost decrease.

We also hypothesized that passive stiffness at the knee could reduce energetic cost by promoting the transfer of kinetic energy between the shank and thigh during swinging. We found that energy transfer improved with all mechanisms that restrict knee hyperextension, including the constant stiffness, the variable stiffness, and the knee angle hard stop. In our experiments, variable knee stiffness provided the largest reduction in energetic cost. A post-hoc analysis showed that the reason for the superior performance of the variable stiffness function was that it is essentially a combination of a constant knee stiffness (biased about $\theta_k = 0.29$ rad) and an exponential-stiffness knee stop. The constant stiffness component increases the magnitude of knee flexion during swing and, as a result, increases the shank's kinetic energy at knee extension; the hard stop component improves the amount of this kinetic energy that is transferred to the thigh. Increasing the level of thigh kinetic energy reduces energetic cost because larger-amplitude leg swinging is produced.

Passive stiffness properties were found to also benefit the energetic cost of leg swinging by preventing non-conservative collisions at knee strike. The elastic hard stop used in

115

these experiments passively stores potential energy as the knee reaches its extension limit during forward (anterior) swinging. This energy is then released during backward (posterior) swinging to produce increased knee flexion. The method commonly used in passive dynamic walking robots is to allow the shank to swing forward until it impacts a rigid limit created by the physical construction of the knee. At impact, kinetic energy is dissipated, and a latch engages that prevents the knee from flexing during stance [16, 131]. By reusing rather than dissipating energy, out method reduces the energetic cost of leg swinging by approximately 7%.[4]

We found that variable stiffness at either joint during leg swinging does not present a benefit that justifies its more complex implementation because 1) the variable hip stiffness actually increases energetic cost and 2) the performance of the variable knee stiffness can be theoretically reproduced by altering the parameters of the linear stiffness and exponential hard stop functions so that the torque curve from Figure 34 is approximately replicated (data not shown). In a true mechanical implementation, however, nonlinear elastic components may still be necessary to implement the exponential knee-stop stiffness.

Using the variable stiffness functions as models of human joint stiffness, our experimental data suggest that the energetic cost of human leg swinging is decreased by passive knee stiffness and increased by passive hip stiffness. A likely explanation for the poor performance of the hip stiffness in our experiments is that the human leg's passive stiffness properties are better tuned to the swing phase of walking rather than to the more uncommon behavior of isolated leg swinging. The primary difference between these behaviors is that in the swing phase of walking, the leg acquires much of its needed energy from ankle plantarflexion; in isolated swinging, the leg relies solely on less-efficient hip flexion. Because the leg receives a large burst of mechanical energy from plantarflexion, passive hip stiffness torque attenuates as the hip flexes, and a small burst of hip extension torque is used to actively stiffen the joint and prevent hyperflexion [25]. The swinging leg model does not include plantarflexion. As a result, passive hip stiffness maintains large-amplitude oscillations by continuing to produce

---

[4]This comparison was made using a simulation of the double pendulum model in which the elastic hard stop was replaced with the impact model from [70] using $n = 1$, $k = 50000$ Nm/rad, and $\alpha = 0.4$.

flexion torque during late swing rather than attenuating. This behavior corresponds to high-bias stiffness or a continuous torque.

Although this study focused on the task of leg swinging, our results suggest that passive stiffness properties would also increase the energy efficiency of walking. Previous studies have shown that the metabolic cost of leg swinging during walking is 10% [38] and the metabolic cost of propulsion is 48% [39]. This research has shown that the energetic cost of leg swinging can be reduced 66% by using passive stiffness at the knee alone. Furthermore, passive knee stiffness could also reduce the energetic cost of propulsion in walking because the energy stored during late swing (*i.e.,* knee extension) could contribute directly to propulsion during mid- to late-stance. A significant limitation in relating our experimental approach to walking is that we did not include the ankle, which provides the largest amount of passive energy storage during walking. We chose to ignore the ankle because its role is insignificant in no-contact swinging. However, the Achilles tendon has been shown to passively store and reuse up to 50% of the body's mechanical energy during walking [104]. Therefore, in addition to lowering the energetic cost of leg swinging by 66%, we expect that passive elasticity can significantly reduce the energetic cost of propulsion in walking.

In summary, we have demonstrated that passive joint stiffness can be used to reduce the energetic cost of robotic leg swinging. We have validated our hypotheses 1) that hip stiffness can reduce energetic cost by producing anti-gravity torques that lower the amount of required actuator work (provided a high stiffness bias angle was used) and 2) that knee stiffness can reduce energetic cost by promoting the efficient transfer of kinetic energy between the shank and thigh at knee extension. Experiments were performed using a computational model and were validated using a full-scale robotic leg. Physiological models of human joint stiffness proved beneficial at the knee and detrimental at the hip. Constant stiffness combined with a limit on knee hyperextension produced comparable results to the physiological stiffness model without requiring complicated implementation techniques. We expect that passive energy storage will be more effective in walking because the amount of passive energy stored in the ankle is significantly larger than that stored in the hip and knee.

CHAPTER IV

ACTIVE KNEE CONTROL IMPROVES PERTURBATION RESPONSE DURING FORWARD LEG SWING

An impressive feature of legged animals is their ability to minimize the destabilizing effects of perturbations during locomotion. For limited-scale swing-leg perturbations, humans use low-level spinal reflex pathways to control responses in a manner that avoids a fall [108]. In contrast, passive dynamic robots, which have shown tremendous ability to produce efficient locomotion, are particularly sensitive to such perturbations [74, 75]. Although current dynamic robots use minimal actuation to improve stability, these robots are only capable of managing small changes in environmental conditions such as variations in ground slope angle or minor physical perturbations [16, 131]. This research explores the use of active knee control as a means to expand the ability of dynamic walking robots to reject swing-leg perturbations. We use biologically inspired neural oscillators to independently control the hip and knee of a full-scale robotic leg, allowing the leg's inter-joint mechanical coupling to provide whole-leg coordination. We examine the effects of active knee control during both unperturbed and perturbed leg swinging and demonstrate the following: 1) knee actuation is detrimental in unperturbed leg swing because energy efficiency is reduced without a significant improvement in performance and 2) knee actuation is beneficial in leg perturbed swing because the drawback of an energy efficiency reduction is offset by the benefit of a significant improvement in the leg's swing-leg perturbation response. Although this trade-off between energy efficiency and stability is commonly seen in human locomotion, we suggest that both quantities may be improved in walking robots by using a perturbation-detection system that can apply knee actuation only as needed to maintain stability.

4.1 Background

The successful management of unexpected perturbations is a complicated aspect of legged locomotion [130]. In humans, falls can cause serious injury, such as hip fractures; in robots,

falls can cause structural damage and can prevent the completion of a robot's task. Perturbations to the swing leg of bipedal walkers can be particularly destabilizing without appropriate compensation [24, 8, 18]. Although this type of perturbation is regularly encountered by bipedal walkers in real-world environments, neither of the two major types of walking robots (discussed in Chapter 1) are currently capable of managing significant perturbations in a dynamically stable and energy-efficient manner.

Trajectory-control robots are sensitive to environmental perturbations because they use high-stiffness actuators, which prevent significant joint-angle deviations and therefore promote the transmission of disturbances throughout the robot. To avoid instability, these robots either 1) are limited to movement in highly controlled environments or 2) must have the ability to sense and map their environments in real-time with high accuracy [35]. In both cases, the robot must accurately predict the location of each obstacle and avoid them by modifying its joint trajectories. An alternative approach is to use contact sensors to detect the presence of unexpected perturbations and to produce a complex recovery response to prevent a fall. As with unperturbed walking, this approach suffers from the requirement that the robots use highly complex control systems and that large amounts of energy be expended to rigidly manipulate their joints.

In contrast, passive dynamic robots have limited ability to handle disturbances of any significant magnitude. Their sensitivity to environmental perturbations arises because they have no control system and are reliant upon finely tuned mechanics to maintain limit-cycle oscillations of their state variables. As a result, the basin of attraction of these robots is small and even limited-scale perturbations can cause falls [107, 74, 75]. Recent implementations of dynamically walking robots have included minimal actuation at the hip [133, 131] or ankle [16]. These actuators do not dictate trajectories; instead, they inject or dissipate small amounts of mechanical energy into the system as needed to maintain dynamic stability. This approach increases the robots' ability to perform walking in unpredictable environments by increasing the robots' basin of attraction. These robots have physically demonstrated modest stability improvements: they can walk on a range of slope angles including level ground, tolerate variability in initial conditions and parameter values, and manage limited variations

in floor elevation ($< 2\%$ leg length). Although these implementations have demonstrated stability improvement in this type of robot, two significant limitations are still present. The first limitation is that all compensatory actuation in response to a swing-leg perturbation must be performed by the hip because the knee remains uncontrolled. The second is that these robots use state-machine controllers, which only use feedback to regulate the timing of joint-torque application. As a result, the torque level applied to the joints during each step is fixed and does not vary with the state of the robot [133, 131].

The human response to limited-magnitude swing-leg perturbations is energy efficient [20] and places little demand on high-order cognitive processes [53]. Energy efficiency arises because the passive dynamics of the leg continue to be used throughout the perturbation response [29]; control simplicity (from a cognitive perspective) arises because a low-level neural architecture is used to detect perturbations and to produce appropriate muscular responses [53]. The response type varies based on the phase of leg swing at which the perturbation occurs [29, 18, 20, 106], the duration of the perturbation [19, 20], and whether the perturbation increases or decreases the level of mechanical energy [23].

One of the keys to the human perturbation response is that the knee, which is nearly passive during unperturbed swing [78, 81], can be used to produce active perturbation responses. For example, during early-swing perturbations to human walking, the knee actively produces a flexion response that lifts the leg up and over obstacles[29, 23, 18]. This type of response is used to supplement rather than overpower the leg's natural dynamics. The resulting leg movements act to reduce the effect of a perturbation by minimizing the resulting change in the body's mechanical energy [20].

The essential components of the human perturbation response—the use of natural dynamics and active knee control—are not currently used in walking robots. Although trajectory-control robots are able to produce active knee responses to perturbations, they are unable to energetically match human performance because they do not take advantage of the leg's natural dynamics. Alternatively, the strong focus on energy efficiency in dynamic walking robots has prevented the addition of knee actuation and, therefore, has limited the ability of these robots to avoid dramatic changes to their mechanical energy.

The aim of this study was to determine: 1) how active knee control influences the performance of a hip-actuated, dynamically swinging leg and 2) whether active knee control can improve the perturbation response of this system. We tested the following hypotheses:

- Active knee control decreases the energy efficiency of leg swinging without significantly improving performance because hip actuation is sufficient to achieve whole-leg, resonance-tuned oscillations in the absence of perturbations.

- Active control of both joints reduces the effect of a perturbation by distributing the perturbation's effect among both joints.

We use a two-degree-of-freedom (DoF) swinging leg with a closed-loop, neurally inspired controller to compare active-knee and passive-knee leg performance. We demonstrate, in support of the design of current dynamic walkers, that unperturbed leg swing is energetically optimized by using a passive knee. When swing-leg perturbations are present, however, active knee control minimizes their effect and, therefore, maximizes stability. Taken together, these results indicate the presence of a common engineering trade-off between energy efficiency and stability.

4.2 Methods

Two types of experiments were performed in this study: 1) a characterization of swinging leg performance with active knee control and 2) an analysis of the leg's ability to reject small force perturbations during forward swing. In each case, experiments were performed on the complete leg model (described in Chapter 2), which includes the knee angle hard stop. Based on the results of Chapter 3, which demonstrated that passive knee stiffness provides an energetic cost benefit, we included a small-magnitude, linear passive stiffness at the knee.

The canonical parameters values used for these experiments (Table 10) were chosen by selecting the first parameter set that produced stable leg swinging while maintaining a reasonable stride length (> 0.20 m). We chose not to optimize the values to demonstrate that the results of this study are not specific to an optimal parameter set. In addition,

Object	Test Parameter	Canonical Value		
		Hip	Knee	Unit
HCO	τ_1	0.224	0.224*	sec
Leg	B	0.25	1.00	Nm sec/rad
	K	2.00	0.00	Nm/rad
	θ_{sb}	0.60	0.00	rad
Control	G_{ff}	4.00	3.00*	Nm
	G_{fb}	5.00	5.00*	rad^{-1}
	θ_{ab}	0.15	0.475*	rad

Table 10: Canonical parameter set used for the complete swinging leg model. Stars indicate parameter values that are only relevant in the active-knee case.

the use of an optimized parameter set would necessarily cause all parameter variations to reduce performance.

For each experiment, we investigated the effects that the following three variables had on system performance:

- ω_{hco} (rad/sec) is the natural frequency of the Half Center Oscillator (HCO), which is set by τ_1 (see Section 2.2.4)

- G_{ff} (Nm) is the feed-forward gain from the HCO to the joint actuator

- G_{fb} (rad^{-1}) is the feedback gain from the joint angle sensor to the HCO

We measured system performance using a number of criteria that varied depending on the type of experiment performed. The two types of experiments—steady-state swinging and perturbed-rejection analysis—are described in the following sections.

4.2.1 Steady-State Swinging

The first series of experiments were performed to characterize the effects that the six test parameters (three for each joint) have on active-knee leg swinging. The experiments consisted of two-dimensional sweeps of the hip (h) and knee (k) values of each test variable ($\omega_{\text{hco,h}}$ vs. $\omega_{\text{hco,k}}$, $G_{\text{ff,h}}$ vs. $G_{\text{ff,k}}$, and $G_{\text{fb,h}}$ vs. $G_{\text{fb,k}}$). For each experiment we analyzed whether whole-leg resonance tuning occurred, and, if so, we measured the leg's performance based on six criteria (described later in this section).

To make comparisons with existing dynamic walking robots that do not actuate their knees [131, 16], we also performed passive-knee leg swinging experiments. In these experiments, we performed one-dimensional sweeps of $\omega_{\mathrm{hco,h}}$, $G_{\mathrm{ff,h}}$ and $G_{\mathrm{fb,h}}$ and calculated the values of each of the six performance criteria. By comparing the performance of the system with and without active knee control, we were able to make predictions regarding the potential benefit of adding knee actuation to existing passive dynamic walking robots.

To determine whether whole-leg resonance tuning (Section 1.1.2.2) occurred for each experiment, we swept the test variables and mapped the regions in parameter space that met two conditions. The first condition was that the frequencies of all four oscillators—the hip angle (ω_{h}), the knee angle (ω_{k}), the hip HCO ($\omega_{\mathrm{hco,h}}$), and, if active, the knee HCO ($\omega_{\mathrm{hco,k}}$)—must be matched to within the minimum frequency resolution. The resulting common frequency is defined as the system frequency, ω_{sys}. The second condition is that ω_{sys} be approximately equal to the natural (*i.e.,* resonant) frequency of the leg, ω_{n}, which can be found using Equation 29 to be 4.0 rad/sec (0.64 Hz). This value is only an approximation, however, because it ignores the effect of the actuation system in the robotic implementation, and it does not consider the effect of the knee bending, which changes the leg's moment of inertia (MoI) (see Section 2.3.3.3). Additionally, ω_{sys} can vary slightly around the value of ω_{n} while maintaining resonance tuning based on: 1) the relationship between the HCO natural frequencies and ω_{n} and 2) the gain values used [126]. To compensate for the potential frequency-match error, we assume that resonance tuning occurs when ω_{sys} is within 10% of ω_{n}.

In trials that achieved resonance tuning, we calculated the values of each of the following six measures of system performance: 1) the system frequency (ω_{sys}), 2) the inter-joint phase (ϕ_{sys}), 3) the energetic cost of leg swinging (σ), 4) the system's maximum Floquet multiplier (λ_{max}), 5) the stride time (T_{s}), and 6) the stride length (L_{s}). The value of ω_{sys} was calculated by performing a fast Fourier transform (FFT) on one of the four system oscillators (the specific oscillator chosen was irrelevant because the system was resonance tuned). The inter-joint phase was calculated as the phase delay from the hip angle oscillator

to the knee angle oscillator according to the following equation:

$$\phi_{\mathrm{sys}} = 2\pi \left(\frac{t_{\mathrm{hp}} - t_{\mathrm{kp}}}{T_{\mathrm{sys}}} \right) \tag{73}$$

where t_{hp} is the time of the hip angle flexion peak, t_{kp} is the time of the knee angle flexion peak, and $T_{\mathrm{sys}} = 2\pi/\omega_{\mathrm{sys}}$ is the system oscillation period. The methods used to calculate the σ and λ_{max} are described in Section 2.4.2 and Section 2.4.3, respectively. Stride time was calculated as the amount of time needed for the leg's center of mass (CoM) to move from its most posterior position to its most anterior position.[1] Stride length was calculated as the distance that the leg's CoM traveled in the sagittal plane during a single stride.

4.2.2 Perturbation-Rejection Analysis

The second series of experiments involved the application of a small force perturbation to the leg during forward swing. We chose to apply a horizontal force to the ankle in the posterior direction because this type of force roughly mimics the effect of the leg encountering a temporary obstacle such as a twig or tall grass. The canonical perturbation force used had a magnitude $F_{\mathrm{p}}= 20.0$ N, a duration $T_{\mathrm{p}} = 0.10$ sec, and an application phase $\phi_{\mathrm{p}} = 15.0\%$. (The perturbation application phase was defined as a percentage of unperturbed forward swing phase duration.) The force level and duration were chosen such that the perturbation produced a visually noticeable disturbance of the system without producing an abrupt alteration of the dynamics as a collision with a rigid obstacle would. For these experiments, a trial was defined as one forward-swing phase, where forward swing is the period during which the hip angular velocity is positive. (We assume that the hip angular velocity oscillates in a smooth, period-1 manner.) To ensure the application of consistent perturbations to the robotic leg, the perturbation torques were added virtually (using actuators), as described in Section 2.3.4.

The response of the leg to perturbations was determined by comparing the system's performance during perturbed and unperturbed trials. For each type of trial, unperturbed leg swinging was first performed for 150 sec to assure that the system had reached steady

---

[1]Stride time is, in general, not equal to half of the oscillation period because the leg's forward and backward movements are asymmetric.

state. After this period, the experimental trial was performed during which a perturbation was applied, if appropriate. At the end of each trial, the following quantities were recorded: 1) the total mechanical energy of the system, 2) the energetic cost of swinging the leg forward, 3) the stride time, and 4) the stride length. We define the effect of the perturbation on the leg according to the following equation:

$$\chi = \frac{|\Delta E|}{E_{\text{ref}}} + \frac{|\Delta \sigma_{\text{f}}|}{\sigma_{\text{f,ref}}} + \frac{|\Delta T_{\text{s}}|}{T_{\text{s,ref}}} + \frac{|\Delta L_{\text{s}}|}{L_{\text{s,ref}}} \tag{74}$$

where χ is the perturbation response of the system; E is the system energy at the end of a trial; σ_{f} is the energetic cost of forward leg swing, T_{s} is the stride time; L_{s} is the stride length; and E_{ref}, $\sigma_{\text{f,ref}}$, $T_{\text{s,ref}}$, and $L_{\text{s,ref}}$ are reference values from unperturbed trials. Complete perturbation rejection occurs when χ is zero. (The energetic cost of *forward* leg swinging (σ_{f}) is calculated in the same manner as the energetic cost of leg swinging (σ) (see Section 2.4.2) with the exception that σ_{f} only considers the active work produced during the forward swing phase of motion.)

Because χ varies as a function of the phase at which the perturbation is applied, the first experiment we performed was to set all test variables to their canonical values and produce phase response curves (PRCs) by applying perturbations of varying magnitude and application phase.

We then calculated the relative contribution of each joint's controller to a canonical perturbation. These calculations were made by 1) measuring the change in active work at each joint between the perturbation onset and the end of the trial ($\Delta W_{\text{h}}(t)$ and $\Delta W_{\text{k}}(t)$), 2) calculating the root-mean-square (RMS) of each value ($\Delta W_{\text{h,rms}}$ and $\Delta W_{\text{k,rms}}$), and 3) calculating the percentage contribution that each joint made to the total RMS work

change in the system (C_h and C_k). The equations used for these calculations follow:

$$\Delta W_{\mathrm{h,rms}} = \sqrt{\frac{1}{T_\mathrm{s} - t_\mathrm{p}} \int_{t_\mathrm{p}}^{T_\mathrm{s}} \left(\Delta W_\mathrm{h}(t)\right)^2 dt} \tag{75}$$

$$\Delta W_{\mathrm{k,rms}} = \sqrt{\frac{1}{T_\mathrm{s} - t_\mathrm{p}} \int_{t_\mathrm{p}}^{T_\mathrm{s}} \left(\Delta W_\mathrm{k}(t)\right)^2 dt} \tag{76}$$

$$C_\mathrm{h} = \frac{\Delta W_{\mathrm{h,rms}}}{\Delta W_{\mathrm{h,rms}} + \Delta W_{\mathrm{k,rms}}} \tag{77}$$

$$C_\mathrm{k} = \frac{\Delta W_{\mathrm{k,rms}}}{\Delta W_{\mathrm{h,rms}} + \Delta W_{\mathrm{k,rms}}} \tag{78}$$

where t_p is the time of the perturbation onset and W_h and W_k are the active work performed on each joint.

To quantitatively compare the effects that the leg's test variables have on χ, we then performed a series of experiments in which perturbations were applied at three phases of swing commonly used in clinical testing of humans—early swing ($\phi_\mathrm{p} = 15\%$), mid-swing ($\phi_\mathrm{p} = 40\%$), and late swing ($\phi_\mathrm{p} = 65\%$) [106]. In these experiments, only the six test variables and the value of ϕ_p were varied; the perturbation magnitude and duration were fixed at 20 N and 100 msec, respectively. We swept each of the test variables and selected the values that minimized the average value of χ obtained for each of the three phases.

4.3 Results

During steady-state swinging, the values of $\omega_{\mathrm{hco,h}}$, $G_{\mathrm{ff,h}}$ and $G_{\mathrm{ff,k}}$ had the largest effect on system performance. Although active knee control improved the performance range of the system, it also reduced both energy efficiency and stability. During perturbed swinging, active knee control improved perturbation rejection by up to 20.4%, with the most significant improvements occurring for early-swing perturbations.

4.3.1 Steady-State Swinging

The benefits of using active knee control in unperturbed leg swinging are: 1) the system can move between in-phase and out-of-phase modes, 2) the ranges of achievable system frequencies and stride times are improved, and 3) the active hip torque that is required to maintain constant-magnitude oscillations is reduced. However, the disadvantages are substantial: 1) the minimum achievable energetic cost is increased, and 2) the range of

Criterion	Variable	Passive-Knee	Active-Knee	Unit
System Frequency	ω_{sys}	3.88	3.84	rad/sec
Inter-Joint Phase Angle	ϕ_{sys}	0.67	0.61	rad
Energetic Cost of Leg Swinging	σ	0.057	0.086	-
Maximum Floquet multiplier	λ_{max}	0.87	0.85	-
Stride Time	T_{s}	0.86	0.87	sec
Stride Length	L_{s}	0.44	0.50	m

Table 11: Performance criteria of steady-state swinging leg with canonical parameter values.

hip actuation gains that produce stable oscillations is reduced (for a given value of knee actuation gain).

The system performance is significantly influenced by the actuation gains ($G_{\text{ff,h}}$ and $G_{\text{ff,k}}$) and, to a lesser extent, by the hip HCO natural frequency ($\omega_{\text{hco,h}}$). The system is relatively insensitive to changes in the knee HCO natural frequency ($\omega_{\text{hco,k}}$) and to the feedback gains ($G_{\text{fb,h}}$ and $G_{\text{fb,k}}$) provided that the feedback gains are not close to zero. The canonical values of the performance criteria are given in Table 11.

4.3.1.1 Effect of HCO Natural Frequency

The effects of $\omega_{\text{hco,h}}$ and $\omega_{\text{hco,k}}$ on the leg's unperturbed performance criteria are shown in Figure 44. Stable, resonance-tuned leg oscillations were obtained for $\omega_{\text{hco,h}}$ values in the range of 0.7 to 4.1 rad/sec. The system was found to be significantly more robust to changes in the value of $\omega_{\text{hco,k}}$, with acceptable values ranging from 0.5 to 60.2 rad/sec. (Figure 44 only displays $\omega_{\text{hco,k}}$ in the range from 0.0 to 5.0 rad/sec.) All stable frequency-locked oscillations corresponded to resonance-tuned behavior because all values of ω_{sys} were within 8.0% of $\omega_{\text{n}} = 4.0$ rad/sec, the leg's natural (resonant) frequency (see Figure 44). At all edges of the stable region, stability was lost when $\omega_{\text{hco,k}}$ deviated from the frequency of the remaining three oscillators. The cause of the deviation was that the leg-swing amplitude (*i.e.,* stride length) reduced to such an extent that the value of θ_{k} remained at all times significantly below $\theta_{\text{ab,k}}$. When this occurs, the joint-angle feedback to the knee HCO becomes largely asymmetric, and one of the HCO's "neurons" continuously receives high levels of excitatory feedback. Eventually, the asymmetric feedback drives the HCO to a non-oscillating state in which the output signal becomes a constant. To increase the size of

Effects of $\omega_{\text{hco,h}}$ and $\omega_{\text{hco,k}}$ on Active-Knee Swinging Performance
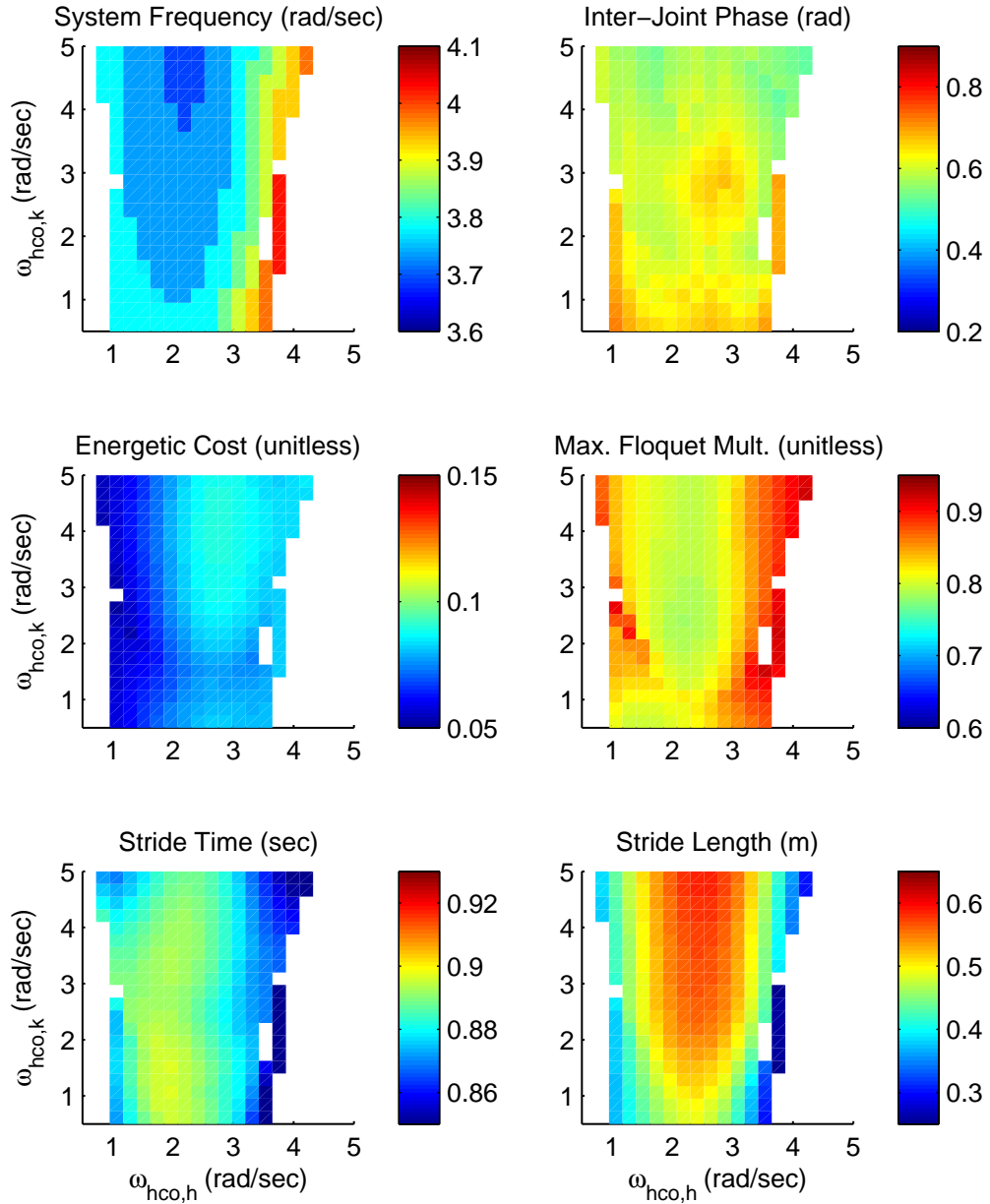
Figure 44: Effects of the hip and knee HCO natural frequencies, $\omega_{\text{hco,h}}$ and $\omega_{\text{hco,k}}$, on the active-knee leg's system frequency (top left), inter-joint phase angle (top right), energetic cost (middle left), maximum Floquet multiplier (middle right), stride time (bottom left), and stride length (bottom right). (The display ranges for certain criterion appear too wide because they were chosen to be consistent with those of Figures 46 and 48.)
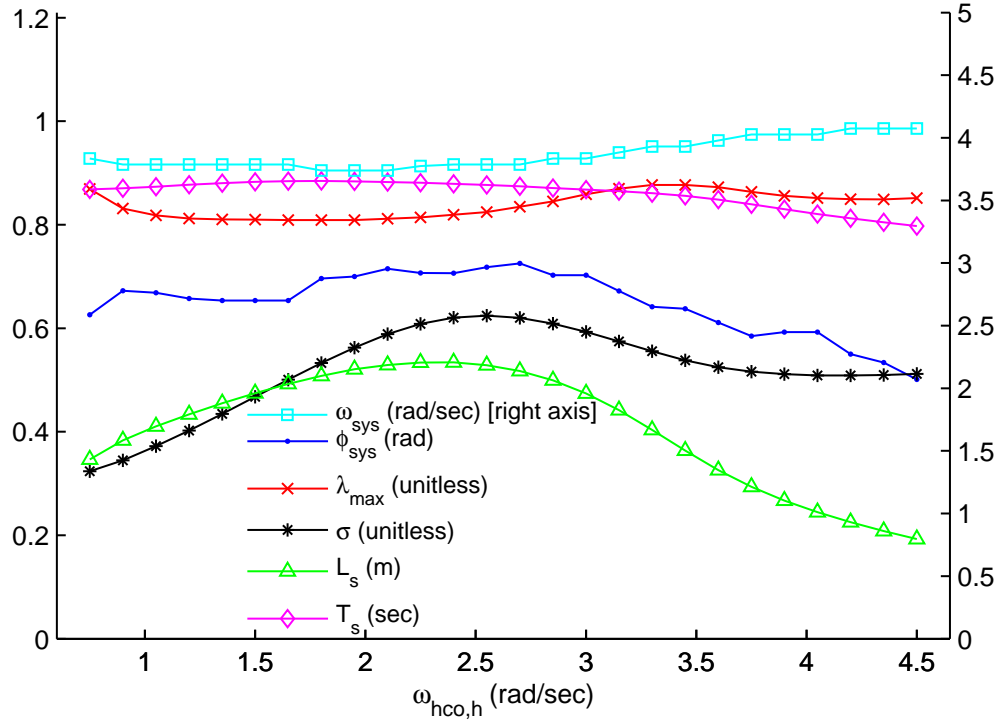
Figure 45: Effects of the hip HCO natural frequency, $\omega_{hco,h}$, on the six performance criteria of unperturbed leg swinging. Each criterion produces similar behavior to the active-knee case, reinforcing the point that leg swinging performance is insensitive to the knee HCO natural frequency, $\omega_{hco,k}$. (The criterion ω_{sys} uses the *right* vertical axis, and all other criteria use the *left* vertical axis.)

the stable region, the value of $G_{fb,k}$ can be decreased, which reduces the magnitude of the feedback signal, thereby limiting its ability to drive the HCO toward a non-oscillating state (data not shown).

Only σ and L_s exhibited significant changes over the entrainment region, with maximum deviations from their canonical values of 44.2% and 39.1%, respectively, occurring when $\omega_{hco,h} = 2.53$ rad/sec. The maximum canonical-value deviations of the remaining performance criteria were 5.0% for ω_{sys}, 3.9% for ϕ_{sys}, 8.6% for λ_{max}, and 5.9% for T_s. The value of $\omega_{hco,k}$ had little effect on system performance.

This experiment was repeated for the passive-knee version of the leg. The data (Figure 45) reveal that resonance tuning was produced for a similar range of hip HCO frequencies ($\omega_{hco,h} = 0.8 - 4.4$ rad/sec). The boundaries of this region are determined by the strength

of the feedback signal, $G_{\text{fb,h}}$, and the magnitude of the stride length. At low values of $\omega_{\text{hco,h}}$, the difference between $\omega_{\text{hco,h}}$ and ω_{n} was too significant for the feedback gain to maintain frequency lock and, as a result, the hip HCO output signal was driven to a non-oscillating state. The lower boundary can be reduced (*i.e.,* improved) by increasing $G_{\text{fb,h}}$ (data not shown). At high values of $\omega_{\text{hco,h}}$, the stride length falls below the minimum value we require for normal leg swinging (0.20 m). The higher boundary can be increased (*i.e.,* improved) by increasing $G_{\text{ff,h}}$ (data not shown).

As with the active-knee case, the system frequency was resonance tuned for all frequency-locked operating points. Additionally, the energetic cost and stride length were the only criteria to produce significant ($> 10\%$) variations from their canonical values. The maximum canonical-value deviations for the passive-knee case (and their changes from the active-knee case) were: 43.7% for E, 56.6% for L_{s}, 4.9% for ω_{sys}, 6.9% for ϕ_{sys}, 6.9% for λ_{max}, and 7.8% for T_{s}.

4.3.1.2   Effect of Actuation Gain

The most significant effects on the unperturbed system's performance criteria were produced by the feed-forward (actuation) gains ($G_{\text{ff,h}}$ and $G_{\text{ff,k}}$) (Figure 46). As with the previous experiment, the left boundary of the stable region resulted from loss of frequency lock with the knee HCO. In contrast to the previous experiment, the right boundary resulted from *excessive* stride length (> 0.65 m). Both test variables ($G_{\text{ff,h}}$ and $G_{\text{fb,k}}$) were strongly correlated with all six performance metrics, indicating that hip control does not necessarily dominate the performance aspects of this system.

The *system frequency* remained within 6.2% of ω_{n} for the entire frequency-locked region. A slight decrease in ω_{sys} occurred as either $G_{\text{ff,h}}$ or $G_{\text{fb,k}}$ was increased because the natural frequency of the HCOs ($\omega_{\text{hco,h}} = \omega_{\text{hco,k}} = 3.1$ rad/sec) was lower than that of the leg ($\omega_{\text{n}} = 4.0$ rad/sec). Therefore, higher feed-forward gains increased the influence of the HCOs on ω_{sys} and cause a modest frequency reduction.

The *inter-joint phase* showed a strong correlation to the ratio of $G_{\text{ff,h}}$ to $G_{\text{fb,k}}$: ϕ_{sys} was maximized (0.89 rad) when $G_{\text{ff,h}}$ was large (8.0 Nm) and $G_{\text{ff,k}}$ was small (0.0 Nm), and ϕ_{sys}
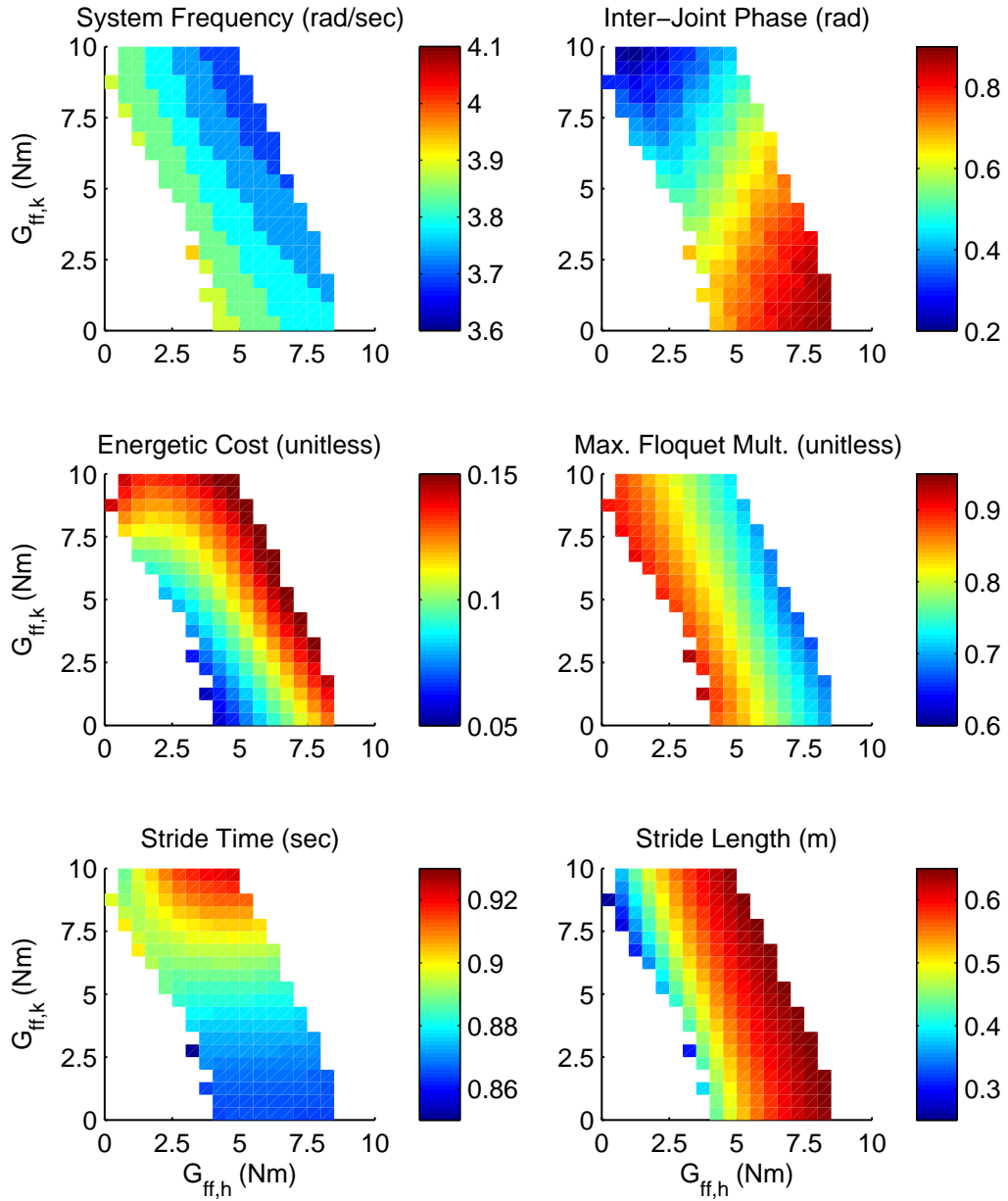
Figure 46: Effects of the feed-forward (actuation) gains, $G_{\mathrm{ff,h}}$ and $G_{\mathrm{ff,k}}$, on the active-knee leg's system frequency (top left), inter-joint phase angle (top right), energetic cost (middle left), maximum Floquet multiplier (middle right), stride time (bottom left), and stride length (bottom right). The effects of each criterion are significantly higher than those resulting from changes to $\omega_{\mathrm{hco,h}}$ or $\omega_{\mathrm{hco,k}}$. Furthermore, the criteria are sensitive to changes in both hip and knee feed-forward gains, indicating that active knee control has a significant influence on system dynamics.

was minimized (0.17 rad) when $G_{\mathrm{ff,h}}$ was small (0.5 Nm) and $G_{\mathrm{ff,k}}$ was large (10.0 Nm). This behavior indicates that two operating modes exist for leg swinging depending on whether the leg is hip-driven or knee-driven. Strong hip drive tends to produce an out-of-phase relationship between the joints in which the knee lags the hip by just over $\pi/4$ rad; strong knee drive tends to produce a nearly in-phase relationship between the joints.

The *energetic cost* was directly correlated to both $G_{\mathrm{ff,h}}$ and $G_{\mathrm{ff,k}}$. A linear relationship existed ($R^2 = 0.99$) between $G_{\mathrm{ff,h}}$ and energetic cost for $G_{\mathrm{ff,k}} < 7.5$ Nm. Similarly, a linear relationship existed ($R^2 = 0.99$) between $G_{\mathrm{ff,k}}$ and energetic cost for all tested values of $G_{\mathrm{ff,h}}$. The linear relationships arise because energetic cost is proportional to active torque, and active joint torque is scaled by feed-forward gain.

The *maximum Floquet multiplier* was inversely related to energetic cost—increasing the value of either $G_{\mathrm{ff,h}}$ or $G_{\mathrm{ff,k}}$ decreased $\lambda_{\max}$ (*i.e.,* moved the system further from instability). Therefore, the more energetically efficient the system performed, the closer to instability it operated. Because of this relationship, we found that, for a given value of $G_{\mathrm{ff,h}}$, increasing $G_{\mathrm{ff,k}}$ reduces the system's $\lambda_{\max}$. Despite the theoretical usefulness of calculating $\lambda_{\max}$, however, this quantity was not particularly significant in these unperturbed experiments because the system never achieved oscillatory instability (*i.e.,* $\lambda_{\max}$ never reached unity). Instead, one of three alternative sources of failure occurred first. The three causes of failure were: 1) cessation of oscillatory output signals in one of the HCOs, 2) insufficient stride length (< 0.2 m), or 3) excessive stride length (> 0.65 m).

The *stride time* was primarily a function of $G_{\mathrm{ff,k}}$ (although $G_{\mathrm{ff,h}}$ played a small role). At low levels of $G_{\mathrm{ff,k}}$, T_{s} was reduced because 1) the system frequency decreased (*i.e.,* system period increased) and 2) the knee swung with increased phase delay. The larger phase delay acts to reduce swing time by increasing the amount of kinetic energy impulsively delivered to the thigh when the knee reaches its hard stop during forward swing. The impulsive force assists the thigh in quickly reaching its maximum angle and, therefore, the end of forward swing. The range of stride time variations in this experiment was limited to 77 msec.

The *stride length* varied in a manner similar to energetic cost. The value of L_{s} was linearly related to $G_{\mathrm{ff,k}}$ ($R^2 = 0.99$) and directly, though not linearly, related to $G_{\mathrm{ff,h}}$. As

Effects of $G_{\mathrm{ff,h}}$ on Passive-Knee Swinging Performance
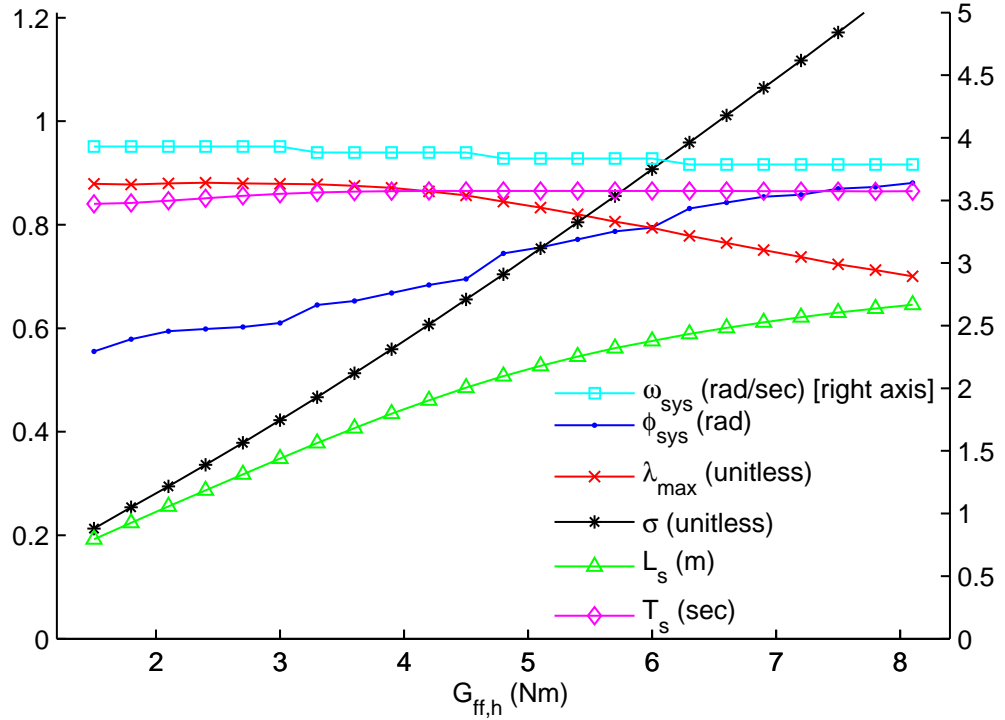
Figure 47: Effects of hip feed-forward (actuation) gain, $G_{\mathrm{ff,h}}$ on the six performance criteria of unperturbed leg swinging. As compared to the active-knee case, the size of the stability region improved and the performance criteria followed similar trends. (The criterion ω_{sys} uses the *right* vertical axis, and all other criteria use the *left* vertical axis.)

with the energetic cost, these relationships are a result of the feed-forward gains scaling the active torque applied to the joints because increasing active torque at either joint extends the distance that the CoM swings.

The results for sweeping $G_{\mathrm{ff,h}}$ in the passive-knee leg (Figure 47) show that the left boundary of the stability region was lowered (*i.e.*, improved) when knee actuation was removed. The boundary moves because the passive-knee system does not require that the knee HCO maintain frequency lock with the remaining oscillators. Therefore, the primary cause of instability when $G_{\mathrm{ff,h}}$ is low was removed. The performance criteria varied in much the same manner as in the active-knee leg. Higher values of $G_{\mathrm{ff,h}}$ produced: 1) slight reductions in system frequency, 2) increased phase difference between the joint angles, 3) increased system stability (*i.e.*, decreased λ_{max}), 4) linearly increasing energetic cost,

Criterion	Variable	Passive-Knee	Active-Knee
Δ Mechanical Energy	ΔE	-17.2%	-11.3%
Δ Energetic Cost of Forward Leg Swing	$\Delta \sigma_{\mathrm{f}}$	0.0%	-0.2%
Δ Stride Time	ΔT_{s}	5.5%	4.2%
Δ Stride Length	ΔL_{s}	-4.4%	-2.7%

Table 12: Performance criteria of perturbed leg swing with canonical parameter values.

5) increasing stride length, and 6) approximately constant stride time.

4.3.1.3 Effect of Feedback Gain

Relative to the actuation gains, the feedback gains ($G_{\mathrm{fb,h}}$ and $G_{\mathrm{fb,k}}$) had only modest influence on system performance (Figure 48). The stability region covered the entire non-zero range of tested gain values, indicating that the only system requirement is that the gains be large enough to achieve resonance tuning. Significant variations in σ, λ_{max}, and ϕ_{sys} of up to 34.6% occurred for low-gain values, but these variations were reduced to less than 10% for feedback gains larger than 2.5 rad^{-1}. The results for sweeping $G_{\mathrm{fb,h}}$ in the passive-knee were qualitatively similar to those of the active-knee leg (data not shown).

4.3.2 Perturbation-Rejection Analysis

Active knee control improved the leg's perturbation response in all tested cases. Comparison of the phase-dependent response of the system demonstrated that similar performance trends existed for the active and passive knee control, but the average perturbation response was improved by 20.4% in the active-knee case. In both cases, increasing the actuation gain(s) produced substantial decreases (improvements) to the perturbation response because these gains increase stride length, and stride length is indirectly correlated with the perturbation response magnitude. The canonical values of the perturbation-analysis performance criteria are given in Table 12.

4.3.2.1 Phase-Dependent Response with Passive Knee

The phase- and magnitude-dependent responses of the passive-knee leg to perturbations are shown in Figure 49. For all perturbation response criteria, a behavioral bifurcation occurred when the perturbation application phase (ϕ_{p}) reached 45%, which corresponded
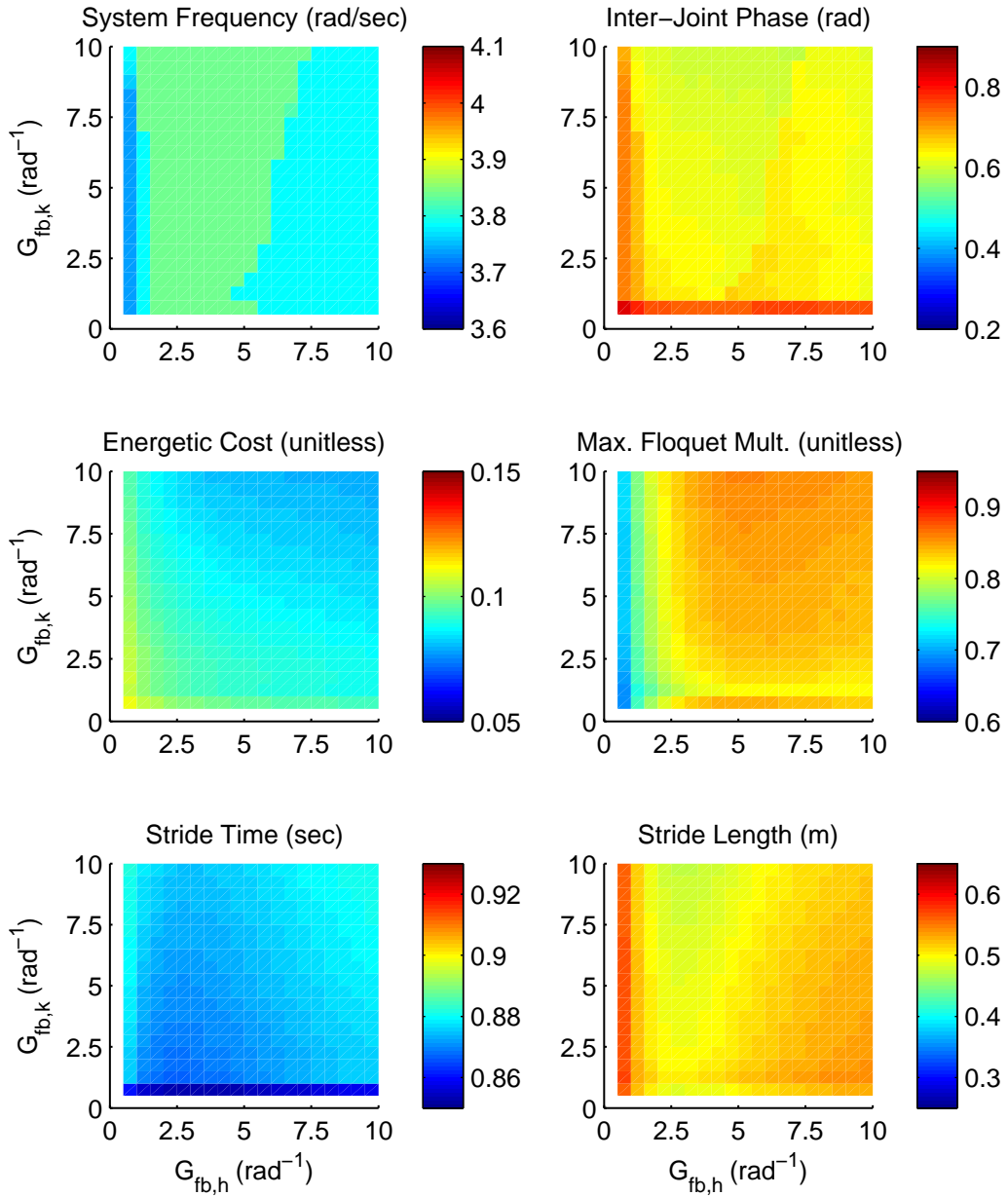
Figure 48: Effects of the feedback gains, $G_{\mathrm{fb,h}}$ and $G_{\mathrm{fb,k}}$, on the active-knee leg's system frequency (top left), inter-joint phase angle (top right), energetic cost (middle left), maximum Floquet multiplier (middle right), stride time (bottom left), and stride length (bottom right). The only significant influence that these gains had on system performance occurred when the gains were near zero.

Perturbation Response with Passive Knee
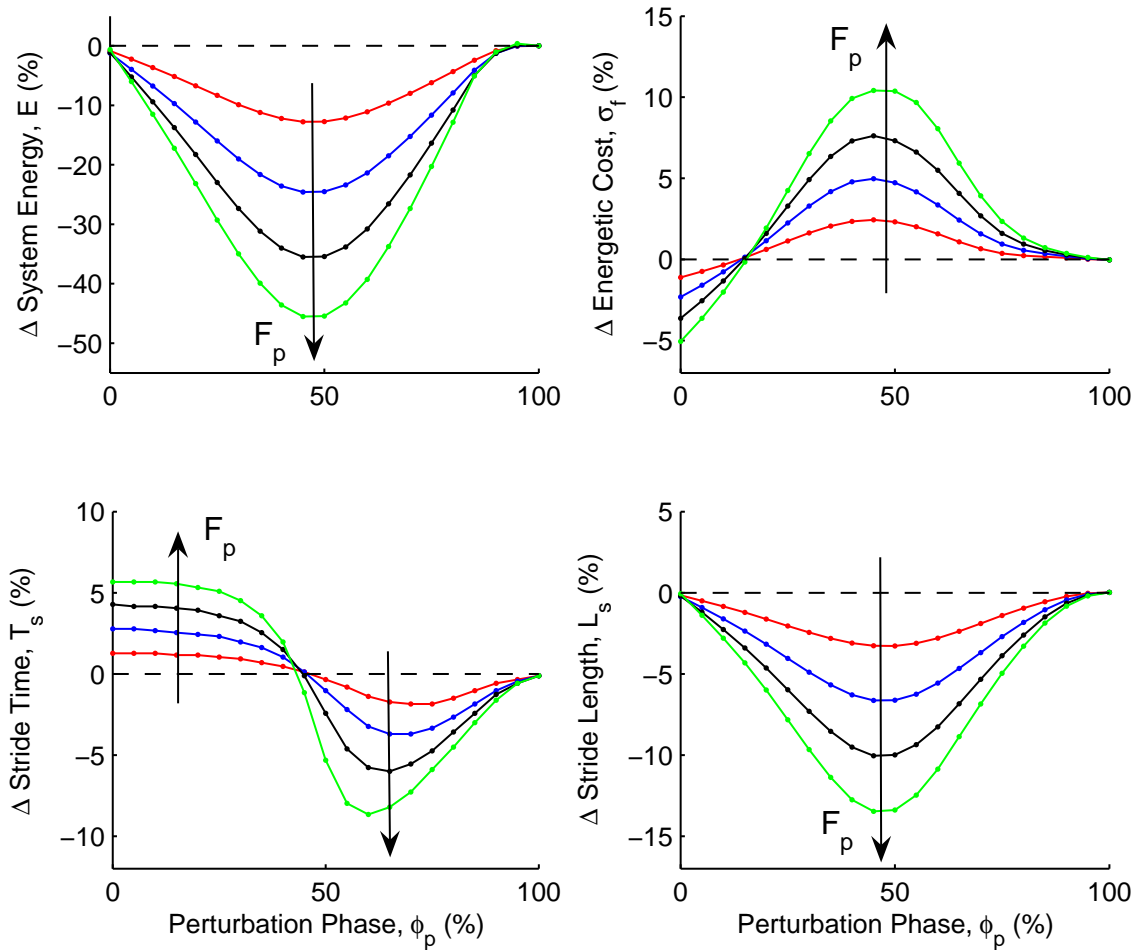
Figure 49: Effect of perturbation magnitude (F_p) and phase (ϕ_p) on the following *passive-knee* system performance metrics: the change in system energy at the end of forward swing (top left), the change in the energetic cost of forward leg swinging (top right), the change in stride time (bottom left), and the change in stride length (bottom right). The arrows indicate the direction of increasing F_p from 5.0 to 20.0 N in increments of 5.0 N. The value of ϕ_p was calculated as a percentage of the unperturbed stride time.

to θ_h becoming zero. For the standard perturbation of 20 N, the maximum changes in performance criteria values (from Figure 49) were -45.5% for E, 10.4% for σ_f, -8.7% for T_s, and -13.5% for L_s. For a given value of ϕ_p, all performance criteria were directly related to the perturbation magnitude (F_p).

System energy was reduced for all perturbations because the perturbation force was directed toward the posterior direction, producing negative work on the leg. Energy loss was directly related to F_p because the amount of negative work performed on the system is proportional to F_p. Energy loss was maximized when the perturbation force was applied at approximately mid-swing ($\phi_p = 45\%$) because at this point the leg's moment arm was maximized and the perturbation force was approximately parallel (with opposite direction) to the leg's CoM trajectory. At earlier or later phases, the magnitude of energy loss was reduced because a trigonometric relationship exists between the horizontal perturbation force and the resulting perturbation torque (due to the changing vertical distance between the hip and ankle).

The *energetic cost of forward leg swing* was reduced for $\phi_p \leq 15\%$ and increased for all other phases. The early-swing cost reduction occurred because the perturbation force hyperflexed the knee without performing significant negative work on the leg (due to the small vertical moment arm). Knee hyperflexion is energetically beneficial because it decreases the leg's MoI, which reduces the amount of actuator torque that is required to accelerate the leg. Beyond early swing, the primary effect of the perturbation force is to reduce the leg's mechanical energy level; the perturbation's effect on knee flexion is less significant. To compensate for energy loss, the hip actuator injects additional energy into the system, resulting in an energetic cost increase.

Stride time was increased for $\phi_p \leq 40\%$ and was decreased otherwise; *stride length* was reduced for all perturbations. To explain this behavior, we describe the performance of the system when perturbations were applied at early ($\phi_p = 15\%$) and late ($\phi_p = 60\%$) swing. An *early-swing perturbation* increases knee flexion and slightly decelerates the leg. As swing progresses, the leg swings forward slowly while the knee extends quickly. Eventually, the knee reaches full extension and kinetic energy is transferred from the shank to the thigh,

causing the leg to quickly reach the end of its stride. The slow movement during mid-swing causes the stride time to increase, but the kinetic energy transfer during late swing minimizes the reduction in stride length. At the onset of a *late-swing perturbation*, the knee has approximately reached full extension, and the level of kinetic energy in the leg is minimal. When the perturbation is applied, negative work further reduces kinetic energy, causing the hip's angular velocity to reverse direction, which, by definition, ends the stride. Therefore, the effect of a late-swing perturbation is to prematurely terminate normal leg swing, causing a decrease in both stride time and stride length.

4.3.2.2 Phase-Dependent Response with Active Knee

Active knee control reduced the magnitude of the perturbations' effect on all performance criteria (Figure 50) by the following amounts: 9.9% for E, 29.3% for σ_f, 47.1% for T_s, and 17.8% for L_s. The qualitative trends in the performance criteria in Figure 50 closely matched those of the passive-knee case (Figure 49) with one exception: the energetic cost increase that occurred for $\phi_\mathrm{p} > 15\%$ transitioned from one large peak at $\phi_\mathrm{p} = 45\%$ to two smaller overlapping peaks that produced a cost increase over a wider range of ϕ_p. The cause of this effect was that the magnitude of the hip response (*i.e.,* the original peak at $\phi_\mathrm{p} = 45\%$) was reduced and the active knee response added a second component to the energetic cost that peaked at $\phi_\mathrm{p} = 70\%$.

To quantitatively compare the effects of active and passive knee control, we sampled the values of the performance criteria in Figures 49 and 50 at early ($\phi_\mathrm{p} = 15\%$), mid- ($\phi_\mathrm{p} = 40\%$), and late ($\phi_\mathrm{p} = 60\%$) swing. The results (Figure 51) demonstrate that active knee control reduced the canonical value of the perturbation response (χ) by 20.4%. Improvements in specific criteria ranged from 15.8% to 32.9%, with the largest improvements occurring for energetic cost and stride time. When analyzed by phase, the largest improvement (32.4%) was seen in early swing.

The relative contributions of the hip and knee controller to the active-knee perturbation response (Figure 52) indicate that both joints significantly contribute to the response for much of the stride. The exception is very late swing during which the knee contribution

Figure 50: Effect of perturbation magnitude and phase on the following *active-knee* system performance metrics: the change in system energy at the end of forward swing (top left), the change in the energetic cost of forward leg swinging (top right), the change in stride time (bottom left), and the change in stride length (bottom right). The arrows indicate the direction of increasing F_p from 5.0 to 20.0 N in increments of 5.0 N. The value of ϕ_p was calculated as a percentage of the unperturbed stride time.
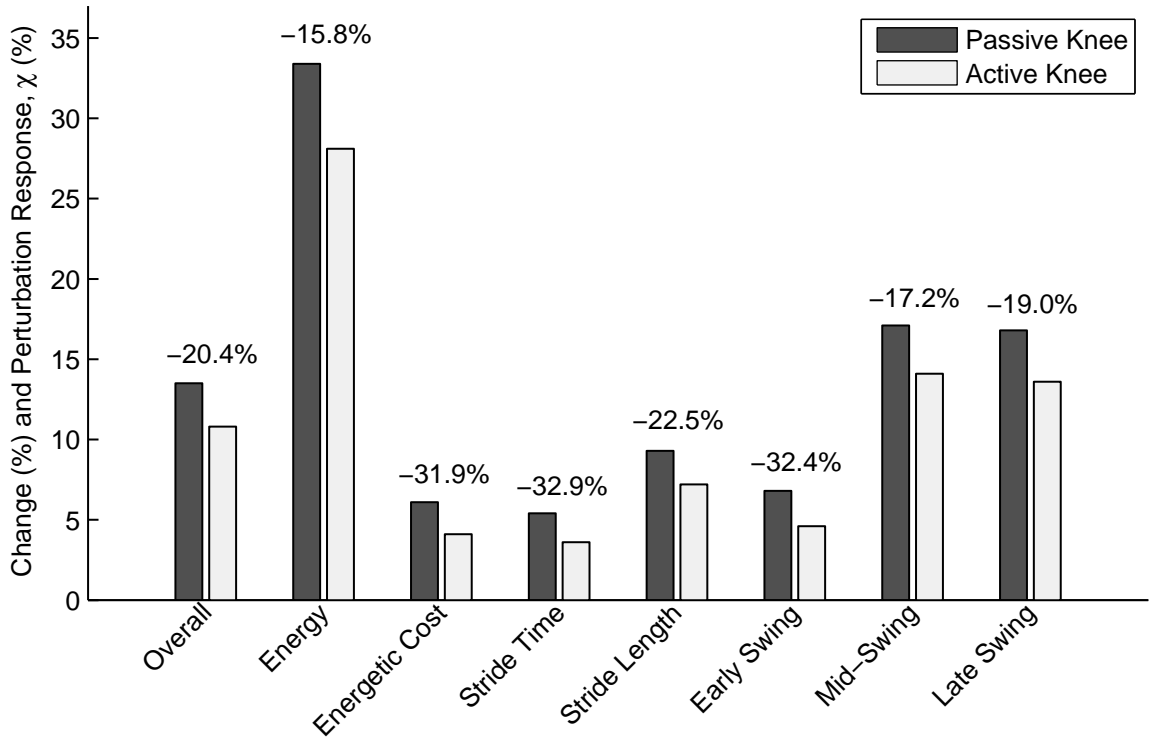
Figure 51: Improvement in perturbation rejection resulting from the use of an actively controlled knee. The overall improvement of 20.4% is broken down by individual performance criteria—energy change, energetic cost change, stride time change, and stride length change—and by perturbation phase—early swing, mid-swing, and late swing—using the 'Base Test' data from Table 13. The values used for the individual performance criteria were calculated by averaging the magnitudes of the performance change at early-, mid-, and late-swing for each criterion. The values used for the perturbation phases were calculated by averaging the change magnitudes of the four individual performance criteria for each phase. The percentages indicate the change (relative to the canonical, passive-knee case) of χ for 'Overall' and the three perturbation phases and of the individual performance criteria values otherwise.
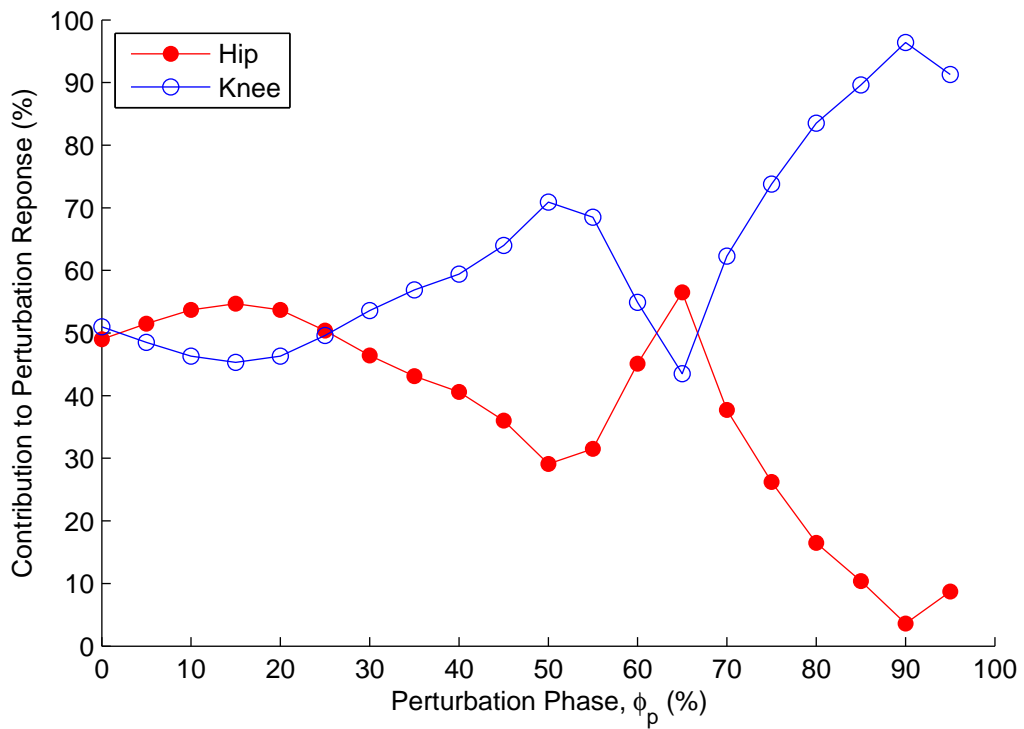
Figure 52: Relative contribution of the hip and knee to the perturbation response, indicating that the knee plays a substantial role in the response for all perturbation phases. (The two traces sum to 100% because the leg's perturbation response is completely determined by active joint control.)
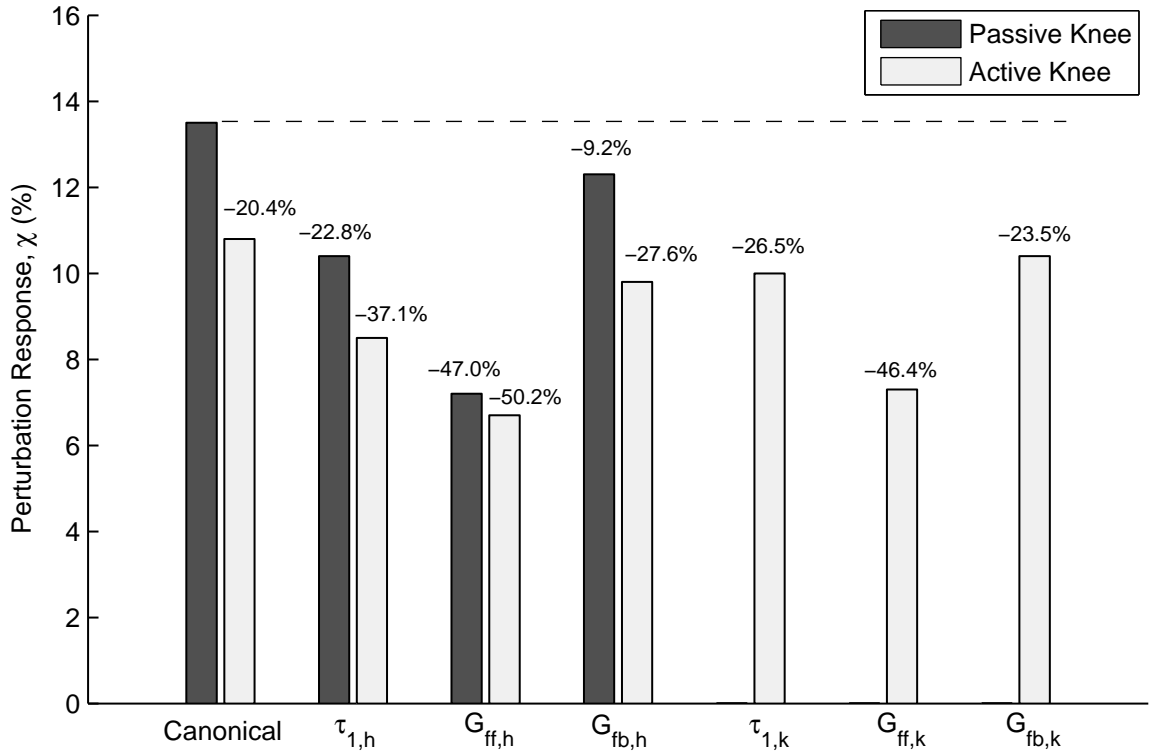
Figure 53: Improvement in perturbation response resulting from tuning the system's test variables. Each of the test variables was capable of improving the system's perturbation response relative to the canonical cases. The most significant perturbation rejection was achieved with high actuation gain. The percentages indicate the change in χ between the active- and passive-knee cases.

dominates the response. The late-swing effect correlates with the late-phase peak in the active-knee energetic cost (Figure 50).

4.3.2.3   Effect of Test Variables on Perturbation Response

In this experiment, the active- and passive-knee responses of the system to each of the test variables was examined. The results (Figure 53 and Table 13) indicate that the performance of both the active- and passive-knee swinging leg can be improved by tuning any of the variables, confirming that the canonical test variable values were not optimized. Even when using the optimized value of each test variable, the system consistently produced lower values of χ when active knee control was used. The largest reductions in χ (up to 50.2%) were produced by increasing the actuation gains because both gains increase stride

142

length, and stride length is indirectly correlated with χ. Large stride lengths reduce χ by increasing two of the denominators in Equation 74—the reference stride length (L_{ref}) and the reference energy (E_{ref}). (Stride length indirectly affects E_{ref} by altering the mechanical energy necessary to efficiently maintain high-amplitude leg oscillations.)

4.3.3 Robotic Leg Validation

As in Chapter 3, all analysis in this study was performed using our computational model of leg swinging (Section 2.2) because computational models are fast and provide a simpler means of analyzing the performance of this system. However, physical validation of the computational results is a crucial step in demonstrating that our results are applicable to real robotic systems. To validate our computational analyses for this study, we present sample robotic leg data for both steady-state (unperturbed) and perturbed leg swing experiments. Figure 54 replicates the results of Figure 46, which demonstrates that both $G_{\text{ff,h}}$ and $G_{\text{ff,k}}$ influence the swinging dynamics of the leg, and Figure 55 replicates the results of Figure 50, which demonstrates that the leg's perturbation response is a function of the perturbation magnitude, F_{p}, and application phase, ϕ_{p}. Although fewer data points are presented and the ranges of each test parameter are reduced (due to the physical limitations of the actuators), the qualitative trends match those of the computational model.

4.4 Discussion

The aim of this chapter was to determine how active knee control affects the performance of unperturbed and perturbed leg swing. In the unperturbed case, we varied the six control system parameters—the oscillator natural frequencies ($\omega_{\text{hco,h}}$ and $\omega_{\text{hco,k}}$), the actuation gains ($G_{\text{ff,h}}$ and $G_{\text{ff,k}}$), and the feedback gains ($G_{\text{fb,h}}$ and $G_{\text{fb,k}}$)—and analyzed performance based on six performance criteria—system frequency (ω_{sys}), inter-joint phase (ϕ_{sys}), energetic cost (σ), maximum Floquet multiplier (λ_{max}), stride time (T_{s}), and stride length (L_{s}). In the perturbed case, we varied the same control system parameters and analyzed performance based on four performance criteria—system energy (E), the energetic cost of forward leg swing (σ_{f}), T_{s}, and L_{s}. The perturbation response (χ) was calculated as a function of the change in value of these four criteria at the end of perturbed and unperturbed strides.

Knee Control	Test Var.	Units	Range Tested	Best Value	Δ Energy (%) Early	Mid	Late	Δ Energetic Cost (%) Early	Mid	Late	Δ Stride Time (%) Early	Mid	Late	Δ Stride Len. (%) Early	Mid	Late
Passive			Base Test		-17.2	-43.6	-39.3	-0.2	9.9	8.1	5.5	1.9	-8.7	-4.3	-12.8	-10.9
	$\omega_{hco,h}$	rad/sec	0.0–5.0	2.25	-12.2	-36.8	-28.5	0.9	6.7	7.3	4.2	2.5	-6.7	-2.8	-9.8	-7.0
	$G_{ff,h}$	Nm	0.0–10.0	7.5	-4.8	-28.1	-23.3	-1.3	5.4	4.0	2.4	1.7	-2.9	-0.9	-6.4	-4.9
	$G_{fb,h}$	rad^{-1}	0.0–10.0	10.0	-16.1	-41.2	-31.2	-0.3	11.4	8.6	5.1	2.5	-7.4	-3.9	-11.7	-8.0
Active			Base Test		-11.3	-37.7	-35.3	-0.3	6.1	6.0	4.2	2.7	-3.9	-2.6	-10.0	-9.1
	$\omega_{hco,h}$	rad/sec	0.0–5.0	2.25	-7.7	-32.6	-25.8	-0.3	3.9	6.4	3.1	2.4	-4.4	-1.6	-7.9	-6.0
	$G_{ff,h}$	Nm	0.0–10.0	7.0	-2.8	-26.8	-22.3	-3.1	3.8	3.9	2.5	1.6	-3.3	-0.5	-5.6	-4.6
	$G_{fb,h}$	rad^{-1}	0.0–10.0	10.0	-10.3	-35.8	-27.6	-0.8	6.3	7.1	3.9	2.7	-4.7	-2.3	-9.3	-6.7
	$\omega_{hco,k}$	rad/sec	0.0–5.0	5.0	-10.4	-36.3	-28.0	-3.0	3.0	10.7	3.4	1.6	-4.4	-2.4	-9.3	-6.9
	$G_{ff,k}$	Nm	0.0–10.0	10.0	-2.0	-26.6	-19.2	1.3	11.4	7.9	1.9	1.6	-4.3	-0.5	-6.0	-4.3
	$G_{fb,k}$	rad^{-1}	0.0–10.0	6.0	-11.6	-37.9	-29.9	0.0	6.3	6.6	4.3	2.8	-4.4	-2.7	-10.1	-7.6

Table 13: Perturbation responses to test variable variations. Percentages indicate the changes in criterion values relative to unperturbed values.

Robot: Effects of $G_{\text{ff,h}}$ and $G_{\text{ff,k}}$ on Active-Knee Swinging Performance
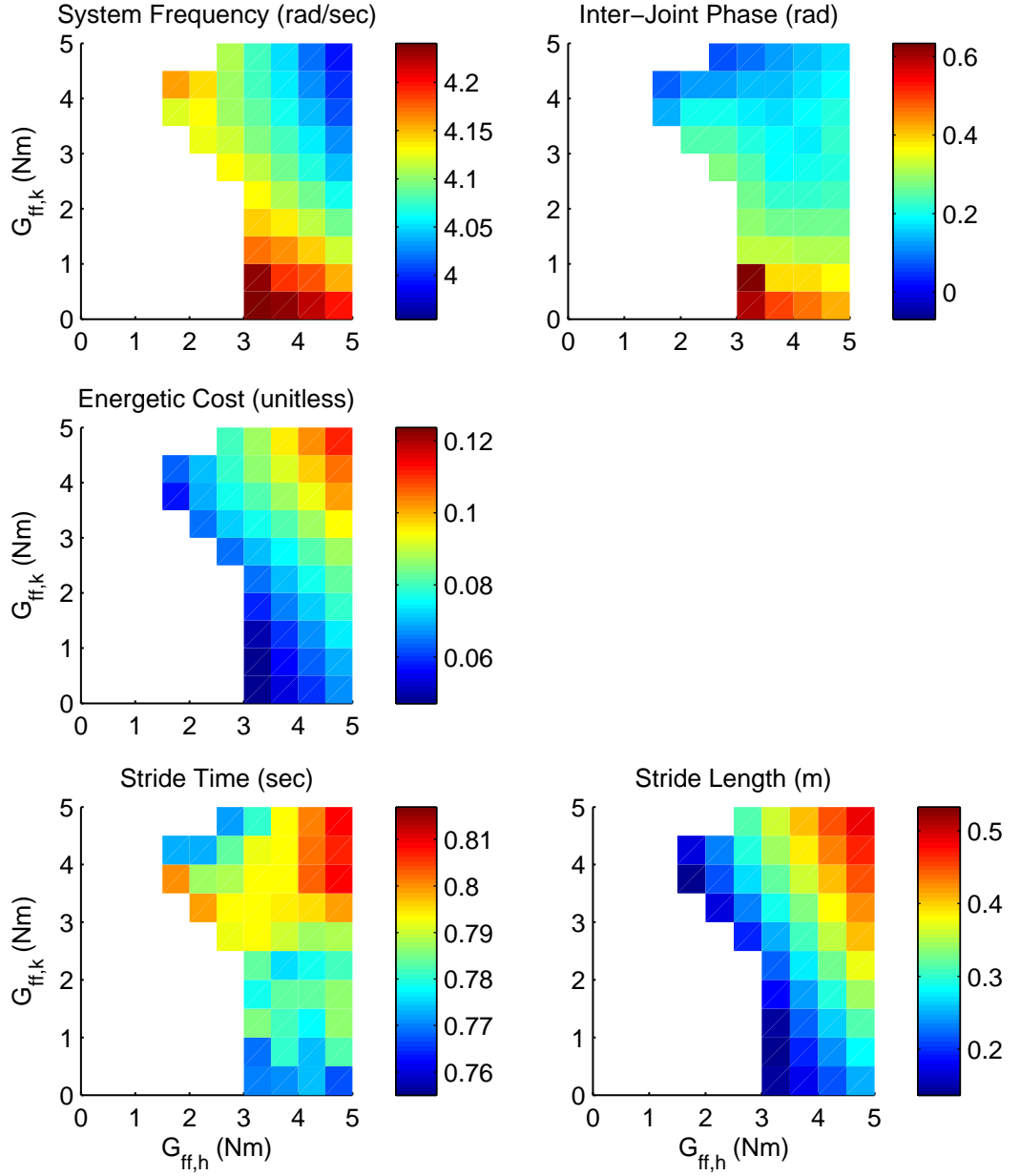
Figure 54: Robotic validation of data presented in Figure 46 demonstrating: 1) that ω_{sys} remained within 5.8% of its canonical value for all frequency-locked operating points, 2) that high ratios of $G_{\text{ff,h}}/G_{\text{ff,k}}$ produced knee-angle oscillation lag (relative to the hip angle) of up to 0.61 rad, and low ratios produced more in-phase relationships (ϕ_{p} reached values as low as 0.05 rad), 3) that E was directly related to both $G_{\text{ff,h}}$ and $G_{\text{ff,k}}$ and ranged between 0.05 and 0.11, 4) that T_{s} was maximized (0.81 sec) for high values of $G_{\text{ff,h}}$ and $G_{\text{ff,k}}$, and 5) that L_{s} was directly related to both $G_{\text{ff,h}}$ and $G_{\text{ff,k}}$ and ranged between 0.15 m and 0.47 m. (We did not calculate λ_{max} for the robotic leg because the technique is difficult to perform on a physical system [68].)
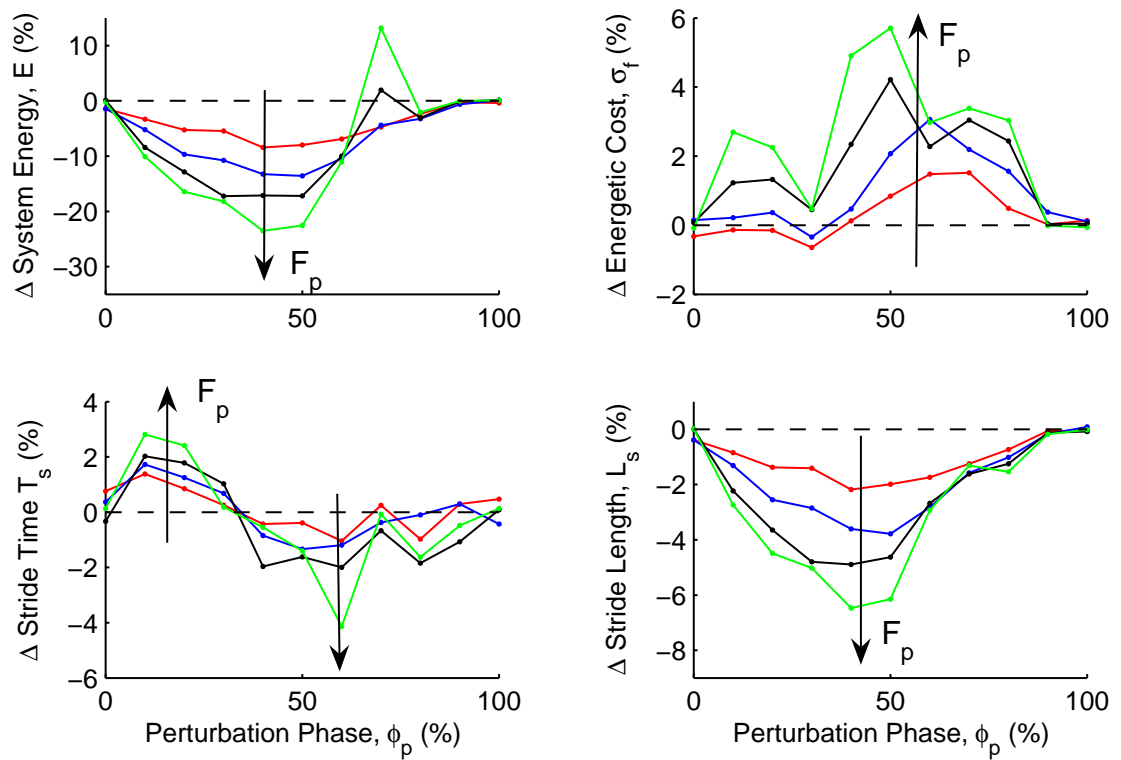
Figure 55: Robotic validation of data presented in Figure 50 demonstrating that the four perturbation response criteria varied in a manner qualitatively similar to the computational model (with the exception of some noisy data points).

We hypothesized that active knee control would decrease the energy efficiency of leg swinging without significantly improving performance because hip actuation is sufficient to achieve resonance-tuned oscillations in the absence of perturbations. We first confirmed that hip actuation alone was sufficient to produce stable, resonance-tuned leg swinging. We then analyzed the effect of active knee control on energetic cost and found that σ was linearly related to $G_{\mathrm{ff,k}}$ (*i.e.,* the level of active knee control), even when trials were normalized for L_{s}. (The value of σ was 33.0% higher in the canonical active-knee case than in the canonical passive-knee case.) Knee control did provide some small advantages: 1) the system's $\lambda_{\max}$ was reduced, 2) the system could move between in-phase and out-of-phase modes, 3) the achievable ranges of ω_{sys} and T_{s} were slightly improved, and 4) the active hip torque required to maintain constant-magnitude oscillations was reduced. Despite these advantages, we conclude that active knee control, in general, is disadvantageous in unperturbed dynamic walkers because the significant negative impact on energy efficiency is a more important design consideration than the minor performance improvements we achieved.

We also hypothesized that active knee control would reduce the effect of a swing-leg perturbation by distributing the perturbation's effect among both joints. We found that active knee control improved all four performance criteria, with an overall improvement to χ of 20.4%. In support of our hypothesis, we found that the relative contribution of the knee to χ was significant at all phases of swing ($C_{\mathrm{k}} = 51\%$ for early swing, $C_{\mathrm{k}} = 63\%$ for mid-swing, and $C_{\mathrm{k}} = 55\%$ for late swing).

The intent of this study was not to emulate the perturbation recovery techniques employed by humans because the human stumble response involves the production of complex, multi-step recoveries [18]. Rather, our intent was to analyze the efficacy of a simple, closed-loop knee controller in improving the perturbation responses of dynamic walking robots. Because these robots must maintain limit-cycle trajectories to avoid falling, they rely on the limited and prudent use of actuation to limit the magnitude of trajectory excursions. We contend that walking stability of these robots can be improved by moving from state-machine controllers to feedback-modulated controllers that can smoothly vary joint torques

147

in response to changing environmental conditions. To this effect, we have demonstrated that neurally-inspired oscillatory knee control can improve perturbation response in dynamic robots at a cost of decreased energy efficiency. The trade-off between stability and energy-efficiency that we encountered is consistent with that seen both in the human stumble response [20] and in toddlers learning to walk [42].

In the swinging-leg experiments, we determined stability by calculating the system's maximum Floquet multiplier. Stability, in this sense, is synonymous with perturbation rejection capability. When comparing the passive- and active-knee systems, however, we found that the active knee control only improved (decreased) $\lambda_{\max}$ by 2.6%. Rather than relying on the maximum Floquet multiplier, which is a theoretical measure of a system's ability to recover from infinitesimal disturbances, we chose to assess the leg's stability by measuring changes to practical performance measures, such as stride time, that can be directly correlated with robot falling. In contrast to the small stability improvement determined by the change in $\lambda_{\max}$, our results using the practical performance measure (χ) showed that active knee control (with canonical parameter values) improved stability by 20.4%. (The most significant improvement (32.9%) was achieved with the stride time criterion, which has been shown to be one of the most important factors in maintaining stability in limit-cycle walkers [46].) This technique of focusing on practical stability measures has been shown to predict the actual perturbation rejection ability of physical robots with higher accuracy than more theoretical measures such as the maximum Floquet multiplier [46].

In this study, we used the swinging-leg system to make predictions regarding the potential performance of walking robots. Although the stance phase of walking is used to set the initial conditions for the swing phase [78, 81], we made the assumption that modeling of the stance phase dynamics are not necessary to determine the relative perturbation response of the leg with passive and active knee control. This assumption was based on two factors. The first factor was that only swing-phase perturbations were considered, and the performance was assessed at the end of swing. Therefore, the stance phase of the ipsilateral leg was not relevant. The second factor was that the effect of the active perturbation response had minimal effect on the hip reaction forces, meaning that the dynamics of the swing leg

148

would not have significantly influenced the torso or contralateral leg of an actual walking robot. (The variation between the reaction forces in the canonical passive- and active-knee cases was less than 6.0%.)

In summary, we have examined the role of active knee control in dynamic walking robots by performing experiments on a single swinging leg. We have validated the following hypotheses: 1) knee actuation is detrimental to the control of unperturbed leg swinging because it increases energetic cost and provides only limited performance improvements and 2) knee actuation improves the swing-leg perturbation response of dynamic walking robots by distributing the response among both joints. Experiments were performed using a computational model and were validated using a full-scale robotic leg. Perturbation experiments focused on maintaining stable, limit-cycle behavior in robots rather than on producing human-like, multi-step stumble recoveries. The perturbation responses were calculated using practical, performance-based criteria such as stride time rather than using theoretical calculations such as the maximum Floquet multiplier. A design trade-off exists between energy efficiency and the degree of perturbation rejection. We suggest that a perturbation detection system may be useful in gating the knee actuation such that it is only active when necessary to maintain stability. Not coincidentally, the design of this system would closely resemble that of humans, which use cutaneous stimuli on the dorsum of the foot to trigger reflexes that conservatively actuate the knee (and other joints) in response to perturbations [53].

CHAPTER V

CONCLUSIONS

The primary theme of this dissertation is that the energy efficiency and stability of dynamic walking robots can be improved using components inspired by the reverse-engineering of biological systems. The field of autonomous walking robots has been dominated by trajectory-control approaches, but the development of these robots will eventually reach a performance ceiling set by practical limitations on the amount of computing hardware and energy storage systems that can be physically carried. The use of natural dynamics both as a energy-saving mechanism and as a source of control represents an alternative solution to the task of robot walking—and one that is founded on more elegant biological principles [81]. In this dissertation, we demonstrated that the energy efficiency and perturbation rejection capability (*i.e.,* stability) of dynamic walking robots can be improved using two biologically inspired components—passive joint stiffness and active knee control.

5.1 Project Summary

We began this work with the development of a simple swinging-leg model and its robotic and computational implementations (Chapter 2). Because our goal was to focus on the fundamental actuation and control principles for a central pattern generator (CPG)-driven dynamic robot, we chose to avoid using ground contact in our model. The rationale for this decision was that ground contact (and the accompanying stance-phase dynamics) would have unnecessarily complicated both implementations, and substantial effort would have been redirected from the project focus to the management of ground contact issues. Furthermore, we felt that despite the limited relationship between leg swinging and walking, at a minimum, our model provides a basis for making predictions about the benefit biologically inspired components may have on the swing-leg dynamics of walking robots.

The swinging-leg model (Section 2.1) consists of a double pendulum in which the mass properties of each segment are anthropomorphically matched to those of a female human.

Joints are driven by torques that supplement, rather than override, the leg's natural mechanical dynamics. To prevent knee hyperextension, a hard stop was used at the knee to provide an asymmetric limitation on knee angle. Closed-loop control was provided to each joint by Matsuoka half-center oscillators (HCOs) [72, 73] that used joint angle feedback to adjust their oscillation frequency to match the resonant frequency of the leg, a process called *resonance tuning*. Matsuoka HCOs were chosen because the have large stability regions when controlling multi-joint pendulums [32] and entrain quickly and robustly to the movements of multi-joint limbs [129, 6]. Inter-joint synchronization was provided by the mechanical coupling between the hip and knee joints, as in [129].

The model was computationally implemented (Section 2.2) using object-oriented C++, and separate objects were created for the mechanical system and the HCOs. The equations of motion for the mechanical system were developed using a symbolic mechanical engineering analysis tool called AUTOLEV.

The robotic implementation (Section 2.3) consisted of a custom-designed aluminum leg suspended at the hip from a fixed platform. Actuation was provided by low gear-ratio DC motors via steel transmission cables, and sensory information was provided by optical angle encoders at each joint. The HCO-based control system was developed on a computer using MATLAB's SIMULINK and interfaced with the leg via a dSPACE real-time I/O controller board. Passive viscoelastic properties were applied virtually to each joint by modeling the viscoelastic components and applying their effects using the actuators, a process called *virtual model control* [94, 95, 96].

The two primary performance measures that were used for steady-state leg swinging were energy efficiency and stability. To measure energy efficiency (Section 2.4.2), we adapted an existing quantity commonly applied to walking robots—the *specific cost of transport* [16]— to fit our application. This new quantity—the *specific cost of leg swinging*—is equal to the active energy injected into the leg by the motors[1] normalized by the leg's weight and stride length. (For simplicity, this quantity is referred to as *energetic cost* for the remainder of

---

[1]Active energy, in this case, is equal to the total mechanical energy injected by the motors into the leg less the energy injected to virtually model the passive viscoelastic components.

the chapter.) To measure stability (Section 2.4.3), we calculated the system's maximum Floquet multiplier, $\lambda_{\max}$, using an 11-dimensional Poincaré section.

The first scientific question we addressed was whether the energy efficiency of dynamic leg swinging could be improved by adding passive joint stiffness properties to the joints (Chapter 3). We used a simplified version of the leg model with no knee actuation so that comparisons could be made with current dynamic walkers, which have passive knees. We tested both joints of the leg with two types of passive stiffness components—constant stiffness springs and a physiologically based variable stiffness trajectory.

In support of our first hypothesis, we found that, for non-zero actuation bias angles, passive hip stiffness reduced energetic cost by countering the gravitational torque on the leg, thereby reducing the actuator load. The lowest energetic cost was produced with a low-gain, high-bias angle stiffness function that most closely resembles a constant torque. Our results indicate that the variable stiffness, which had a relatively low bias angle, increased energetic cost by only 10%; constant stiffness, which had a high bias angle, decreased energetic cost by 39%; and constant torque produced the largest energetic cost decrease (48%).

In support of our second hypothesis, we found that passive knee stiffness reduced energetic cost by promoting the transfer of kinetic energy between the shank and thigh during swinging. Shank-to-thigh energy transfer can be increased in two ways: 1) by increasing the shank's kinetic energy at knee extension and 2) by increasing the percentage of the shank's kinetic energy that is transferred to the thigh at knee extension. Regardless of whether the knee angle hard stop was used, the variable knee stiffness function provided the largest energetic cost reduction (66%). The large reduction was achieved because the variable function: 1) increased shank kinetic energy at knee extension by increasing the level of knee flexion (*i.e.,* potential energy) at the beginning of forward swing and 2) increased the energy transfer percentage by exponentially increasing the knee stiffness at knee extension. Substantial energetic cost reduction (48%) was also achieved using a constant knee stiffness function and the knee angle hard stop. Incidentally, the combined use of hip and knee stiffness produced *less* energetic cost reduction than the use of variable knee stiffness

only.

The second scientific question we addressed was whether the perturbation rejection capability of a dynamic walker could be improved by using actively controlled knees (Chapter 4). We specifically focused on the effect of a constant-force swing-leg perturbation that mimics the effect of tripping over a temporary obstacle. This question was approached by first analyzing the effect of active knee control on steady-state (unperturbed) leg swinging and then by assessing perturbation responses for a series of early-, mid-, and late-swing perturbations.

In support of our first hypothesis, we found that active knee control is detrimental in unperturbed leg swinging because it decreases energy efficiency without significantly improving performance (Section 4.3.1). To make this determination, we first demonstrated that hip actuation alone is sufficient to produce stable, resonance-tuned leg swinging. We then noted the following disadvantages: 1) energetic cost increases linearly with the level of active knee control (even when trials are normalized for stride length) and 2) active knee control reduces the range of hip actuation gain values that can produce stable oscillations. We also noted three, less-significant advantages provided by active knee control: 1) the system could move between in-phase and out-of-phase modes, 2) the achievable ranges of system frequency and stride time were slightly improved, and 3) the active hip torque required to maintain constant-magnitude oscillations was reduced. Despite these advantages, we conclude that active knee control, in general, is disadvantageous in unperturbed robotic systems because the significant negative impact on energy efficiency is a more important design consideration for autonomous walking robots than the minor performance improvements we achieved.

In support of our second hypothesis, we found that active knee control is beneficial when the leg is subject to swing-leg perturbations because the effects of the perturbations are distributed among both joints (Section 4.3.2). To assess perturbation response, we measured the average change, χ, of four quantities—the mechanical energy level of the system, the energetic cost of forward leg swing, the stride time, and the stride length—at

the end of perturbed and unperturbed strides. When the values of χ obtained for early-, mid-, and late-swing perturbations were averaged, we found that active knee control provided an overall perturbation response improvement (*i.e.,* reduction) of 20.4% over passive knee control. Among the three stride phases, the response was most improved for early-swing perturbations because the knee had additional time (before the end of stride) to actively counter the energetic loss produced by the perturbation. Additionally, we found that the relative contribution of the knee to χ was significant at all phases of swing (51% for early swing, 63% for mid-swing, and 55% for late swing).

5.2 Contributions

The contributions of this dissertation are:

- The development of a dynamic leg-swinging model that provides a simplified means of analyzing aspects of dynamic walking.

- The computational implementation of this model, which can perform repeatable experiments quickly and without physical limitations on actuators, sensors, or measurement techniques.

- The robotic implementation of this model, which can be used to physically validate computational results and to provide a means for the experimenter to physically interact with the leg. (In our experience, physical interaction is useful to gain an intuitive understanding of the system's dynamics and how they change following parameter variations or perturbations.)

- The demonstration that the energy efficiency of leg swinging can be improved by using passive elastic components at the joints in parallel with the actuators.

- The demonstration that active knee control can improve the ability of dynamic walkers to reject swing-leg perturbations.

5.3 Future Directions

The work performed in this dissertation is intended to be the first step of a long-term project to develop a "naturally actuated" biped walker. To achieve this long-term goal, several additional directions must be explored with the existing system and its future expansions.

The current experimental setup is well-suited for a variety of more complex experiments including the following expansions of this work:

Rigid Obstacle Perturbations. The horizontally directed, constant-force perturbations that were used in Chapter 4 can be replaced with collision forces that emulate the swing leg striking a rigid object such as a rock.

Feedback Signal Diversity. The types of feedback signals used by the HCOs can be diversified to include actuator torque level and joint angular velocity. Additionally, the use of positive feedback arrangements may be useful [126].

Phase-Dependent Reflexes. The constant-gain feedback signals used in this work can be replaced with phase-dependent neural reflexes to produce context-appropriate perturbation responses. For example, to emulate the human response, the swing leg should be lifted up and over obstacles encountered during early swing (to minimize the robot's loss of mechanical energy) and should be extended toward the ground in response to a late-swing obstacles (to quickly place the foot and avoid falling forward) [29].

With a thorough understanding of the swing-phase dynamics, ground contact can then be applied to the leg to introduce stance-phase dynamics. This process will be challenging because ground contact is difficult to model computationally [69, 70] and because a degree of freedom must be added to the robotic model to allow the hip to move vertically. Because falls will be possible in this system, stable rhythmic movements will be 1) harder to realize due to increased sensitivity to initial conditions and 2) easier to assess because the primary criterion will be whether or not a fall occurs. The addition of ground contact is a crucial step in the achievement of our long-term goal because it moves the system from an abstract representation of walking to a robot whose performance can be directly compared to that

of a walking human. Once stable, one-legged walking can be performed, a second leg can be constructed and the lower half of our robot should be capable performing stable, two-dimensional biped walking.

An interesting set of additional experiments that can be performed at any stage during development are those that replace the Matsuoka HCO-based control system with living neurons. At the time of writing, an effort was already underway to interface a culture of cortical neurons with the leg to explore whether the culture could "learn" to provide adaptive, real-time control. This effort represents one component of a broader project to develop a "smart" prosthetic that can be controlled using *in vivo* motor cortex activity.

The common theme in both this work and the proposed future work is that the performance of walking robots can be continuously improved by developments that lead them to be more human-like. By emulating the underlying dynamics of human movement rather than simply mimicking the observed kinematics, it is our hope that this work will contribute to the improved energy efficiency and stability of walking robots.

APPENDIX A

AUTOLEV SOURCE CODE

Autolev requires only one input file to run. Example files and a tutorial are included in the software distribution package. The input file can be divided into several sections that contain the following information:

Settings High-level settings such as computational precision and whether computational optimizations should be used.

Object Declarations Declarations of the Newtonian and other coordinate frames, rigid bodies, massless points, and massive particles.

Declarations of Variables and Parameters Declarations of motion variables and their derivatives (including state variables) and any parameters, such as masses and lengths of bodies.

Mass Properties Assignment of masses, centers of mass, and moments of inertia to bodies and points.

Geometry Relating Unit Vectors Definitions of how the local coordinate frames of each body are oriented.

Position Vectors Definition of the vectors between points (including body centers of mass).

Velocities Definition of angular velocities of each rotational joint and the overall velocities of each point in the system.

Forces / Torques Definitions of external forces and/or torques acting on the system. These forces can include friction, stiffness, damping, or the effects of actuators.

Equations of Motion Calls for Autolev to find the equations of motion given the provided system definitions.

Input Constants Assignments of the unit system, the integration constants, and the initial values of each state variable to be used during simulation.

Output Specification of which variables should be output to file and calls on Autolev to output simulation code in either C, MATLAB, or Fortran.

This is not an exhaustive list and additional sections may be added depending on the complexity of the system. The actual input file used for our system follows:

```
%       File:  swingingleg.al
%---------------------------------------------------------------------
%         Settings

AutoZ   ON       %enables intermediate variables to lower computational cost
Digits  10       %number of significant digits

%---------------------------------------------------------------------
%         Object declarations

Newtonian  N                  %Newtonian reference frame
Bodies     T, S               %thigh(T) and shank(S)
Points     H,K,A              %hip(H), knee(K), ankle(A)

%---------------------------------------------------------------------
%         Declarations of Variables and Parameters

MotionVariables'    qH'', qK''  %joint angles + 1st and 2nd derivatives

% all SPECIFIED parameters are defined later at simulation time
Specified       Mt              %thigh mass
Specified       Ms              %shank mass
Specified       Jt              %thigh moment of inertia (sagittal plane)
Specified       Js              %shank moment of inertia (sagittal plane)
Specified       Lt              %thigh length
Specified       Ls              %shank length
Specified       Lcmt            %thigh center of mass
Specified       Lcms            %shank center of mass
Specified       g               %gravitational acceleration
Specified       HIPTORQUE       %applied hip torque
Specified       KNEETORQUE      %applied knee torque

%---------------------------------------------------------------------
%         Mass and Inertia
%specify mass of each body
Mass    T = Mt
Mass    S = Ms

%specify inertia at each body's CoM
Inertia T, 0, 0, Jt Inertia S, 0, 0, Js

%---------------------------------------------------------------------
%         Geometry Relating Unit Vectors

Simprot(N, T, 3,  qH)   %assign qH as angle btw. Newtonian and thigh ref. frames
```

```
Simprot(T, S, -3, qK)    %assign qK as angle btw. shank and thigh ref. frames

%--------------------------------------------------------------------
%       Position Vectors
%assign the position of each point using specified lengths and body ref. frame vectors
P_H_K> = Lt * T1>
P_K_A> = Ls * S1>
P_H_To> = Lcmt * T1>
P_K_So> = Lcms * S1>

%--------------------------------------------------------------------
%       Velocities
%define angular velocity and angular acceleration of each joint
W_T_N> = qH' * T3>
W_S_T> = -qK' * S3>
ALF_T_N> = Dt(W_T_N>, N)
ALF_S_T> = Dt(W_S_T>, T)

%define the linear velocity and acceleration of each point
v_H_N> = 0>
a_H_N> = 0>
V2pts(N, T, H, To)
V2pts(N, T, H, K)
V2pts(N, S, K, So)
V2pts(N, S, K, A)

A2pts(N, T, H, To)
A2pts(N, T, H, K)
A2pts(N, S, K, So)
A2pts(N, S, K, A)

%--------------------------------------------------------------------
%      Forces / Torques

Gravity(g*N1>)                          %define the gravitational force
Torque_T> += HIPTORQUE*T3>              %define the applied hip torque
Torque(T/S, -KNEETORQUE*S3>)            %define the applied shank torque

%--------------------------------------------------------------------
%       Equations of Motion

Zero = Fr() + FrStar()                  %form the equations of motion
Kane()

%--------------------------------------------------------------------
%       Input Constants
%specify unit system, integration parameters and initial values of state vars

UnitSystem  kg, meter, sec Input tFinal=100, integStp=0.001, absErr=1.0E-10, relErr=1.0E-10

Input qH = PI/4 rad, qK = 0 rad Input qH' = 0 rad/sec, qK' = 0 rad/sec

%--------------------------------------------------------------------
%       Output

Output t sec, qH rad, qK rad           %quantities to be output during simulation
CODE Dynamics()  swingingleg.c         %generate C code
Save swingingleg.all                   %record Autolev responses during compilation
```

REFERENCES

[1] ABE, M. and YAMADA, N., "Modulation of elbow stiffness in a vertical plane during cyclic movement at lower or higher frequencies than natural frequency," *Exp. Brain Res.*, vol. 153, no. 3, pp. 394–399, 2003.

[2] AHLBORN, B., BLAKE, R., and MEGILL, W., "Frequency tuning in animal locomotion," *Zoology*, vol. 109, pp. 43–53, 2006.

[3] AZEVEDO, C., ANDREFF, N., and ARIAS, S., "BIPedal walking: From gait design to experimental analysis," *Mechatronics*, vol. 14, pp. 639–665, 2004.

[4] AZEVEDO, C., POIGNET, P., and ESPIAU, B., "Artificial locomotion control: From humans to robots," *Robot. Auton. Syst.*, vol. 47, pp. 203–223, 2004.

[5] BADJ, T. and BOWMAN, B., "Testing and modeling of spasticity," *Journal of Biomedical Engineering*, vol. 4, pp. 90–96, 1982.

[6] BAILEY, S., *Biomimetic Control with a Feedback Coupled Nonlinear Oscillator: Insect Experiments, Design Tools, and Hexapedal Robot Adaptation Results*. PhD thesis, Stanford Univ., July 2004.

[7] BARBEAU, H., MCCREA, D., O'DONOVAN, M., ROSSIGNOL, S., GRILL, W., and LEMAY, M., "Tapping into spinal circuits to restore motor function," *Brain Res. Rev.*, vol. 30, pp. 27–51, 1999.

[8] BELANGER, M. and PATLA, A., "Phase-dependent compensatory responses to perturbation applied during walking in humans," *J. Mot. Behav.*, vol. 19, pp. 434–453, 1987.

[9] BRINCKMANN, P., FROBIN, W., and LEIVSETH, G., *Musculoskeletal Biomechanics*. New York: Thieme, 2002.

[10] BROWN, T., "On the nature of the fundamental activity of the nervous centres; together with an analysis of rhythmic activity in progression, and a theory of the evolution of function in the nervous system," *J. Physiol.*, vol. 48, pp. 18–46, 1914.

[11] CANG, J. and FRIESEN, W., "Model for intersegmental coordination of leech swimming: Central and sensory mechanisms," *J. Neurophysiol.*, vol. 87, pp. 2760–2769, 2002.

[12] CAUX, S. and ZAPATA, R., "Modeling and control of biped robot dynamics," *Robotica*, vol. 17, pp. 413–426, 1999.

[13] CAVAGNA, G., HEGLUND, N., and TAYLOR, C., "Mechanical work in terrestrial locomotion: two basic mechanisms for minimizing energy expenditure," *Am. J. Physiol.*, vol. 233, pp. R243–R261, November 1977.

[14] CAVAGNA, G. and MARGARIA, R., "Mechanics of walking," *J. Appl. Physiol.*, vol. 21, pp. 271–278, 1966.

[15] CHAKAROV, D., "Study of the antagonistic stiffness of parallel manipulators with actuation redundancy," *Mech. Mach. Theory*, vol. 39, pp. 583–601, June 2004.

[16] COLLINS, S. and RUINA, A., "A bipedal walking robot with efficient and human-like gait," in *Proceedings of the 2005 IEEE International Conference on Robotics and Automation*, (Barcelona, Spain), pp. 1995–2000, April 2005.

[17] COLLINS, S., WISSE, M., and RUINA, A., "A 3-D passive-dynamic walking robot with two legs and knees," *Int. J. of Robotics Research*, vol. 20, no. 7, pp. 607–615, 2001.

[18] CORDERO, A., KOOPMAN, H., and VAN DER HELM, F., "Multiple-step strategies to recover from stumbling perturbations," *Gait and Posture*, vol. 18, pp. 47–59, 2003.

[19] CORDERO, A., KOOPMAN, H., and VAN DER HELM, F., "Mechanical model of the recovery from stumbling," *Biological Cybernetics*, vol. 91, pp. 212–220, 2004.

[20] CORDERO, A., KOOPMAN, H., and VAN DER HELM, F., "Energy analysis of human stumbling: the limitations of recovery," *Gait and Posture*, vol. 21, pp. 243–254, 2005.

[21] DAERDEN, F., *Conception and realization of pleated pneumatic artificial muscles and their use as compliant actuation elements*. PhD thesis, Vrije Universiteit Brussel, July 1999.

[22] DESAI, J. and HOWE, R., "Towards the development of a humanoid arm by minimizing interaction forces through minimum impedance control," in *Proceedings of the 2001 IEEE International Conference on Robotics and Automation*, (Seoul, Korea), pp. 4214–4219, May 2001.

[23] DIETZ, V., COLOMBO, G., and MÜLLER, R., "Single joint perturbation during gait: Neuronal control of movement trajectory," *Experimental Brain Research*, vol. 158, pp. 308–316, 2004.

[24] DIETZ, V., QUINTERN, J., BOOS, G., and BERGER, W., "Obstruction of the swing phase during gait: Phase-dependent bilateral leg muscle coordination," *Brain Res.*, vol. 384, pp. 166–169, 1986.

[25] DOKE, J., DONELAN, J., and KUO, A., "Mechanics and energetics of swinging the human leg," *J. Exp. Biol.*, vol. 208, pp. 439–445, 2005.

[26] DOLLAR, A. and HOWE, R., "Towards grasping in unstructured environments: Grasper compliance and configuration optimization," *Adv. Robotics*, vol. 19, no. 5, pp. 523–543, 2005.

[27] EKEBERG, Ö. and GRILLNER, S., "Simulations of neuromuscular control in lamprey swimming," *Phil. Trans. R. Soc. Lond.*, vol. 354, pp. 895–902, 1999.

[28] ENDO, G., NAKANISHI, J., MORIMOTO, J., and CHENG, G., "Experimental studies of a neural oscillator for biped locomotion with QRIO," in *Proceedings of the 2005 IEEE International Conference on Robotics and Automation*, (Barcelona, Spain), pp. 598–604, April 2005.

[29] ENG, J., WINTER, D., and PATLA, A., "Intralimb dynamics simplify reactive control strategies during locomotion," *J. Biomech.*, vol. 30, no. 6, pp. 581–588, 1997.

[30] ENGLISH, C. and RUSSELL, D., "Implementation of variable joint stiffness through antagonistic actuation using rolamite springs," *Mech. Mach. Theory*, vol. 34, pp. 27–40, 1999.

[31] ENGLISH, C. and RUSSELL, D., "Mechanics and stiffness limitations of a variable stiffness actuator for use in prosthetic limbs," *Mech. Mach. Theory*, vol. 34, pp. 7–25, January 1999.

[32] FERRIS, D., VIANT, T., and CAMPBELL, R., "Artificial neural oscillators as controllers for locomotion simulations and robotic exoskeletons," in *4th World Congress of Biomechanics*, (Calgary, Alberta), August 2002.

[33] FREEMAN, R., "Active suspension control via redundant actuation," in *Proceedings of the 2004 ASME Design Engineering Technical Conferences and Computer and Information in Engineering Conference*, (Salt Lake City, UT), September 2004.

[34] FUKUOKA, Y., KIMURA, H., and COHEN, A., "Adaptive dynamic walking of a quadruped robot on irregular terrain based on biological concepts," *Int. J. Control*, vol. 22, pp. 187–202, March-April 2003.

[35] FURUTA, T., TAWARA, T., OKUMURA, Y., SHIMIZU, M., and TOMIYAMA, K., "Design and construction of a series of compact humanoid robots and development of biped walk control strategies," *Robot. Auton. Syst.*, vol. 37, pp. 81–100, 2001.

[36] GARCIA, M., *Stability, Scaling, and Chaos in Passive-Dynamic Gait Models.* PhD thesis, Cornell University, January 1999.

[37] GORDON, A., HUXLEY, A., and JULIAN, F., "The variation in isometric tension with sarcomere length in vertebrate muscle fibers," *J. Physiol.*, vol. 184, pp. 170–192, May 1966.

[38] GOTTSCHALL, J. S. and KRAM, R., "Energy cost and muscular activity required for leg swing during walking," *J. Appl. Physiol.*, vol. 99, pp. 23–30, 2005.

[39] GRABOWSKI, A., ROBERTS, T., and KRAM, R., "Metabolic cost of generating muscular force in human walking: Insights from load-carrying and speed experiments," *J. Appl. Physiol.*, vol. 98, pp. 579–583, 2005.

[40] GUAN, L., KIEMEL, T., and COHEN, A., "Impact of movement and movement-related feedback on the lamprey central pattern generator for locomotion," *J. Exp. Biol.*, vol. 204, no. 13, pp. 2361–2370, 2001.

[41] HAESSIG, D. and FRIEDLAND, B., "On the modeling and simulation of friction," *Transactions of the ASME, Journal of Dynamic Systems, Measurement, and Control*, vol. 113, no. 3, pp. 354–362, 1991.

[42] HALLEMANS, A., AERTS, P., OTTEN, B., DEYN, P. D., and CLERC, D. D.

[43] HATSOPOULOS, N., "Coupling the neural and physical dynamics in rhythmic movements," *Neural Computation*, vol. 8, pp. 567–581, 1996.

[44] HILL, A., *First and last experiments in muscle mechanics.* Cambridge: Cambridge University Press, 1970.

[45] HIRAI, K., HIROSE, M., HAIKAWA, Y., and TAKENAKA, T., "The development of the honda humanoid robot," in *Proceedings of the 1998 IEEE International Conference on Robotics and Automation*, (Leuven, Belgium), pp. 1321–1326, May 1998.

[46] HOBBELEN, D. and WISSE, M., "A disturbance rejection measure for limit cycle walkers: The gait sensitivity norm," *IEEE Transactions on Robotics*, 2007. in press.

[47] HODGKIN, A. and HUXLEY, A., "A quantitative description of membrane current and its application to conduction and excitation in nerve," *J. Physiol.*, vol. 117, pp. 500–544, 1952.

[48] HOF, A., *Multiple Muscle Systems: Biomechanics and Movement Organization.* New York: Springer-Verlag, Inc., 1990.

[49] HOGAN, N., "Adaptive control of mechanical impedance by coactivation of antagonist muscles," *IEEE Trans. Automat. Control*, vol. 28, pp. 681–690, August 1984.

[50] HURMUZLU, Y., BASDOGAN, C., and CAROLLO, J., "Presenting joint kinematics of human locomotion using phase plane portraits and Poincaré maps," *J. Biomech.*, vol. 27, no. 12, pp. 1495–1499, 1994.

[51] HURST, J., CHESTNUTT, J., and RIZZI, A., "An actuator with physically variable stiffness for highly dynamic legged locomotion," in *Proceedings of the 2004 IEEE International Conference on Robotics and Automation*, (New Orleans, LA), pp. 4662–4667, April 2004.

[52] KANDA, T., ISHIGURO, H., IMAI, M., and ONO, T., "Development and evaluation of interactive humanoid robots," *Proc. of the IEEE*, vol. 92, no. 11, pp. 1839–1850, 2004.

[53] KANDEL, E., SCHWARTZ, J., and JESSELL, T., eds., *Principles of Neural Science.* New York: McGraw-Hill, 4th ed., 2000.

[54] KANE, T. and LEVINSON, D., "Multibody dynamics," *ASME Journal of Applied Mechanics*, vol. 50, no. 4b, pp. 1071–1078, 1983.

[55] KANEKO, K., KANEHIRO, F., KAJITA, S., HIRUKAWA, H., KAWASAKI, T., HIRATA, M., AKACHI, K., and ISOZUMI, T., "Humanoid robot HRP-2," in *Proceedings of the 2004 IEEE International Conference on Robotics and Automation*, (New Orleans, LA), pp. 1083–1090, April 2004.

[56] KHATIB, O. and ROTH, B., "New robot mechanisms for new robot capabilities," in *Proceedings of the 1991 IEEE/RSJ International Conference on Intelligent Robots and Systems*, vol. 1, (Osaka, Japan), pp. 44–49, November 1991.

[57] KIM, J.-Y., PARK, I.-W., LEE, J., KIM, M.-S., CHO, B.-K., and OH, J.-H., "System design and dynamic walking of humanoid robot KHR-2," in *Proceedings of the 2005 IEEE International Conference on Robotics and Automation*, (Barcelona, Spain), pp. 1443–1448, April 2005.

[58] Koganezawa, K., Watanabe, Y., and Shimizu, N., "Antagonistic muscle-like actuator and its application to multi-d.o.f. forearm prosthesis," *Adv. Robotics*, vol. 12, no. 7,8, pp. 771–789, 1999.

[59] Kolacinski, R. and Quinn, R., "A novel biomimetic actuator system," *Robot. Auton. Syst.*, vol. 25, pp. 1–18, 1998.

[60] Kuo, A., "Energetics of actively powered locomotion using the simplest walking model," *ASME Journal of Biomechanical Engineering*, vol. 124, pp. 113–120, 2002.

[61] Kuo, A., "Choosing your steps carefully," *IEEE Robotics and Automation Magazine*, vol. 14, no. 2, pp. 18–29, 2007.

[62] Lacker, H., Chaudhry, H., Choi, T., Boda, W., Tapp, W., Reisman, S., Findley, T., and Engler, P., "Calculation of mechanical energy cost in a simple model of human walking," in *Proceedings of the 1993 IEEE Nineteenth Annual Northeast Bioengineering Conference*, (Newark, NJ), pp. 121 – 123, March 1993.

[63] Laurin-Kovitz, K., "Design of components for programmable passive impedance," in *Proceedings of the 1991 IEEE International Conference on Robotics and Automation*, vol. 2, (Sacramento, CA), pp. 1476–1481, April 1991.

[64] Lin, D. and Rymer, W., "A quantitative analysis of pendular motion of the lower leg in spastic human subjects," *IEEE Transactions on Biomedical Engineering*, vol. 38, no. 9, pp. 906–918, 1991.

[65] Loffler, K., Gienger, M., and Pfeiffer, F., "Model based control of a biped robot," in *Proceedings of the 7th International Workshop on Advanced Motion Control*, pp. 443–448, May 2002.

[66] Loncaric, J., *Geometrical Analysis of Compliant Mechanisms in Robotics*. PhD thesis, Harvard University, Cambridge, MA, 1985.

[67] Looije, R., Cnossen, F., and Neerincx, M., "Incorporating guidelines for health assistance into a socially intelligent robot," in *The 15th IEEE Int. Symp. on Robot and Human Interactive Communication, 2006 (ROMAN 2006)*, (Hatfield), pp. 515–520, Sept 2006.

[68] Marghitu, D. and Nalluri, P., "Nonlinear dynamic stability of normal and arthritic greyhounds," *Nonlinear Dynamics*, vol. 12, pp. 237–250, 1997.

[69] Marhefka, D. and Orin, D., "Simulation of contact using a nonlinear damping model," in *Proceedings of the 2005 IEEE International Conference on Robotics and Automation*, (Minneapolis, MN), April 1996.

[70] Marhefka, D. and Orin, D., "A compliant contact model with nonlinear damping for simulation of robotic systems," *IEEE Transactions on Systems, Man, and Cybernetics—Part A: Systems and Humans*, vol. 29, no. 6, pp. 566–572, 1999.

[71] Mason, P., "Dynamic stiffness and crossbridge action in muscle," *Biophys. Struct. Mechanisms*, vol. 4, pp. 15–25+, December 1978.

[72] MATSUOKA, K., "Sustained oscillations generated by mutually inhibiting neurons with adaptation," *Biol. Cybern.*, vol. 52, pp. 367–376, 1985.

[73] MATSUOKA, K., "Mechanisms of frequency and pattern control in the neural rhythm generators," *Biol. Cybern.*, vol. 56, pp. 345–353, 1987.

[74] MCGEER, T., "Passive dynamic walking," *Int. J. of Robotics Research*, vol. 9, no. 2, pp. 62–82, 1990.

[75] MCGEER, T., "Passive dynamic walking with knees," in *Proceedings of the 1990 IEEE International Conference on Robotics and Automation*, (Cincinnati, OH), pp. 1640–1645, April 1990.

[76] MCGEER, T., "Dynamics and control of bipedal locomotion," *J. Theor. Biol.*, vol. 163, pp. 277–314, 1993.

[77] MCGEER, T., "Dynamic walking robots and the W Prize," *IEEE Robotics and Automation Magazine*, vol. 14, no. 2, pp. 13–15, 2007.

[78] MENA, D., MANSOUR, J., and SIMON, S., "Analysis and synthesis of human swing leg motion during gait and its clinical applications," *J. Biomech.*, vol. 14, pp. 823–832, 1981.

[79] MIGLIORE, S., BROWN, E., and DEWEERTH, S., "Biologically inspired joint stiffness control," in *Proceedings of the 2005 IEEE International Conference on Robotics and Automation*, (Barcelona, Spain), pp. 4519–4524, April 2005.

[80] MIGLIORE, S., BROWN, E., and DEWEERTH, S., "Novel nonlinear elastic actuators for passively controlling robotic joint compliance," *ASME Journal of Mechanical Design*, vol. 129, pp. 406–412, April 2007.

[81] MOCHON, S. and MCMAHON, T., "Ballistic walking," *Biomechanics*, vol. 13, pp. 49–57, 1980.

[82] MORITA, T. and SUGANO, S., "Design and development of a new robot joint using a mechanical impedance adjuster," in *Proceedings of the 1995 IEEE International Conference on Robotics and Automation*, vol. 3, (Nagoya, Japan), pp. 2469–2475, May 1995.

[83] MORITA, T. and SUGANO, S., "Development of one-DoF robot arm equipped with mechanical impedance adjuster," in *Proceedings of the 1995 IEEE/RSJ International Conference on Intelligent Robots and Systems*, vol. 1, (Pittsburgh, PA), pp. 407–412, August 1995.

[84] NAKANISHI, J., MORIMOTO, J., ENDO, G., CHENG, G., SCHAAL, S., and KAWATO, M., "Learning from demonstration and adaptation of biped locomotion," *Robot. Auton. Syst.*, vol. 47, pp. 79–91, 2004.

[85] NAYFEY, A. and BALACHANDRAN, B., *Applied Nonlinear Dynamics*. New York: Wiley-Interscience, 1995.

[86] OGURA, Y., LIM, H. A. H., and TAKANISHI, A., "Development of a human-like walking robot having two 7-DoF legs and a 2-DoF waist," in *Proceedings of the 2004 IEEE International Conference on Robotics and Automation*, (New Orleans, LA), pp. 134–139, April 2004.

[87] OLENŠEK, A. and MATJAČIĆ, Z., "Further steps toward more human-like passive bipedal walking robots," in *Proceedings of the 2005 IEEE International Conference on Robotics and Automation*, (Barcelona, Spain), pp. 7–11, April 2005.

[88] ORLOVSKY, G., DELIAGINA, T., and GRILLNER, S., *Neuronal Control of Locomotion: From Mollusc to Man.* New York: Oxford Univ. Press, 1999.

[89] ORTEGA, R., SPONG, M., and GÓMEZ-ESTERN, F., "Stabilization of underactuated mechanical systems via interconnection and damping assignment," *IEEE Trans. Aut. Control*, vol. 47, no. 8, pp. 1281–1233, 2002.

[90] PANAT, P., *Classical Mechanics.* Harrow, U.K.: Alpha Science Int'l Ltd., 2004.

[91] PATAL, A. and PRENTICE, S., "The role of active forces and intersegmental dynamics in the control of limb trajectory over obstacles during locomotion in humans," *Exp. Brain Res.*, vol. 106, pp. 499–504, 1995.

[92] PIAZZA, S. and DELP, S., "The influence of muscles on knee flexion during the swing phase of gait," *J. Biomech.*, vol. 29, no. 6, pp. 723–733, 1995.

[93] PIAZZA, S. and DELP, S., "The influence of muscles on knee flexion during the swing phase of gait," *J. Biomech.*, vol. 29, no. 6, pp. 723–733, 1996.

[94] PRATT, G. and WILLIAMSON, M., "Series elastic actuators," in *Proceedings of the 1995 IEEE/RSJ International Conference on Intelligent Robots and Systems*, vol. 1, (Pittsburg, PA), pp. 399–406, July 1995.

[95] PRATT, J., DILWORTH, P., and PRATT, G., "Virtual model control of a bipedal walking robot," in *Proceedings of the 1997 IEEE International Conference on Robotics and Automation*, (Albuquerque, NM), pp. 193–198, 1997.

[96] PRATT, J., TORRES, A., DILWORTH, P., and PRATT, G., "Virtual actuator control," in *Proceedings of the 1996 IEEE/RSJ International Conference on Intelligent Robots and Systems*, vol. 3, (Pittsburg, PA), pp. 1219–1226, November 1996.

[97] PRATT, J. and PRATT, G., "Exploiting natural dynamics in the control of a 3D bipedal walking simulation," in *Proceedings of the 1999 International Conference on Climbing and Walking Robots (CLAWAR99)*, (Portsmouth, UK), September 1999.

[98] REID, M., "A parameter-space search algorithm tested on a Hodgkin-Huxley model," *Biol. Cybern.* submitted.

[99] RIENER, R. and EDRICH, T., "Identification of passive elastic joint moments in the lower extremities," *J. Biomech.*, vol. 32, pp. 539–544, 1999.

[100] ROBINSON, D., PRATT, J. E., PALUSKA, D. J., and PRATT, G. A., "Series elastic actuator development for a biomimetic walking robot," in *Proceedings of the 1999 IEEE/ASME International Conference on Advanced Intelligent Mechatronics*, pp. 561–568, September 1999.

[101] Rossignol, S., *Neural Control of Stereotypic Limb Movements*, ch. 5 of Handbook of Physiology, pp. 173–216. New York: The American Physiological Society, 1996.

[102] Sabourin, C. and Bruneau, O., "Robustness of the dynamic walk of a biped robot subjected to disturbing external forces by using CMAC neural networks," *Robot. Auton. Syst.*, vol. 51, pp. 81–99, 2005.

[103] Salisbury, K., "Active stiffness control of a manipulator in Cartesian coordinates," in *Proceedings of the 19th IEEE International Conference on Design and Control*, (Albuquerque, NM), pp. 95–100, September 1980.

[104] Sasaki, K. and Neptune, R., "Muscle mechanical work and elastic energy utilization during walking and running near the preferred gait transition speed," *Gait and Posture*, vol. 23, pp. 383–390, 2006.

[105] Schaal, S. and Sternad, D., "Programmable pattern generators," in *Proceedings of the International Conference on Computational Intelligence in Neuroscience (ICCIN '98)*, (Triangle Park, NC), 1998.

[106] Schillings, A., van Wezel, B., Mulder, T., and Duysens, J., "Muscular responses and movement strategies during stumbling over obstacles," *J. Neurophysiol.*, vol. 83, pp. 2093–2102, 2000.

[107] Schwab, A. and Wisse, M., "Basin of attraction of the simplest walking model," in *Proc. ASME Design Engineering Tech. Conf.*, no. DETC2001/VIB-21363, (Pittsburgh, PA), 2001.

[108] Sillar, K., "Spinal pattern generation and sensory gating mechanisms," *Current Opinion in Neurobiology*, vol. 1, pp. 583–589, 1991.

[109] Simoni, M., *Synthesis and Analysis of a Physical Model of Biological Rhythmic Motor Control with Sensorimotor Feedback*. PhD thesis, Georgia Inst. of Tech., April 2002.

[110] Sparrow, W., Hughes, K., Russell, A., and Rossignol, P., *Energetics of Human Activity*. Chicago: Human Kinetics, 2000.

[111] Strogatz, S., *Nonlinear Dynamics and Chaos*. Cambridge, MA: Perseus Books Publishing, LLC, 1994.

[112] Sugar, T. and Kumar, V., "Design and control of a compliant parallel manipulator," *ASME J. Mech. Des.*, vol. 124, pp. 676–683, December 2002.

[113] Taga, G., "A model of the neuro-musculo-skeletal system for human locomotion. i. emergence of basic gait," *Biol. Cybern.*, vol. 73, pp. 97–111, 1995.

[114] Taga, G., "A model of the neuro-musculo-skeletal system for human locomotion. II. real-time adaptability under various constraints," *Biol. Cybern.*, vol. 73, pp. 113–121, 1995.

[115] Taga, G., Yamaguchi, Y., and Shimizu, H., "Self-organized control of bipedal locomotion: Strategies for changing direction and for going over obstacles," *Biol. Cybern.*, vol. 65, pp. 147–159, 1991.

[116] Trease, B., Moon, Y.-M., and Kota, S., "Design of large-displacement compliant joints," *ASME J. Mech. Des.*, vol. 127, pp. 788–798, July 2005.

[117] Tucker, V., "The energetic cost of moving about," *American Scientist*, vol. 63, no. 4, pp. 413–419, 1975.

[118] U.S. Department of Labor, Washington, D.C., *OSHA Technical Manual*, 1999. TED 1-0.15A. Retrieved November 11, 2007.

[119] van der Linde, R., "Design, analysis, and control of a low power joint for walking robots, by phasic activation of McKibben muscles," *IEEE Trans. Rob. Autom.*, vol. 15, pp. 599–604, August 1999.

[120] Verrelst, B., Vanderborght, B., Vermeulen, J., Ham, R. V., Naudet, J., and Lefeber, D., "Control architecture for the pneumatically actuated dynamic walking biped "Lucy"," *Mechatronics*, vol. 15, pp. 703–729, 2005.

[121] Vukobratovic, M. and Juricic, D., "Contribution to the synthesis of biped gait," *IEEE Trans. Biomed. Eng.*, vol. 16, no. 1, pp. 1–6, 1969.

[122] Wadden, T. and Ekeberg, Ö., "A neuro-mechanical model of legged locomotion: Single leg control," *Biol. Cybern.*, vol. 79, pp. 161–173, 1998.

[123] Wadden, T., Hellgren, J., Lansner, A., and Grillner, S., "Intersegmental coordination in the lamprey: Simulations using a network model without segmental boundaries," *Biol. Cybern.*, vol. 76, pp. 1–9, 1997.

[124] Wheeless, C., *Wheeless' Textbook of Orthopaedics*. http://www.wheelessonline.com: Data Trace Publishing Company, 2005. Book on-line. Retrieved October 3, 2006.

[125] Wieber, P., "On the stability of walking systems," in *Proceedings of the Third IARP International Workshop on Humanoid and Human Friendly Robotics*, (Tsukuba, Japan), 2002.

[126] Williams, C. and DeWeerth, S., "A comparison of resonance tuning with positive versus negative sensory feedback," *Biol. Cybern.*, vol. 96, June 2007.

[127] Williamson, M., "Series elastic actuators," Master's thesis, Mass. Inst. Technol., January 1995.

[128] Williamson, M., "Neural control of rhythmic arm movements," *Neural Networks*, vol. 11, pp. 1379–1394, 1998.

[129] Williamson, M., *Robot Arm Control Exploiting Natural Dynamics*. PhD thesis, Mass. Inst. Technol., June 1999.

[130] Winter, D., "Human balance and posture control during standing and walking," *Gait and Posture*, vol. 3, pp. 193–214, 1995.

[131] Wisse, M., Guillaume, F., Frankenhuyzen, J., and Moyer, B., "Passive-based walking robot," *IEEE Robotics and Automation Magazine*, vol. 14, pp. 52–62, June 2007.

[132] WISSE, M., SCHWAB, A., and LINDE, R., "A 3D passive dynamic biped with yaw and roll compensation," *Robotica*, vol. 19, pp. 275–284, 2001.

[133] WISSE, M. and VAN FRANKENHUYZEN, J., "Design and construction of MIKE; a 2D autonomous biped based on passive dynamic walking," in *Proceedings of the Second International Symposium on Adaptive Motion of Animals and Machines*, (Kyoto, Japan), March 2003.

[134] YAMAGUCHI, J., NISHINO, D., and TAKANISHI, A., "Realization of dynamic biped walking varying joint stiffness using antagonistic driven joints," in *Proceedings of the 1998 IEEE International Conference on Robotics and Automation*, (Leuven, Belgium), pp. 2022–2029, May 1998.

[135] YAMAGUCHI, J. and TAKANISHI, A., "Design of biped walking robots having antagonistic driven joints using nonlinear spring mechanism," in *Proceedings of the 1997 IEEE/RSJ International Conference on Intelligent Robots and Systems*, vol. 1, (Grenoble, France), pp. 251–259, September 1997.

[136] YU, X., NGUYEN, B., and FRIESEN, W., "Sensory feedback can coordinate the swimming activity of the leech," *J. Neurosci.*, vol. 19, no. 11, pp. 4634–4643, 1999.

[137] ZATSIORSKY, V., *Kinetics of Human Motion*. Champaign, IL: Human Kinetics, 2002.

VITA

Shane Migliore was born in Lawrenceville, GA in 1979 and moved to South Florida in 1980. He attended both private and public schools within Palm Beach County, eventually graduating in 1996 as co-valedictorian of William T. Dwyer High School in Palm Beach Gardens, FL. From 1996 through 2001, he attended Boston University in Boston, MA, earning a B.S. in Biomedical Engineering. During this period, he also completed a one-year Co-Op with Johnson & Johnson Professional, specializing in orthopedic instrument manufacturing. He then attended the Georgia Institute of Technology in Atlanta, GA from 2001 through 2007. In 2004, he earned a M.S. in Electrical Engineering. In December 2007, he completed the requirements for a Ph.D. in Electrical Engineering and subsequently graduated in April 2008. He currently lives in Albuquerque, NM with his wife, Bobbi-Jo.